ANALYSIS OF BOUNDARY LAYER FLOW OVER A BULLET-SHAPED OBJECT WITH A QUASI-LINEARIZATION ITERATIVE SCHEME

by

Mohammad Ali
Roll No.: 0413094001, Session: April 2013
Registration No: 1005282

DOCTOR OF PHILOSOPHY
IN
MATHEMATICS

Department of Mathematics
BANGLADESH UNIVERSITY OF ENGINEERING AND TECHNOLOGY
Dhaka 1000, Bangladesh

March 2021

The thesis entitled **"ANALYSIS Of BOUNDARY LAYER FLOW OVER A BULLET-SHAPED OBJECT WITH A QUASI-LINEARIZATION ITERATIVE SCHEME"**, submitted by **Mohammad Ali**, ROLL NO: 0413094001, Session: April 2013 has been accepted as satisfactory in partial fulfillment of the requirement for the degree of Doctor of Philosophy in Mathematics on March 28, 2021.

BOARD OF EXAMINERS

A. Alim

1.______________________________

Dr. Md. Abdul Alim — Chairman (Supervisor)
Professor
Department of Mathematics, BUET, Dhaka-1000

2.______________________________

Head — Member (Ex-officio)
Department of Mathematics
BUET, Dhaka-1000

3.______________________________

Dr. Md. Mustafa Kamal Chowdhury — Member
Professor
Department of Mathematics, BUET, Dhaka-1000

4.______________________________

Dr. Md. Abdul Hakim Khan — Member
Professor
Department of Mathematics, BUET, Dhaka-1000

5.______________________________

Dr. Md. Manirul Alam Sarker — Member
Professor
Department of Mathematics, BUET, Dhaka-1000

6. ______________________________

Dr. Md. Mashud Karim Member
Professor
Department of NAME
BUET, Dhaka-1000

7. ______________________________

Dr. S. Reaz Ahmed Member
Professor
Department of Mechanical Engineering
BUET, Dhaka-1000

8. ______________________________

Dr. Md. Abdus Samad Member (External)
Professor
Department of Applied Mathematics
University of Dhaka, Dhaka-1000, Bangladesh.

AUTHORS' DECLARATION

This is to certify that the outcome of this dissertation has been presented by the author under the supervision of Dr. Md. Abdul Alim, Professor, Department of Mathematics, Bangladesh University of Engineering and Technology (BUET), Dhaka-1000, and that it has not been submitted anywhere for the award of any degree or diploma.

Mohammad Ali

Date: 28 March 2021

DEDICATION

I would like to dedicate this present work to my dear beautiful parents for their supplication to Allah for helping me to succeed in my work.

This dissertation is dedicated to the memory of my family members. I wish Allah to give forgiveness to them.

In the end, I would like to dedicate this work to all of my colleagues and friends who know me and love the best things happening to me.

ACKNOWLEDGMENT

I am bending my head with the heartiest gratitude to Almighty Allah, who helped me to finish this piece of work. He is only powerful, compassionate, kind, and merciful in this Universe. I also offer my deepest gratitude to the Holy Prophet Muhammad who was the torch of guidance for humanity.

During the period of this degree, there have been many people who have assisted, encouraged, and supported me to complete my doctorate. In particular, I wish to thank my honorable and respected supervisor, Professor Dr. Md Abdul Alim, and all of my board members, for their guidance, advice, comments, and support throughout this research work. It was an honor and privilege of working with my supervisor and being exposed to his infinite source of knowledge in the field of computational fluid dynamics. I would like to thank Dr. Khandker Farid Uddin Ahmed, Professor, and Head of, Department of Mathematics, BUET, for his support in allowing me to use the departmental facilities in various stages of my research work and also the staff of this Department for their cooperation in this work. Then I should not forget to acknowledge Prof. Dr. Syed Ali Afzal Computational Mathematics Laboratory, Department of Mathematics, BUET, Dhaka, and also faculty members in this Department. I would like to express my gratitude to my juniors Mishkat Mohammad, Mahathir Mohammad, and Muhimin Mohammad, and also to my mother, wife, brothers, and sisters. I wish to thank the Deptartment of Mathematics, CUET, Chittagong, and all faculty members in this Department particularly Professor Dr. Mohammad Shah Alam for his patience, good humor, and unfailing interest in my work.

Finally, I'll never forget the support of my board of examiner members during the study period at the Ph.D. level. That is how I'd like to thank a lot Professor Dr. S. Reaz Ahmed, Professor Dr. Md. Mashud Karim, Professor Dr. Md. Mustafa Kamal Chowdhury, Professor Dr. Md. Manirul Alam Sarker, Professor Dr. Md. Abdul Hakim Khan, Professor Dr. Khandker Farid Uddin Ahmed and Professor Dr. Md. Abdus Samad for the valuable scientific criticism, good cooperation, and patience. I wish to register my appreciation and gratitude to the Ministry of Science and Technology, Bangladesh (NST fellowship) for supporting me financially during the period of study at the Ph.D. level.

ABSTRACT

The two-dimensional steady and unsteady incompressible axisymmetric mixed convection magnetohydrodynamic boundary layer flow with heat transfer over a power-law stretching bullet-shaped object has been investigated. The main purpose of this dissertation is to discuss the effect of shape and size (surface thickness parameter *s*) and the stretching factor of the bullet-shaped object on the fluid velocity and temperature distributions within the boundary layer. So, the present study focuses on the boundary layer flow of the physical relevance and accurate trends which are sufficient in the theory of laminar boundary layer flow. Therefore, fluid flow and heat transfer have been investigated in two types of flow geometries such as the thicker surface $\left(s \geq 2\right)$ and the thinner surface $\left(0 < s < 2\right)$ of the bullet-shaped object. The equations for momentum and heat transfer have been transformed into a system of ordinary differential equations (ODEs) by using suitable local similarity transformations. In this dissertation, the spectral quasi-linearization method (SQLM) has been applied to solve the system of non-linear ODEs. This method helps to identify the accuracy, validity, and convergence of the present solution. It is seen that the SQLM is highly accurate, computationally efficient, and easy to implement. The investigation shows the surface thickness parameter and stretching ratio parameter have a significant effect on fluid flow and heat transfer processes and which cannot be neglected. The numerical results have been compared with the previous work, and the results reveal that the accuracy is acceptable which validating the present numerical code. The impact of various controlling parameters on velocity profile, temperature profile, skin friction, and Nusselt number have been analyzed and computed through graphs. The including parameters are the Prandtl number (Pr), Eckert Number (Ec), magnetic parameter (M), power-law index parameter (m), the suction/injection parameter (f_w), mixed convection parameter (λ), heat generation parameter (Q^*), stretching ratio parameter (ϵ), surface thickness parameter (s), Darcy number (Da), drag inertia coefficient (γ), unsteady parameter (A) and stream-wise coordinate (X) on the fluid flow and heat transfer characteristics. The investigation shows that in the case of a thicker bullet-shaped object $\left(s \geq 2\right)$ the velocity profile does not approach the ambient condition asymptotically but intersects the axis with a steep angle

and the boundary layer structure has no definite shape whereas in the case of a thinner bullet-shaped object $(0 < s < 2)$ the velocity profile converge the ambient condition asymptotically and the boundary layer structure has a definite shape. It is also noticed that thinner bullet-shaped object acts as good cooling conductor compared to thicker bullet-shaped object and the wall friction can be reduced much when thinner bullet-shaped object $(0 < s < 2)$ is used rather than the thicker bullet-shaped object $(s \geq 2)$ in both types of static or moving bullet-shaped object $(\varepsilon = \text{or} > 0)$. The correlation coefficient and the regression model have been established for the mentioned parameters. The correlation analysis represents that the stretching ratio parameter, surface thickness parameter, and drag inertia coefficient are positively correlated with the velocity gradient but the magnetic parameter, location parameter, and suction parameter are negatively correlated. Again, the temperature gradient is positively correlated with the Prandtl number, unsteady parameter, stretching ratio parameter, mixed convection parameter, and suction parameter but negatively correlated with magnetic parameter, heat generation parameter, Eckert number, drag inertia coefficient, Darcy number, and surface thickness parameter. Hence, the major outcome of the current research work shows that the thinner bullet-shaped object is suitable for fluid flow and heat transfer compared with the thicker-bullet object. The results may be useful in explaining the heat transfer rate and the skin friction in industrial sectors such as the purpose of the cooling device in nuclear reactors, automotive engineering, electronic engineering, biomedical engineering, control the cooling rate, and quality of the desired product.

TABLE OF CONTENTS

LIST OF TABLES

LIST OF FIGURES

NOMENCLATURE

Latin alphabet

Symbols	Designation	Unit
P	Pressure force	$kg.m^{-1}.s^{-2}$ (Pa)
c_p	Specific heat at constant pressure	kj/kg.K
C_f	The local skin friction coefficient	
K	Thermal conductivity	$[kgm^{-1}s^{-1}K^{-1}]$
B_0	Magnetic field coefficient	$[Wbm^{-2}]$
x	Dimensional axial direction along the surface	[m]
r	The dimensional radial direction is perpendicular to the axial direction	[m]
u	Velocity component along the axial direction	$[ms^{-1}]$
v	Velocity component along radial direction	$[ms^{-1}]$
U_w	Stretching velocity of the bullet-shaped object	$[ms^{-1}]$
U	Free stream velocity of the fluid	$[ms^{-1}]$
f_w	Suction/injection	
$f(\eta)$	Dimensionless stream function	
$f'(\eta)$	Dimensionless velocity	
$f''(\eta)$	Dimensionless velocity gradient	
t	time	[s]
a	Stretching rate constant	
b	Free stream rate constant	

c	Positive constant with dimension temperature	
d	Positive constant with dimension per unit time	
s	Surface thickness parameter	
L	Reference length of the body	
q_w	Local surface heat flux	[Wm^2]
Q	Heat generation/absorbsion	[Wm^3]
Q*	Dimensionless heat source/sink parameter	
g	Acceleration due to gravity vector	[ms^{-2}]
T	The absolute free temperature of the fluid	[K]
T_w	The surface temperature of the bullet-shaped object	[K]
T_∞	The temperature of the free stream fluid	[K]

Greek alphabet

τ_w	Shear stress at the surface	
ε	Dimensionless stretching ratio parameter	
β	Coefficient of thermal expansion	
λ	Mixed convection parameter	
γ	Drag inertia coefficient	
δ	Boundary layer thickness	
μ	Dynamic viscosity of the fluid	[$kgm^{-1}s^{-1}$]
η	Dimensionless similarity variable	
σ_{ij}	Total stress tensor	[Nm^{-2}]
ρ	The density of the fluid	[kgm^{-3}]

α	Thermal diffusivity	$[m^2s^{-1}]$
ν	Kinematic viscosity of the fluid	$[m^2s^{-1}]$
Ψ	Stream function	$[m^{-2}s^{-1}]$
$\theta(\eta)$	Dimensionless temperature	
$\theta'(\eta)$	Temperature gradient	
∇	Gradient operator	

Dimensionless numbers/parameters

Pr	Prandtl number
$\mathrm{Re}_x = \frac{Ux}{\nu}$	Local Reynolds number
Gr	Grashof number
Ec	Eckert number
Da	Darcy number
Nu	Local Nusselt number
A	Unsteadiness parameter
M	Magnetic parameter
X	Location parameter (Stream-wise coordinate)

Superscript

'	Prime denotes differentiation concerning η
m	Power-law index parameter

Subscript

w	Condition at the surface of the bullet-shaped object
∞	Condition of free stream

Abbreviations

MHD	Magnetohydrodynamic
NS	Navier-Stokes
BL	Boundary layer
ODE’s	Ordinary differential equations
QLM	Quasi-linearization Method
SQLM	Spectral Quasi-linearization Method
PDE’s	Partial Differential Equations

CHAPTER ONE

INTRODUCTION

1.1 Introduction

The boundary layer theory [1] is important when fluid flows over a solid surface that is moving or stationary. The effective shape of the body may change leading to changes in pressure distribution, as a result, the overall lift and drag forces change for the effect of the boundary layer. Besides the application of this theory, one can calculate the local skin friction drag of a body when the body moves through the fluid such as the wing of an airplane or a complete ship and a turbine blade. Therefore, the Boundary layer theory helps in designing aerofoil's, to calculate the lift and drag forces for the aerospace and automobile designers, to control the heat transfer rate from the device, etc. Therefore, the current research will help design various types of bullet-shaped objects such as Rocket, Missile, Airplane, Bullet Train, and Submarine, etc. The fluid flow over a static surface is a fundamental problem of fluid mechanics which is well known as the Blasius problem. In this case, Blasius considers that the velocity of the free stream is constant and parallel to the plate. If the free stream fluid makes a positive angle with the solid objects then the free stream accelerates along with the objects and this type of flow is known as wedge flow. Falkner and Skan [2] established a similar solution in the case of wedge flow like Blasius's problem. Most of the work has been done with the assumption of constant fluid properties. When the fluid has constant properties then the problem is uncoupled, as a result, the momentum equation has an effect on the energy equation but the energy equation does not affect the momentum equation. However, most fluids are temperature-dependent viscosity, and this property changes significantly when the temperature changes largely. In this situation, the two equations are coupled and each equation influences the other. However, in many real-world problems, this assumption is not valid and it is necessary to analyze such problems by assuming variable viscosities. It is known that viscosities of liquids vary with temperature, since if the temperature changes from 10ºC to 50ºC then the viscosity of water reduces by about 24%. The present problem has been described as the transport of momentum, and temperature distribution. Therefore, heat transfer is related to the movement of fluids. So, fluid properties are the heat transport mechanism. But two types of convection are occurred such as (i) natural or free convection, and (ii) forced convection. In the case of natural convection, the molecules are moved for buoyancy forces that arise from density variation in the fluid. Forced convection is occurred due to additional forces such as a pump or fan. A combined effect of natural and forced is called mixed convection. Radiation is another mode of heat transfer due to electromagnetic waves which are not in direct physical contact with each other or when the bodies are separated from each other in space with different temperatures. The fluid is driven by the movement of the fluid which is resting upon or the surfaces contained in, pressure gradient and buoyancy force for density variation. The density gradient occurs when temperature or concentration differences arise. Therefore, the Boundary layer theory can serve humanity and the design of solid objects which move through fluids either liquid or gas. The fluid dynamics in the case of a stretching surface have important applications in engineering technology and also in the industrial sector such as polymers processing, recovery of oil, processing of food, and paper production, etc. In the process of drawing, their surfaces need to be stretched and the quality of the desired product depends on the rate of heat transfer and mass transfer of the stretching surface. Therefore, rates of cooling and mass transfer have to be controlled effectively to attain the expected quality of the desired product. In this regard, the present analysis is to extend the class of stretching problems by introducing a linear stretching velocity and variable wall temperature distribution on the surface with variable fluid properties. Most of the problems in fluid dynamics are related to nonlinearity and most of them don't have an analytical solution. Therefore, these types of nonlinear equations need to be solved using suitable methods. Some of them are solved using the analytical method of perturbation and some of them are solved using the numerical technique. So the governing PDEs have been transformed into ODEs by applying local similarity transformation. These equations are then solved by SQLM with MATLAB.

1.2 Types of Fluid

The three states of the fluid are liquid, gaseous, and plasma. The fluid dynamics deals of 1^{st} 2^{nd} states and the third one in plasma dynamics. Again, fluid dynamics are classified as hydrodynamics that is related to liquids and aerodynamics that are related to air and other gases. So various types of fluids are discussed in the following subsection.

1.2.1 Ideal fluid or frictionless fluid

When the fluids are in motion and if no tangential force exists between the two layers of fluids but act only normal force with each other and this type of fluids is called Ideal fluids or Inviscid fluids or frictionless fluids. That is ideal fluid has no internal friction. This type of fluid is absent but this property helps us to simplify the mathematical analysis. Therefore, the low viscosity of fluids such as water and air can be treated as ideal fluids with specific conditions.

1.2.2 Viscous fluid or real fluid

Viscosity is a phenomenon that is related to surface tension and compressibility that resists their shear deformation by providing resistance between the layers of the fluid. There are two types of viscous or real fluids such as Newtonian fluids and non-Newtonian fluids.

1.2.3 Viscosity and Newtonian fluid

Newtonian fluids are defined which obey the linear relationship between the shear stress and the shear strain rate. Therefore, these fluids have a linear relationship between viscosity and shear stress. The diagram between shear stress and the rate of shear for Newtonian fluids represents a straight line. The Newtonian fluids are water, kerosene, gasoline, air and other gases, and other oil-based liquids. In two-dimensional laminar, incompressible flow the shear stress is directly proportional to velocity gradient and is defined as $\tau_w = \mu \frac{\partial u}{\partial y}$, where τ_w is the wall shear stress, μ is the proportionality constant and is called dynamic viscosity. The maximum shear stress has occurred at the wall because of the no-slip condition. This linear relationship is observed in the case of Newtonian fluids.

1.2.4 Non-Newtonian fluid

The Non-Newtonian fluids do not obey the Newtonian law of viscosity. These types of fluids are polymer solutions, lubricants, paints, condensed milk, coal-tar, paste, honey, plastics, molasses, printer ink, molten rubber, collides, macro/molecular materials, etc.

1.2.5 Compressible and incompressible fluid

In the case of an incompressible fluid, the density remains constant with the change of pressure, temperature, and velocity, etc. but in the case of the compressible fluid, the density is not constant. The actual condition for incompressible flow is that divergence of velocity must be zero which comes from the continuity equation. This also means that if the density changes even then the flow can be incompressible if the divergence of velocity is zero. Hence liquid can be treated as incompressible fluid and gases are compressible fluid.

1.3 The Basic Definition of Important Keywords

1.3.1 Magnetohydrodynamics (MHD)

Magnetohydrodynamics (MHD) is the flow of electrically conducting fluid in the presence of a magnetic field. Magnetohydrodynamic consists of the words magnetic meaning magneto, hydro-meaning water (or liquid), and dynamics meaning the motion of an object under influence of forces. The main concept of magnetohydrodynamic is that in the case of the conductive fluid magnetic field can induce a current, that creates forces on the fluid and also changes the magnetic field itself. Magnetohydrodynamics occurs when the effective collision frequency of electrons is far more than the frequency of the applied fields and also where inertial effects and displacement currents are neglected. Therefore, when an electrically conducting solid or denser fluid moves in a magnetic field, it experiences a force that tends to move it perpendicularly to the electric field. In the case of fluid, this happens due to the magnetic field acting on both electrons and ionized atoms. The motion of the electrically conducting fluid past a magnetic field induces a current known as Hall current. A mechanical force is created by the magnetic field on the induced electric currents. This electric current flows perpendicularly to both the magnetic field and the direction of the fluid flow. This induced current, in turn, produces an induced magnetic field. The above statements have proposed by Faraday when he worked on magnetohydrodynamic (MHD) flows. When the liquid or gas is used as a conductor, then a force is generated which is called electromagnetic force. Therefore, the boundary layer equations take this electromagnetic force (Lorentz forces). These phenomena are called magneto-hydrodynamics (MHD). Besides, when the fluid moves in the presence of the magnetic field two key physical factors arise. If gravitational force is absent, then a regular magneto-fluid dynamics assumption is equal to the electric force and Lorentz force. Since the density of electric force is less than the Lorentz force, then the density of electric force can be neglected. Hence, the MHD is added to the momentum equation to handle the electromagnetic force. The magnetic effect will also be helpful to the field of cell separation, magnetic resonance imaging (MRI), drug and gene delivery, artificial muscle application, etc.

1.3.2 Boussinesq approximation

The Boussinesq approximation is considered for the two aspects. The first one is density variation which is ignored in the continuity equation. The second one happens for the temperature variation. In presence of temperature or concentration variation in the fluid then density differences occur in the fluid, as a result, the gravitational force drives the flow. Due to temperature and density differences, the hot particles lose potential energy and gain kinetic energy, as a result, bulk fluid motion arises. This type of flow is called the buoyancy force. The body force and the gravitational force are related to the temperature variation which is known as the Boussinesq approximation.

1.3.3 Prandtl boundary layer theory

The boundary-layer concept began with Ludwig Prandtl's [3] examined the motion of a fluid by considering very low viscosity which was submitted at the Third International Congress of Mathematicians in August 1904, at Heidelberg and also published this paper in the Proceedings of the Congress in the current year. This paper highlighted the history of fluid flow and the way for understanding the motion of real fluids. He showed that when the fluid flows past a body which is divided into two regions: a very thin layer close to the solid body where the viscosity is important known as the viscous region, and the other region outside this layer is called the inviscid region where the viscosity can be neglected. When the fluid flows over a solid surface that is moving or stationary a “no-slip condition” arises because of the viscosity of the fluid. That is the velocity of the fluid near the solid body continuously decreases downstream. But far from the surface, this speed is equal to the free stream velocity. Thus a thin layer will be formed near the solid body with a velocity gradient. This thin layer is called the boundary layer. The thickness of the boundary layer depends on various factors such as viscosity, velocity, injection/suction, etc. The thickness of the boundary layer is increasing along the downstream direction.

Prandtl’s consider the two conditions for developing the boundary layer equations from NS equations such as

I. The viscous layer must be a very thin region relative to the characteristic dimension of the object, that is, $\frac{\delta}{L} << 1$, where L is the characteristic length of the body and δ is the distance far from the surface of the body at which velocity attains its free-stream velocity. Therefore, the BL thickness is directly proportional to the viscosity and inversely proportional to the Reynolds number.

II. The largest viscous term and any inertia term must be the same approximate in magnitude.

1.3.4 Similarity solutions

Blasius first derived the similarity solution of Prandtl’s boundary layer equations in 1908. He considered the flow along with a thin flat plate. For this region, he introduced a new independent variable, called the similarity variable. Therefore, the continuity and momentum equations were transformed into a single ordinary differential equation by using this variable.

The continuity and momentum equations for laminar flows are explained by the similarity concept when these are applied to an external boundary-layer flow subject to the boundary conditions (section 2.7) $v_w = 0$. In general, the solution of Equations (2.4.3) and (2.4.6) for a laminar flow with *u(x)* and $u_e(x)$ given, is $\frac{u}{u_e} = f(x,y)$. Here *f* is a general function and η is called a similarity variable. If η is a function of *x* and *y*, then $\frac{u}{u_e} = f(\eta)$. Further, Falkner-Skan have been used similarity variable η, dimensionless stream function $f(\eta)$, and dimensional stream function $\psi(x,y)$ which defined as

$$\eta = y\sqrt{\frac{u_e}{\nu x}} \tag{1.3.1}$$

$$\psi(x,y) = f(\eta)\sqrt{u_e \nu x}\text{ , and } u = \frac{\partial \psi}{\partial x} \quad \text{and } v = -\frac{\partial \psi}{\partial y} \tag{1.3.2}$$

By using this transformation, the Falkner-Skan equation can be converted to,

$$f'''(\eta) + \frac{(1+m)}{2} f(\eta) f''(\eta) + m\left[1 - f'^2(\eta)\right] = 0 \tag{1.3.3}$$

Where *m* is the pressure gradient parameter and is related to wedge angle. The velocity components *u* and *v* are defined as

$$u = u_e f'(\eta) \text{ and } v = -\sqrt{u_e \nu x}\left[\frac{f(\eta)}{\sqrt{u_e x}} \frac{d}{dx}\sqrt{u_e x} + f'(\eta)\frac{\partial \eta}{\partial x}\right] \tag{1.3.4}$$

The transformed boundary conditions are

$$\begin{aligned} f(\eta) = f_w(\eta) &= -\frac{1}{\sqrt{u_e \nu x}} \int_0^x v_w(x)dx \text{ at } \eta = 0 \\ f'(\eta) &= 1 \text{ at } \eta = \eta_e \end{aligned} \tag{1.3.5}$$

Here η_e is a transformed boundary-layer thickness and is defined as $\eta_e = \delta\sqrt{\frac{u_e}{\nu x}}$

The nonzero $f_w(\eta)$ corresponds to suction\injection for the surface mass transfer. The requirement for the parameter m to be constant is satisfied if the external velocity varies with x as

$$u_e = Cx^m \tag{1.3.6}$$

where C is constant and m is the pressure gradient parameter.

When there is surface mass transfer and u_e varies with x then $v_w(x)$ can take the form $v_w(x) = x^n$ where n is constant, then $f_w(\eta)$ must vary with x as $f_w(\eta) = x^{\frac{(2n+1-m)}{2}}$ and $f_w(\eta)$ becomes constant only when

$$2n+1-m=0 \Rightarrow n = \frac{m-1}{2} \tag{1.3.7}$$

Therefore, the free stream velocity varies with x as power-law index m but in absence of mass transfer, then n varies with m. These types of flow are known as similar flow.

1.3.5 Velocity boundary layer

The velocity boundary layer is associated with the presence of velocity variation and shear stress. The fluid particles adjacent to the solid surface are motionless relative to the solid boundary, as a result, the no-slip condition arises which is limited to much thin region close to the solid surface, known as the viscous or momentum boundary layer. In this thin region, there is a quick change in the velocity of the fluid from zero to the free stream value. Therefore, in the case of viscous fluid, the thickness of the velocity boundary layer is denoted by the perpendicular distance from the solid surface, where the velocity of the fluid becomes 0.99% of the free stream velocity. The thickness of the boundary layer decreases with a decrease in viscosity of the medium, but even for small viscosity, the shear stress $\tau_w = \mu \frac{\partial u}{\partial y}$ is important due to the large velocity gradient. Besides, the porosity of the porous surface also has a great effect on the size of the viscous boundary layer.

1.3.6 Thermal boundary layer

The thermal boundary layer is formed due to the presence of temperature gradients and heat transfer between the solid-fluid interface and the fluid in the free stream. In the solid-fluid interface, the contact of the fluid particles takes the temperature of the interface. Therefore, the interface temperature is higher than the surrounding fluid temperature, as a result, the kinetic energy of the molecules of the adjacent fluid particles enhances. These particles transfer the gained kinetic energy in the adjacent fluid layers. This process continues in the adjacent fluid layers and the temperature gradients develop in the fluid. Besides the thermal BL depends on the thermal conductivity of the medium i.e. the thermal BL thickness is directly proportional to the thermal conductivity of the medium.

1.3.7 No-slip condition

When fluid flows over a solid surface that is moving or stationary a layer of fluid in contact with the solid surface is motionless relative to the surface. This layer of fluid has zero velocity and is known as the no-slip condition.

1.4 Heat Transfer

Heat transfer is defined as the transfer of thermal energy from a hotter place to a cooler place. When an object is situated at a different temperature the heat flow or heat exchange occurs in three different ways such as conduction, convection, and radiation so that the temperature reaches thermal equilibrium. Therefore, heat transfer always occurs from a higher temperature to a lower temperature.

1.5 Methodology

1.5.1 Spectral Quasi-linearization method (SQLM)

The SQLM [4] is a combination of two methods: (i) the Quasi-linearization method (QLM) and (ii) the Chebyshev spectral collocation method. The QLM is the generalization of Newton–Raphson-based method and is used to linearize the non-linear ODEs into linear ODEs. The QLM approaches that the difference between the approximate solution at the present iteration and the previous iteration is very small. Suppose if Y_{r+1} and Y_r are the presents and previous iteration then $\left[Y_{r+1} - Y_r\right] < 0$. The non-linear ODEs and PDEs which arise in the field of engineering, science, fluid dynamics, solid mechanics, heat, and mass transfer are solved by using the QLM. Bellman and Kalaba [5] were the first to apply the QLM about half a century ago to solve nonlinear ordinary and partial differential equations. Since the differential equation is highly non-linear and it is almost impossible to find the closed-form analytic solution. Later Bellman et al. [6] estimated the chemical reaction rate by using the QLM. Thus, for numerical calculation, we need to choose an appropriate numerical technique. The quadratic convergence property is the advantage of this technique. Three to six iterations are needed for getting five-digit accuracy if the technique converges. It has been applied extensively to a lot of research areas. The numerical simulation of the present problem is obtained with the help of SQLM which gives highly accurate results. Since the similarity variable converges to $\eta \to \infty$ but the present simulation has been performed for a finite domain of η. Therefore, the dimensionless velocity and energy distribution within the boundary layer asymptotically tends to a free stream velocity that satisfies the boundary conditions. The mentioned all other parameters are considered to be some fixed values for finding the self-similar solution.

1.5.1.1 Quasi-linearization algorithm

The higher-order non-linear differential equation converts into a system of first-order non – linear differential equations by using suitable substitution. Therefore, the following steps are considered:

Step-1: First linearization of the given differential equations about the guess solution.

Step-2: These may be calculated in case of initial value problems by using initial conditions.

Step-3: The present solution is compared with the previous (guess) solution, if the difference is within the tolerable limit, and then stops the procedure otherwise by considering the present solution as the guess solution and go to step -2.

The general form of m-th order non-linear system of first-order ODEs with $x_1, x_2, x_3, \ldots\ldots x_m$ as dependent variables and η as an independent variable may be represented as:

$$\overline{X'} = \overline{f}\left(\overline{X}, \eta\right) \tag{1.5.1}$$

Where

$$\overline{X} = \left[x_1,\ x_2,\ x_3,\ x_4,\ \ldots\ldots x_m\right]^T$$
$$\overline{X'} = \left[x_1',\ \mathrm{x}_2',\ \mathrm{x}_3',\ \mathrm{x}_4',\ \ldots\ldots \mathrm{x}_\mathrm{m}'\right]^T$$
$$\overline{f} = \left[f_1, f_2, f_3, f_4,\ \ldots\ldots f_m\right]^T = \overline{f}\left(\overline{X}, \eta\right)$$

Now the nominal trajectories which are known as the known solution and neighboring trajectories which are known as solutions in the neighborhood of nominal trajectories are denoted by $\overline{X^0}$ and $\overline{X^1}$. By performing Taylor's series expansion of the differential equations in (1.5.1) about the nominal trajectories $\overline{X^0}$, and retaining the terms up to the first order only, the neighboring trajectories $\overline{X^1}$ may be approximated. For example, $X_1'^1(\eta)$ maybe expressed in terms of $\overline{X^0}(\eta)$ as,

$$\begin{aligned} X_1'^1(\eta) &= f_1\left(\overline{x^0}, \eta\right) + \left[\frac{\partial f_1}{\partial x_1}\right]_{\overline{x^0}} \left[x_1^1(\eta) - x_1^0(\eta)\right] + \left[\frac{\partial f_1}{\partial x_2}\right]_{\overline{x^0}} \left[x_2^1(\eta) - x_2^0(\eta)\right] \\ &+ \left[\frac{\partial f_1}{\partial x_3}\right]_{\overline{x^0}} \left[x_3^1(\eta) - x_3^0(\eta)\right] + \ldots\ldots + \left[\frac{\partial f_1}{\partial x_m}\right]_{\overline{x^0}} \left[x_m^1(\eta) - x_m^0(\eta)\right] \end{aligned} \tag{1.5.2}$$

The equations (1.5.2) can be rearranged as

$$X_1'^1(\eta) = a_{11}x_1^1(\eta) + a_{12}x_2^1(\eta) + a_{13}x_3^1(\eta) + \ldots\ldots + a_{1m}x_m^1(\eta) + e_1(\eta) \tag{1.5.3}$$

Where $a_{1j} = \left[\dfrac{\partial f_1}{\partial x_j}\right]_{\overline{x^0}}$ *and* $\mathrm{e_i} = f_1\left(\overline{x^0}, \eta\right) - \sum_{j=1}^{m} \left[\dfrac{\partial f_1}{\partial x_j}\right]_{\overline{x^0}} x_j^0$

Similarly, the other differential equations can be performed and all the resulting differential equations may be collectively written as

$$\overline{X'} = A\overline{X} + \bar{e} \tag{1.5.4}$$

The elements of A and $\bar{e}$ may be expressed as

$$a_{ij} = \left[\frac{\partial f_i}{\partial x_j}\right]_{\overline{x^0}} \; and \; \mathrm{e_i} = f_1\left(\overline{x^0}, \eta\right) - \sum_{j=1}^{m}\left[\frac{\partial f_i}{\partial x_j}\right]_{\overline{x^0}} x_j^0, for \text{ i,j = 1 to m}$$

To illustrate the method let us consider m = 5. Therefore, the general form of a fifth-order linear system of ordinary differential with $[x_1,\ x_2,\ x_3,\ x_4 \text{ and } x_5]$ as dependent variables and η as an independent variable may be represented as $\overline{X'} = A\overline{X} + \bar{e}$.

Where

$$\overline{X} = [x_1,\ x_2,\ x_3,\ x_4,\ x_5]^T$$
$$\overline{X'} = [x_1',\ x_2',\ x_3',\ x_4',\ x_5']^T \left(Note : x' = \frac{dx}{d\eta}\right)$$

Let the following three initial boundary conditions: $x_1(\eta_0) = x_{10}, x_2(\eta_0) = x_{20}$ and $x_4(\eta_0) = x_{40}$. The other two final boundary conditions may be specified for any two of the dependent variables. Let us first consider the homogeneous part of the differential equation (1.5.4) as,

$$\overline{X'} = A\overline{X} \text{ with the condition } \overline{X}(\eta_0) = [0\ 0\ 1\ 0\ 0]^T \tag{1.5.5}$$

The solution is $\overline{X^{H1}}(\eta)$ [Homogeneous solution 1]

Now, for another initial condition of equation (1.5.5) are $\overline{X}(\eta_0) = [0\ 0\ \ 0\ 0\ 1]^T$ and the solution is $\overline{X^{H2}}(\eta)$ [Homogeneous solution 2].

For getting the particular solution, we get $\overline{X'} = A\overline{X} + \bar{e}$ with the conditions $\overline{X^0}(\eta_0) = [x_{10},\ x_{20},\ 0,\ x_{40},\ 0]^T$. Therefore, the solution is $\overline{X^p}(\eta)$ [particular solution]. Since the differential equations are linear, the principle of superposition holds and the complete solution may be written as,

$\overline{X}(\eta) = C_1\overline{X^{H1}}(\eta) + C_2\overline{X^{H2}}(\eta) + \overline{X^p}(\eta)$, where C_1 and C_2 are integrating constants.

To get the integrating constants to let x_2 and x_4 be imposed with final conditions as:

$$x_2(\eta_f) = x_{2f}, x_4(\eta_f) = x_{4f}$$

1.5.1.2 Condition for convergence

Let us assume x_r represents the solution at previous iterations and x_{r+1} represents the solution at the next iteration. So, the convergence of this iteration scheme is defined by the expression $\|Ax_{r+1} - Ax_r\| < \delta$, where $\|.\|$ is the vector norm and $\delta \neq 0$ is very small. The crucial expectation of a numerical method are the ability to converge to a fixed point. In the case where the method does not converge, divergence occurs and the iterative method is observed to be unstable.

1.6 Dimensionless Numbers

Every physical problem has some physical quantities that can be measured in different units. In the dimensional analysis, we use the fundamental units of each physical quantity. So the dimensionless number is defined as without these units. There are two different methods for finding the dimensionless parameters such as inspection and dimensionless analysis. The dimensionless analysis method has been used for the current study. The governing equations are converted into dimensionless equations by using certain similarity variables. In this process, some dimensionless numbers appear as the co-efficient of various terms in these equations. Some of them are used in this thesis that explained below.

1.6.1 Reynolds number

Reynolds number is the ratio of inertia forces to viscous forces within a fluid and it is defined as $\mathrm{Re} = \frac{\rho u L}{\mu}$. Where ρ is the fluid density, u is the fluid velocity, L is the characteristic dimension of the body, μ is the fluid dynamic viscosity. In the case of low Reynolds number that is viscous force is high compared to inertia force and as a result, any disturbance that arises in the flow field will be damped by the action of viscous force. So when viscous force dominates on inertia force then the flow will be laminar. On the other hand, if the reverse trend arises then the flow will be turbulent.

1.6.2 Prandtl number

Prandtl number is the characteristic behavior of the fluid property and it is denoted as $\Pr = \frac{\nu}{\alpha} = \frac{\mu c_p}{\kappa}$. Where ν is the kinematic viscosity, $\nu = \frac{\mu}{\rho}$, α is the thermal diffusivity, $\alpha = \frac{\kappa}{\rho c_p}$, μ is the dynamic viscosity, K is the thermal conductivity, c_p is the specific heat capacity at constant pressure, ρ is the density. A fluid with a Prandtl number equal to one means thermal and velocity boundary layers thickness is equal. For instance, water vapor at 700K has a Prandtl number of 1. Fluids that are good conductors of heat have a relatively large value of α and this occurrence is found in liquid metals whose Prandtl numbers are correspondingly small, such as Mercury (Pr = 0.023).

1.6.3 Eckert number

The Eckert number is defined as $Ec = \frac{U^2}{c_p\left(T_w - T_\infty\right)}$. Therefore, Ec is the ratio of kinetic energy and enthalpy in the flow. The Eckert number converts the kinetic energy into internal energy. The Eckert number is greater than zero means cooling of the stretching surface that is heat loss from the sheet to the fluid and the negative value of Ec represents the opposite meaning.

1.6.4 Skin friction coefficient

The skin friction occurred between the friction of the fluid layers and the surface of the body which is moving through the fluid. Therefore, the skin friction coefficient is defined in terms of wall shear stress at the surface as $c_f = \frac{2\tau_w}{\rho U^2}$, where $\tau_w = \mu\left(\frac{\partial u}{\partial y}\right)_{y=0}$ is the wall shear stress, ρ is the fluid density, U is the fluid free stream velocity.

1.6.5 Nusselt number

Nusselt number (Nu) is defined as the dimensionless heat transfer coefficient. Nusselt number is measured as the ratio of conduction and convection. Nusselt number is thus defined as the dimensionless temperature gradient at the surface and provides a measure of the convection heat transfer. Therefore, the Nusselt number can be defined as $Nu = \frac{h(T_w - T)}{\kappa (T_w - T)/L} = \frac{hL}{\kappa}$, where h is the heat transfer coefficient, T_w and T is the surface and fluid temperature respectively, L is the characteristic length of the surface, K is the thermal conductivity, and then the convective heat transfer from the wall will depend upon the magnitude of $h(T_w - T)$. On the other hand, in the case of conduction, the heat transfer rate measure would be the quantity $\kappa (T_w - T)/L$.

1.7 Literature Survey for the Present Problem

The study of laminar two-dimensional boundary layer flow and energy transfer over a stretching bullet-shaped object or any other geometrical object has obtained important applications in automobile engineering and aerodynamic engineering. For this reason, the boundary layer theory helps us to calculate the lift and the drag forces for the aerospace and automobile designers, to control the energy transfer from the device, etc. Therefore, the present work will help design various types of bullet-shaped objects such as Rocket, Missile, Airplane, Bullet Train, and Submarine, etc.

Ludwig Prandtl concluded that when fluid flows over a solid surface it's divided into two regions. One is near the solid surface due to the viscosity of the fluid and another one is far from the solid boundary which is known as non-viscous flow. The fluid layer which is in contact with the surface is motionless relative to the surface. This layer of fluid retards the movement of an adjacent layer of fluid, as a result, a thin layer is developed due to the viscosity of the fluid. This is known as the Prandtl BL theory. Falkner and Skan [2] proved that the similarity solution exists when the fluid layer is not parallel to the surface and the free stream velocity is non-linear. This type of flow is known as wedge flow. It is derived from the N-S equations by considering the steady, laminar, two-dimensional, and incompressible flow for a single-sided bounded flow applying the local similarity transformation with adverse or favorable pressure gradient. Due to the high applicability of the problem, a huge work related to the present problem has been done by many authors. Abbasbandy and Hayat [7] studied the MHD Falkner-Skan boundary flow by homotopy analysis method. Abo-Eldahab [8] investigated the laminar BL flow of non-Newtonian fluid and energy transfer over a stretching surface by taking power-law index and heat flux. The thermal BL thickness decreases for the increasing values of mixed convection but the reverse trend arises due to viscous dissipation, as a result, the energy transfer decreases. Aftab et al. [9] analyzed the boundary layer power-law fluid flow over a moving permeable flat plate with viscous dissipation and heat generation. Ahmad et al. [10] studied the mixed convection BL flow by using the SQLM. This study concluded that the SQLM is suitable than another method. Later Ahmad et al. [11] performed Bellman QLM for Neumann problems. Ajala et al. [12] analyzed the BL flow and energy transfer by the effect of the magnetic field, variable viscosity, and thermal radiation. Ajaykumar and Srinivasa [13] studied the effect of variable viscosity on unsteady MHD laminar BL flow with heat transfer over a stretching surface. Alam et al. [14] discussed the results through the graph and also tabular form. It is obtained that the velocity field decreases for increasing values of velocity ratio parameter but increases for the magnetic parameter, unsteady parameter, permeability parameter, and pressure gradient parameter. The temperature profiles decrease for thermophoresis parameter Prandtl number and velocity ratio parameter whereas the temperature remains unchanged for Brownian motion parameter. Again, nanoparticle concentration profile increases for Brownian motion parameter but decreases for thermophoresis parameter, Lewis number, and velocity ratio parameter. Alarifi, et al. [15] discussed the influence of the sink or source on MHD boundary layer flow with heat transfer over a vertical stretching surface. Asaithambi [16] discussed the Falkner – Skan equation by applying the finite difference method and found a similar solution. Ashwini [17] discussed that the boundary layer separation is delayed due to magnetic field parameter and the dual solutions are arises in case of decelerating flow regime. Ashwini and Eswara [18] performed the unsteady MHD decelerating boundary layer wedge flow with heat generation. Awaludin et al. [19] developed the stability model of MHD boundary layer flow over a stretching wedge. Daba et al. [20] studied the mixed convection BL flow and heat transfer with convective boundary conditions over a vertical stretching surface. Fatheah and Hendi [21] established the analytic solution of the MHD boundary layer Falkner-Skan flow over a porous surface. Fenuga et al. [22] studied the mixed convection MHD boundary layer stagnation-point flow with heat over a non-linear vertical stretching surface. Ganapathirao [23] investigated that the unsteady parameter is significantly affected the velocity, energy, and concentration profiles, the local skin friction coefficient, the local Nusselt, and Sherwood numbers. Hartree [24] solved the Falkner – Skan problem and find the numerical solution for wall shear stress for various values of the pressure gradient parameter. Hayat et al. [25] analyzed the MHD BL stagnation point flow past a stretching surface. The results obtained that the velocity distribution decreases for increasing values of Weisenberg number and the temperature profile decrease for increasing values of the Prandtl number. Later Hayat et al. [26] investigated the MHD stagnation point flow and heat transfer over a stretching surface. Herwig et al. [27] were the first who attempted to solve the Falkner-Skan problem by considering variable viscosity. Irfan et al. [28] studied the unsteady MHD BL stagnant point flow over a porous stretching/shrinking surface with thermal radiation. Ismoen et al. [29] studied the impermeable wedge flow for the effects of buoyancy force and power-law index of wall temperature and free stream velocity and found that the velocity and energy profiles are significantly affected by these parameters. Jabeen et al. [30] studied the MHD BL flow past a nonlinear stretching surface by using the semi-analytical method and see that the flow field is significantly affected by the injection /suction parameters. Further, Jabeen et al. [31] studied the MHD boundary layer flow and heat transfer in a porous medium by applying the differential transformation method. Jenifer et al. [32] discussed the unsteady mixed convection MHD flow and mass transfer over a sphere with mass transfer in the case of water. Kandasamy et al. [33] analyzed the MHD BL flow with chemical reaction and heat source and observed that the increasing values of chemical reaction decelerate the fluid motion, energy distribution, and mass of the fluid along the wall of the wedge due to the uniform suction and heat source. Keshtkar [34] performed Falkner-Skan boundary layer flow with variable parameters over a wedge-shaped geometry and observed that the shear stress and heat transfer rate are an increasing function of the pressure gradient parameter. Krishna et al. [35] studied the hall and ion slip effects on BL flow by considering various conditions. It is observed that the resultant velocity increases with an enhancing the Hall and ion slip parameters throughout the boundary layer region. Later Krishna et al. [36] discussed the MHD boundary layer oscillatory rotating micro-polar fluid flow with Thermal radiation and chemical reaction. Further Krishna et al. [37] developed the influence of the Hall and ion slip-on unsteady magnetohydrodynamic boundary layer rotating flow over an exponentially accelerated surface through a saturated porous medium. Next, Krishna et al. [38] analyzed the boundary layer flow over an infinite vertical flat porous surface with heat and mass transfer. Kumar and Krishnan [39] examined the boundary layer flow over an axisymmetric circular cylinder and seen that the analytical solution reduce to establish the result for planar boundary layer with infinite radius of curvature. Lakshmikantham [40] discussed the extension of the quasi-linearization method. Lin et al. [41] studied the Falkner-Skan problem by applying the similarity solution and suggest that this method is valuable for the cases in which the exact solutions are not available. Mandelzweig and Tabakin [42] applied the Quasi-linearization method in physics for solving nonlinear problems. Marneni [43] observed that the BL thicknesses reduce with the increase of the Eckert number when the free stream flow is faster than the wedge stretching velocity. Megahed et al. [44] analyzed the unsteady MHD BL flow and heat transfer along a stretching surface by the effect of heat flux. Menni et al. [45] presented the fluid flow and heat transfer analysis in the presence of various conditions. Mustaqim [46] analyzed the stability analysis of the boundary layer stagnation-point flow over a shrinking sheet with radiation and slip effects. Muthukumaran [47] discussed the BL flow of heat and mass transfer over a continuously stretching isothermal vertical surface in case of uniform suction and chemical reaction. It is seen that the mass and velocity distribution increase for increasing the reaction rate and decrease for decreasing reaction rate. Muzara et al. [48] studied the BL flow of Jeffrey's fluid over a vertical porous plate with the effect of the thermal radiation and chemical reaction. Later Muzara et al. [49] studied the two-dimensional Bratu problem using vibrate SQLM. Further Muzara et al. [50] analyzed the Bratu Problem by applying SQLM. Nageeb et al. [51] discussed the mixed convection boundary layer nanofluid flow over a stretching surface by using the spectral relaxation method. Further, Nageeb et al. [52] investigated the mixed convection MHD nanofluid flow and heat transfer over a stretching surface using the SRM. Najwa et al. [53] discussed the BL flow over an exponentially shrinking cylinder with heat transfer and established the dual solutions. Nandy et al. [54] performed the MHD boundary layer nanofluid flow and heat transfer over a permeable shrinking surface. Naramgari and Sulochana [55] analyzed the MHD boundary layer nanofluid flow over a permeable stretching/shrinking surface with suction/injection. Nasrin and Alim [56] investigated the relationship between the forced convective semi-empirical analysis through a solar collector. Nield and Bejan [57] presented a detailed analysis of the convection in porous media. Nieto [58] proposed the generalized quasi-linearization method in the case of second-order ODEs with Dirichlet boundary conditions. Norihan et al. [59] studied the effect of a convective boundary condition on the boundary layer flow over a stretching surface. Rajagopal et al. [60] initiated the analysis of non-Newtonian fluid on the Falkner–Skan flow. The boundary layer flow and heat transfer over a stretching sheet with the effect of the inclined magnetic field and cross-diffusion are examined by Raju et al. [61]. It is seen that the velocity profiles increase for increasing aligned angle and magnetic field strength and increases the energy transfer rate. Ramesh et al. [62] addressed the MHD boundary layer flow over a constant wedge within porous media by using local similarity transformation. Reddy et al. [63] analyzed the comparative study of boundary layer non-Newtonian fluid flows and heat transfer over a stretching surface with the help of chemical reaction and radiation effects. Magnetohydrodynamic boundary layer slips Cu nanofluids flow over a stretching surface with variable thermal conductivity was provided by Reddy et al. [64]. Rehman et al. [65] examined an unsteady boundary layer thin-film flow and heat transfer over a stretching surface with the influence of the dynamic viscosity. Rudra and Sharma [66] studied the steady laminar BL free-forced flow of a Newtonian fluid past a wedge-shaped surface. It is observed that the skin friction, heat flux, and mass flux increases for increasing values of the magnetic parameter and at a low level of chemical reaction parameter the velocity, temperature and concentration increases gradually but for a higher level the reverse is true. The steady mixed convection BL flow over a wedge with variable viscosity and variable surface temperature were analyzed by

Rudra and Sharma [67]. It is observed that the flow separation can be controlled by varying the surface temperature and the shape of the wedge. Sakiadis [68] was first discussed the forced convective BL flow over a stretching solid surface with constant velocity. Salleh et al. [69] studied the MHD boundary layer nanofluid flow over a vertical thin needle with the help of stability analysis. Numerical analysis of MHD forced convection flow with heat transfer over a shrinking surface with nonlinear radiation and viscous dissipation was provided by Samuel Raj et al. [70]. Seddeek et al. [71] discussed the influence of the variable viscosity and thermal conductivity on magnetohydrodynamic Falkner-Skan boundary layer flow and heat transfer over a wedge. Shaw et al. [72] studied the effects of slip parameters on boundary layer nanofluid flow over a stretching surface. It is observed that the solutions depend on the slip parameters and the dual solution enhances with this parameter. Soid et al. [73] analyzed the unsteady MHD stagnation flow along with a stretching/shrinking sheet by considering the viscous dissipation and Ohmic heating. The results indicate that dual solutions exist only for the shrinking sheet case. Srinivas and Kishan [74] studied the unsteady magnetohydrodynamic boundary layer nanofluid flow with heat transfer over a permeable shrinking surface with the influence of the thermal radiation and chemical reaction parameters. Sulochana et al. [75] studied the MHD boundary layer nanofluid flow over an exponentially stretching sheet with the cross-diffusion effect. It is noticed that an increase in the aligned magnetic field decreases the velocity profiles of the flow. The heat transfer rate enhances with the increasing effect of the soret and Dufour numbers. Ullah et al. [76] discussed the MHD boundary layer Casson fluid flow and heat transfer over a stretching wedge by considering viscous dissipation and Newtonian heating. Yohannes, et al. [77] examined the MHD boundary layer nanofluid flow past a stretching surface with viscous dissipation and chemical reaction through a porous media. The results observed that Cu-water nanofluid shows a thicker momentum boundary than Ag-water nanofluid whereas the reverse trend occurs in the case of the thermal boundary layer. Nandy et al. [78] studied the unsteady magnetohydrodynamic boundary layer nanofluid flow with heat and mass transfer over a permeable shrinking surface due to thermal radiation.

The literature review shows that the above works are limited to the flow of either a flat plate or a cone-shaped surface or wedge or cylindrical shape surface with various physical conditions but the present research work is not available in the literature so the results are novel. The innovation of this present problem lies in the unification of more physical parameters into the governing equations and an attempt to give a detailed analysis of how the flow properties are affected by these parameters. Also, the novelty of the current paper lies in the application of the recently developed numerical method to solve these highly nonlinear equations. In all these studies related to non-linear PDEs, the SQLM has been established to be accurate and computationally efficient. It is because finding the numerical calculation the authors are encouraged to choose the SQLM. The effects or influences of non-dimensional governing pertinent parameter on the dimensionless velocity field, and temperature field as well as velocity gradient and temperature gradient, has been discussed with the aid of graphs also developed the correlation coefficient and multiple regressions. The main purpose of this work is to investigate the magnetohydrodynamic boundary layer flow and heat transfer over a stretching bullet-shaped object with the effect of the surface thickness parameter (shape and size of the object), magnetic parameter, stretching ratio parameter, mixed convection parameter, Prandtl number, Eckert number, heat generation parameter, Darcy number, drag inertia coefficient, location parameter on velocity and energy distribution, skin friction coefficient, Nusselt number, nature of solutions within the boundary layer region by using SQLM.

1.8 Problem Statement

The literature review shows that the above works are limited to the flow of either a flat plate or a cone-shaped surface or wedge or cylindrical shape surface with various physical conditions but on basis of the Google search, no research work has been published related to bullet-shaped geometry. The purpose of this present problem is to investigate the magnetohydrodynamic axisymmetric boundary layer flow and energy transfer over a stretching/shrinking bullet-shaped object with the influence of the surface thickness parameter, magnetic parameter, surface stretching parameter, mixed convection parameter, Prandtl number, Eckert number, heat generation parameter, Darcy number, drag inertia coefficient, location parameter on fluid velocity and temperature distribution within the boundary layer region, skin friction coefficient (velocity gradient), Nusselt number (rate of energy transfer), nature of solutions within the BL region by applying SQLM.

1.9 Research Objectives

The proposed work is to investigate the fluid flow and thermal behavior of fluid inside the boundary layer around a bullet-shaped object by using the SQLM. Therefore, the present study has been analyzed the effect of various physical parameters within the BL and its impact on the development of the boundary layer thickness. The specific aims of this work are

i. To predict the effects of the shape and size (surface thickness parameter) of the bullet-shaped object on the fluid flow and heat transfer within the boundary layer region.

ii. To determine the velocity and energy distribution within the BL for the effect of the various dimensionless parameters.

iii. To analyze the local skin friction coefficient and local Nusselt number for the effect of the various dimensionless parameters.

iv. To evaluate the correlation coefficient and multiple regression model among the controlling parameters, velocity, and temperature gradient.

v. To identify the parameters which are either positively or negatively correlated with velocity and temperature gradient.

vi. To identify the flow separation and critical points within the boundary layer.

1.10 Applications

The common area of boundary layer flow along a solid surface is the field of aerodynamics. The main purpose of this theory is to calculate the skin friction drag of a surface like the drag of an airplane, wing of the airplane, drag of a ship or boat, etc. Besides the design of a moving object is performed based on the BL theory like the design of a tennis ball, golf ball and cricket ball, etc. Therefore, the current research will be helpful in the field of automobile and aerospace engineering. Besides, this type of flow has attracted many researchers due to its applications in MHD generators, heat transfer, paper production, wire drawing, glass fiber, plasma studies, nuclear reactors, geothermal energy extractions, etc.

1.11 Structure of this Dissertation

The present work has been focused on two-dimensional axisymmetric MHD BL flow and heat transfer over a power-law stretching bullet-shaped object under various controlling parameters. The numerical computation has been discussed for the two types of bullet-shaped objects. The main body of the dissertation consists of seven chapters with a conclusion. In each chapter, a specific problem has been investigated. The chapters are:

Chapter one is purely introductory and gives motivation to the investigations carried out of this dissertation also contains the methodology, history, and literature related to the present problem.

Chapter two has been performed with basic equations and governing the flow and heat transfer. The governing equations of continuity, momentum, and energy have also been presented. A detailed description of the fundamental equations of boundary layer theory has been discussed. This chapter contains the elementary field equations of fluid dynamics as partial differential equations in terms of unknown parameters such as velocity, pressure, and energy variables. The boundary layer equations for continuity, momentum, and energy transport are developed for reference to physical models and consider subsequently.

Chapter three has been made on forced convection MHD axisymmetric BL flow and heat transfer over a linear stretching bullet-shaped object. The numerical calculations have been performed for two different velocities of stretching surface (ϵ) such as (i) the surface velocity is slower than free stream velocity ($\epsilon > 1$), and (ii) the surface velocity is greater than the free stream velocity ($\epsilon < 1$) and also two different shapes and size of the bullet-shaped object.

In this chapter, the governing PDEs and their associated boundary conditions have been converted into a dimensionless form by applying local similarity transformations. The resulting system of equations is then solved numerically by using the SQLM. The obtained numerical results have been compared with previously published work and found to be in good agreement. The effects of the magnetic parameter (M), power-law index parameter (m), stretching ratio (ϵ), surface thickness parameter (s), and Prandtl number (Pr) on the fluid velocity and temperature profiles have been investigated and depicted through graphs. Besides, the skin friction coefficient and the Nusselt number have been presented in a tabular form. The correlation coefficient and multiple regression model have been developed between the controlling parameters and the fluid velocity and temperature gradient

Chapter four contains the study of two-dimensional mixed convection axisymmetric BL flow with heat transfer over a non–linear stretching bullet-shaped object in the presence of internal heat generation and viscous dissipation. The numerical calculation has been done for the same cases as discussed in chapter three. The effect of magnetic parameter, mixed convection parameter, heat generation parameter, power-law index parameter, stretching ratio parameter, Prandtl number, Eckert number, and surface thickness parameter, on velocity and temperature distributions, skin friction coefficient, and Nusselt number have been examined and displayed through graphs. Also, the numerical values of velocity and temperature gradient have been tabulated in tabular form. The correlation coefficient and multiple regression model have been analyzed for the velocity gradient and temperature gradient with the mentioned parameters.

Chapter five has been performed on mixed convection axisymmetric boundary layer flow and heat transfer over an exponentially stretching bullet-shaped object in the presence of internal heat generation and viscous dissipation for the same cases as discussed in chapter three. The effect of magnetic parameter, mixed convection parameter, heat generation parameter, power-law index parameter, location parameter, Darcy number, drag inertia coefficient, Eckert number, Prandtl number, stretching ratio parameter, and surface thickness parameter, on velocity profile, temperature profile, skin friction coefficient, and Nusselt number have been presented graphically and elucidated in detail. Also, the numerical values of velocity gradient and temperature gradient have been tabulated in tabular form. The correlation coefficient and multiple regression model have also been developed for the velocity and temperature gradient with the mentioned parameters.

Chapter six depicts the unsteady mixed convection axisymmetric MHD BL flow and heat transfer over an exponentially stretching bullet-shaped object. The effect of unsteady parameter, magnetic parameter, mixed convection parameter, heat generation parameter, power-law index parameter, location parameter, Darcy number, drag inertia coefficient, Eckert number, Prandtl number, stretching ratio parameter, and surface thickness parameter, on velocity distribution, temperature distribution, skin friction coefficient, and Nusselt number have been presented graphically and explained in detail. Also, the numerical values of velocity gradient and temperature gradient have been displayed in tabular form. The correlation coefficient and multiple regression model have been established for velocity gradient and temperature gradient with the mentioned parameters.

Chapter seven is organized by the conclusion and recommendations of chapters 2 - 6. In this chapter, the authors have been discussed the conclusions of the present work and also further extension of this work. The bibliography has also been added to this chapter.

CHAPTER TWO

GOVERNING EQUATIONS

In case of any real-world problem for deriving a mathematical model fluid dynamics performs some basic criteria for developing the model. These criteria are converted into governing equations such as the NS equations. These equations perform the fluid motion and arise from Newton's second law of motion including the viscous force and pressure force.

2.1 Navier-Stokes (NS) Equations

The NS equations are the fundamental PDEs of fluid dynamics. The NS equations may be derived by applying infinitesimal or finite control volume, and the governing equations can be expressed in differential or integral forms. In the case of the three-dimensional incompressible flow, the following continuity and momentum equations can be written as:

Continuity equation

$$\frac{\partial u}{\partial x}+\frac{\partial v}{\partial y}+\frac{\partial w}{\partial z}=0 \tag{2.2.1}$$

Momentum equation for X-component

$$\frac{Du}{Dt}=-\frac{1}{\rho}\frac{\partial p}{\partial x}+\frac{1}{\rho}\left(\frac{\partial \sigma_{xx}}{\partial x}+\frac{\partial \sigma_{xy}}{\partial y}+\frac{\partial \sigma_{xz}}{\partial z}\right)+f_x \tag{2.2.2}$$

Momentum equation for Y-component

$$\frac{Du}{Dt}=-\frac{1}{\rho}\frac{\partial p}{\partial y}+\frac{1}{\rho}\left(\frac{\partial \sigma_{yx}}{\partial x}+\frac{\partial \sigma_{yy}}{\partial y}+\frac{\partial \sigma_{yz}}{\partial z}\right)+f_y \tag{2.2.3}$$

Momentum equation for Z-component

$$\frac{Du}{Dt}=-\frac{1}{\rho}\frac{\partial p}{\partial z}+\frac{1}{\rho}\left(\frac{\partial \sigma_{zx}}{\partial x}+\frac{\partial \sigma_{zy}}{\partial y}+\frac{\partial \sigma_{zz}}{\partial z}\right)+f_z \tag{2.2.4}$$

where $\frac{D}{Dt}$ represents the substantial derivative given by

$$\frac{D(\ )}{Dt} = \frac{\partial(\ )}{\partial t} + u\frac{\partial(\ )}{\partial x} + v\frac{\partial(\ )}{\partial y} + w\frac{\partial(\ )}{\partial z} = \frac{\partial(\ )}{\partial t} + \vec{V}.\nabla(\ ) \qquad (2.2.5)$$

The above equations represent Newton's second law of motion in which the L.H.S represents acceleration and R.H.S. represents the sum of net forces per unit volume. The first term on the right-hand side of equations (2.2.2) - (2.2.4) denotes the net pressure force per unit volume and the minus sign arises because a positive pressure acts inward. The second, third, and fourth terms defined the viscous forces per unit volume, and arise as a result of the different components of normal and shear stresses which shown in Figure 2.1 the first subscript to the symbol represents the direction of the stress, and the second the direction normal to the surface. By convention, outward normal stress acting on the fluid in the control volume is positive, and the shear stresses are taken as positive on the faces furthest from the origin of the coordinates. Thus σ_{xy} acts in the positive x-direction on the visible (upper) face perpendicular to the y-axis; corresponding shear stress acts in the negative x-direction on the invisible lower face perpendicular to the y-axis.

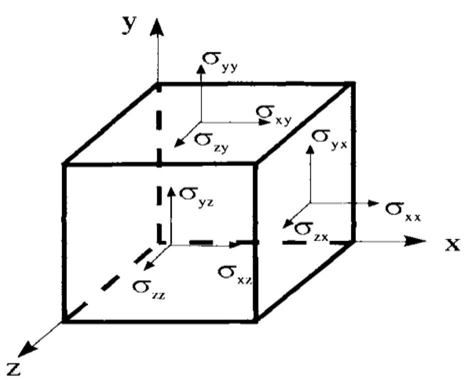

Figure 2. 1 The control volume faces of the viscous stress components surrounding the fluid

In tensor notation, the viscous terms in the momentum equations can be written as

$$\frac{\partial \sigma_{ij}}{\partial x_j} \qquad (2.2.6)$$

Where i, j = 1, 2 ,3 for three dimensional flows.

In the case of a Newtonian viscous fluid with constant density, the normal viscous stresses $\sigma_{ij}\left(i=j\right)$ and shear stresses $\sigma_{ij}\left(i\neq j\right)$ are obtained from the viscous stress tensor given by

$$\sigma_{ij}=\mu\left(\frac{\partial u_i}{\partial x_j}+\frac{\partial u_j}{\partial x_i}\right) \tag{2.2.7}$$

Equation (2.2.7) can be written as $\sigma_{ij}=2\mu S_{ij}$

Here $S_{ij}=\frac{1}{2}\left(\frac{\partial u_i}{\partial x_j}+\frac{\partial u_j}{\partial x_i}\right)$ is called the rate of the strain tensor. By using Equation (2.2.7), the normal viscous stress σ_{xx} and the shear stresses σ_{xy} and σ_{xz} in Equation (2.2.2) are given by

$$\sigma_{xx}=2\mu\frac{\partial u}{\partial x},\sigma_{xy}=\mu\left(\frac{\partial u}{\partial y}+\frac{\partial v}{\partial x}\right),\sigma_{xz}=\mu\left(\frac{\partial u}{\partial z}+\frac{\partial w}{\partial x}\right) \tag{2.2.8}$$

With similar expressions for the viscous stress tensor terms in Equations (2.2.3) and (2.2.4). According to Equation (2.2.7), the Navier-Stokes equations can be simplified, for example, the x-momentum equation of (2.2.2) for a Newtonian fluid becomes

$$\frac{Du}{Dt}=-\frac{1}{\rho}\frac{\partial p}{\partial x}+\nu\nabla^2 u+f_x \tag{2.2.9}$$

Similar expressions for the *y* and *z*-components were obtained from Equations (2.2.3) and (2.2.4). The equation (2.2.9) can be written in vector form as

$$\frac{D\vec{V}}{Dt}=-\frac{1}{\rho}\nabla p+\nu\nabla^2\vec{V}+\vec{f} \tag{2.2.10}$$

Where ∇^2 denoting the Laplacian operator and equivalent to

$$\frac{D\vec{V}}{Dt}=-\frac{1}{\rho}\nabla p+\nu\nabla^2\vec{V}+\vec{f}$$

2.2 Conservation Equations

The three conservation equations of mass, momentum, and energy can be written as

Equation of continuity:

$$\frac{\partial \rho}{\partial t}+\frac{\partial}{\partial x_j}\left(\rho u_j\right) \tag{2.3.1}$$

Conservation equation of momentum

$$\frac{\partial}{\partial t}\left(\rho u_j\right)+\frac{\partial}{\partial x_j}\left(\rho u_i u_j\right)+\frac{\partial p}{\partial x_i}=\frac{\partial}{\partial x_j}\left[\mu\left\{\frac{\partial u_i}{\partial x_j}+\frac{\partial u_j}{\partial x_i}-\frac{2}{3}\frac{\partial u_k}{\partial x_k}\delta_{ij}\right\}\right] \tag{2.3.2}$$

Conservation equation of energy

$$\rho\frac{Dh}{Dt}=\frac{Dp}{Dt}+\frac{\partial}{\partial x_j}\left(k\frac{\partial T}{\partial x_j}\right)+\frac{\partial u_i}{\partial x_j}\left[\mu\left\{\frac{\partial u_i}{\partial x_j}+\frac{\partial u_j}{\partial x_i}-\frac{2}{3}\frac{\partial u_k}{\partial x_k}\delta_{ij}\right\}\right] \tag{2.3.3}$$

These fundamental equations are applied to calculate all flow properties over any object. These equations are also the bottom of the BL theory.

2.3 Boundary-Layer Equations and Order Analysis

The BL equations are the reduced form of the NS equations based on some conditions and it occurs when the ratio of two length scales near the wall such L and δ, which represent the length of the body, and the BL thickness is sufficiently small because the δ terms are very small than the length of the body and the factor of $\frac{\delta}{L}$ can be neglected. Therefore, the ratio must be very less than one (i.e. $\frac{\delta}{L}<<1$). These equations are known as the BL equations. The BL thickness will decrease with the increases in Reynolds number and decrease in viscosity. Therefore, the BL thickness is directly proportional to the square root of the kinematic viscosity($\delta \propto \sqrt{\nu}$). By applying this relationship together with the free-stream velocity U_∞ and characteristic length of the body L, we have the relationship

$$\delta=\frac{L}{\sqrt{\mathrm{Re}_x}}, \text{ where } \mathrm{Re}_x=\frac{U_\infty L}{\nu} \tag{2.4.1}$$

From equation (2.4.1) it is observed that the BL thickness decreases for the larger values of the Reynolds number as compared with the length of the body.

According to Prandtl's [3] ideas for finding the order of magnitude, the scaled variables have been used so that L and U_∞ are reference length, and reference velocity. The symbols x and y are the physical coordinates in the diagram, and the symbols u and v are the dimensionless velocity components along the x and y directions, respectively. The continuity equation is

$$\frac{\partial u}{\partial x}+\frac{\partial v}{\partial y}=0$$

From the scaling transformation, we know that order of u is $o(1)$. This means that the value of u lies between 0 and 1.

Since the velocity u varies in the range mentioned above, so the scaled variable x also varies from 0 to 1, that is the order of x is also $o(1)$. We can conclude that the derivative $\frac{\partial u}{\partial x}$ is also $o(1)$. From the continuity equation, we see that the sum of $\frac{\partial u}{\partial x}$ and $\frac{\partial v}{\partial y}$ must be zero; this forces the derivative $\frac{\partial v}{\partial y}$ to the order of $o(1)$. We know that the order of y is $o(\delta)$, where δ represents the BL thickness divided by the length L. In other words, δ is the scaled BL thickness. Because the order of the derivative $\frac{\partial v}{\partial y}$ is $o(1)$, we conclude that the scaled velocity component v varies across the BL must be off $o(\delta)$. We know from the kinematic condition that $v=0$ at the surface y = 0. Therefore, the magnitude of v must of $o(\delta)$. We note that δ is a very small quantity when the Reynolds number $\mathrm{Re}_L \ll 1$. We express this fact by stating $\delta \ll 1$. Therefore, the velocity component along the y-direction within the boundary is a very small quantity.

Now, according to Schlichting [1], we can use similar arguments for the two components of the NS equation. First, consider the component of x

$$u\frac{\partial u}{\partial x}+v\frac{\partial u}{\partial y}=-\frac{\partial p}{\partial x}+\frac{1}{\mathrm{Re}_L}\left(\frac{\partial^2 u}{\partial x^2}+\frac{\partial^2 u}{\partial y^2}\right)$$

$$1\ \frac{1}{1}\ +\delta\frac{1}{\delta}\qquad\qquad \delta^2\quad\left(\frac{1}{1}+\frac{1}{\delta^2}\right)$$

Under the equation of each term is the order of magnitude of that term. We have already discussed the order of magnitude of *u v*, and $\frac{\partial u}{\partial x}$. To estimate the order of magnitude $\frac{\partial u}{\partial y}$, we observe that u varies from 0 to 1 within the BL, while the variable y varies from 0 to δ. This is the reason for the estimate $\frac{\partial u}{\partial y}=o\left(\frac{1}{\delta}\right)$. For finding the order of magnitude of the second derivatives, we must use similar arguments. We have $\frac{\partial u}{\partial x}=o(1)$. So, this quantity must change from zero to one of the orders of unity in a scaled distance *x* that also changes from zero to one. This is the reason for estimating the order of $\frac{\partial^2 u}{\partial x^2}=o(1)$. In the same way, the derivative $\frac{\partial u}{\partial y}=o\left(\frac{1}{\delta}\right)$ which means that it varies from 0 to $\frac{1}{\delta}$ across the boundary layer, in a distance of the order *δ*. Therefore, we have the second derivative $\frac{\partial^2 u}{\partial y^2}=o\left(\frac{1}{\delta^2}\right)$.

Now, let us consider the y component of the NS equation.

$$u\frac{\partial v}{\partial x}+v\frac{\partial v}{\partial y}=-\frac{\partial p}{\partial y}+\frac{1}{\mathrm{Re}_L}\left(\frac{\partial^2 v}{\partial x^2}+\frac{\partial^2 v}{\partial y^2}\right)$$

$$1\ \delta\quad \delta\ 1\qquad\qquad \delta^2\quad\left(\delta\quad \frac{1}{\delta}\right)$$

In the same way, the order of magnitude of the derivatives is estimated which was outlined earlier. Since the viscous term of momentum equation along the *y*-direction is much weaker than that the *x*-direction and therefore neglected. The important factor of the above equation is that all the remaining terms are off $o(\delta)$. So that the pressure gradient term

$\frac{\partial p}{\partial y}$ must be in the same order. Because the variation of pressure along the y-direction within the BL must overcome the distance of $o(\delta)$. Hence, the scaled pressure changes across the BL will be $\Delta p = o(\delta^2)$. This is very small and can be neglected, which was Prandtl's assumption. In the BL the pressure change is negligible, but the pressure distribution over the surface of the object is calculated from the potential flow and will be assumed to be affected on the BL. This means that $\frac{\partial p}{\partial x}$ the momentum equation is inhomogeneity form, and we can neglect the v component momentum equation because all the terms are very small.

Therefore, in the scaling analysis, the viscous term along the x-component is negligible compared to the viscous term along the normal direction. Furthermore, the potential flow theory shows that the pressure gradient term along the x - momentum equation is neglected compared to the y momentum equation. Thus, we have two velocity equations for the two unknowns. Therefore, Prandtl's [3] BL equations for Newtonian flow can be written in the following form to avoid complexity. To avoid confusion, we have used the same symbols for the velocities and coordinates that were used earlier for scaled variables.

Equation of continuity

$$\frac{\partial u}{\partial x} + \frac{\partial v}{\partial y} = 0$$

Momentum equation

$$u\frac{\partial u}{\partial x} + v\frac{\partial u}{\partial y} = -\frac{1}{\rho}\frac{\partial p}{\partial x} + \nu\frac{\partial^2 u}{\partial y^2}$$

From this equation, p is not an unknown function but it has been absorbed into the boundary conditions by equating $\frac{dp}{dx}$ equal to the free stream value where Bernoulli's equation applies.

$$\frac{dp}{dx} = -\rho U_\infty \frac{dU_\infty}{dx}$$

In the case of a flat plate, the potential flow is taken as $u = U_\infty$. That is the pressure gradient is zero. Therefore, the NS equation of momentum refers to $u\frac{\partial u}{\partial x} + v\frac{\partial u}{\partial y} = \nu\frac{\partial^2 u}{\partial y^2}$.

2.4 Axisymmetric Flow

Axisymmetric flow means that satisfy the conditions such as (i) the flow pattern must be similar in every plane and passes through a particular straight-line and (ii) the pressure (p) force and the velocity components are independent of the angular variable. The flow is most conveniently described in terms of the cylindrical and spherical coordinates. This type of flow is considered over the fore shape body such as a bullet, cone, and sphere, etc.

2.5 Boundary-Layer Equations for Axisymmetric Flow

An axisymmetric flow arises when an object revolved around its axis then the flow is directed towards the axis of the body. Therefore, the boundary-layer equations of continuity and momentum are similar to Prandtl's boundary layer equation because the gradients around the circumference of the body are zero. The present work deals with the axisymmetric laminar boundary layer flow of free stream velocity U_∞ along bullet-shaped objects of radius *R*. The shape of the front of the body is immaterial but it is supposed to be smooth enough not to cause boundary layer separation. Near the front, the layer is closely similar to the Blasius layer on a flat plate because the radius of the objects is very large compared with the boundary layer thickness and so the boundary curvature can be neglected. We know the boundary layer thickness δ is proportional to $\sqrt{\frac{\nu x}{U}}$, where x is the distance from the front, and ν is the kinematic viscosity of the fluid. Hence the Blasius solution begins to be inadequate when $\sqrt{\frac{\nu x}{UR^2}}$ ceases to be small. So we have to find the inviscid, incompressible axisymmetric potential flow. By using cylindrical coordinates,

(r,θ,z) where r = 0 is the axis of the axisymmetric flow and (u_r,u_θ,u_z) are the velocity components in (r,θ,z) directions then the continuity equation is

$$\frac{\partial u_r}{\partial r}+\frac{u_r}{r}+\frac{\partial u_z}{\partial z}=0 \tag{2.5.1}$$

We have the definition of another stream function, ψ, known as Stokes' stream function (different from the stream function used in planar flow) defined as

$$u_z=\frac{1}{r}\frac{\partial\psi}{\partial r},u_r=-\frac{1}{r}\frac{\partial\psi}{\partial z} \tag{2.5.2}$$

And this assures that the continuity equation (2.5.1) is satisfied.

In incompressible axisymmetric flow, the vorticity components (by setting $\frac{\partial}{\partial\theta}$ to zero) are

$$\omega_r=-\frac{\partial u_\theta}{\partial z},\omega_\theta=\frac{\partial u_r}{\partial z}-\frac{\partial u_z}{\partial r},\omega_z=\frac{1}{r}\frac{\partial(ru_\theta)}{\partial r}$$

In the absence of swirl that is $u_\theta=0$ and therefore only the θ component remains:

$$\omega_r=\omega_z=0 \text{ and } \omega_\theta=\omega=\frac{\partial u_r}{\partial z}-\frac{\partial u_z}{\partial r}$$

Therefore, we have the equations of motion

$$u_r\frac{\partial u_r}{\partial r}+\frac{u_\theta}{r}\frac{\partial u_r}{\partial\theta}+u_z\frac{\partial u_r}{\partial z}-\frac{u_r^2}{r}=\nu\frac{\partial^2u_r}{\partial r^2}-\frac{1}{\rho r}\frac{\partial p}{\partial\theta} \tag{2.53}$$

$$u_r\frac{\partial u_\theta}{\partial r}+\frac{u_\theta}{r}\frac{\partial u_\theta}{\partial\theta}+u_z\frac{\partial u_\theta}{\partial z}+\frac{u_\theta u_r}{r}=\nu\frac{\partial^2u_\theta}{\partial r^2}-\frac{1}{\rho r}\frac{\partial p}{\partial\theta} \tag{2.5.4}$$

$$u_r\frac{\partial u_z}{\partial r}+\frac{u_\theta}{r}\frac{\partial u_z}{\partial\theta}+u_z\frac{\partial u_z}{\partial z}=\nu\frac{\partial^2u_z}{\partial r^2}-\frac{1}{\rho}\frac{\partial p}{\partial z} \tag{2.5.5}$$

From equations (2.5.3) and (2.5.4), the terms $\frac{u_\theta^2}{r}$ and $\frac{u_\theta u_r}{r}$ are the centripetal and Coriolis components of acceleration. In the case of axisymmetric flow, the terms $\frac{\partial}{\partial\theta}$ are set to zero. Therefore, the equations (2.5.3) to (2.5.5) become

$$u_r\frac{\partial u_r}{\partial r}+u_z\frac{\partial u_r}{\partial z}-\frac{u_\theta^2}{r}=\nu\frac{\partial^2 u_r}{\partial r^2}-\frac{1}{\rho}\frac{\partial p}{\partial r} \quad (2.5.6$$

$$u_r\frac{\partial u_\theta}{\partial r}+u_z\frac{\partial u_\theta}{\partial z}+\frac{u_\theta u_r}{r}=\nu\frac{\partial^2 u_\theta}{\partial r^2}-\frac{1}{\rho r}\frac{\partial p}{\partial\theta} \quad (2.5.7)$$

$$u_r\frac{\partial u_z}{\partial r}+u_z\frac{\partial u_z}{\partial z}=\nu\frac{\partial^2 u_z}{\partial r^2}-\frac{1}{\rho}\frac{\partial p}{\partial z} \quad (2.5.8)$$

In absence of swirl, the equations for axisymmetric potential flow are

$$u_r\frac{\partial u_r}{\partial r}+u_z\frac{\partial u_r}{\partial z}=\nu\frac{\partial^2 u_r}{\partial r^2}-\frac{1}{\rho}\frac{\partial p}{\partial r} \quad (2.5.9)$$

$$u_r\frac{\partial u_z}{\partial r}+u_z\frac{\partial u_z}{\partial z}=\nu\frac{\partial^2 u_z}{\partial r^2}-\frac{1}{\rho}\frac{\partial p}{\partial z} \quad (2.5.10)$$

The Stokes' stream function, ψ, can be defined as $u_z=\frac{1}{r}\frac{\partial\psi}{\partial r}, u_r=-\frac{1}{r}\frac{\partial\psi}{\partial z}$ which ensures that the continuity equation is satisfied.

The boundary conditions are

$u_z=u_r=0$ at r = R and $u_z\rightarrow$ U as r $\rightarrow\infty$

2.6 Physical Model and Coordinate System

Let us consider the steady two-dimensional axisymmetric MHD boundary layer flow and energy transfer over a stretching bullet-shaped object with surface velocity U_w and free stream velocity U_∞. The temperature of the surface and free stream is T_w and T_∞ respectively. Assume that, x and r are the axes and radial coordinates with u and v are the components of the coordinates of the axisymmetric body where $r = R(x)$ is the radius of the axisymmetric body. The *x*-axis measures from the leading edge of the axisymmetric body and, *r* are measured normal to the axis.

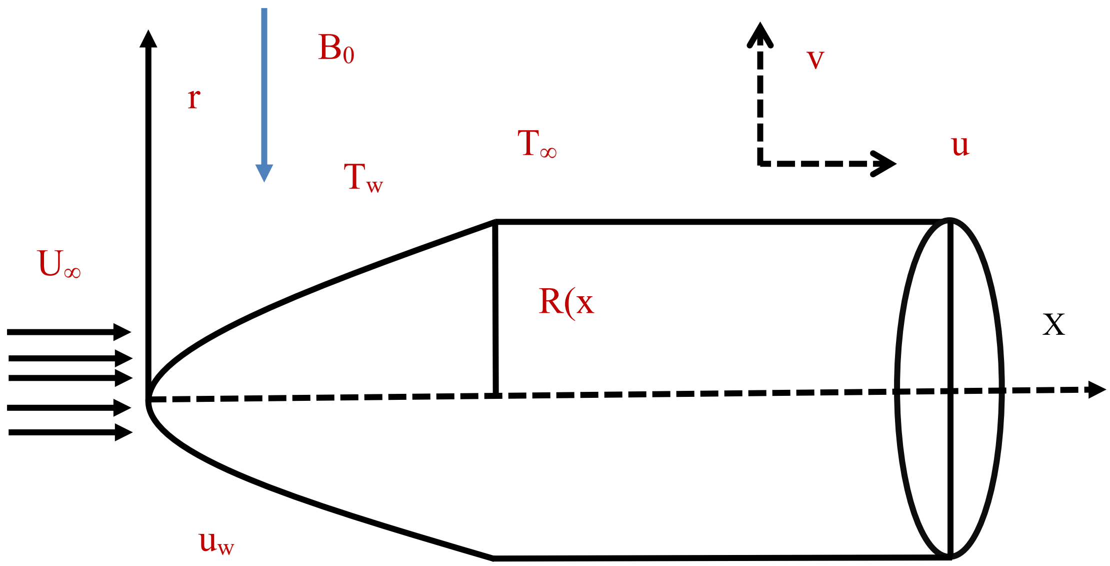

Figure 2. 2 Physical model and coordinate system

The magnetic field B_0 is applied perpendicularly to the flow direction and for the smallest magnetic Reynolds number, the induced magnetic field has been neglected. The pressure gradient is in the positive *x*-axis direction and is directed upward parallel to the direction of gravity. The fluid flows upwards against the force of gravity due to a constant pressure gradient $\frac{\partial p}{\partial x}$ transmitted to the fluid by the contracting surface.

2.7 Boundary and Initial Conditions

The boundary-layer equations are parabolic and very much easier to solve compared with the Reynolds averaged NS equations which are elliptical. These equations are related to the inviscid flow equations but the approximations used to obtain these are not valid in the same region of the flow. The BL equations apply close to the solid body and the wakes which form behind the body whereas the inviscid flow equations apply outside the BL. Therefore, if we wish to calculate the BL equations in a particular domain then the boundary or initial conditions are required along the upstream normal line to the wall, over the wall, and the outer edge of this domain. This choice of boundary conditions is justified by the fact that a perturbation introduced along these bounding lines influences the flow in the specific domain. Again, towards the downstream boundary, there is no need for the boundary conditions because a perturbation does not affect the calculating domain. Besides, the two-dimensional steady BL equations are singular at the point of vanishing the shear stress (τ_w). This is the separation point. For this reason, let us assume a flat surface at $y = 0$ with constant speed U_∞ which is parallel to the surface. We want to find the steady-state solution but are not interested outside the boundary layer. At this stage, we have to consider boundary conditions only. Since there is no flow across the plate surface, which means that

$$v = 0 \text{ at } y = 0 \tag{2.5.1}$$

Due to the viscosity of the fluid, we have the no-slip condition at the plate. i.e.

$$u = 0 \text{ at } y = 0 \tag{2.5.2}$$

Far from the plate that is outside the boundary layer, we have

$$u \to U_\infty \text{ as } y \to \infty \tag{2.5.3}$$

Along with a flat plate that is parallel to the free stream velocity U_∞, so consider no pressure gradient and therefore the appropriate boundary conditions are

$$\begin{aligned} &u = v = 0, x > 0 \text{ at } y = 0, u = U_\infty, \text{ at y } = 0 \\ &u \to U_\infty, \text{ all } x, \text{ as } y \to \infty \end{aligned} \tag{2.5.4}$$

Therefore, we have to reduce the BL equation into single dependent variable. The stream function ψ related to the velocity component u and v can be written as

$$u = \frac{\partial \psi}{\partial y} \text{ and v} = -\frac{\partial \psi}{\partial x} \tag{2.5.5}$$

and if we substitute the equations (2.5.5) into the following equation

$$u\frac{\partial u}{\partial x} + v\frac{\partial u}{\partial y} = \nu\frac{\partial^2 u}{\partial y^2} \tag{2.5.6}$$

We obtain a partial differential equation for ψ, which is given by

$$\frac{\partial \psi}{\partial y}\frac{\partial^2 \psi}{\partial x \partial y} - \frac{\partial \psi}{\partial x}\frac{\partial^2 \psi}{\partial y^2} = \nu \frac{\partial^3 \psi}{\partial y^3} \tag{2.5.7}$$

The boundary conditions assume the form

$$\begin{aligned} &\frac{\partial \psi}{\partial y} = \frac{\partial \psi}{\partial x} = 0, \text{ at } x > 0 \text{ and } y = 0 \\ &\frac{\partial \psi}{\partial y} \to U_\infty, \text{ as } y \to \infty \text{ and all } x \end{aligned} \tag{2.5.8}$$

2.8 Approximations and Assumptions

- The bullet-shaped object is considered thin and its thickness is smaller than the boundary layer thickness.
- The flow is axisymmetric two-dimensional, laminar, viscous, incompressible, and electrically conductive.
- The velocity of the fluid is too small with that of light that is the velocity scale in this study is non-relativistic.
- There is no chemical reaction between the fluid and the diffusing species.
- The surface of the bullet-shaped object is heated.
- The density is a linear function of temperature and concentration so that the usual Boussinesq's approximation is applicable in the boundary-layer flow.
- The force $\rho e_e \mathbf{E}$ due to the electric field is negligible compared with the force $J \times B$ due to the magnetic field.
- The induced magnetic field, the external electric field, and the electric field due to polarization of charges are negligible.

CHAPTER THREE

MAGNETOHYDRODYNAMIC (MHD) BOUNDARY LAYER FLOW AND HEAT TRANSFER OF VISCOUS FLUID OVER A LINEAR STRETCHING BULLET-SHAPED OBJECT

This chapter performs the MHD boundary layer flow and heat transfer over a linear stretching bullet-shaped object. The surface is assumed to be at a different temperature from the fluid and the temperature is defined in terms of the power-law index parameter. Boundary layer approximation is used to write the equations for momentum and energy balance. Since no buoyancy force is considered, the flow does not affect the temperature distribution in the fluid domain but the effect of temperature changes on the fluid flow is not there. There is only a one-way coupling of the momentum and energy equation. The skin friction coefficient and rate of heat transfer (Nusselt number), along with velocity field and temperature field are computed by applying the SQLM with MATLAB. The equation is formulated in terms of momentum and energy along with boundary conditions. The mathematical formulation is based on Blasius and Falkner – Skan boundary layer equation. The local similarity transformations are applied by converting the governing PDEs into ODEs. The analysis is made by the effect of physical parameters such as magnetic parameter (*M)*, stretching ratio parameter (ϵ), surface thickness parameter (s), power-law index parameter (m), and Prandtl number (Pr). The velocity profile, temperature profile, the local skin friction coefficient, and the local Nusselt number has been displayed graphically and the values of skin friction coefficient, and Nusselt number displays in tabular form by considering the two different cases of stretching ratio parameter and surface thickness parameter such as $\varepsilon > 1$ or <1 and $s = 0.05$, $s = 2.0$ respectively.

3.1 Mathematical Formulation and Analysis of the Present Problem

The mathematical model is developed for the steady two-dimensional MHD laminar BL viscous fluid flow with heat transfer over a linear stretching bullet-shaped object. A flow diagram has been displayed in chapter 2 with Figure 2.2. Nield and Bejan [57] discussed the boundary layer flow of heat and mass transfer by considering different types of boundary conditions in a Newtonian fluid. Hence the present problem deals with a power-law stretching velocity at the boundary and impermeability of the bullet-shaped surface.

The present flow model has been assumed a linear stretching rate. The surface extends along the axis of the axisymmetric body (x-direction) and the coordinate r is taken normal to the axis. There is no fluid movement along with the r–axis and the steady flow is considered along the axis only.

Therefore, the surface is maintained at power-law velocity and temperature. Hence, if the surface velocity and temperature are $U_w\left(x\right)$ and T_w, the free stream velocity and temperature are $U_\infty\left(x\right)$ and T_∞ respectively then it can be written as $U_w\left(x\right)=ax^m, U_\infty\left(x\right)=bx^m, T_w\left(x\right)=x^{2m-1}$, where a and $b\left(b>0\right)$ are the initial surface stretching rate and free stream rate with a is positive for stretching case, negative for shrinking case, and zero no stretching of the surface.

Therefore, the governing PDEs of continuity, momentum, and thermal energy is taken in the following way.

Equation of continuity:

$$\frac{\partial}{\partial x}\left(ru\right)+\frac{\partial}{\partial r}\left(rv\right)=0 \tag{3.1.1}$$

Momentum equation:

$$u\frac{\partial u}{\partial x}+v\frac{\partial u}{\partial r}=U_\infty\frac{dU_\infty}{dx}+\frac{\nu}{r}\left(\frac{\partial u}{\partial r}+r\frac{\partial^2 u}{\partial r^2}\right)+\frac{\sigma {B_0}^2}{\rho}\left(U_\infty-u\right)$$
$$\text{where } -\frac{1}{\rho}\frac{\partial p}{\partial x}=U_\infty\left(x\right)\frac{dU_\infty\left(x\right)}{dx} \tag{3.1.2}$$

Energy equation:

$$u\frac{\partial T}{\partial x}+v\frac{\partial T}{\partial r}=\frac{\alpha}{r}\left(\frac{\partial T}{\partial r}+r\frac{\partial^2 T}{\partial r^2}\right) \qquad (3.1.3$$

The boundary conditions are taken as

$$u=U_w\left(x\right),\ v=0,\ T=T_w\ at\ \ r=R\left(x\right) \text{ and}$$
$$u\to U_\infty\left(x\right)=U, T\to T_\infty, as\quad r\to\infty \tag{3.1.4}$$

Where *R(x)* prescribes the radius of the axisymmetric bullet-shaped object, u and *v* are the velocity components for the coordinates (x, r) respectively, ν is the kinematic viscosity of the fluid, ρ is the density of the fluid, the term $\frac{\sigma B_0^2}{\rho}u$ denotes the magnetic field of *x* component and $\frac{\sigma B_0^2}{\rho}$ is the magnetic parameter, B_0 is the strength of the magnetic field. Thus $J \times B$, represent the Lorentz force becomes - $\frac{\sigma B_0^2}{\rho}u$. The negative sign means in the term is decreasing. Therefore, the term $\frac{\sigma B_0^2}{\rho}u$ denotes the Lorentz force which arises from the interaction of the fluid velocity and the applied magnetic field. In equation (3.1.2) the induced magnetic field is ignored for the smallest magnetic Reynolds number. This consideration is justified due to electrically conductive fluids such as mercury and liquid sodium. Equation (3.1.3) represents that heat can be transported in a fluid by convection and conduction only. Hence in equation (3.1.3) the convection and conduction terms are $u\frac{\partial T}{\partial x} + v\frac{\partial T}{\partial r}$ and $\alpha\frac{\partial^2 T}{\partial r^2}$ respectively.

The following axisymmetric similarity transformations have been applied for finding the similarity solutions of the equation (3.1.1) – (3.1.3) with boundary conditions (3.1.4).

$$\eta = \frac{U_\infty r^2}{\nu x},\ \psi = \nu x f(\eta), T = x^{2m-1}\theta(\eta) \tag{3.1.5}$$

The stream function ψ is denoted by the velocity components $u = \frac{1}{r}\frac{\partial \psi}{\partial r}$ and $v = -\frac{1}{r}\frac{\partial \psi}{\partial x}$ respectively. From the similarity variable $\eta = \frac{U_\infty r^2}{\nu x}$, the dimensionless radius is $R(x) = \sqrt{\frac{\nu \eta x}{U_\infty}}$. By applying the equation (3.1.5) into the equations (3.1.2) and (3.1.3), the following reduced ODEs as

$$\eta f''' + f'' + \frac{1}{2} ff'' + \frac{m}{8}\left(1 - 4f'^2\right) + \frac{M}{8}\left(1 - 2f'\right) = 0 \tag{3.1.6}$$

$$\eta\theta'' + \frac{1}{2}\theta' + \frac{1}{2}\Pr\left[f\ \theta' - \left(2m-1\right)f'\ \theta\right] = 0 \tag{3.1.7}$$

and the converted boundary conditions are

$$\begin{aligned} &f(\eta) = 0,\ f'(\eta) = \frac{\varepsilon}{2}, \theta\ (\eta) = 1,\ at\ \eta = 0,\ and \\ &f'(\eta) \to \frac{1}{2}, \theta\ (\eta) \to 0\ \ as\ \eta \to \infty \end{aligned} \tag{3.1.8}$$

The parameter ϵ is the ratio of bullet-shaped object velocity to the free stream velocity and is called the stretching ratio parameter. It is observed that if the stretching ratio parameter $\varepsilon > 1.0$, then the bullet-shaped velocity is greater than the free stream velocity, and when $\varepsilon < 1.0$, then the bullet-shaped velocity is lower than the free stream velocity. On the other hand, when $\epsilon = 1$ then the bullet-shaped and free stream are equal velocities. The dimensionless parameters M, ε and Pr are defined as $M = \frac{\sigma B_0^2 x}{\rho U}, \varepsilon = \frac{U_w}{U},\ \Pr = \frac{\nu}{\alpha}$.

The skin friction coefficient and the local Nusselt number: The shear stress and the local skin friction coefficient are defined as $\tau_w = -\mu\left(\frac{\partial u}{\partial r}\right)_{r=\eta}$ and $C_f = \frac{-2\tau_w}{\rho U^2}$ respectively. By applying the equations (3.1.4) and (3.1.5), the local skin friction coefficient can be written as

$$C_f = \frac{-2\mu}{\rho U_\infty^{\ 2}}\left(\frac{\partial u}{\partial r}\right)_{r=\eta} = -8\sqrt{\frac{\eta}{\mathrm{Re}_x}} f''(\eta) \Rightarrow C_f\sqrt{\mathrm{Re}_x} = -8\sqrt{\eta} f''(\eta) \tag{3.1.9}$$

The local Nusselt number can be defined as $Nu_x = \frac{xq_w}{\kappa\left(T_w - T_\infty\right)}$, where q_w is the wall heat flux and taken as $q_w = -\kappa\left(\frac{\partial T}{\partial r}\right)_{r=\eta}$. After using the equations (3.1.4) and (3.1.5), the local Nusselt number, $Nu_x\left(\mathrm{Re}_x\right)^{-1/2} = -2\sqrt{\eta}\theta'(\eta)$ (3.1.10)

3.2 The Procedure of Numerical Solution

The coupled system of non-linear ODEs (3.1.6) and (3.1.7) has been solved numerically by applying SQLM with MATLAB. The SQLM is the combination of QLM and CSCM which were developed by Shateyi and Muzara [79]. The system of equations (3.1.6) and (3.1.7) are converted to

$$\mathrm{a}_{0,\mathrm{t}} f'''_{\mathrm{t}+1}(\eta) + \mathrm{a}_{1,\mathrm{t}} f''_{\mathrm{t}+1}(\eta) + \mathrm{a}_{2,\mathrm{t}} f'_{\mathrm{t}+1}(\eta) + \mathrm{a}_{3,\mathrm{t}} f_{\mathrm{t}+1}(\eta) = R_{1,\mathrm{t}}(\eta) \tag{3.2.1}$$

$$\mathrm{b}_{0,\mathrm{t}} \theta''_{t+1}(\eta) + \mathrm{b}_{1,\mathrm{t}} \theta'_{t+1}(\eta) + \mathrm{b}_{2,\mathrm{t}} \theta(\eta) + \mathrm{b}_{3,\mathrm{t}} f'_{t+1}(\eta) + \mathrm{b}_{4,\mathrm{t}} f_{t+1}(\eta) = R_{2,t}(\eta) \tag{3.2.2}$$

The subscripts t and $t + 1$ denote previous and current approximations.

The transformed boundary conditions are

$$f_{t+1}(xN_x) = 0, f_{t+1}(xN_{x-1}) = \frac{\varepsilon}{2}, \theta_{\mathrm{t}+1}(xN_x) = 1, \text{ at } \eta = 0$$
$$f_{t+1}(x_0) = 0, f_{t+1}(x_0) = \frac{1}{2}, \theta_{\mathrm{t}+1}(x_0) = 0, \text{ as } \eta \to \infty$$

The variable coefficients obtained from the previous iteration are given by

$$a_{0,t} = \frac{\partial f}{\partial f'''} = \eta, a_{1,t} = \frac{\partial f}{\partial f''} = \frac{1}{2} + \frac{1}{2} f_t, a_{2,t} = \frac{\partial f}{\partial f'} = -mf'_t - \frac{M}{4}, a_{3,t} = \frac{\partial f}{\partial f} = \frac{1}{2} f''_t$$

$$b_{0,t} = \frac{\partial \theta}{\partial \theta''} = \eta, b_{1,t} = \frac{\partial \theta}{\partial \theta'} = \frac{1}{2} + \frac{\Pr}{2} f_t, b_{2,t} = \frac{\partial \theta}{\partial \theta} = -\frac{\Pr(2m-1)}{2} f'_t$$
$$b_{3,t} = \frac{\partial \theta}{\partial f'} = -\frac{\Pr(2m-1)}{2} \theta_t, b_{4,t} = \frac{\partial \theta}{\partial f} = \frac{\Pr}{2} \theta'_t$$

$$R_{1,t}(\eta) = a_{0,t} f'''_t + a_{1,t} f''_t + a_{2,t} f'_t + a_{3,t} f_t - F\left[\eta, f(\eta), f'(\eta), f''(\eta) \ldots\ldots f^n(\eta)\right]$$
$$= \frac{1}{2} f_t f'' - \frac{m}{2} f_t^2 - \frac{m}{8} - \frac{M}{8}$$

$$R_{2,t}(\eta) = b_{0,t} \theta''_t + b_{1,t} \theta'_t + b_{2,t} \theta_t + b_{3,t} f'_t + b_{4,t} f_t$$
$$-F\left[\eta, f(\eta), f'(\eta), f''(\eta) \ldots\ldots f^n(\eta)\right] = \frac{\Pr}{2}\left[f_t \theta'_t - (2m-1) f'_t \theta_t\right]$$

The linear differential equations (3.2.1) and (3.2.2) are solved iteratively by using the Chebyshev spectral collocation method (CSCM). The linear transformation $x = \frac{2\eta}{L_\infty} - 1$ is used to convert the domain [0, ∞) into the computational domain [−1, 1]. The unknown functions f_{r+1} and θ_{r+1} are determined with the help of CSCM, and Chebyshev interpolating polynomials. The derivatives of the functions f_{r+1} and θ_{r+1} at the Gauss–Lobatto collocation points are

$$x_i = \cos\left(\frac{\pi i}{N}\right), i = 0,1,2,....N \text{ gives } \frac{d^n f_{t+1}(x_i)}{dx} = \sum_{k=0}^{N_1} D_{ik}^n f_{t+1}(x_k) = D^n F \tag{3.2.3}$$

Where, $D = \frac{L_\infty}{2}\mathbb{k}$, $\mathbb{k}$ is (N_1 + 1) × (N_1 + 1) differentiation matrix and $F = \left[f_{t+1}(x_0), f_{t+1}(x_1), f_{t+1}(x_2), ...f_{t+1}(x_{N-1}), f_{t+1}(x_N)\right]^T$. Similarly, the nth derivatives of θ_{t+1} are given by

$$\frac{d^n \theta_{t+1}(x_i)}{dx} = \sum_{k=0}^{N_1} D_{ik}^n \theta_{t+1}(x_k) = D^n \Theta \tag{3.2.4}$$

By applying the Equations (3.2.3) and (3.2.4), the Equations (3.2.1) and (3.2.2) yields

$$\begin{bmatrix} A_{11} & A_{12} \\ A_{21} & A_{22} \end{bmatrix} \begin{bmatrix} F_{t+1} \\ \Theta_{t+1} \end{bmatrix} = \begin{bmatrix} R_{1,t} \\ R_{2,t} \end{bmatrix}, \text{ Where } \begin{array}{l} A_{11} = a_{0,t}D^3 + a_{1,t}D^2 + a_{2,t}D + a_{3,t}, A_{12} = 0I, \\ A_{21} = b_{3,t}D^2 + b_{4,t}, A_{22} = b_{0,r}D^2 + b_{1,t}D + b_{2,t} \end{array}$$

The matrix **I** is of order (N_1 + 1) × (N_1 + 1).

3.3 Code Verification

The numerical values $f''(\eta)$ have been compared with the results of Afridi [80] for different values of η to validate the convergence and accuracy of the present method. The results are almost similar to the previous results which are shown in Table 3.1.

Table 3. 1 Comparison of skin friction $f''(\eta)$ for different values of η with Afridi [80] by taking $M = m = 0$ and Pr = 1

	Afridi [80]	Present results
η	$f''(0)$	$f''(\eta)$
0.001	**62.1637**	**62.1572**
0.01	**8.4924**	**8.4912**
0.10	**1.2888**	**1.2839**
0.15	-	**0.9359**

3.4 Results and Discussion

The non-linear ODEs of the present problem are solved by applying SQLM. The convergence criteria of the solution are performed by the use of solution-based errors. These errors are defined by the differences between approximate solutions at the previous and current iteration levels t and $t + 1$, respectively. The error norms are defined as:

$$Error_f = \max_{0 \le i \le N} \left\| F_{t+1,i} - F_{t,i} \right\| \text{ and } Error_\theta = \max_{0 \le i \le N} \left\| \theta_{t+1,i} - \theta_{t,i} \right\|$$

The infinity norms of the residual errors are defined by

$$\left\| \mathrm{Re}\, s(f) \right\|_\infty = \left\| \eta f''' + f'' + \frac{1}{2} ff'' + \frac{m}{8}\left(1 - 4f'^2\right) + \frac{M}{8}\left(1 - 2f'\right) \right\| \text{ and}$$

$$\left\| \mathrm{Re}\, s(\theta) \right\|_\infty = \left\| \eta\theta'' + \frac{1}{2}\theta' + \frac{1}{2}\Pr\left[f\ \theta' - (2m-1) f'\ \theta \right] \right\| \text{ respectively.}$$

The impact of physical parameters on velocity $f'(\eta)$, temperature $\theta(\eta)$, skin friction, and the local Nusselt number is shown graphically. The numerical values of skin friction ($C_f \sqrt{\mathrm{Re}_x}$) and Nusselt number ($Nu_x \left(\sqrt{\mathrm{Re}_x}\right)^{-1}$) which are equivalent to velocity gradient $f''(\eta)$ and temperature gradient $\theta'(\eta)$ have been shown in Table 3.2 and Table 3.3 respectively. The computations are done by taking N = 50 collocation points and solution-based errors are defined for the convergence of the numerical method. Again, Figures 3.14(a) and 3.14(b) show the error infinity norms and residual error infinity norms against iterations. Figure 3.14(a) represents the convergence for the present problem with iterations. From this, it is noticed that the error infinity norm decreases with the increasing number of iterations that confirm the convergence of the present method. So, it is observed that the present method converges after five iterations. On the other hand, Figure 3.14(b) assure the accuracy of the present method of less than 10^{-8} and 10^{-14} for $f(\eta)$ and $\theta(\eta)$ against after fourth iterations. It is seen that the residual error decreases with increasing the iterations. This proves the validity of the present method. The errors show that the SQLM is accurate giving errors of less than 10^{-8} within the fourth iteration. In this chapter the default parameters are taken as $M = 1.0$, $m = 1.0$, Pr = 0.71, ϵ = 0.0, 2.0 and s = 0.05, 2.0 throughout the calculation. The fluid velocity profile and skin friction have been depicted graphically versus boundary layer co-ordinate (η) in Figures 3.1 – 3.6 for the increasing effect of the controlling parameters such as magnetic (M), power-law index (m), stretching ratio (ϵ), and surface thickness (s) in the following sub-section.

3.4.1 Velocity profiles and skin friction coefficient with parameter variations

3.4.1.1 Effect of the magnetic parameter (*M*) on the velocity profile and skin friction coefficient

Figure 3.1 (a) and Figure 3.1 (b) represent the influence of magnetic parameter on viscous fluid velocity profile for thinner (s = 0.05) and thicker surfaces (s = 2.0) when $\varepsilon < 1$, ϵ = 1.0 and $\varepsilon > 1$ respectively. It is noticed from these figures that the variation of the stretching ratio parameter has a significant effect on the velocity profile in connection with the magnetic parameter. These plots depict that the velocity profile of the viscous fluid and boundary layer thickness affected significantly with increasing magnetic parameters. From these figures, it is seen that the velocity profile of the viscous fluid and boundary layer thickness squeezes when $\varepsilon > 1$ and the fluid flow form an inverted boundary layer pattern but in the case of $\varepsilon < 1$, the reverse trend occurs in velocity profile both of the thinner and thicker surfaces of the bullet-shaped object. This happens because in presence of the term

$\frac{\sigma B_0^{\ 2}}{\rho}(U_\infty - u)$ in equation (3.1.2) which is the combination of pressure force ($\frac{\sigma B_0^{\ 2}}{\rho} U_\infty$) and Lorentz force ($\frac{\sigma B_0^{\ 2}}{\rho} u$) terms.

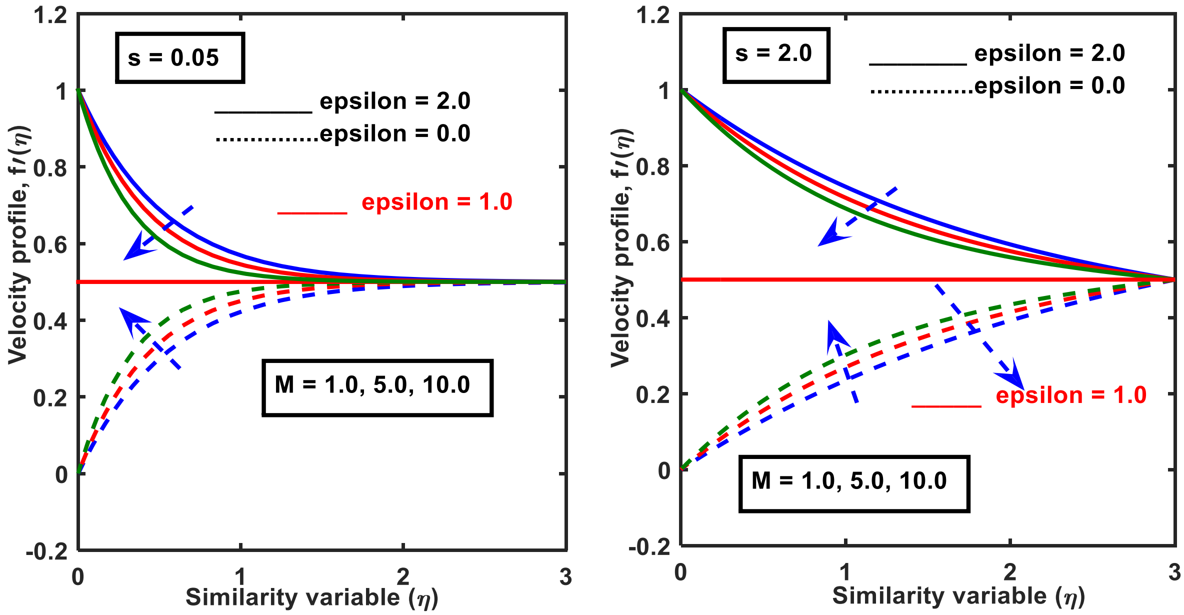

(a) (b)

Figure 3. 1 Effect of magnetic parameter (*M)* on velocity profile taking (a) s = 0.05 and ϵ = 0.0 (lower panel), ϵ =1.0 (separation line), ϵ = 2.0 (upper panel), and (b) s = 2.0 and ϵ = 0.0 (lower panel), ϵ =1.0 (separation line), ϵ = 2.0 (upper panel)

The velocity profile squeezes when Lorentz's force is greater than the pressure force and vice-versa. Again, it is also seen that the surface velocity and the free stream velocity are equal in the case of ϵ = 1.0. It is also observed that, if the surface thickness parameter (s) reduces then the fluid flow form a certain boundary layer structure and the fluid velocity satisfies the far-field boundary condition. On the other hand, while surface thickness parameter (s) increases then the fluid flow does not satisfy the far-field boundary condition and the boundary layer structure has no definite shape. Therefore, the velocity boundary layer thickness is higher in the case of a thicker bullet-shaped object (s = 2.0) than the thinner bullet-shaped object (s = 0.05).

Figures 3.2(a) and 3.2(b) display the skin friction coefficient for the effect of the magnetic parameter (M) with stretching ratio parameter $\varepsilon < 1$ and $\varepsilon > 1$, and the surface thickness parameter s = 0.05, s = 1.0, respectively. From these figures, it is observed that the skin friction coefficient enhances in the case of $\varepsilon < 1$ but reduces while $\varepsilon > 1$ for both of the thinner and thicker surfaces of the bullet-shaped object. It is observed from equation (3.1.9) that the skin friction coefficient is directly proportional to the dimensionless velocity gradient. The velocity gradient at the surface is positive when $\varepsilon < 1$ and negative due to $\varepsilon > 1$ but zero while ϵ = 1.0 for all values of the controlling parameters. The positive values of the velocity gradient indicate that the fluid applies a drag force on the bullet-shaped object, on the other hand, the bullet-shaped object exerts a drag force on the fluid flow while the velocity gradient is negative.

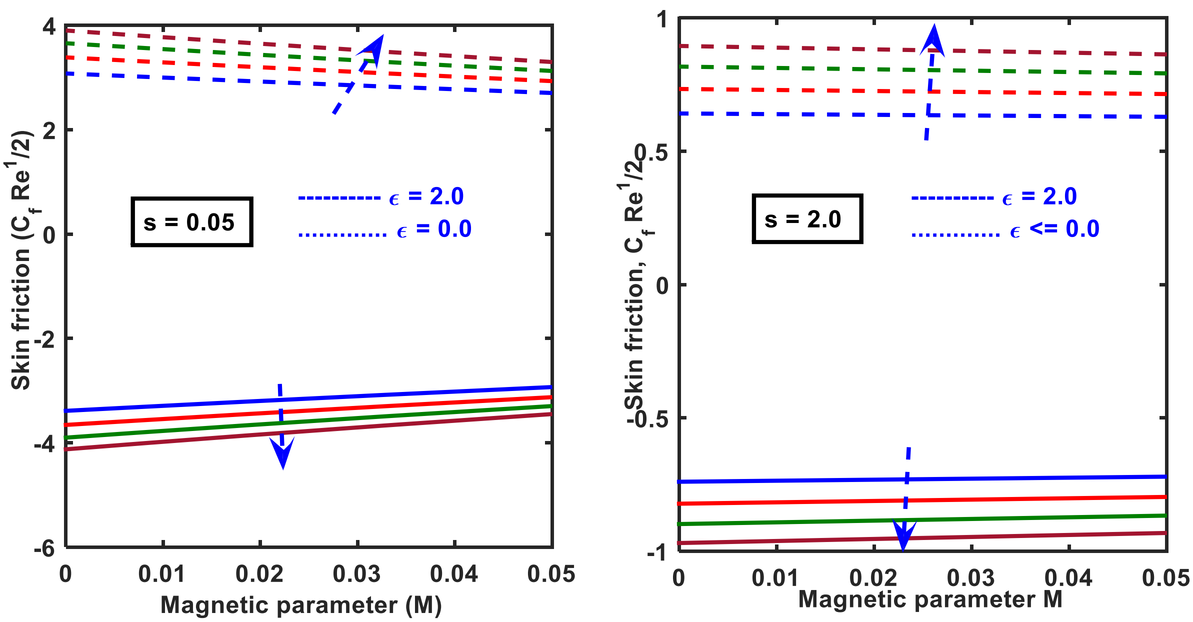

(a) (b)

Figure 3. 2 Effect of magnetic parameter (M) on skin friction coefficient taking (a) s = 0.05 and ϵ = 0.0 (upper panel), ϵ = 2.0 (lower panel), and (b) s = 2.0 and ϵ = 0.0 (upper panel), ϵ = 2.0 (lower panel).

Therefore, the parameter M is directly proportional to skin friction in the case of $\varepsilon < 1$ but inversely proportional when $\varepsilon > 1$. It is observed from Table 3.2 that, when M changes from 1.0 to 10.0 for s = 0.05 and ϵ = 0.0, the skin friction increases 37.5 % whereas for s =

1.0 and ϵ = 0.0 the skin friction increases 56.1%. Hence, the skin friction is higher for the thicker surface (s = 1.0) than the thinner surface (s = 0.05).

3.4.1.2 Influence of power-law index parameter (m) on the velocity profile and skin friction coefficient

Figures 3.3(a) and 3.3(b) show the variation of a velocity profile for the effect of power-law index parameter when the stretching ratio parameter $\varepsilon < 1$ and $\varepsilon > 1$, and the surface thickness parameter s = 0.05, s = 2.0, respectively.

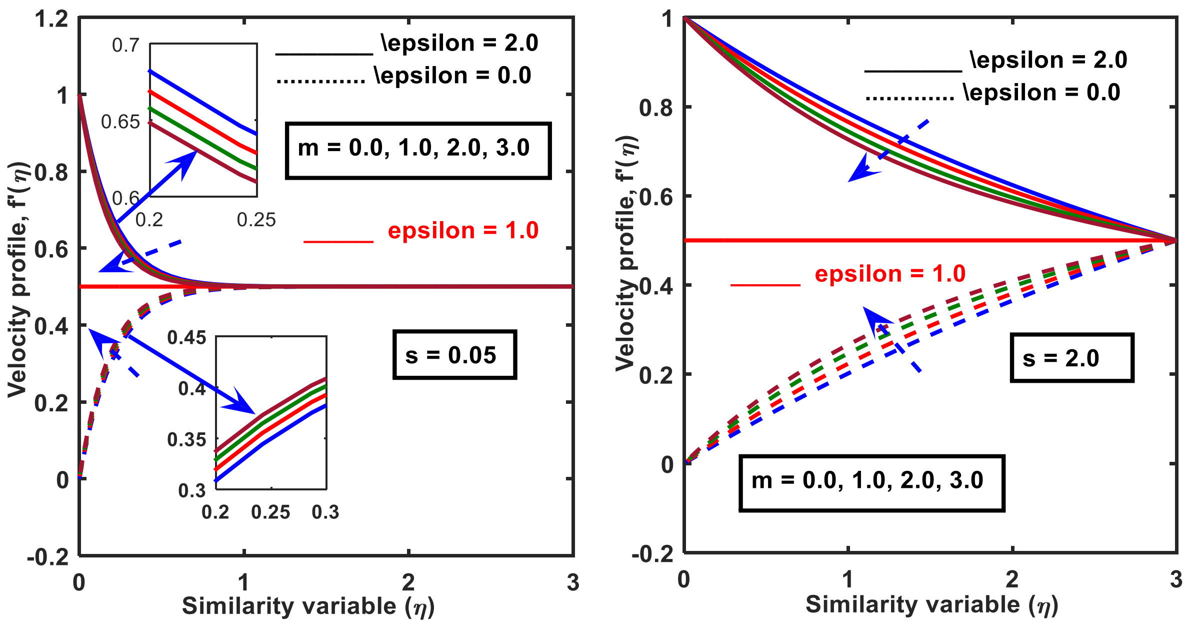

(a) (b)

Figure 3. 3 Influence of power-law index parameter (m) on velocity profile taking (a) s = 0.05 and ϵ = 0.0 (lower panel), ϵ =1.0 (separation line), ϵ = 2.0 (upper panel), and (b) s = 2.0 and ϵ = 0.0 (lower panel), ϵ =1.0 (separation line), ϵ = 2.0 (upper panel).

These plots represent that the velocity profile of the viscous fluid and boundary layer thickness affected insignificantly with an increasing power-law index parameter due to thinner surface (s = 0.05) whereas the reverse trend happens in the case of thicker surface (s = 2.0). From these figures, it is noticed that the velocity profile and boundary layer thickness squeezes when $\varepsilon > 1$ and the fluid flow form an inverted boundary layer pattern whereas, in the case of $\varepsilon < 1$, the velocity profile expands but boundary layer thickness squeezes the and fluid flow form a certain boundary layer pattern. It is also observed that the velocity profile and boundary layer thickness satisfy the far-field boundary condition in the case of a thinner surface (s = 0.05). On the other hand, due to the thicker surface (s = 2.0), the velocity profile, and boundary layer thickness are not in parabolic shapes, so this is insignificant with the physical behavior of the boundary layer concept because in this case, the boundary condition does not satisfy. Therefore, the velocity boundary layer thickness is higher in the case of a thicker bullet-shaped object (s = 2.0) than a thinner bullet-shaped object (s = 0.05).

Figure 3.4(a) and 3.4(b) display the skin friction coefficient for the effect of power-law index parameter (m) by taking the stretching ratio parameter $\varepsilon < 1$ and $\varepsilon > 1$,

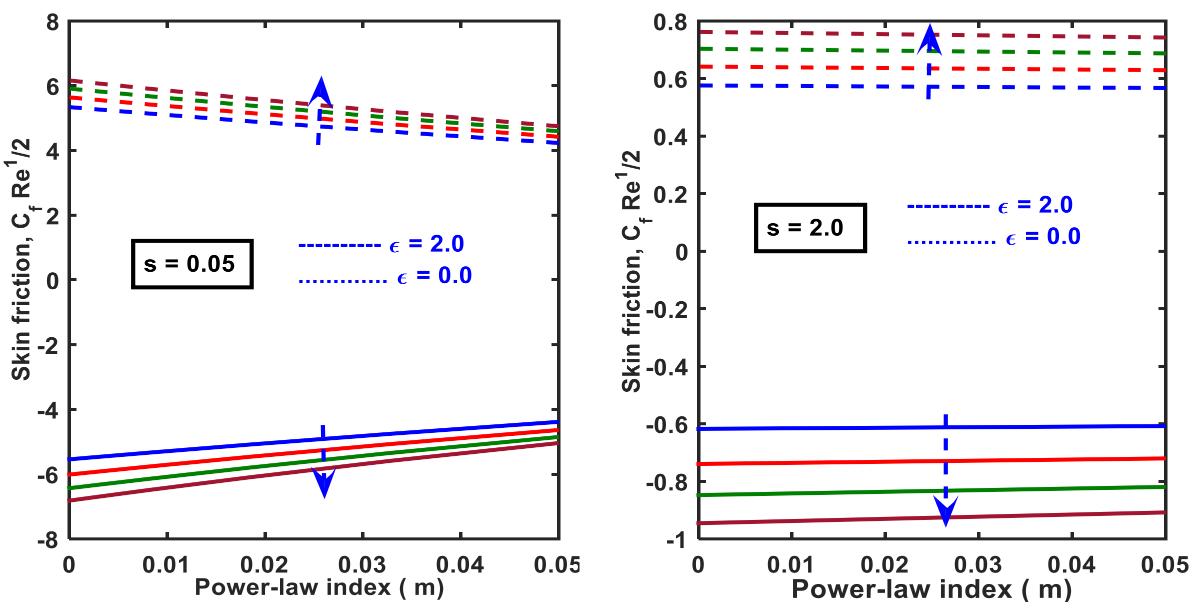

(a) (b)

Figure 3. 4 Effect of power-law index parameter (*m)* on skin friction coefficient taking (a) s = 0.05 and ϵ = 0.0 (lower panel), ϵ = 2.0 (upper panel), and (b) s = 2.0 and ϵ = 0.0 (lower panel), ϵ = 2.0 (upper panel)

and the surface thickness parameter s = 0.05, s = 1.0, respectively. From these figures, it is seen that the skin friction coefficient enhances in the case of $\varepsilon < 1$ but reduces while $\varepsilon > 1$ for both of the thinner and thicker surfaces. These graphs also show that the velocity gradient at the surface is a positive when $\varepsilon < 1$ and negative while $\varepsilon > 1$ but zero while ϵ = 1.0 for all values of the controlling parameters. Therefore, the positive values

$f''(0)$ indicate that the fluid applies a drag force on the bullet-shaped object and the negative value indicates the bullet-shaped object exerts a drag force on the fluid flow. It is observed from Table 3.2 that, when m changes from 0.0 to 3.0 for s = 0.05 and ϵ = 0.0, the skin friction increases 15.4 % whereas for s = 1.0 and ϵ = 0.0 the skin friction increases 32.3%. Hence, the skin friction is higher for the thicker surface (s = 1.0) than the thinner surface (s = 0.05).

3.4.1.3 Effect of surface thickness parameter (*s*) on velocity profiles and skin friction coefficient

Figures 3.5(a) and 3.5(b) illustrate the effects of surface thickness parameter (s) ($0.05 \le s \le 2.0$) on the velocity distribution and skin friction coefficient when the other parameters are fixed by considering the stretching ratio parameter $\varepsilon < 1$ and $\varepsilon > 1$, and the surface thickness parameter s = 0.05, s = 2.0, respectively. These plots show that the velocity profile of the viscous fluid and boundary layer thickness affected significantly with increasing surface thickness parameters. From Figure 3.5(a) it is seen that the velocity profile and boundary layer thickness expands when $\varepsilon > 1$ and the fluid flow form an inverted boundary layer pattern but in the case of $\varepsilon < 1$ the velocity profile squeezes but velocity boundary layer thickness increases and the fluid flow forms a definite boundary layer pattern. This happens because the increase in shape and size of the bullet-shaped object enhances the surface area of the object that provides more resistance against the fluid motion as a result the fluid velocity decreases. Therefore, the velocity boundary layer thickness is higher in the case of a thicker bullet-shaped object (s = 2.0) than the thinner bullet-shaped object (s = 0.05). From Figure 3.5(b), it is noticed that the skin friction coefficient reduces in the case of $\varepsilon < 1$ but increases while $\varepsilon > 1$ for both of the thinner and thicker surfaces. Hence, the parameter s is inversely proportional to $C_f \sqrt{\mathrm{Re}_x}$ in the case of $\varepsilon < 1$ but directly proportional when $\varepsilon > 1$. This graph also shows that the velocity gradient at the surface is a positive when $\varepsilon < 1$ and negative while $\varepsilon > 1$ but zero while ϵ = 1.0 for all values of the controlling parameters. Therefore, the fluid applies a drag force on the bullet-shaped object for the positive values $f''(\eta)$ while the bullet-shaped object exerts a drag force on the fluid flow for the negative values $f''(\eta)$.

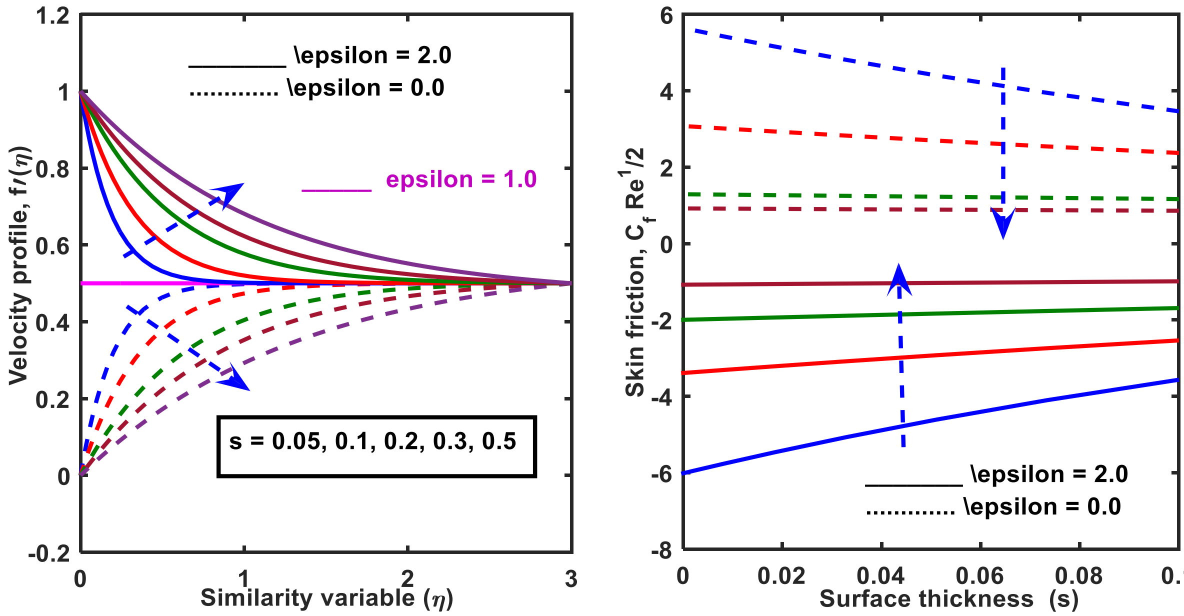

(a) **(b)**

Figure 3. 5 Effect of surface thickness parameter (*s*) on (a) velocity profile for $\epsilon = 0.0$ (lower panel), 1.0 (separation line), 2.0 (upper panel), and (b) skin friction for $\epsilon = 0.0$ (lower panel), 2.0 (upper panel)

It is observed from Table 3.2 that, when *s* changes from 0.05 to 0.5 for $\epsilon = 0.0$, the skin friction decreases 83.7 % whereas for $\epsilon = 2.0$ the skin friction increases 82.1%. Hence, the skin friction is higher for $\epsilon = 0.0$ than $\epsilon = 2.0$.

3.4.1.4 Influence of stretching ratio parameter (ϵ) on the velocity profile

Figure 3.6(a) and 3.6(b) illustrate the velocity profile for the increasing effect of stretching ratio parameter $\left(0 \le \varepsilon \le 2.0 \right)$ consider the surface thickness parameter $s = 0.05$ and $s = 1.0$, respectively. From these figures, it is noticed that the velocity profile and boundary layer thickness expands when $\varepsilon > 1$ and the fluid flow form an inverted boundary layer pattern but in the case of $\varepsilon < 1$ the fluid flow form a certain boundary layer pattern. It is also observed that the velocity profile and boundary layer thickness satisfy the far-field boundary condition in the case of a thinner surface ($s = 0.05$). On the other hand, while the thicker surface ($s = 2.0$), the velocity profile is not in a parabolic shape, this is insignificant with the physical behavior because in this case, the boundary condition does not satisfy by the velocity profile.

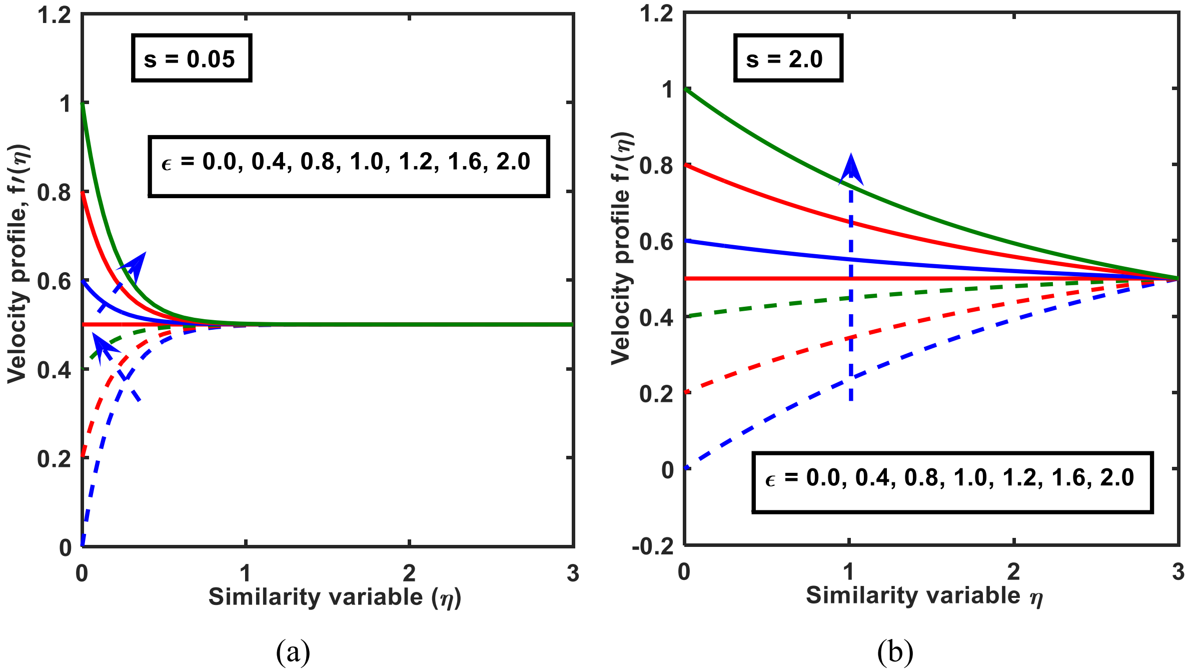

Figure 3. 6 Effect of stretching ratio parameter (ϵ) on velocity profile taking (a) s = 0.05 and ϵ = 0.0 (lower panel), ϵ =1.0 (separation line), ϵ = 2.0 (upper panel), and (b) s = 2.0 and ϵ = 0.0 (lower panel), ϵ =1.0 (separation line), ϵ = 2.0 (upper panel).

Therefore, the velocity boundary layer thickness is higher in the case of the thicker bullet-shaped object (s = 2.0) than the thinner bullet-shaped object (s = 0.05).

From these figures, it is observed that the velocity profile and momentum boundary layer thickness is getting expand due to power-law index parameter (m), surface thickness parameter (s), and stretching ratio parameter (ϵ) whereas magnetic parameter (M) has a reverse effect on it in the case of $\varepsilon > 1$ for both of the thicker (s = 2.0) and thinner (s = 0.05) surfaces. On the other hand, in the case of $\varepsilon < 1$ the velocity profile and momentum boundary layer thickness are getting expand due to magnetic parameter (M), power-law index parameter (m), and stretching ratio parameter (ϵ) but squeezes for the surface thickness parameter (s). Again, it is also revealed that in the case of a thicker bullet-shaped object (s = 2.0) the velocity profile does not approach the ambient condition asymptotically but intersects the vertical axis with a steep angle and the boundary layer structure has no definite shape whereas in the case of a thinner bullet-shaped object (s = 0.05) the velocity profile converge the ambient condition asymptotically and the boundary layer structure has a definite shape. It is also noticed that the thinner bullet-shaped object represents a thinner momentum boundary layer than the thicker bullet-shaped object in both static and moving bullet-shaped objects.

Table 3.2 represents the variation in skin friction coefficient for different values of the magnetic parameter (M), surface thickness parameter (s), Prandtl number (Pr), and power-law index parameter (m) for various movements of the bullet-shaped object.

Table 3. 2 Variation in skin friction coefficient for distinct values of M, m, s, and Pr with ϵ = 0.0, 0.2, 2.0, s = 0.05

Parameters				$-C_f\sqrt{\mathrm{Re}_x}$	$-C_f\sqrt{\mathrm{Re}_x}$	$\lVert -C_f\sqrt{\mathrm{Re}_x} \rVert$
M	m	s	Pr	$\epsilon = 0.0, s = 0.05$	$\epsilon = 0.2, s = 0.05$	$\epsilon = 2.0, s = 0.05$
1.0	1.0	0.05	1.0	**5.6404**	**4.5437**	**6.0131**
5.0	1.0	0.05	1.0	**6.3441**	**5.1011**	**6.6555**
10.0	1.0	0.05	1.0	**7. 0787**	**5.6847**	**7.3436**
1.0	**0.0**	0.05	1.0	**5.3397**	**4.2886**	**5.5421**
1.0	**1.0**	0.05	1.0	**5.6404**	**4.5437**	**6.0131**
1.0	**2.0**	0.05	1.0	**5.9128**	**4.7745**	**6.4342**
1.0	1.0	**0.05**	1.0	**5.6404**	**4.5437**	**6.0131**
1.0	1.0	**0.2**	1.0	**1.7491**	**1.4322**	**1.9969**
1.0	1.0	**0.3**	1.0	**1.3251**	**1.0771**	**1.4993**
1.0	1.0	0.05	**0.71**	**5.6404**	**4.5437**	**6.0131**
1.0	1.0	0.05	**1.0**	**5.6404**	**4.5437**	**6.0131**
1.0	1.0	0.05	**7.0**	**5.6404**	**4.5437**	**6.0131**

It is observed from equation (3.1.9) that the skin friction coefficient is inversely proportional to the velocity gradient, $f''(\eta)$ at the bullet-shaped object. So, the velocity gradient at the surface of the object is negative for all values of mentioned parameters in the case of $\varepsilon > 1$ but positive when $\varepsilon < 1$. The negative values $f''(\eta)$ mean that the bullet-shaped object exerts a drag force on the fluid flow whereas the positive values $f''(\eta)$ mean that the fluid flow exerts a drag force on the bullet-shaped object. From Table 3.2, it is observed that the magnetic parameter (*M)* and power-law index parameter (*m*) reducing the friction factor coefficient in the case of $\varepsilon < 1$ but boosting the friction factor in the case of $\varepsilon > 1$. On the other hand, the surface thickness parameter reduces the friction factor in both of the mentioned cases. It is interesting to note that friction factor coefficient is less in $\epsilon = 0.2$ case when compared with $\epsilon = 0.0$, $\epsilon = 2.0$ cases. At this point, it is highlighted that for reducing the friction between the particles we have to use $\epsilon = 0.2$ cases. It is evident from this table that the skin friction coefficient is higher in $\epsilon = 2.0$ case when comparing with $\epsilon = 0.0$, $\epsilon = 0.2$ cases. It is also noticed that the Prandtl number (Pr) does not affect the skin friction coefficient.

Table 3.3 displays the variation in Nusselt number for different values of the magnetic parameter (*M*)*,* surface thickness parameter (*s*), Prandtl number (Pr), and power-law index parameter (*m*) for various movements of the bullet-shaped object. It is observed from equation (3.1.10) that the Nusselt number is directly proportional to the heat transfer rate $\theta'(\eta)$ at the bullet-shaped object. The heat transfer rate at the surface of the object $\theta'(\eta)$ is negative for all values of mentioned parameters. From table 3.3, it is possible to observe that the heat transfer rate increases for the magnetic parameter (*M*), Prandtl number (Pr), and power-law index parameter (*m*) but decreases for the surface thickness parameter (*s*) for all three cases of stretching ratio parameter ($\epsilon = 0.0$, $\epsilon = 0.2$, $\epsilon = 2.0$) and s = 0.05 respectively. On the other hand, in the case of $\epsilon = 2.0$, and s = 0.05 the heat transfer rate increases for the magnetic parameter (*M*) and surface thickness parameter (*s*) whereas decreases for Prandtl number (Pr), and power-law index parameter (*m*). Therefore, heat transfer rate is high in $\epsilon = 0.0$ case, when compared with $\epsilon = 0.2$, $\epsilon = 2.0$ cases. At this point, it is highlighted that for reducing the heat transfer rate we have to consider the static ($\epsilon = 0.0$) bullet-shaped object.

Table 3. 3 Variation in Nusselt number, $Nu_x\left(\sqrt{\mathrm{Re}_x}\right)^{-1}$ for different values of *M*, *m, s*, and Pr with ϵ = 0.0*,* 0.2, 2.0, *s* = 0.05

Parameters				$\left\lVert -Nu_x\left(\sqrt{\mathrm{Re}_x}\right)^{-1}\right\rVert$ $\epsilon = 0.0$, s = 0.05	$\left\lVert -Nu_x\left(\sqrt{\mathrm{Re}_x}\right)^{-1}\right\rVert$ $\epsilon = 0.2$, s = 0.05	$\left\lVert -Nu_x\left(\sqrt{\mathrm{Re}_x}\right)^{-1}\right\rVert$ $\epsilon = 2.0$, s = 0.05
M	*m*	*s*	Pr			
1.0	1.0	0.05	1.0	**10.4671**	**10.6800**	**11.2800**
5.0	1.0	0.05	1.0	**10.4911**	**10.6912**	**11.2611**
10.0	1.0	0.05	1.0	**10.5134**	**10.7019**	**11.2426**
1.0	**0.0**	0.05	1.0	**10.0001**	**10.0001**	**10.0000**
1.0	**1.0**	0.05	1.0	**10.4671**	**10.6800**	**11.2800**
1.0	**2.0**	0.05	1.0	**10.8845**	**11.2824**	**12.3826**
1.0	1.0	**0.05**	1.0	**10.4671**	**10.6800**	**11.2800**
1.0	1.0	**0.2**	1.0	**2.9202**	**3.1327**	**3.4985**
1.0	1.0	**0.3**	1.0	**1.4899**	**2.3417**	**2.5867**
1.0	1.0	0.05	**0.71**	**10.3431**	**10.4981**	**10.9376**
1.0	1.0	0.05	**1.0**	**10.4671**	**10.6800**	**11.2800**
1.0	1.0	0.05	**7.0**	**12.1862**	**13.3201**	**16.2761**

The fluid temperature profile and Nusselt number have been depicted graphically versus boundary layer co-ordinate (η) in Figures 3.8 – 3.13 for the increasing effect of Prandtl Number (Pr), power-law index parameter (m), stretching ratio parameter (ϵ), and surface thickness parameter (s) in the following sub-section. The two-layer variation is observed in the thermal boundary layer due to s = 0.05 (thinner surface) and s = 2.0 (thicker surface).

3.4.2 Temperature profiles and Nusselt number with parameter variations

3.4.2.1 Effect of Prandtl number (Pr) on the temperature profile

Figures 3.7(a) and 3.7(b) depicts the variation of Prandtl number (Pr) $\left(0.71 \le \mathrm{Pr} \le 10.0\right)$ on temperature profile when stretching ratio parameter $\varepsilon < 1$ or > 1 and the surface thickness parameter s = 0.05, s = 1.0, respectively. These plots represent that the temperature profile of the viscous fluid and thermal boundary layer thickness affected significantly with increasing Prandtl number.

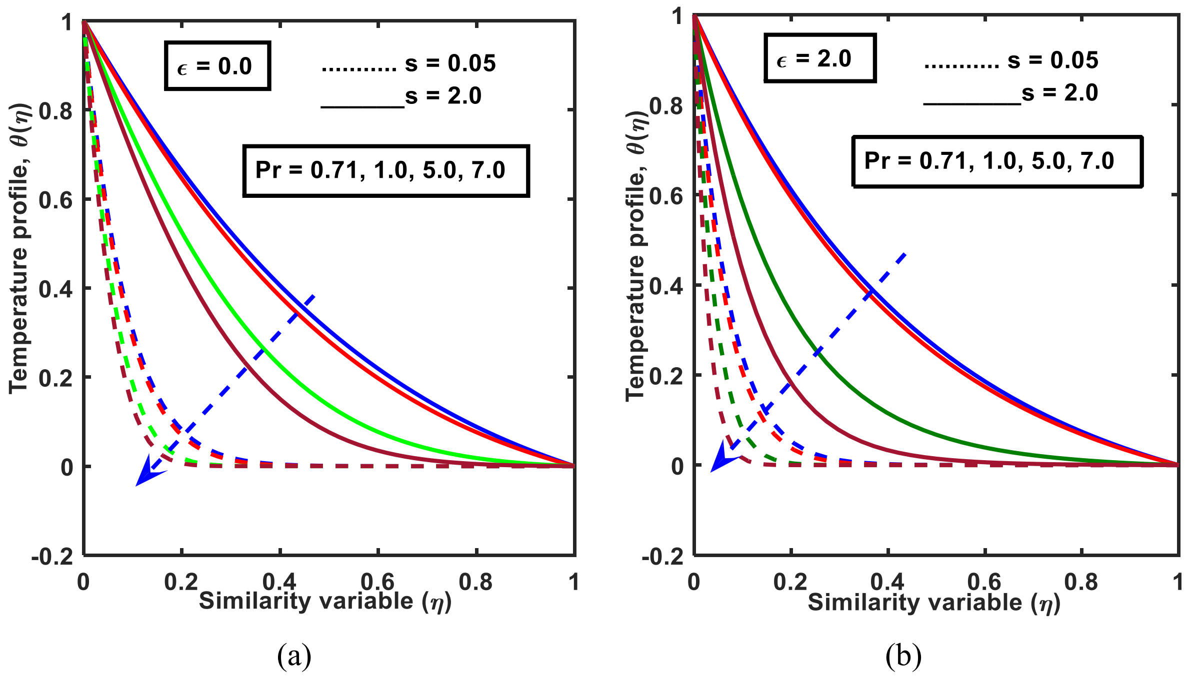

Figure 3. 7 Temperature profile for different values of Prandtl number when (a) $\epsilon = 0$, s = 0.05, s = 2.0, and (b) $\epsilon = 2.0$, s = 0.05, s = 2.0

It is seen from these figures that the variation of surface thickness parameter has a significant effect on fluid temperature in connection with the Prandtl number. From these figures, it is seen that the temperature profile and boundary layer thickness squeezes for both the thicker (s = 2.0, and thinner (s = 0.05) surfaces of the bullet-shaped object. It is also observed that the thermal boundary layer thickness is higher in the case of the thicker surface (s = 2.0) than the thinner surface (s = 0.05). This happens because a smaller Prandtl number means heat is quickly diffuse from the heated surface than for higher values of Pr. For increasing values of Prandtl number, the temperature profiles are closing to the solid surface. So, for cooling purposes, the Prandtl number can be used. A smaller surface thickness has a greater decelerating effect than a thicker surface. Therefore, it is noticed that for higher values of surface thickness parameter, the maximum temperature shows in the thermal boundary layer compared to that of lower surface thickness parameter.

3.4.2.2 Influence of power-law index parameter (*m*) on the temperature profile

Figure 3.8 (a) and Figure 3.8 (b) depict the influence of power-law index parameter on viscous fluid temperature for thinner surface ($s = 0.05$) and thicker surface ($s = 2.0$) when $\epsilon = 0.2$ and 2.0 respectively. It is noticed from these figures that the variation of the surface thickness parameter has a significant effect on viscous fluid temperature in connection with the power-law index parameter. A lower surface thickness parameter has a greater decelerating effect. For thicker surfaces ($s = 2.0$) with increasing m, the decelerating effect is more prominent than for thinner surfaces ($s = 0.05$). Therefore, the thermal boundary layer thickness is higher due to the thicker surface when compared with the thinner surface. Figure 3.8 (c) and Figure 3.8 (d) also represent the influence of power-law index parameter on viscous fluid temperature for air ($Pr = 0.71$) and water ($Pr = 7.0$) when $s = 0.05$ and 2.0 respectively. It is seen from these figures that the variation of the Prandtl number has a significant effect on viscous fluid temperature in connection with the power-law index parameter. A higher Prandtl number has a greater decelerating effect. For air ($Pr = 0.71$) with increasing m, the decelerating effect is more prominent than for water ($Pr = 7.0$).

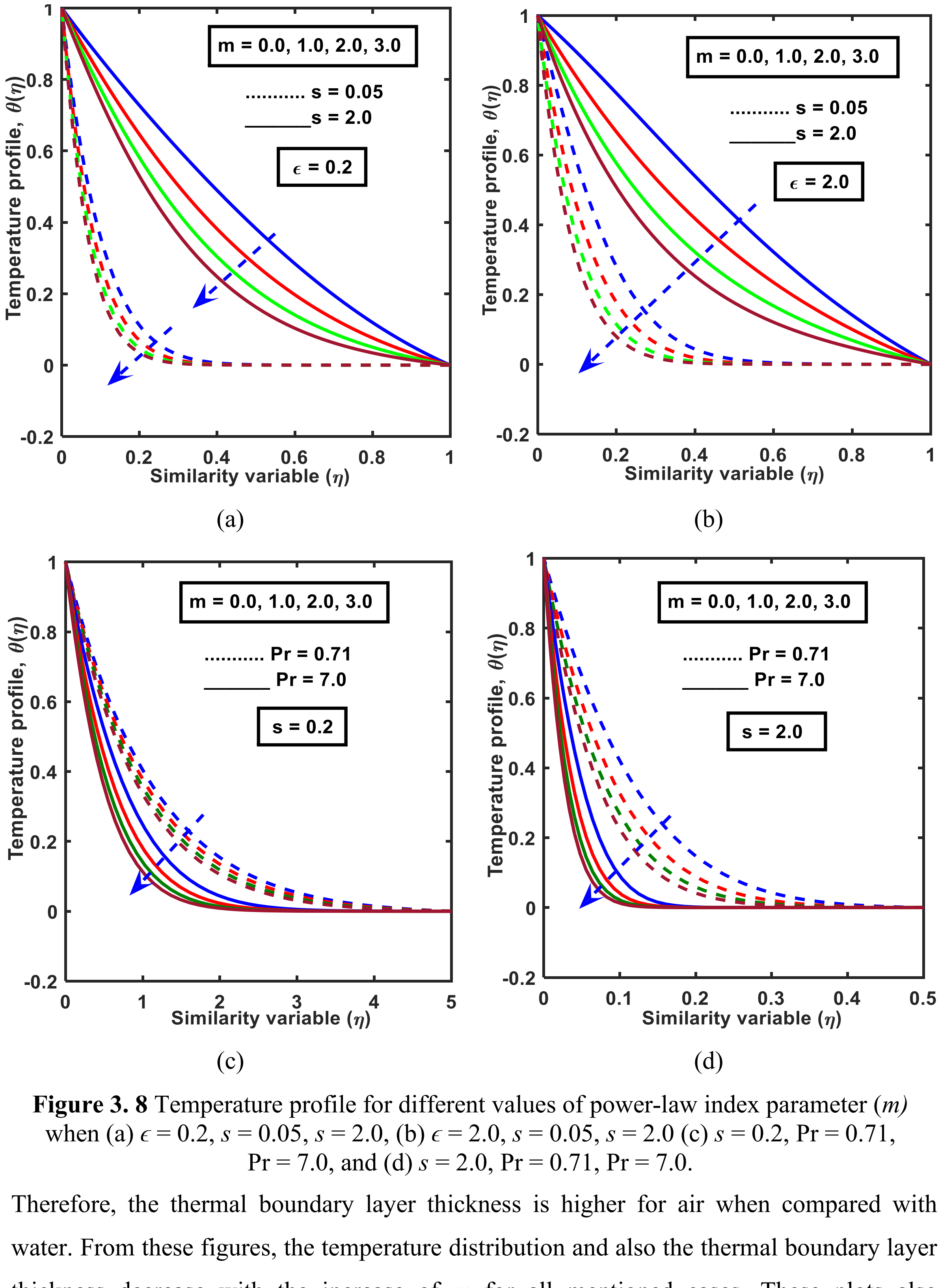

Figure 3. 8 Temperature profile for different values of power-law index parameter (*m*) when (a) $\epsilon = 0.2$, $s = 0.05$, $s = 2.0$, (b) $\epsilon = 2.0$, $s = 0.05$, $s = 2.0$ (c) $s = 0.2$, Pr = 0.71, Pr = 7.0, and (d) $s = 2.0$, Pr = 0.71, Pr = 7.0.

Therefore, the thermal boundary layer thickness is higher for air when compared with water. From these figures, the temperature distribution and also the thermal boundary layer thickness decrease with the increase of *m* for all mentioned cases. These plots also represent that the temperature profile of the viscous fluid and thermal boundary layer thickness affected significantly with increasing power-law index parameter. Therefore, it is seen that for higher values of surface thickness parameter, the maximum temperature shows in the thermal boundary layer compared to that of lower surface thickness parameter. Again, in the case of air (Pr = 0.71), the highest temperature shows in the thermal boundary layer compared to that of water (Pr = 7.0).

3.4.2.3 Effect of surface thickness parameter (*s*) on the temperature profile

Figure 3.9 (a) and Figure 3.9 (b) portray the influence of surface thickness parameter (*s*) on viscous fluid temperature for air (Pr = 0.71) and water (Pr = 7.0) when ϵ = 0.2 and 2.0 respectively. It shows that the temperature profile and thermal boundary layer thickness expand with an increase of surface thickness parameter because the heat transfer rate enhances.

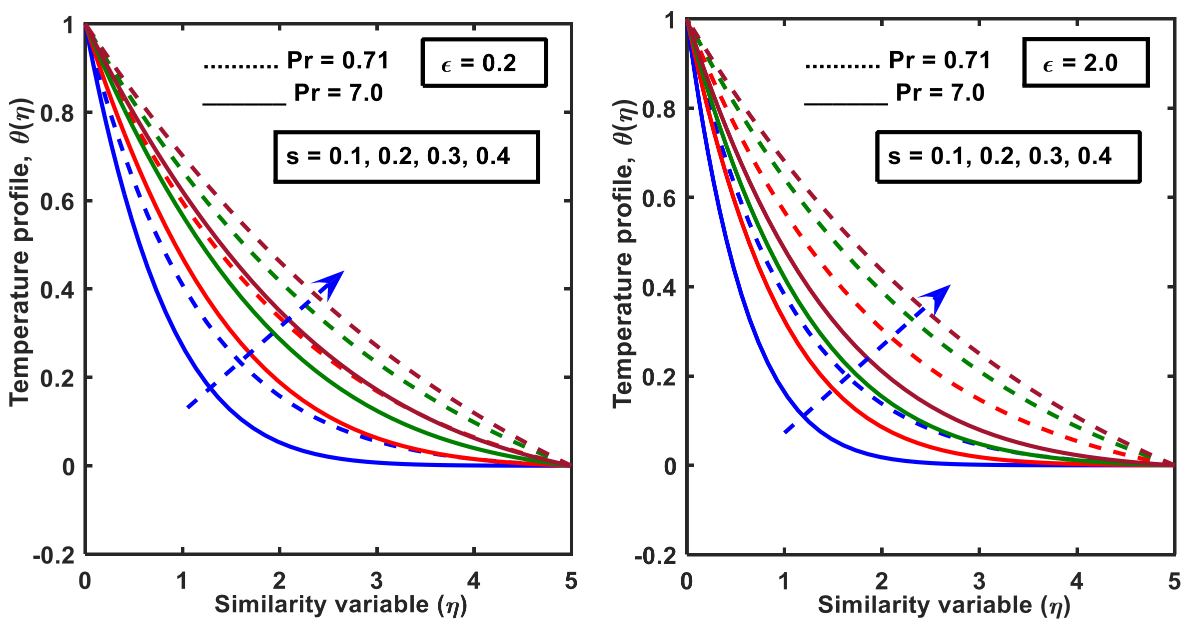

(a) (b)

Figure 3. 9 Temperature profile for different values of surface thickness parameter (*s)* when (a) ϵ = 0.2, Pr = 0.71, 7.0 and (b) ϵ = 2.0, Pr = 0.71, 7.0

It is seen from these figures that the variation of the Prandtl number has a significant effect on viscous fluid temperature in connection with the surface thickness parameter. A higher Prandtl number has a greater decelerating effect than a lower Prandtl number. For air (Pr =

0.71) with increasing s, the accelerating effect is more prominent than for water (Pr = 7.0). Therefore, the thermal boundary layer thickness is higher for air when compared with water. Again, in the case of air (Pr = 0.71), the highest temperature shows in the thermal boundary layer compared to that of water (Pr = 7.0).

3.4.2.4 Effect of stretching ratio parameter (ϵ) on the temperature profile

Figure 3.10 (a) and Figure 3.10 (b) display the effects of the stretching ratio parameter (ϵ) on viscous fluid temperature for air (Pr = 0.71) and water (Pr = 7.0) when s = 0.05 and 2.0 respectively. It shows that the temperature profile and thermal boundary layer thickness squeeze with an increase of the stretching ratio parameter because the velocity profile increases for the effect of this parameter which tends to pass more fluid from the boundary layer region to the surrounding fluid.

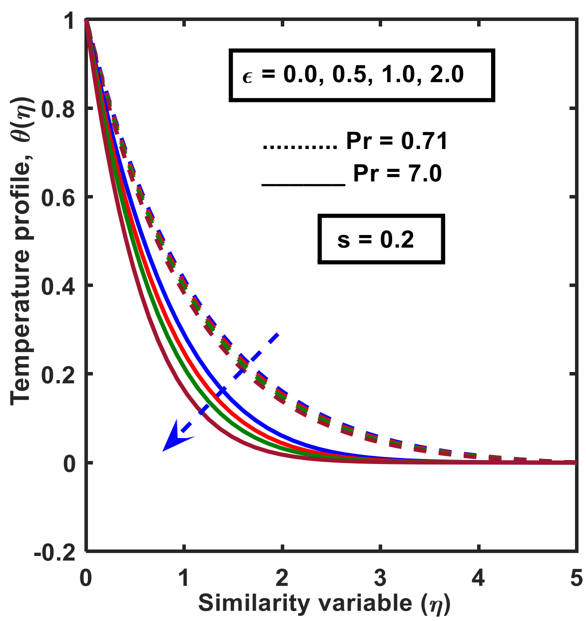

(a)

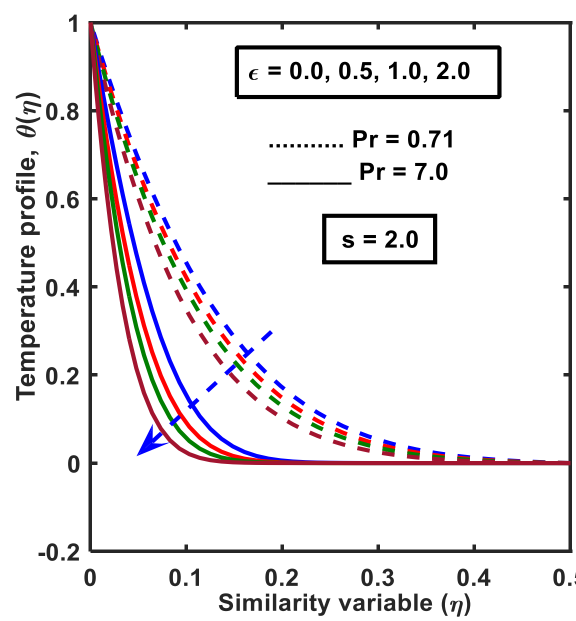

(b)

Figure 3. 10 Temperature profile for different values of stretching ratio parameter (ϵ) when (a) s = 0.2, Pr = 0.71, Pr = 7.0 and (b) s = 2.0, Pr = 0.71, Pr = 7.0

It is seen from these figures that the variation of the Prandtl number has a significant effect on viscous fluid temperature in connection with the stretching ratio parameter. A higher Prandtl number has a greater decelerating effect. For water (Pr = 7.0) with increasing the stretching ratio parameter, the decelerating effect is more prominent than for air (Pr =

0.71). Again, in the case of air (Pr = 0.71), the highest temperature shows in the thermal boundary layer compared to that of water (Pr = 7.0).

The graph of temperature profile represents that the fluid temperature within the boundary layer region is getting lower due to Prandtl number, power-law index parameter, and stretching ratio parameter whereas surface thickness parameter has a reverse effect on it throughout the boundary layer region. From these figures, it is also revealed that in the case of a thicker bullet-shaped object (s = 2.0) the temperature profile does not approach the ambient condition asymptotically but intersects the axis with a steep angle and the boundary layer structure has no definite shape whereas in the case of a thinner bullet-shaped object (s = 0.05) the temperature profile converge the ambient condition asymptotically and the boundary layer structure has a definite shape. Here also one can notice that the thinner bullet-shaped object acts as a good cooling conductor compared to the thicker bullet-shaped object for both ϵ = 0.0 and 2.0. It is also mentioned that the thinner bullet-shaped object represents a thinner thermal boundary layer because the heat transfer rate is higher than the thicker bullet-shaped object in both static and moving bullet-shaped objects. Hence it is mentioned that the lower values of the surface thickness parameter have a greater depressing effect on the temperature profile than higher values of the surface thickness parameter. It is also noticed that the thermal boundary layer thickness is higher for air when compared with water.

3.4.2.5 Influence of Prandtl number (Pr) on Nusselt number, $Nu_x\left(\sqrt{\mathrm{Re}_x}\right)^{-1}$

The variation of the Nusselt number against the effect of the Prandtl number displays in Figures 3.11 (a) and 3.11(b) by taking the stretching ratio parameter ϵ = 0.0 and ϵ = 2.0, and the surface thickness parameter s = 0.05, respectively.

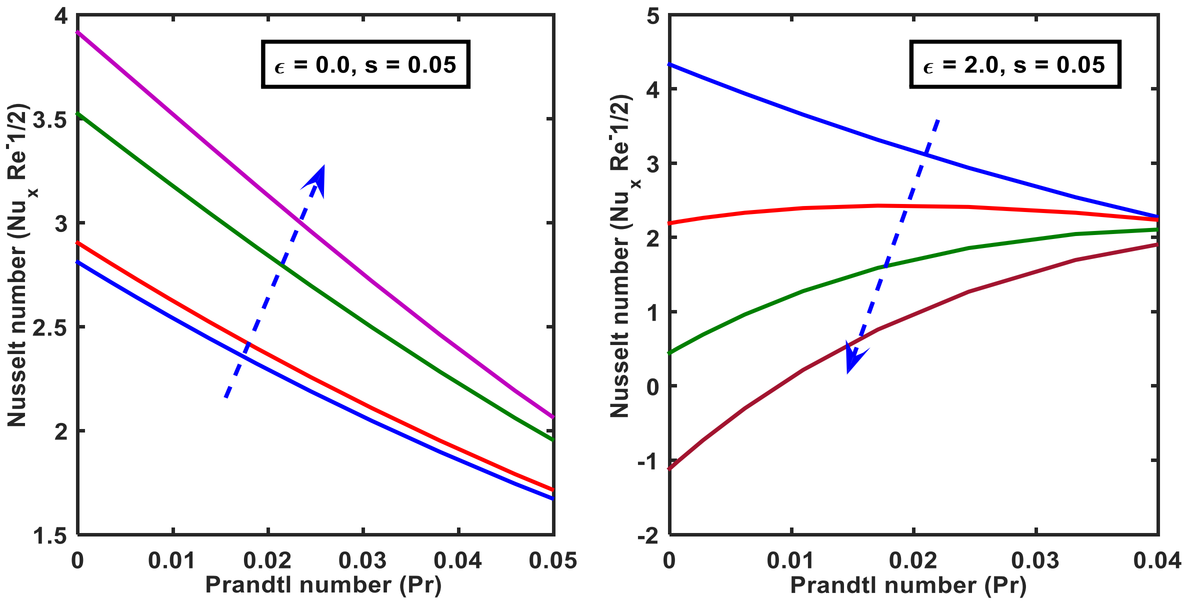

(a) (b)

Figure 3. 11 Nusselt number for different values of Prandtl number when (a) $\epsilon = 0.0$, $s = 0.05$, and (b) $\epsilon = 2.0$, $s = 0.05$

From these figures, it reveals that, the Nusselt number increase as the Prandtl number increases. It is observed from equation (3.1.10) that the Nusselt number is directly proportional to the temperature gradient. The temperature gradient at the surface is always negative for all values of the controlling parameters. Therefore, the Prandtl number is an increasing function of the Nusselt number. It is observed from Table 3.3 that, when Pr changes from 0.71 to 10.0 for $s = 0.05$ and $\epsilon = 0.0$, the Nusselt number increases 17.8 % whereas for $s = 1.0$ and $\epsilon = 0.0$ the corresponding increases 27.7%. Hence, the Nusselt number is higher for the thicker surface ($s = 2.0$) than the thinner surface ($s = 0.05$).

3.4.2.6 Influence of power-law index parameter (*m*) on Nusselt number

Figures 3.12 (a) and 3.12(b) represents the variation of Nusselt number with respect to power-law index parameter by taking the stretching ratio parameter $\epsilon = 0.0$ and $\epsilon = 2.0$, and the surface thickness parameter $s = 0.05$, respectively. From these figures, it reveals that as the values of m increases the Nusselt number also increases. Therefore, the power-law index parameter is directly proportional to the Nusselt number.

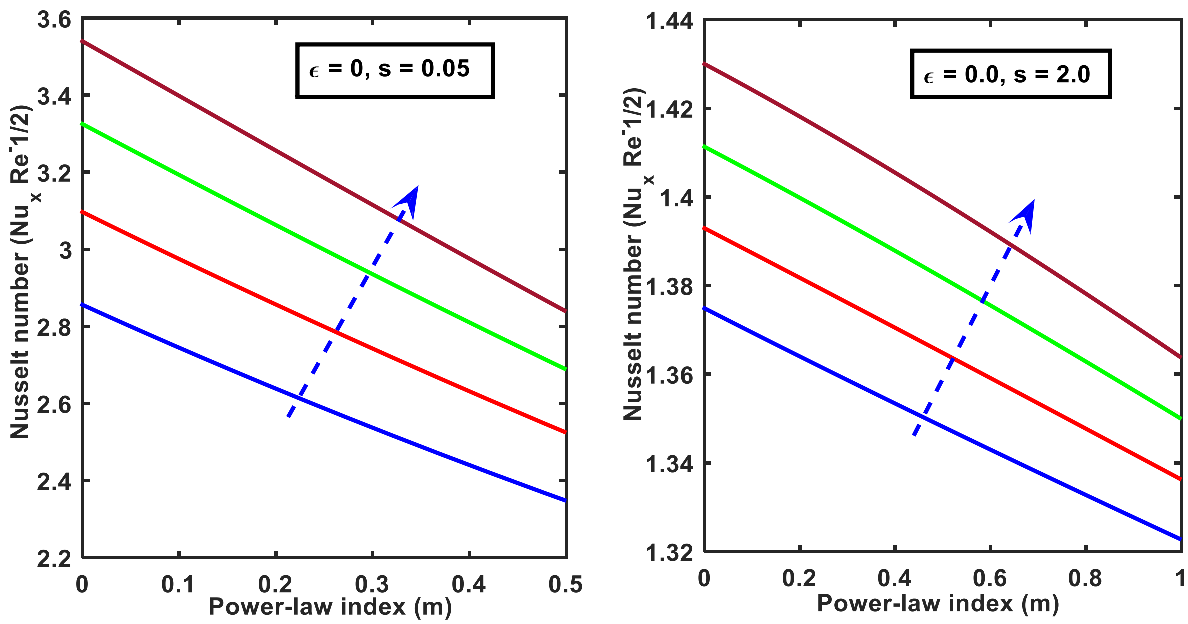

(a) (b)

Figure 3. 12 Nusselt number for different values of power-law index parameter (*m)* when (a) $\epsilon = 0.0$, $s = 0.05$, and (b) $\epsilon = 0.0$, $s = 2.0$

It is observed from Table 3.3 that, when m changes from 0to 3 for $s = 0.05$ and $\epsilon = 0.0$, the Nusselt number increases 12.6 % whereas for $s = 1.0$ and $\epsilon = 0.0$ the corresponding increases 21.64%. Hence, the Nusselt number is higher for the thicker surface ($s = 1.0$) than the thinner surface ($s = 0.05$).

3.4.2.7 Effect of surface thickness parameter (*s*) on Nusselt number

Figures 3.13 (a) and 3.13(b) represents the variation of Nusselt number with respect to surface thickness parameter (s) also taking the stretching ratio parameter $\epsilon = 0.0$ and $\epsilon = 2.0$, respectively. From these figures, it reveals that as the values of s increase the Nusselt number decreases. Therefore, the Nusselt number is a decreasing function of the surface thickness parameter. This implies heat transfer rate is higher in the case of a thinner ($s = 0.05$) bullet-shaped object than the thicker ($s = 2.0$) bullet-shaped object. It is observed from Table 3.3 that, when s changes from 0.05 to 0.5 for $\epsilon = 0.0$, the Nusselt number decreases 85.76 % whereas for $\epsilon = 2.0$ the corresponding decreases 83.6%.

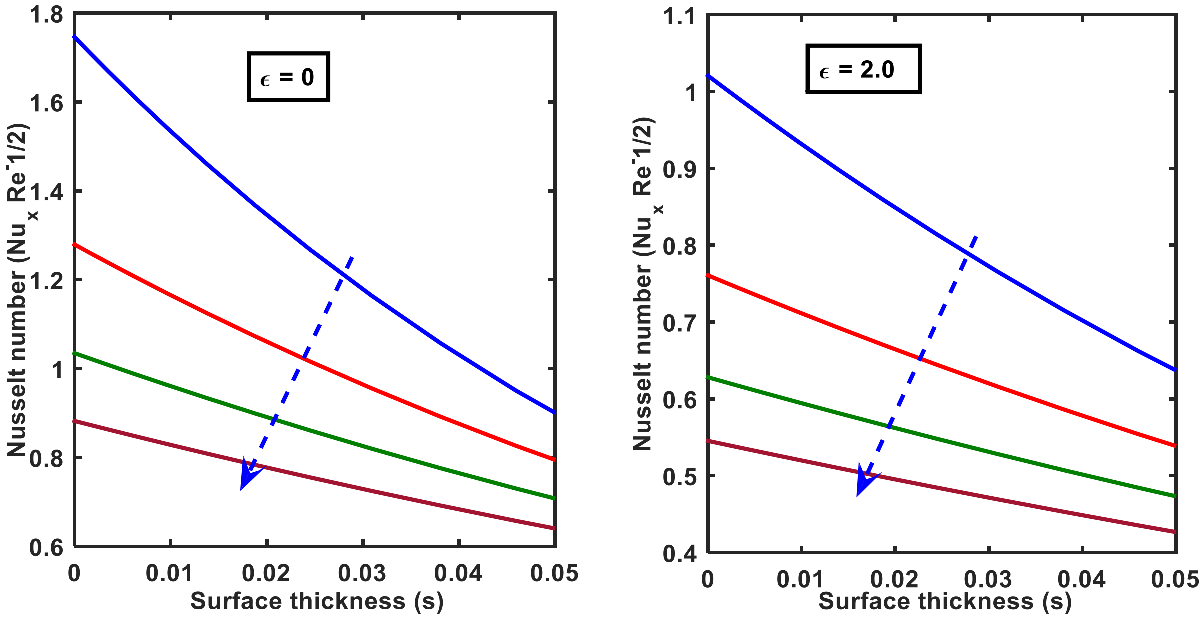

(a) (b)

Figure 3. 13 Nusselt number for different values of surface thickness parameter (*s)* when (a) ϵ = 0.0, and (b) $\epsilon = 2.0$

Hence, the Nusselt number is higher for $\epsilon = 0.0$ than $\epsilon = 2.0$. Figures 3.14(a) and 3.14(b) shows the convergence and accuracy of the present problem.

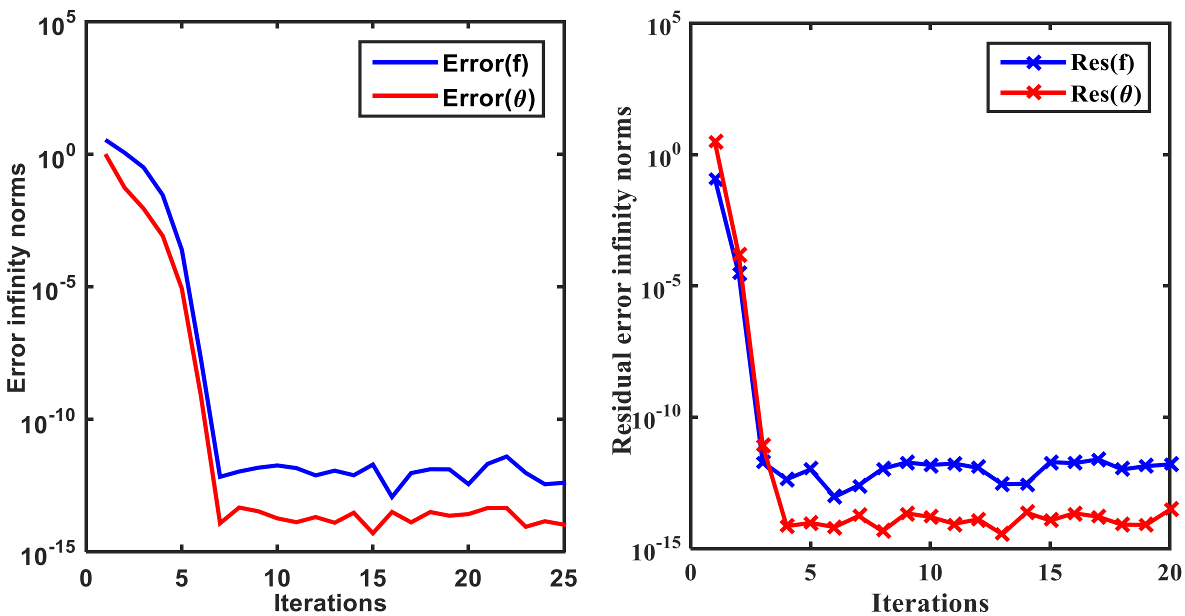

(a) (b)

Figure 3. 14 (a) Error infinity norms and (b) Residual error infinity norms for $f(\eta)$ and $\theta(\eta)$

Figure 3.14(a) depicts the infinity norms with iterations.The error infinity norm decreases with the increasing number of iterations that confirms the convergence of the present method. So, the present method converges after five iterations. Figure 3.14(b) represents the residual error norms of less than 10^{-8} and 10^{-14} for $f(\eta)$ and $\theta(\eta)$ against after fourth iterations. It is seen that the residual error decreases with increasing the iterations. This proves the validity of the present method. The errors show that the SQLM is accurate giving errors of less than 10^{-8} within the fourth iteration.

3.5 Correlation Analysis for Velocity Gradient

A positive correlation means higher values of one variable tend to higher values of another variable but the reverse case arises for the negative correlation. The statistically significant values of the parameters are highlighted in the table because the values are greater equal to 0.25. Then we say that a 95% chance of a relationship between the parameters. So, from Table 3.4 it is observed that the velocity gradient is positively correlated with the magnetic parameter (*M*), and power-law index parameter (*m*) but negatively correlated with the surface thickness parameter (*s*) and stretching ratio parameter (ϵ). Therefore, the fluid velocity and gradient of velocity is an increasing function of the magnetic parameter, and power-law index parameter but *a* decreasing function of the surface thickness parameter and stretching ratio parameter within the boundary layer region.

Table 3. 4 Correlation coefficient between the velocity gradient $f''(\eta)$ and controlling parameters by taking 1st order coefficient in the case of $\epsilon = 0.2$

Parameters	M	s	m	ϵ	$f''(\eta)$
M	1.00				
s	-0.22	1.00			
m	-0.09	-0.08	1.00		
ϵ	0.17	0.15	0.07	1.00	
$f''(0)$	**0.52**	**-0. 43**	**0.21**	**-0.33**	1.00

3.6 Correlation Analysis for Temperature Gradient

A positive correlation means higher values of one variable tend to higher values of another variable but the reverse case arises for the positive correlation. The correlations are significant between the variables if the numerical value of 0.25 or above. Then we say that a 95% chance of a relationship between the parameters. So, from Table 3.5 the correlation is significant for all mentioned parameters except the stretching ratio parameter which is highlighted in the table. The temperature gradient is positively correlated with the parameters Pr, M, m, and ϵ but negatively correlated with the parameter s.

Table 3. 5 Correlation coefficient between the temperature gradient $\theta'(\eta)$ and controlling parameters by taking zero-order coefficient in the case of ϵ = 0.2

Correlation Summary						
Parameters	Pr	M	m	s	ϵ	$\theta'(\eta)$
Pr	1.00					
M	0.59	1.00				
m	-0.08	-0.13	1.00			
s	-0.14	-0.21	-0.08	1.00		
ϵ	0.00	0.00	0.00	0.00	1.00	
$\theta'(\eta)$	**0.45**	**0.44**	**0.28**	**-0.66**	**0.23**	1.00

CHAPTER FOUR

EFFECT OF VISCOUS DISSIPATION AND INTERNAL HEAT GENERATION ON MIXED CONVECTION MAGNETOHYDRODYNAMIC BOUNDARY LAYER FLOW WITH HEAT TRANSFER OVER A NON-LINEAR STRETCHING BULLET-SHAPED OBJECT

This chapter presents an investigation of mixed convection boundary layer flow and heat transfer over a bullet-shaped object by using SQLM with viscous dissipation and internal heat generation. So, the chapter performs the velocity and temperature distribution, local skin friction coefficient, and local Nusselt number by considering two different shapes and sizes (surface thickness parameter) of the bullet-shaped object such as (i) thicker surface (s = 2.0) and (ii) thinner surface (s = 0.05). The numerical results of velocity profile, temperature profile, the local skin friction coefficient, and the local Nusselt number (rate of heat transfer) have been displayed graphically.

4.1 Mathematical Formulation and Analysis of the Present Problem

Let us assume the steady laminar two-dimensional mixed convection MHD axisymmetric boundary layer flow and heat transfer over a non-linear stretching bullet-shaped object. For developing a mathematical model of the present problem, the detailed assumptions are discussed in chapter three when m = 1 represents linear stretching rate and m > 1 implies the surface stretches with non-linearity in nature. The present flow model has been assumed a non-linear stretching rate. The surface extends along the axis of the axisymmetric body (x-direction) and the coordinate r is taken normal to the axis. There is no fluid movement along with the r–axis and the steady flow is considered along the axis only. Therefore, the governing PDEs are as follows

Equation of continuity:

$$\frac{\partial}{\partial x}(ru)+\frac{\partial}{\partial y}(rv)=0 \tag{4.1.1}$$

Momentum equation:

$$u\frac{\partial u}{\partial x}+v\frac{\partial u}{\partial r}=U\frac{\partial U}{\partial x}+\frac{\nu}{r}\left(\frac{\partial u}{\partial r}+r\frac{\partial^2 u}{\partial r^2}\right)+\frac{\sigma B_0{}^2}{\rho}\left(U-u\right)+g\beta\left(T-T_\infty\right) \tag{4.1.2}$$

Energy equation:

$$u\frac{\partial T}{\partial x}+v\frac{\partial T}{\partial r}=\frac{\alpha}{r}\left(\frac{\partial T}{\partial r}+r\frac{\partial^2 T}{\partial r^2}\right)+\frac{Q}{\rho C_p}\left(T-T_\infty\right)+\frac{\nu}{C_p}\left(\frac{\partial u}{\partial r}\right)^2+\frac{\sigma B_0{}^2u^2}{\rho C_p} \tag{4.1.3}$$

The boundary conditions are subjected as

$$u=U_w\left(x\right),\ v=0,\ T=T_w\ \ at\ \ r=R\left(x\right)\ and\ \ u\to U_\infty\left(x\right),T\to T_\infty,as\ \ r\to\infty \tag{4.1.4}$$

For finding the similarity solutions of the equation (4.1.1) – equation (4.1.3) with boundary conditions (4.1.4), we have to use the axisymmetric similarity transformation (4.1.5).

$$\eta=\frac{U_w r^2}{\nu x},\ \ \psi=\nu x f\left(\eta\right),T=x^{2m-1}\theta\left(\eta\right) \tag{4.1.5}$$

The continuity equation (4.1.1) is identically satisfied by the equation (4.1.5). By applying the equation (4.1.5) into the equations (4.1.2) and (4.1.3), we obtain the following reduced ODEs as

$$\eta f'''+f''+\frac{1}{2}ff''\ +\ \frac{m}{8}\left(\varepsilon^2 - 4f'^2\right)+\frac{M}{8}\left(\varepsilon - 2f'\right)+\frac{1}{8}\lambda\theta=0 \tag{4.1.6}$$

$$\eta\theta''+\frac{1}{2}\theta'+\frac{1}{2}\Pr\left[f\ \theta' - \left(2m-1\right)f'\ \theta\right]+\frac{1}{4}\Pr Q^*\theta+\Pr\eta Ec\left(f''\right)^2+\Pr MEcf'^2=0 \tag{4.1.7}$$

and the converted boundary conditions are

$$\begin{gathered} f\left(\eta\right)\ =\ 0,\ f'\left(\eta\right)=\ \frac{1}{2},\theta\ \left(\eta\right)=\ 1,\ at\ \eta\ =\ 0 \\ f'\left(\eta\right)\to\frac{1}{2}\varepsilon,\theta\ \left(\eta\right)\to 0\ \ as\ \eta\to\infty \end{gathered} \tag{4.1.8}$$

It is seen that in the case of $\varepsilon>1.0$, the surface velocity is greater than the free stream velocity and when $\varepsilon<1.0$ the surface velocity is lower than the free stream velocity.

The dimensionless parameters *M, λ,* ε *,* Pr*, Ec, Gr,* Re_x, and Q^* are defined as

$$\mathrm{M} = \frac{\sigma B_0^2 x}{\rho U_w^3}, \lambda = \frac{Gr}{\mathrm{Re}_x^2}, \varepsilon = \frac{b}{a}, \mathrm{Pr} = \frac{\nu}{\alpha}, \mathrm{Ec} = \frac{a^2 x^2 (T_w - T_\infty)}{c_p},$$

$$Gr = \frac{g\beta(T_w - T_\infty)x^3}{\nu^2}, \mathrm{Re}_x = \frac{U_w x}{\nu}, Q^* = \frac{Qx}{\rho U_w c_p}$$

The skin friction coefficient and the local Nusselt number

Now the shear stress and the rate of heat transfer (local Nusselt number, Nu_x) can be expressed in the following way. The shear stress and the local skin friction coefficient are defined as $\tau_w = -\mu\left(\frac{\partial u}{\partial r}\right)_{r=\eta}$ and $C_f = \frac{-2\tau_w}{\rho U^2}$ respectively. By applying the equations (4.1.4) and (4.1.5), the local skin friction coefficient defined as

$$C_f = \frac{-2\mu}{\rho U^2}\left(\frac{\partial u}{\partial r}\right)_{r=\eta} = -8\sqrt{\frac{\eta}{\mathrm{Re}_x}} f''(\eta) \Rightarrow C_f\sqrt{\mathrm{Re}_x} = -8\sqrt{\eta} f''(\eta) \quad (4.1.9)$$

The local Nusselt number can be defined as $Nu_x = \frac{xq_w}{\kappa(T_w - T_\infty)}$. Where q_w is the wall heat flux and taken as $q_w = -\kappa\left(\frac{\partial T}{\partial r}\right)_{r=0}$? By using the equations (4.1.4) and (4.1.5), we obtain the local Nusselt number $Nu_x(\mathrm{Re}_x)^{-1/2} = -2\sqrt{\eta}\theta'(0)$ (4.1.10)

4.2 Methodology

Bellman and Kalaba first introduced the concept of SQLM that is a Newton–Raphson-based QLM. The coupled system of non-linear ODEs (4.1.6) and (4.1.7) are solved numerically by applying SQLM and CSCM with MATLAB. The SQLM is the combination of QLM and CSCM which were developed by Shateyi and Muzara [81]. Applying SQLM, the system of equations (4.1.6) and (4.1.7) are converted into the following iterative sequence of linear differential equations.

$$a_{0,r} f'''_{r+1}(\eta) + a_{1,r} f''_{r+1}(\eta) + a_{2,r} f'_{r+1}(\eta) + a_{3,r} f_{r+1}(\eta) + a_{4,r}\theta_r(\eta) = R_{1,r} \quad (4.2.1)$$

$$c_{0,r}\theta''_{r+1}(\eta)+c_{1,r}\theta'_{r+1}(\eta)+c_{2,r}\theta_r(\eta)+c_{3,r}f''(\eta)+ c_{4,r}f'_{r+1}(\eta)+c_{5,r}f_{r+1}(\eta)=R_{2,r} \qquad (4.2.2)$$

The variable coefficients have the following definitions:

$$a_{0,r}=\frac{\partial f}{\partial f'''}=\eta, a_{1,r}=\frac{\partial f}{\partial f''}=1+\frac{1}{2}f_r, a_{2,r}=\frac{\partial f}{\partial f'}=-mf'_r-\frac{M}{4}, a_{3,r}=\frac{\partial f}{\partial f}=\frac{1}{2}f''_r, a_{4,r}=\frac{\lambda}{8}$$

$$c_{0,r}=\frac{\partial\theta}{\partial\theta''}=\eta, c_{1,r}=\frac{\partial\theta}{\partial\theta'}=\frac{1}{2}+\frac{\Pr}{2}f_r, c_{2,r}=\frac{\partial\theta}{\partial\theta}=-\frac{\Pr(2m-1)}{2}f'_r+\frac{1}{4}\Pr Q^*$$

$$c_{3,r}=\frac{\partial\theta}{\partial f''}=2\eta Ecf''_r, c_{4,r}=\frac{\partial\theta}{\partial f'}=-\frac{\Pr(2m-1)}{2}\theta_r+2MEcf'_r, c_{5,r}=\frac{\partial\theta}{\partial f}=\frac{\Pr}{2}\theta'_r$$

The terms on the right side are defined as follows:

$$R_{1,r}(\eta)=a_{0,r}f'''_r+a_{1,r}f''_r+a_{2,r}f'_r+a_{3,r}f_r+a_{4,r}\theta_r-F\left[\eta,f,f',f''......f^n\right]$$
$$=\frac{1}{2}f_rf''-\frac{m}{2}f'^2_r-\frac{m\varepsilon^2}{8}-\frac{M\varepsilon}{8}$$

$$R_{2,r}(\eta)=c_{0,r}\theta''_r+c_{1,r}\theta'_r+c_{2,r}\theta_r+c_{3,r}f''_r+c_{4,r}f'_r+c_{5,r}f_r-F\left[\eta,f,f',f''......f^n\right]$$
$$=\frac{\Pr}{2}\left[f_r\theta'_r-(2m-1)f'_r\theta_r\right]+MEcf'^2_r+\eta Ec\left(f''_r\right)^2$$

Chebyshev Differentiation

We approximate the solutions of Equations (4.1.6) – (4.1.7) by functions of the form

$$f(\eta)=\sum_{k=0}^{N}f(\eta_k)L_k(\eta), \theta(\eta)=\sum_{k=0}^{N}\theta(\eta_k)L_k(\eta) \qquad (4.2.3)$$

The term $L_k(\eta)=\prod_{j=0}^{N}\frac{\eta-\eta_j}{\eta_k-\eta_j}$ is the Lagrange interpolating polynomial. The detailed calculations have been discussed in section 3.2.

Evaluating equations (4.1.9) – (4.1.10) at the collocation points and the Chebyshev derivatives gives in the vector-matrix form of the following system

$\begin{bmatrix}A_{11} & A_{12}\\ A_{21} & A_{22}\end{bmatrix}\begin{bmatrix}F_{r+1}\\ \theta_{r+1}\end{bmatrix}=\begin{bmatrix}R_{1,r}\\ R_{2,r}\end{bmatrix}$. Where $\begin{matrix}A_{11}=a_{0,r}D^3+a_{1,r}D^2+a_{2,r}D+a_{3,r}, A_{12}=a_{4,r}I,\\ A_{21}=c_{3,r}D^2+c_{4,r}D+c_{5,r}, A_{22}=c_{0,r}D^2+c_{1,r}D+c_{2,r}\end{matrix}$

The transformed boundary conditions

$$f_{r+1}(\eta_0)=0, f'_{r+1}(\eta_0)=\frac{1}{2}, \theta_{r+1}(\eta_0)=1, R_r(\eta_{N_1})= \ \frac{1}{2} \ at \ \eta=0$$

$$f_{r+1}(\eta_{N_1})=0, f'_{r+1}(\eta_{N_1})=\frac{\varepsilon}{2}, \theta_{r+1}(\eta_N)= \ 0, \ R_r(\eta_{N_1+1})$$

4.3 Results and Discussion

The non-linear ODEs of the present problem are solved by applying SQLM. The convergence criteria of the solution are performed by the use of solution-based errors. These errors are defined by the differences between approximate solutions at the previous and current iteration levels t and t + 1, respectively. The error norms have been defined in chapter three.

The infinity norms of the residual errors are defined by

$$\left\|\operatorname{Re}s(f)\right\|_\infty=\left\|\eta f'''+f''+\frac{1}{2}ff'' \ + \ \frac{m}{8}\left(\varepsilon^2 - 4f'^2\right)+\frac{M}{8}\left(\varepsilon - 2f'\right)+\frac{1}{8}\lambda\theta\right\|=0 \text{ and}$$

$$\left\|\operatorname{Re}s(\theta)\right\|_\infty=\left\|\eta\theta''+\frac{1}{2}\theta'+\frac{1}{2}\Pr\left[f \ \theta' - (2m-1) f' \ \theta\right]+\Pr\left[\frac{1}{4}Q^*\theta+\eta Ecf''^2+MEcf'^2\right]\right\|=0$$

The impact of physical parameters on velocity $f'(\eta)$, temperature $\theta(\eta)$, the skin friction coefficient, and the Nusselt number has been shown graphically. The numerical values of skin friction coefficient and Nusselt number ($Nu_x\left(\sqrt{\operatorname{Re}_x}\right)^{-1}$) which are directly proportional to velocity gradient, $f''(\eta)$ and temperature gradient, $\theta'(\eta)$ have been shown in Table 4.1 and Table 4.2 respectively. The numerical calculation has been done by taking N = 60 collocation points and solution-based errors have been defined for the convergence of the numerical method. So, Figures 4.15(a) and 4.15(b) show the convergence and accuracy of the present problem. Figure 4.15(a) represents the infinity norms with iterations. The error infinity norm decreases with the increasing number of iterations that confirms the convergence of the present method. So the present method converges after five iterations. Figure 4.15(b) represents the residual error norms of less than 10^{-8} and 10^{-13}

for $f(\eta)$ and $\theta(\eta)$ against after five iterations. It is seen that the residual error decreases with increasing the iterations. This proves the validity of the present method. The errors show that the SQLM is accurate giving errors of less than 10^{-8} within the fourth iteration. In this chapter the default parameters are taken as M = 1.0, m = 2.0, Pr = 0.71, ϵ = 0.2, s = 0.1, Ec = 0.5, λ = 0.5 and Q^* = 0.4 throughout the calculation. The fluid velocity profile and skin friction have been displayed graphically versus boundary layer co-ordinate (η) in Figures 4.1 – 4.7 for different values of power-law index parameter, magnetic parameter, Eckert number (Ec), heat generation parameter (Q^*), mixed convection parameter (λ), stretching ratio parameter, and surface thickness parameter in the following sub-section.

4.3.1 Velocity profiles and skin friction coefficient with parameter variations

4.3.1.1 Influence of the power-law index parameter (*m*) on the velocity profile and skin friction coefficient

The effect of the power-law index parameter on the velocity profile and skin friction coefficient depicts in Figures 4.1(a) – 4.1(d) by considering the stretching ratio parameter $\varepsilon < 1.0$ and $\varepsilon > 1.0$, and the surface thickness parameter s = 0.05, s = 2.0, respectively. These plots depict that the velocity profile of the viscous fluid and boundary layer thickness affected insignificantly with increasing power-law index parameter. From these figures, it is seen that the velocity profile and boundary layer thickness expands both in the thinner and thicker surfaces (s = 0.05, s = 2.0) and the fluid flow form a definite boundary layer pattern when $\varepsilon > 1.0$ but in the case of $\varepsilon < 1.0$, it forms an inverted boundary layer pattern. It is also noticed that the variation of the stretching ratio parameter has an insignificant effect on the velocity profile in connection with the power-law index parameter. The velocity gradient at the surface is positive when $\varepsilon > 1.0$ and negative due to $\varepsilon < 1.0$ all values of the controlling parameters. It is also seen that the skin friction coefficient increases in the case of $\varepsilon > 1.0$ both of the thinner and thicker surfaces but the opposite result arises in the case of $\varepsilon < 1.0$.

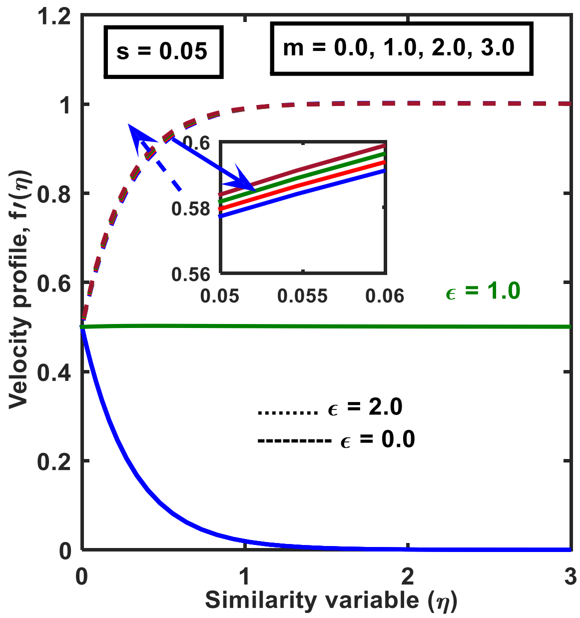

(a)

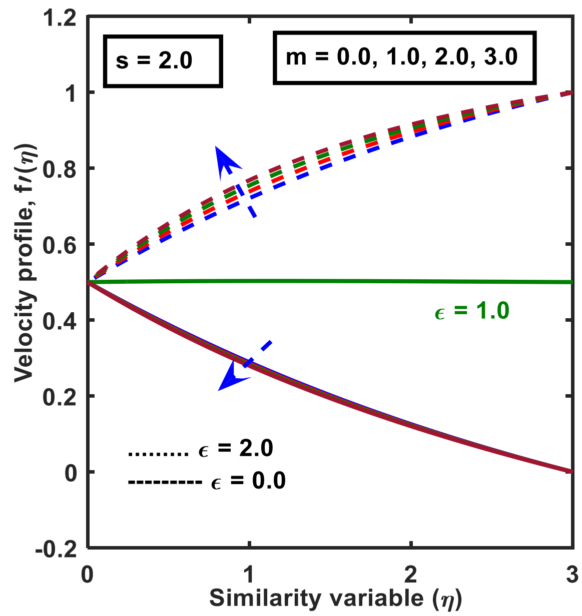

(b)

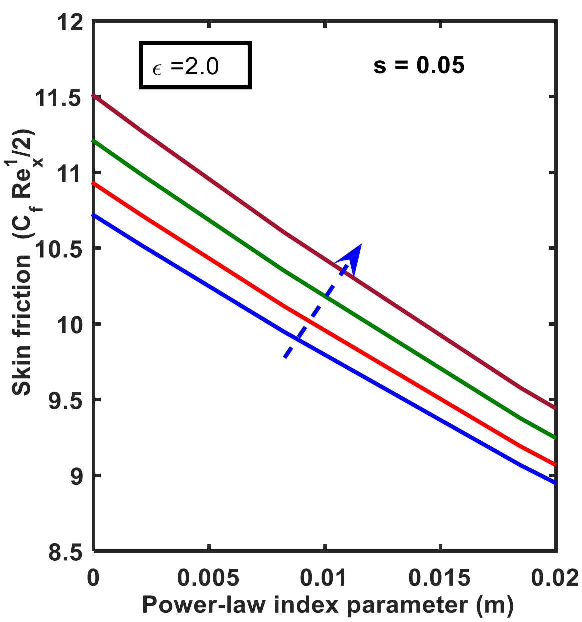

(c)

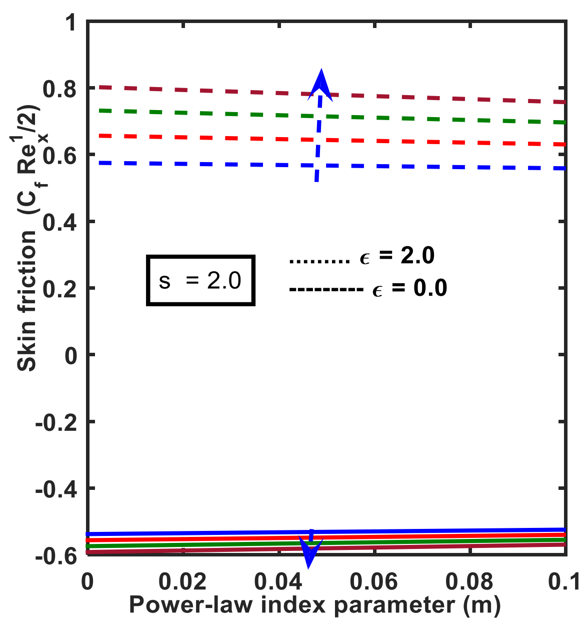

(d)

Figure 4. 1 Effect of power-law index parameter on velocity profile and skin friction taking (a) s = 0.05 and ϵ = 0.0 (lower panel), ϵ =1.0 (separation line), ϵ = 2.0 (upper panel) (b) s = 2.0 and ϵ = 0.0 (lower panel), ϵ =1.0 (separation line), ϵ = 2.0 (upper panel), (c) s = 0.05 and ϵ = 2.0 (upper panel), and (d) s = 2.0 and ϵ = 0.0 (lower panel), ϵ = 2.0 (upper panel).

Therefore, from Figure 4.1(a) – Figure 4.1(d), it is concluded that the hydrodynamic boundary layer thickness increases when $\varepsilon > 1.0$ and decreases when $\varepsilon < 1.0$ but the skin friction coefficient increases in cases of $\varepsilon > 1.0$ but decreases for $\varepsilon < 1.0$. It is also observed that in the case of the thinner surface (s = 0.05) the fluid flow forms a certain boundary layer structure and the fluid velocity satisfies the far-field boundary condition. On the other hand, while thicker surface (s = 2.0) the fluid flow does not satisfy the far-field boundary condition and the boundary layer structure has no definite shape instead it intersects the axis with a steep angle. From the analysis, the velocity boundary layer thickness is higher in the case of the thicker bullet-shaped object (s = 2.0) than the thinner bullet-shaped object (s = 0.05).

4.3.1.2 Effect of the magnetic parameter (*M*) on the velocity profile and skin friction coefficient

Figures 4.2(a) - 4.2(d) represent the variation of velocity profile and skin friction coefficient for the increasing effect of magnetic parameter with the stretching ratio parameter $\varepsilon < 1.0$ and $\varepsilon > 1.0$, and the surface thickness parameter s = 0.05, s = 2.0, respectively. These plots depict that the velocity profile of the viscous fluid and boundary layer thickness affected insignificantly in the case of a thinner surface (s = 0.05) but significantly affected in the case of a thicker surface (s = 2.0) with an increasing magnetic parameter. It is revealed that the velocity profile expands but the boundary layer thickness squeezes and the fluid flow form an inverted boundary layer pattern in both of the thinner and thicker surfaces of the bullet-shaped object when $\varepsilon < 1.0$ whereas in the case of $\varepsilon > 1.0$ the velocity profile form a definite boundary layer pattern. The reason has been discussed in chapter three. It is also seen that the variation of the stretching ratio parameter has an insignificant effect on the velocity profile in connection with the magnetic parameter in the case of a thinner surface (s = 0.05) than the thicker surface (s = 2.0). Therefore, the velocity gradient at the surface is positive when $\varepsilon > 1.0$ and negative due to $\varepsilon < 1.0$ all values of the controlling parameters. Again, it is also observed that the skin friction coefficient increases in case of $\varepsilon > 1.0$ and decreases in case of $\varepsilon < 1.0$. The fluid velocity is directly proportional to M when $\varepsilon > 1.0$ but inversely proportional when $\varepsilon < 1.0$.

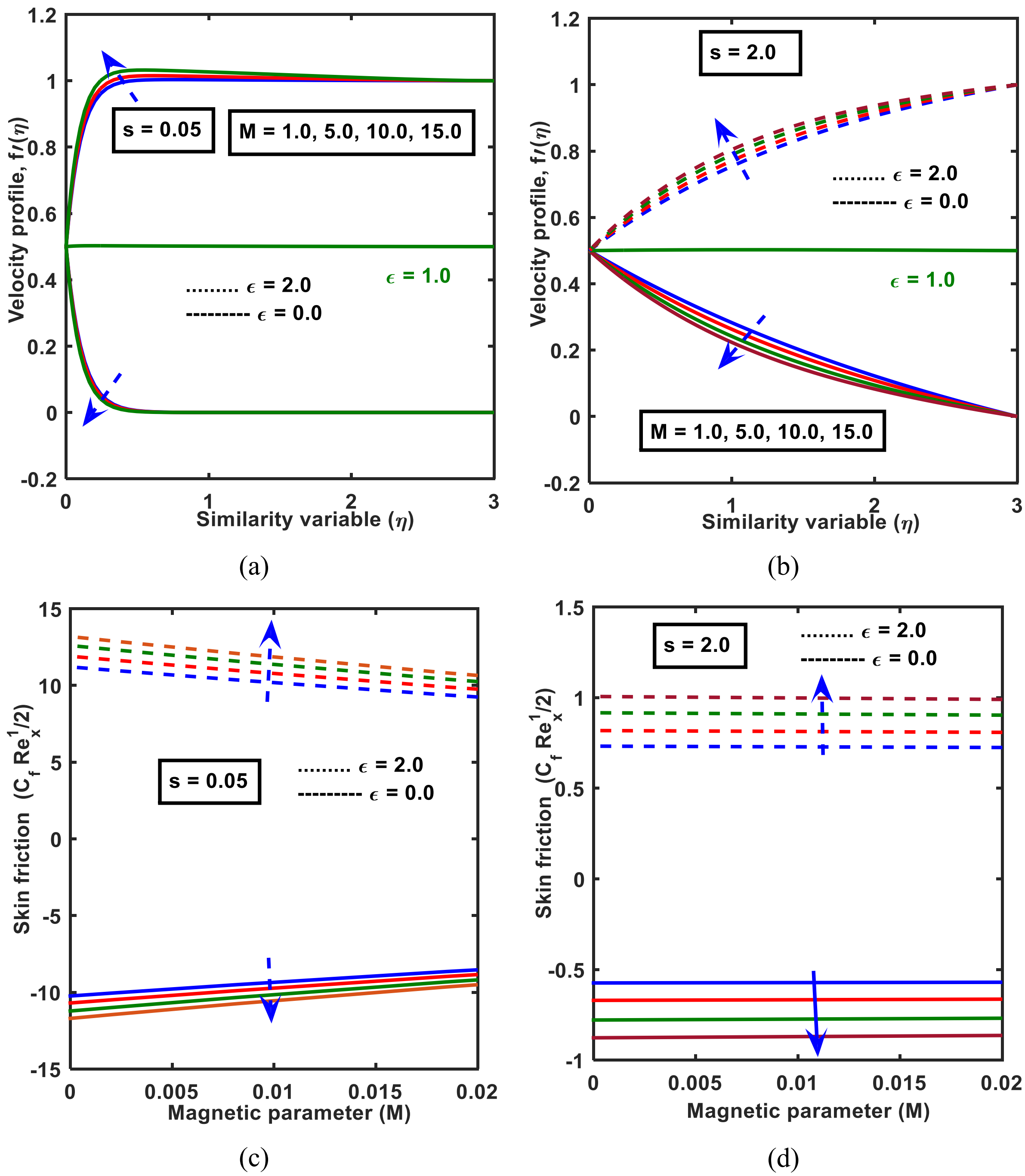

Figure 4. 2 Effect of magnetic parameter (*M)* on velocity profile and skin friction taking (a) $s = 0.05$ and $\epsilon = 0.0$ (lower panel), $\epsilon = 1.0$ (separation line), $\epsilon = 2.0$ (upper panel) (b) $s = 2.0$ and $\epsilon = 0.0$ (lower panel), $\epsilon = 1.0$ (separation line), $\epsilon = 2.0$ (upper panel), (c) $s = 0.05$ and $\epsilon = 0.0$ (lower panel), $\epsilon = 2.0$ (upper panel), and (d) $s = 2.0$ and $\epsilon = 0.0$ (lower panel), $\epsilon = 2.0$ (upper panel).

From the numerical values of the velocity gradient, it is observed that when M increases from 1.0 to 15.0, then there is a 28.73% increase (when ϵ = 0.0, and s = 0.05) of the skin friction coefficient and the corresponding increase is 48.79% in case of ϵ = 2.0, and s = 1.0.

4.3.1.3 Effect of Eckert number (*Ec*) on the velocity profile

Figures 4.3(a) and 4.3(b) represent the variation of a velocity profile for the increasing effect of Eckert number (*Ec*) with the stretching ratio parameter $\varepsilon < 1.0$ and $\varepsilon > 1.0$, and the surface thickness parameter s = 0.05, s = 2.0, respectively. These plots depict that the velocity profile of the viscous fluid and boundary layer thickness affected insignificantly with increasing Eckert number in both the cases of thinner and thicker surfaces. It is revealed that the velocity profile expands but the boundary layer thickness squeezes and the fluid flow forms an inverted boundary layer pattern in the thinner surface of the bullet-shaped object.

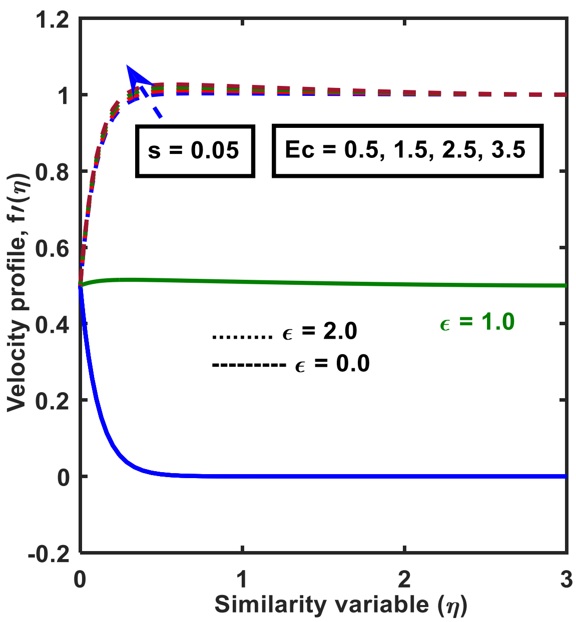

(a)

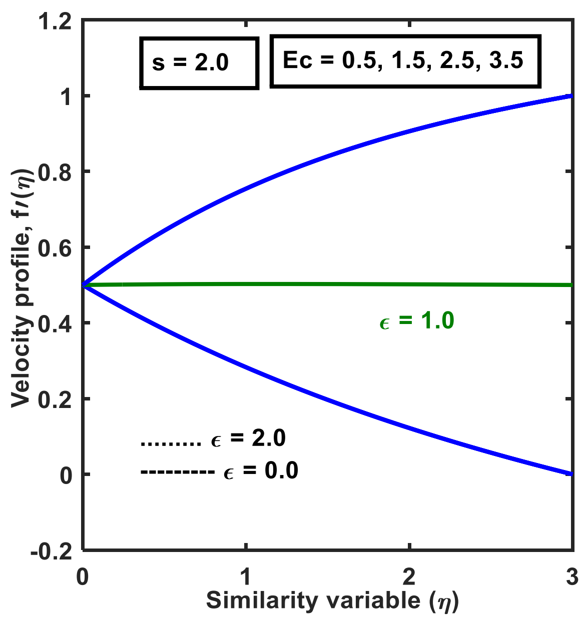

(b)

Figure 4. 3 Effect of Eckert number on velocity profile taking (a) s = 0.05 and ϵ = 0.0 (lower panel), ϵ =1.0 (separation line), ϵ = 2.0 (upper panel), and (b) s = 2.0 and ϵ = 0.0 (lower panel), ϵ =1.0 (separation line), ϵ = 2.0 (upper panel).

Again, it is also observed that the velocity profile and boundary layer thickness expand when $\varepsilon > 1.0$, and the fluid flow forms an inverted boundary layer pattern in the case of the thinner surface of the bullet-shaped object but in the other cases the Eckert number does not affect the velocity profile.

4.3.1.4 Effect of heat generation parameter (Q^*) on the velocity profile

Figures 4.4(a) and 4.4(b) represent the variation of a velocity profile for the increasing effect of heat generation parameter with the stretching ratio parameter $\varepsilon < 1.0$ and $\varepsilon > 1.0$, and the surface thickness parameter s = 0.05, s = 2.0, respectively. From these figures, it is seen that the fluid flow forms an inverted boundary layer pattern in the case of $\varepsilon > 1.0$ but a definite boundary layer forms in the case of $\varepsilon < 1.0$. These plots depict that the velocity profile of the viscous fluid and boundary layer thickness affected insignificantly with increasing heat generation parameters in both the cases of thinner and thicker surfaces. It is also seen that the variation of the stretching ratio parameter has an insignificant effect on the velocity profile in connection with the heat generation parameter in both the thinner and thicker surfaces.

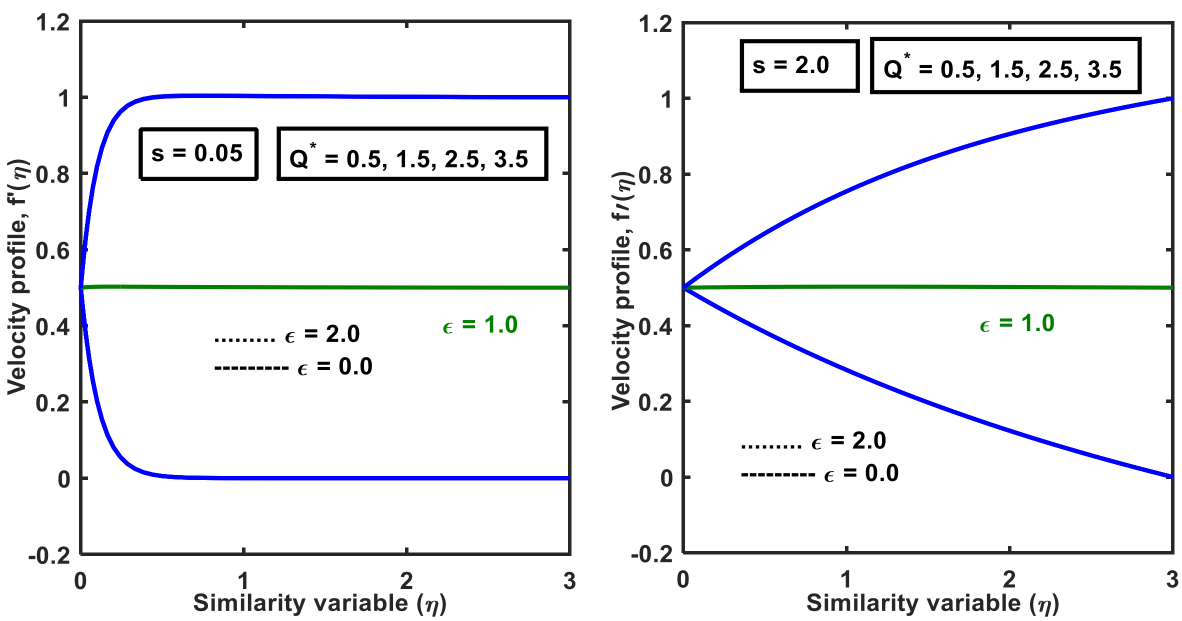

(a) (b)

Figure 4. 4 Effect of heat generation (Q^*) on velocity profile taking (a) s = 0.05 and ϵ = 0.0 (lower panel), ϵ =1.0 (separation line), ϵ = 2.0 (upper panel), and (b) s = 2.0 and ϵ = 0.0 (lower panel), ϵ =1.0 (separation line), ϵ = 2.0 (upper panel)

4.3.1.5 Effect of mixed convection parameter (λ) on the velocity profile and skin friction coefficient

Figure 4.5 (a) – Figure 4.5(d) are the variations of fluid velocity profile and skin friction coefficient for distinct values of mixed convection parameter (λ) with the stretching ratio parameter $\varepsilon < 1.0$ and $\varepsilon > 1.0$, and the surface thickness parameter s = 0.05, s = 2.0, respectively. These plots depict that the velocity profile of the viscous fluid and boundary layer thickness affected insignificantly with increasing mixed convection parameters. It is revealed that the velocity profile and the boundary layer thickness does not affect the mixed convection parameter and the fluid flow form an inverted boundary layer pattern due to the thinner surface of the bullet-shaped object when $\varepsilon < 1.0$ whereas in the case of $\varepsilon > 1.0$, the velocity profile and the boundary layer thickness expand and also forms certain boundary layer pattern for both the thinner and thicker surfaces. It is also noticed that the variation of the stretching ratio parameter has an insignificant effect on the fluid velocity profile in connection with the mixed convection parameter. Hence, the velocity profile, boundary layer thickness, and skin friction increase with increasing values of λ for both the thinner and thicker surfaces (s = 0.05, 2.0) except for the cases $\varepsilon < 1.0$ and s = 0.05.

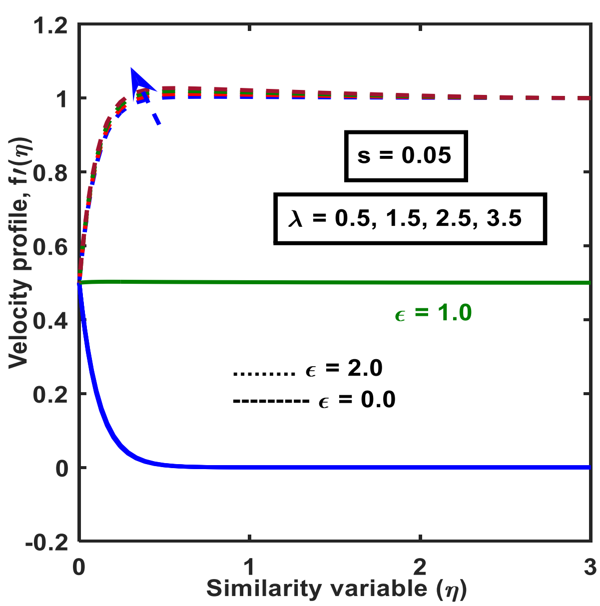

(a)

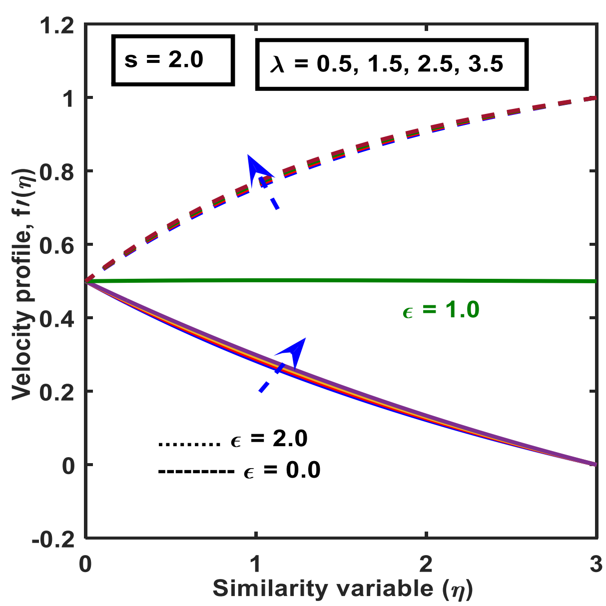

(b)

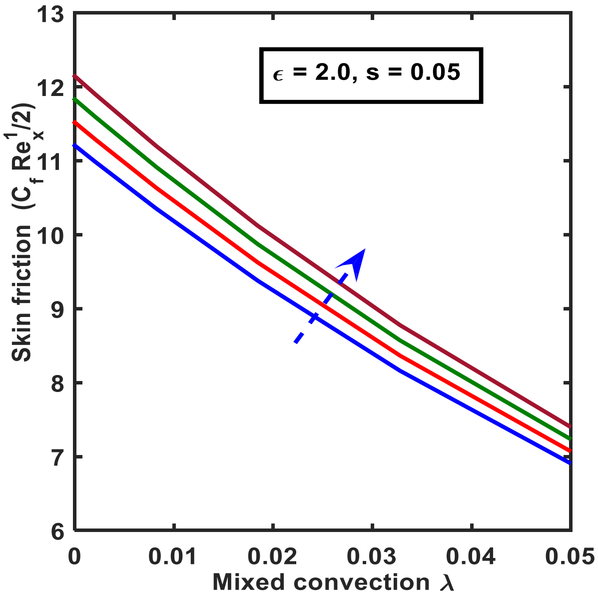

(c)

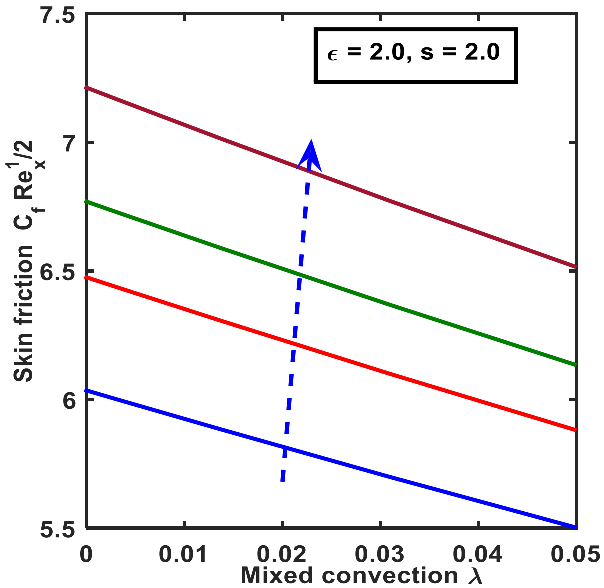

(d)

Figure 4. 5 Effect of mixed convection on velocity profile and skin friction taking (a) s = 0.05 and ϵ = 0.0 (lower panel), ϵ =1.0 (separation line), ϵ = 2.0 (upper panel) (b) s = 2.0 and ϵ = 0.0 (lower panel), ϵ =1.0 (separation line), ϵ = 2.0 (upper panel), (c) s = 0.05 ϵ = 2.0, and (d) s = 2.0 and ϵ = 2.0

This happens because by increasing the mixed convection parameter then the buoyancy force increases which in turn produces more kinetic energy as a result the fluid velocity increases. It is also observed that when λ increases from 0.5 to 2.5 there is a 9.3 % ($\varepsilon < 1.0$) decrease in the skin friction coefficient value, whereas the corresponding decrease is 5.2%, ($\varepsilon < 1.0$) when λ increases from 2.5 to 5.5.

4.3.1.6 Effect of stretching ratio parameter (ϵ) on the velocity profile and skin friction coefficient

Figure 4.6 (a) – Figure 4.6(d) illustrate the increasing effect of the stretching ratio parameter ($0 \le \varepsilon \le 1.8$) on the velocity profiles and skin friction coefficient when the others parameters are fixed in the case of (a) thinner (s = 0.05), and (b) thicker (s = 2.0) bullet-shaped object respectively. These plots depict that the velocity profile of the viscous fluid and boundary layer thickness affected significantly with increasing stretching ratio parameter. It is revealed that the velocity profile expands but the boundary layer thickness squeezes and the fluid flow form an inverted boundary layer pattern in both of the thinner and thicker surfaces of the bullet-shaped object when $\varepsilon < 1.0$ whereas in the case of $\varepsilon > 1.0$, it forms a definite boundary layer pattern.

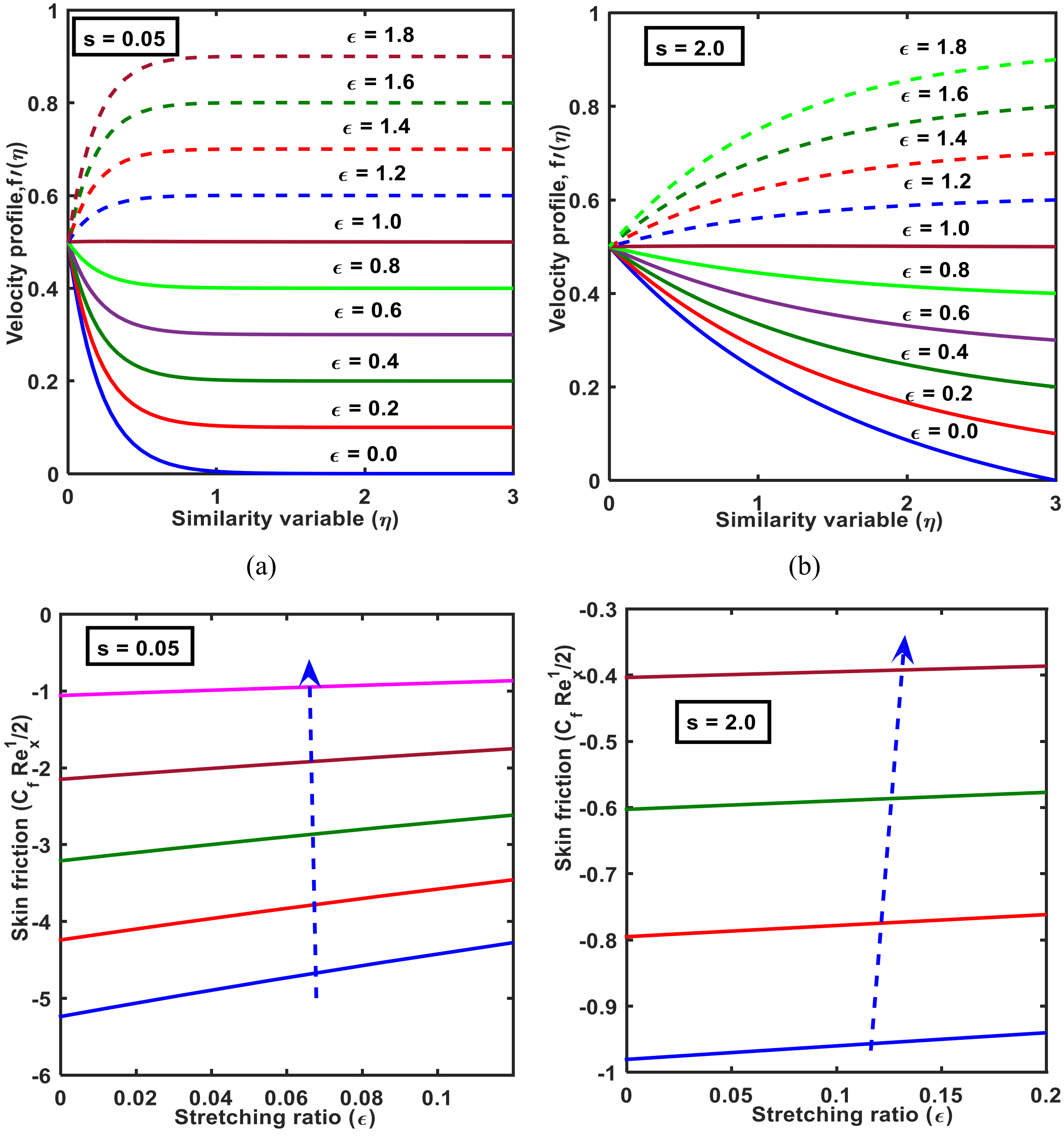

Figure 4. 6 Effect of stretching ratio (ϵ) on velocity profile and skin friction taking (a) $s = 0.05$ (b) $s = 2.0$ (c) $s = 0.05$ $\epsilon = 2.0$, and (d) $s = 2.0$ and $\epsilon = 2.0$

It is also noticed that the variation of the surface thickness parameter has a significant effect on the fluid velocity profile in connection with the stretching ratio parameter. It is also seen that the axial velocity increases just near the bullet-shaped object and decreases far from it when $\varepsilon > 1.0$ but an opposite trend is observed when $\varepsilon < 1.0$. Therefore, when $\varepsilon < 1.0$, the surface velocity dominates the free stream velocity at the edge of the BL. Accordingly, the boundary layer thickness and the skin friction increases for both the thinner and thicker surfaces. Hence, for increasing the ϵ then surface velocity increases as a result the fluid velocity also increases. It is noticed that when ϵ increases from 0.2 to 0.4 there is a 15.3 % ($\varepsilon < 1.0$) increase in the skin friction coefficient value, whereas the corresponding increase is 12.2%, ($\varepsilon < 1.0$) when ϵ increases from 0.4 to 0.6.

4.3.1.7 Effect of surface thickness parameter (*s*) on the velocity profile and skin friction coefficient

Figure 4.7 (a) and Figure 4.7(d) are the variations of fluid velocity profiles and skin friction coefficient for different values of surface thickness parameter in the case of $\epsilon = 0.0$ and $\epsilon = 2.0$ respectively. It is revealed that the fluid velocity profile and the boundary layer thickness squeezes and the fluid flow forms a definite boundary layer pattern when $\varepsilon < 1.0$ whereas in the case of $\varepsilon > 1.0$, the fluid velocity profile expands but the boundary layer thickness squeezes and it forms an inverted boundary layer pattern. On the other hand, the skin friction coefficient decreases for both cases. Therefore, an increase in s enhances the surface area of the object that provides more resistance against the fluid motion as a result the fluid velocity decreases. Although, the skin friction coefficient is negative in the case of $\epsilon = 0.0$ and positive in the case of $\epsilon = 2.0$. It is also seen that when s increases from 0.1 to 0.2 there is a 20.3 % ($\varepsilon < 1.0$) decrease in the skin friction coefficient, whereas the corresponding decrease is 15.2%, ($\varepsilon < 1.0$) when s increases from 0.3 to 0.4.

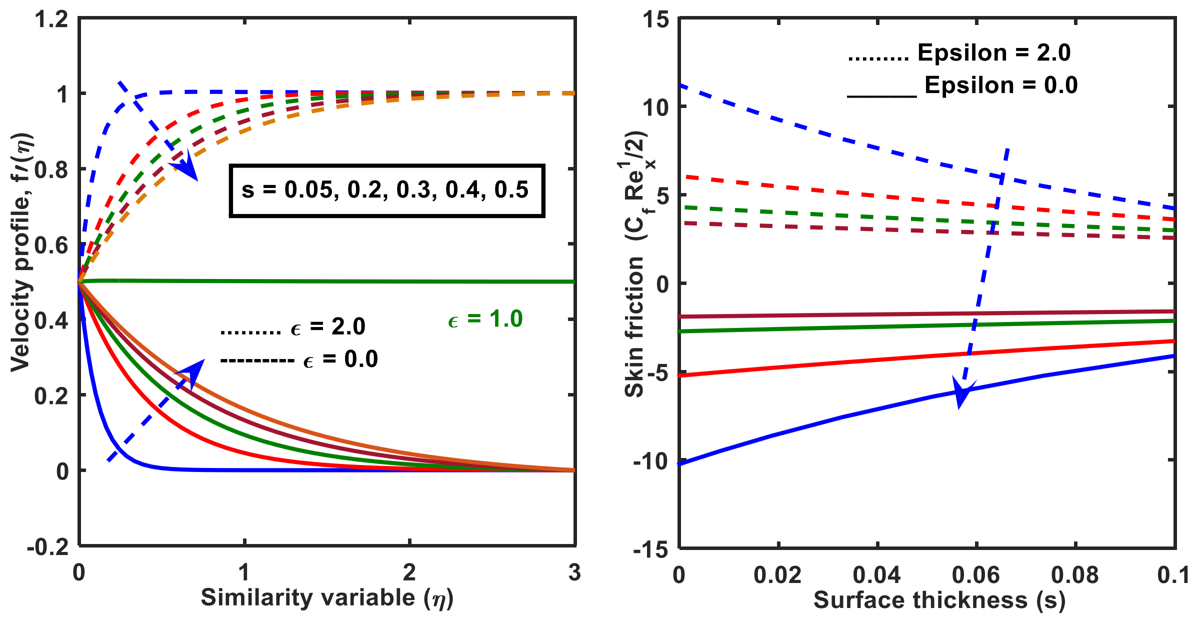

(a) (b)

Figure 4. 7 Effect of surface thickness (s) on velocity profile and skin friction taking (a) ϵ = 0.0 (lower panel), ϵ =1.0 (separation line), ϵ = 2.0 (upper panel), and (b) ϵ = 0.0 (lower panel), ϵ = 2.0 (upper panel)

From these velocity distribution figures, it is observed that the velocity profile and momentum boundary layer thickness is getting expand due to power-law index parameter (m), magnetic parameter (M), Eckert number (Ec), mixed convection parameter (λ), and stretching ratio parameter (ϵ) whereas surface thickness parameter (s) has a reverse effect on it in the case of $\varepsilon > 1.0$ for both of the thicker (s = 2.0) and the thinner (s = 0.05) surfaces. On the other hand, in the case of $\varepsilon < 1.0$ the velocity profile and momentum boundary layer thickness are getting squeezes due to magnetic parameter (M), whereas surface thickness parameter (s) and stretching ratio parameter (ϵ) have a reverse effect on it. On the other hand, the power-law index parameter (m), Eckert number (Ec), mixed convection parameter (λ), and heat generation parameter (Q^*) do not affect velocity profile in the case of $\varepsilon < 1.0$. Therefore, in the case of a thicker bullet-shaped object (s = 2.0), the velocity profile does not approach the ambient condition asymptotically but intersects the vertical axis with a steep angle and the boundary layer structure has no definite shape whereas in the case of a thinner bullet-shaped object (s = 0.05) the velocity profile converge the ambient condition asymptotically and the boundary layer structure has a definite shape. It is also observed that the thinner bullet-shaped object represents a thinner momentum boundary layer than the thicker bullet-shaped object in both static and moving bullet-shaped objects.

Table 4. 1 Variation in velocity gradient for distinct values of M, Pr, λ, Ec, m, Q^*, and s with $\epsilon = 0.0$, $\epsilon = 2.0$, and $s = 0.2$

M	Pr	λ	Ec	m	Q^*	s	$\lvert -f''(\eta) \rvert$ $\epsilon = 0.0, s = 0.2$	$-f''(\eta)$ $\epsilon = 2.0, s = 0.2$
1.0	1.0	0.2	0.2	2.0	0.2	0.2	**2.7628**	**3.3637**
5.0	1.0	0.2	0.2	2.0	0.2	0.2	**3.1302**	**3.6476**
10.0	1.0	0.2	0.2	2.0	0.2	0.2	**3.5075**	**3.9605**
1.0	**0.71**	0.2	0.2	2.0	0.2	0.2	**2.7628**	**3.3637**
1.0	**1.0**	0.2	0.2	2.0	0.2	0.2	**2.7628**	**3.3637**
1.0	**7.0**	0.2	0.2	2.0	0.2	0.2	**2.7628**	**3.3637**
1.0	1.0	**0.2**	0.2	2.0	0.2	0.2	**2.7628**	**3.3637**
1.0	1.0	**1.5**	0.2	2.0	0.2	0.2	**2.6241**	**3.4871**
1.0	1.0	**2.5**	0.2	2.0	0.2	0.2	**2.5181**	**3.5818**
1.0	1.0	0.2	**0.2**	2.0	0.2	0.2	**2.7628**	**3.3637**
1.0	1.0	0.2	**0.4**	2.0	0.2	0.2	**2.7628**	**3.3637**
1.0	1.0	0.2	**0.6**	2.0	0.2	0.2	**2.7628**	**3.3637**
1.0	1.0	0.2	0.2	**2.0**	0.2	0.2	**2.7628**	**3.3637**
1.0	1.0	0.2	0.2	**3.0**	0.2	0.2	**2.8161**	**3.5983**
1.0	1.0	0.2	0.2	**4.0**	0.2	0.2	**2.8682**	**3.8119**
1.0	1.0	0.2	0.2	2.0	**0.2**	0.2	**2.7628**	**3.3637**
1.0	1.0	0.2	0.2	2.0	**0.8**	0.2	**2.7628**	**3.3637**
1.0	1.0	0.2	0.2	2.0	**1.5**	0.2	**2.7628**	**3.3637**
1.0	1.0	0.2	0.2	2.0	0.2	**0.1**	**5.2731**	**5.9885**
1.0	1.0	0.2	0.2	2.0	0.2	**0.2**	**2.7628**	**3.3637**
1.0	1.0	0.2	0.2	2.0	0.2	**0.3**	**1.9271**	**2.4495**

Table 4.1 shows the influence of magnetic parameter (M), power-law index parameter (m), Prandtl number (Pr), mixed convection (λ), heat generation parameter (Q^*), Eckert number (Ec), and surface thickness parameter on the skin friction coefficient when $\epsilon = 0.0$, $\epsilon = 2.0$ and $s = 0.2$. It is observed that the Prandtl number, heat generation parameter, and Eckert number do not affect the skin friction coefficient whereas the magnetic parameter and power-law index parameter enhance the skin friction coefficient in the case of $\varepsilon < 1.0$ but reduce the skin friction in the case of $\varepsilon > 1.0$. A precisely reverse trend is observed for the surface thickness parameter. On the other hand, the skin friction reduces for the increasing effect of the mixed convection parameter when $\varepsilon > \text{or} < 1$. Therefore, skin friction is an increasing function of the magnetic parameter and power-law index parameter in the case of $\varepsilon < 1.0$ but decreasing function in the case of $\varepsilon > 1.0$ whereas it is constant for the effect of the Prandtl number, heat generation parameter, and Eckert number. It is interesting to note that the friction factor coefficient is less in $\epsilon = 0.0$ case when compared with $\epsilon = 2.0$ case. At this point, it is highlighted that for reducing the friction between the particles and the surface we have to use $\epsilon = 0.0$ case. It is evident from this table that the skin friction coefficient is higher in the $\epsilon = 2.0$ case when comparing with $\epsilon = 0.0$.

The fluid temperature profile and Nusselt number have been depicted graphically versus boundary layer co-ordinate (η) in Figures 4.8 – 4.14 for the increasing effect of Prandtl Number (Pr), magnetic parameter (M), Eckert number (Ec), heat generation parameter (Q^*), mixed convection parameter (λ), stretching ratio parameter (ϵ), and surface thickness parameter (s) in the following sub-section.

4.3.2 Temperature profiles and Nusselt number with parameter variations

4.3.2.1 Effect of Prandtl number (Pr) on temperature profile and Nusselt number

Figures 4.8(a) - 4.8(d) show the variation of temperature profile and Nusselt number for the increasing effect of Prandtl number $\left(0.71 \le \Pr \le 7.0\right)$ when the stretching ratio parameter $\varepsilon < 1.0$ and $\varepsilon > 1.0$, and the surface thickness parameter s = 0.05, s = 2.0, respectively. These plots represent that the temperature profile of the viscous fluid and thermal boundary layer thickness affected significantly with increasing Prandtl number. It is seen from these figures that the variation of surface thickness parameter has a significant effect on fluid temperature in connection with the Prandtl number.

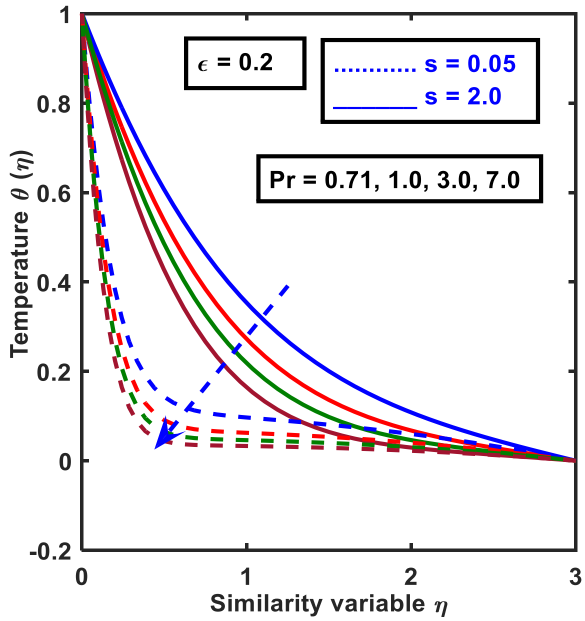

(a)

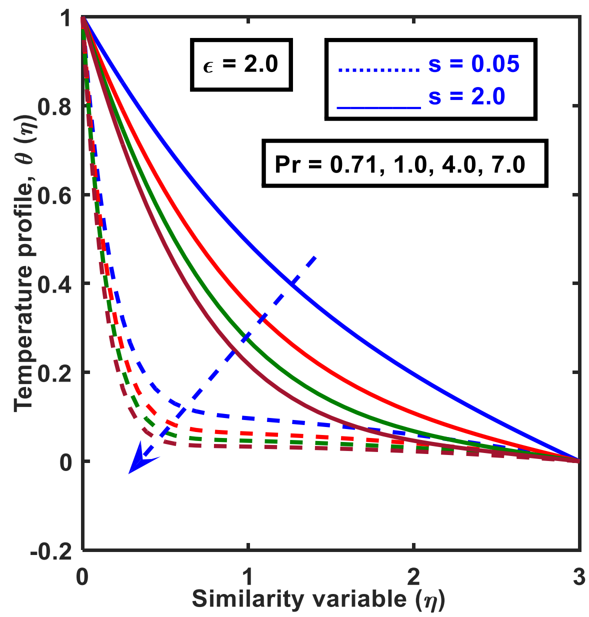

(b)

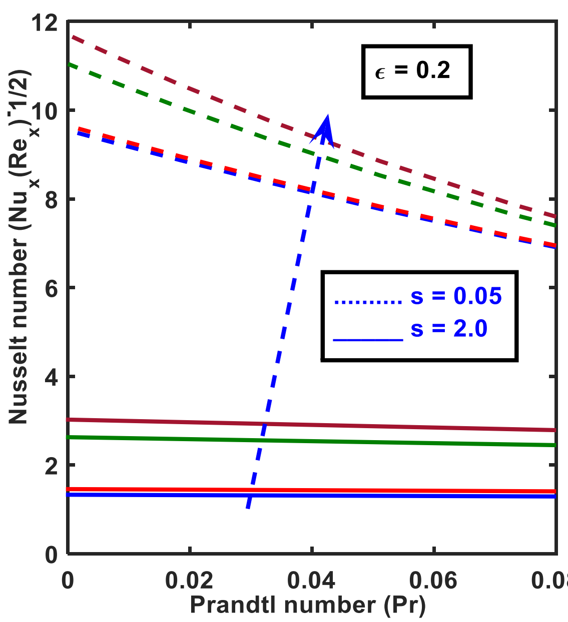

(c)

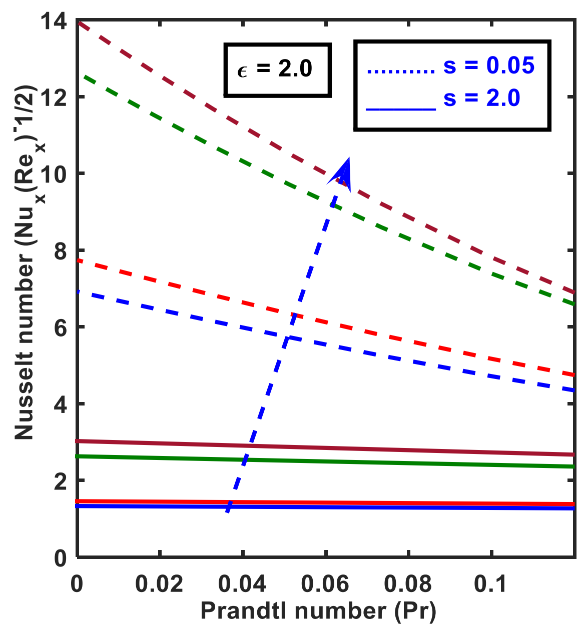

(d)

Figure 4. 8 Effect of Prandtl number (Pr) on temperature profile and Nusselt number when (a) $s = 0.05$, $s = 2.0$, and $\epsilon = 0.2$ (b) $s = 0.05$, $s = 2.0$, and $\epsilon = 2.0$, (c) $s = 0.05$, $s = 2.0$, and $\epsilon = 0.2$, and (d) $s = 0.05$, $s = 2.0$, and $\epsilon = 2.0$.

It is also seen that the temperature profile and boundary layer thickness squeezes for both of the thicker (s = 2.0, and thinner (s = 0.05) surfaces of the bullet-shaped object but the Nusselt number increases. It is also observed that the thermal boundary layer thickness is higher in the case of the thicker surface (s = 2.0) than the thinner surface (s = 0.05). Because, in the case of lower values of the Prandtl number which increase the thermal conductivities, as a result, heat can diffuse more rapidly from the heated plate than for higher values of Pr. So, for the cooling purpose, we can use the higher the Prandtl number. A smaller surface thickness has a greater decelerating effect than a thicker surface. Therefore, it is noticed that for higher values of surface thickness parameter, the maximum temperature shows in the thermal boundary layer compared to that of lower surface thickness parameter. It is observed from Table 4.2 that, when Pr changes from 0.71 to 7.0 for $s = 0.05$ and $\epsilon = 0.2$, the Nusselt number increases 44.21 % whereas for $s = 2.0$ and $\epsilon = 0.2$ the skin friction increases 62.36%. Hence, the Nusselt number is higher for the thicker surface (s = 2.0) than the thinner surface (s = 0.05).

4.3.2.2 Effect of heat generation parameter (Q*) on temperature profile and Nusselt number

Figures 4.9(a) - 4.9(f) display the effect of heat generation parameter on the temperature profile and Nusselt number when the stretching ratio parameter $\epsilon = 0.2$, $\epsilon = 2.0$, the surface thickness parameter $s = 0.05$, $s = 2.0$, and Pr = 0.71, 7.0 respectively. Figure 4.9 (a) and Figure 4.9 (b) depict the influence of heat generation parameter on viscous fluid temperature for thinner surface (s = 0.05) and thicker surface (s = 2.0) when $\epsilon = 0.2$ and 2.0 respectively. These plots represent that the temperature profile of the viscous fluid and thermal boundary layer thickness affected significantly with increasing heat generation parameters. It is noticed from these figures that the variation of heat generation parameter has a significant effect on fluid temperature in connection with the surface thickness parameter and the Prandtl number. A lower surface thickness parameter has a lower accelerating effect. For thicker surfaces (s = 2.0) with increasing Q*, the accelerating effect is more prominent than for thinner surfaces (s = 0.05). Therefore, the thermal boundary layer thickness is higher due to the thicker surface when compared with the thinner surface. Therefore, the temperature profile and boundary layer thickness expand for both of the thicker (s = 2.0) and thinner (s = 0.05) surfaces of the bullet-shaped object whereas the Nusselt number decreases (Figure 3.9 (e) and Figure 3.9 (f)). Figure 3.9 (c) and Figure 3.9 (d) also represent the influence of heat generation parameter on viscous fluid temperature for air (Pr = 0.71) and water (Pr = 7.0) when s = 0.05 and 2.0 respectively.

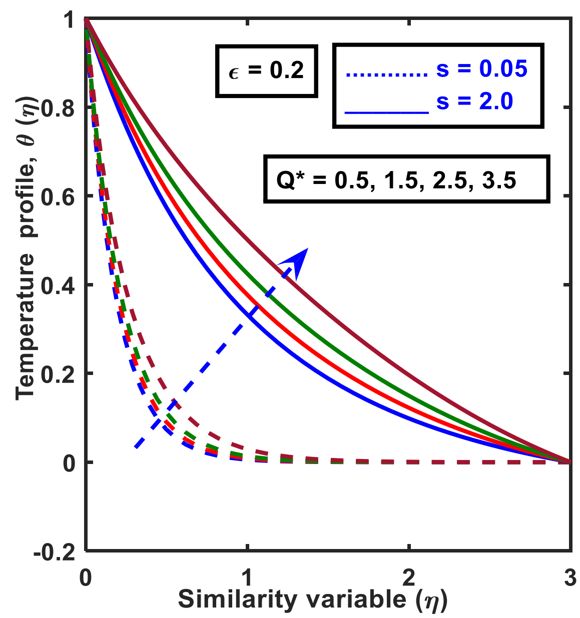

(a)

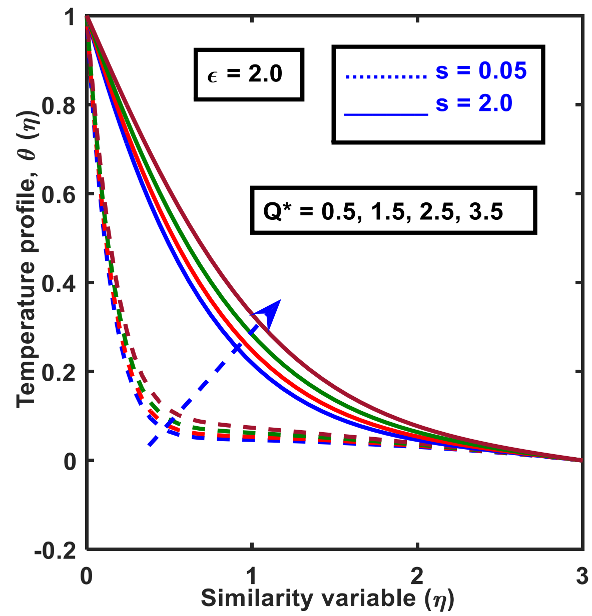

(b)

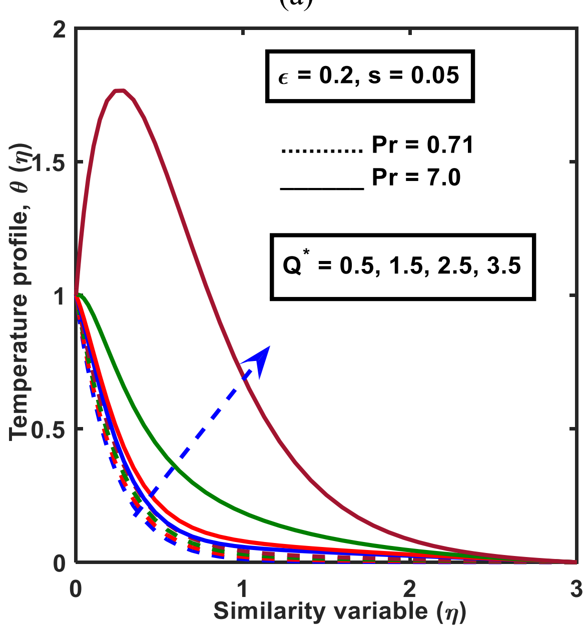

(c)

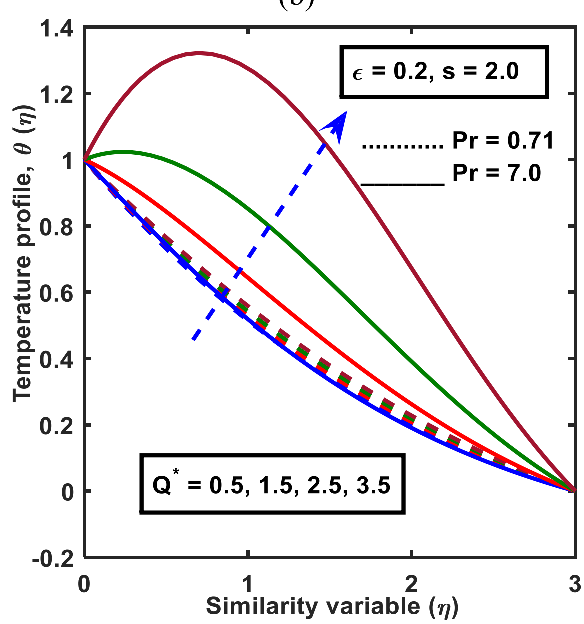

(d)

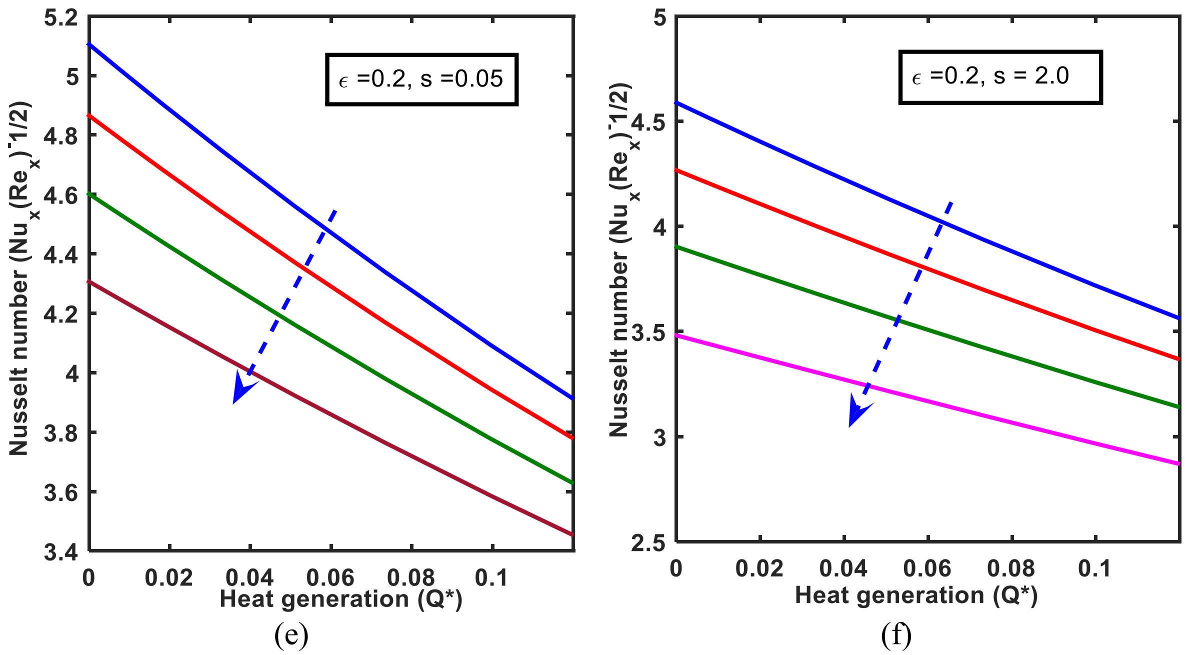

Figure 4. 9 Effect of heat generation Q^* on temperature profile and local Nusselt number when (a) $\epsilon = 0.2$, $s = 0.05$, $s = 2.0$ (b) $\epsilon = 2.0$, $s = 0.05$, $s = 2.0$ (c) $s = 0.05$, Pr = 0.71, Pr = 7.0 (d) $s = 2.0$, Pr = 0.71, Pr = 7.0 (e) $\epsilon = 0.2$, $s = 0.05$, Pr = 0.71, and (f) $\epsilon = 2.0$, $s = 0.05$, Pr = 0.71.

It is seen from these figures that the variation of the Prandtl number has a significant effect on viscous fluid temperature in connection with the heat generation parameter. A higher Prandtl number has a greater accelerating effect on the temperature profile. For water (Pr = 0.71) with increasing Q*, the accelerating effect is more prominent than for air (Pr = 0.71). Therefore, the thermal boundary layer thickness is higher for water when compared with air. However, the temperature attains its minimum for a low value of Prandtl number (Pr = 0.71) and a higher value of Prandtl number (Pr = 7.0) in connection with heat generation parameter shooting up the profiles near the surface of the bullet-shaped object within the region $\eta < 0.4$ and then the profile decreases sharply to meet the boundary condition as well. From these figures, the temperature profile and thermal boundary layer thickness increase with the increase of Q^* for all mentioned cases. Therefore, it is seen that for higher values of surface thickness parameter, the maximum temperature shows in the thermal boundary layer compared to that of lower surface thickness parameter. Again, in the case of water (Pr = 7.0), the highest temperature shows in the thermal boundary layer compared to that of air (Pr = 0.71). It happens because heat sources produce more heat energy near the surface as a result the temperature of the fluid increases. It is observed from Table 4.2 that, when Q^* changes from 0.5 to 3.5 for s = 0.05 and ϵ = 0.2, the Nusselt number decreases 48.9 % whereas for s = 2.0 and ϵ = 0.2 the Nusselt number decreases 19.5%. Hence, the Nusselt number is higher for the thinner surface (s = 0.05) than the thicker surface (s = 2.0).

4.3.2.3 Effect of the magnetic parameter (*M*) on temperature profile and Nusselt number

Figures 4.10(a) - 4.10(f) depict the effect of magnetic parameter on the temperature profile and Nusselt number when the stretching ratio parameter ϵ = 0.2, ϵ = 2.0, the surface thickness parameter s = 0.05, s = 2.0, and Pr = 0.71, 7.0 respectively. Figure 3.10 (a) and Figure 3.10 (b) depict the influence of magnetic parameter on viscous fluid temperature for thinner surface (s = 0.05) and thicker surface (s = 2.0) when ϵ = 0.2 and 2.0 respectively. These plots represent that the temperature profile of the viscous fluid and thermal boundary layer thickness affected significantly with increasing magnetic parameter (M). It is noticed from these figures that the variation of the magnetic parameter has a significant effect on fluid temperature in connection with the surface thickness parameter and the Prandtl number. A lower surface thickness parameter has a lower accelerating effect than a higher surface thickness. For thicker surfaces (s = 2.0) with increasing M, the accelerating effect is more prominent than for thinner surfaces (s = 0.05). Therefore, the thermal boundary layer thickness is higher due to the thicker surface when compared with the thinner surface. Hence, the temperature profile and boundary layer thickness expand for both of the thicker (s = 2.0) and thinner (s = 0.05) surfaces of the bullet-shaped object whereas the Nusselt number decreases (Figure 3.9 (e) and Figure 3.9 (f)). Again, Figure 3.9 (c) and Figure 3.9 (d) also represent the influence of magnetic parameter on viscous fluid temperature for air (Pr = 0.71) and water (Pr = 7.0) when s = 0.05 and 2.0, respectively. It is seen from these figures that the variation of the Prandtl number has a significant effect on viscous fluid temperature in connection with the magnetic parameter. A higher Prandtl number has a greater accelerating effect on the temperature profile. For water (Pr = 0.71) with increasing M, the accelerating effect is more prominent than for air (Pr = 0.71). Therefore, the thermal boundary layer thickness is higher for water when compared with air. From these figures, the temperature profile and thermal boundary layer thickness increase with the increase of M for all mentioned cases. In the case of air (Pr = 0.71), the profile is asymptotic and lower down toward the surface of the object, whereas in the case of water (Pr = 7.0), pick in the temperature distribution, is marked near the surface within the region $\eta < 0.3$ and then the profile decreases sharply to meet the boundary condition. These plots also represent that the temperature profile of the viscous fluid and thermal boundary layer thickness affected significantly with increasing magnetic parameters. Therefore, it is seen that for higher values of surface thickness parameter, the maximum temperature shows in the thermal boundary layer compared to that of lower surface thickness parameter. Again, in the case of water (Pr = 7.0), the highest temperature shows in the thermal boundary layer compared to that of air (Pr = 0.71). It happens because in an electrically conducting fluid if the magnetic field is applied a resistive type force like a drag force is produced, which is called Lorentz force? The nature of Lorentz force retards the force on the velocity field, and therefore, the magnetic field effects decelerate the velocity profiles. Therefore, it is possible for the increase in the temperature.

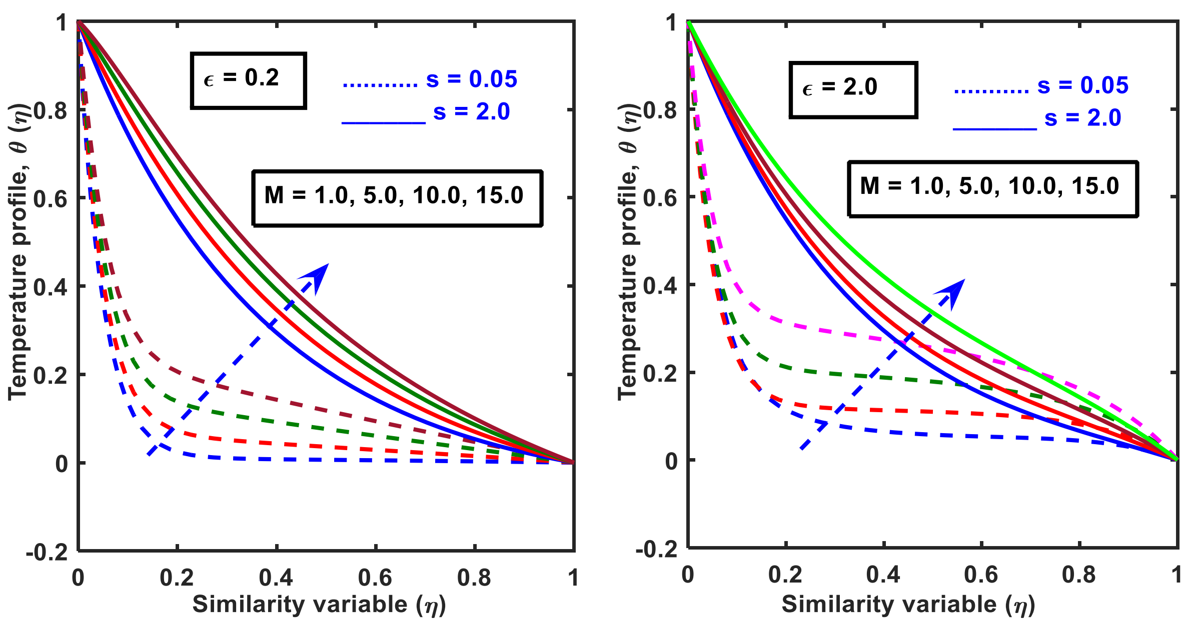

(a) (b)

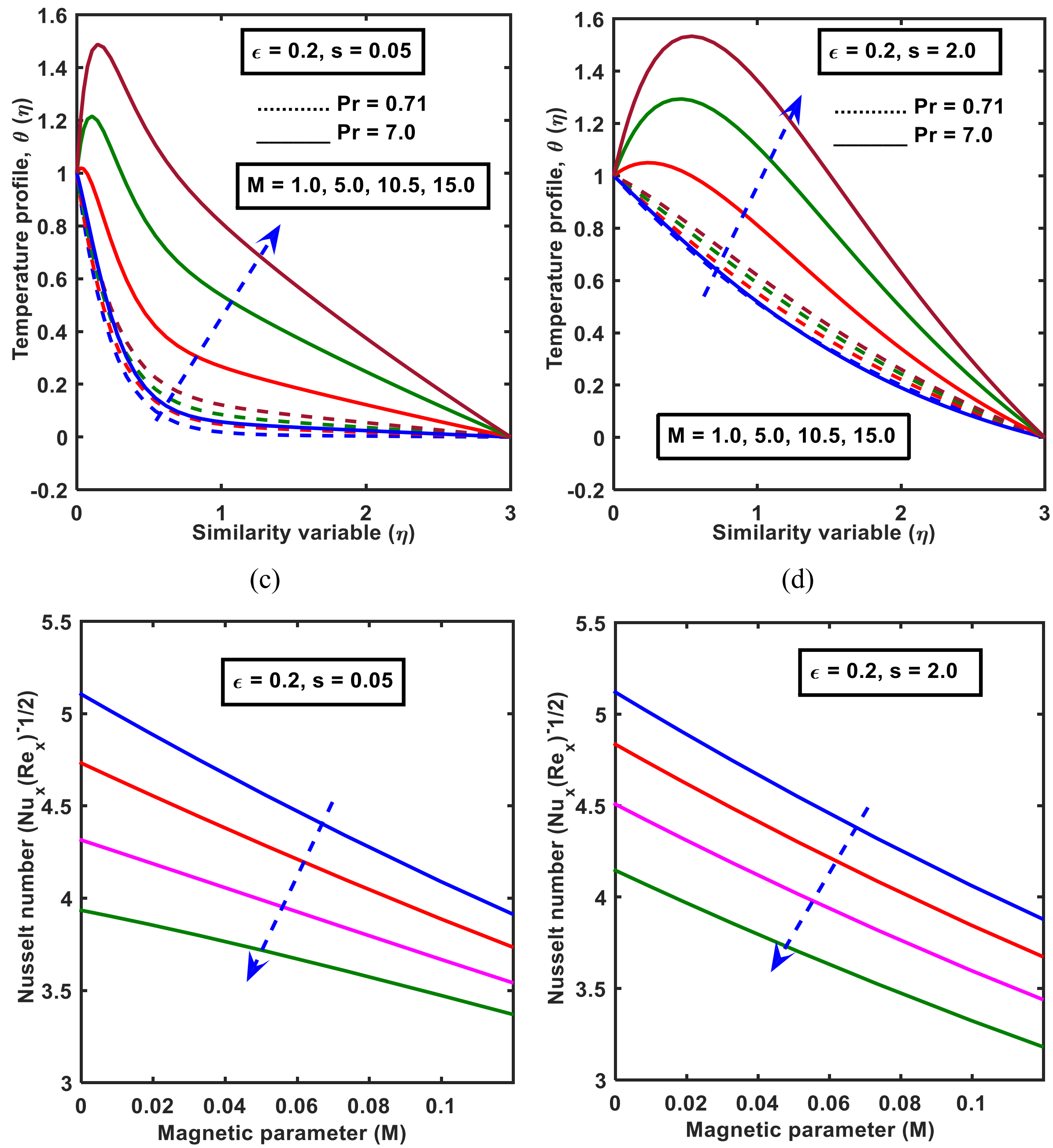

(c) (d)

(e) (f)

Figure 4. 10 Effect of magnetic parameter, M on temperature profile and local Nusselt number, when (a) $\epsilon = 0.2$, $s = 0.05$, $s = 2.0$ (b) $\epsilon = 2.0$, $s = 0.05$, $s = 2.0$ (c) $s = 0.05$, $\mathrm{Pr} = 0.71$, $\mathrm{Pr} = 7.0$ (d) $s = 2.0$, $\mathrm{Pr} = 0.71$, $\mathrm{Pr} = 7.0$ (e) $\epsilon = 0.2$, $s = 0.05$, $\mathrm{Pr} = 0.71$ and (f) $\epsilon = 2.0$, $s = 2.0$, $\mathrm{Pr} = 0.71$.

Hence, the thermal boundary layer thickness is lower in case of thinner surface (s = 0.05) than thicker surface (s = 2.0) because the heat transfer rate is higher due to thinner surface

(s = 0.05) than thicker surface (s = 2.0) for increasing effect of M. It is observed from Table 4.2 that, when M changes from 1.0 to 15.5 for s = 0.2 and ϵ = 0.2, the Nusselt number decreases 22.9 % whereas for s = 2.0 and ϵ = 0.2 the Nusselt number decreases 25.52%. Hence, the Nusselt number is lower for the thinner surface (s = 0.05) than the thicker surface (s = 2.0).

4.3.2.4 Effect of surface thickness parameter (s) on temperature profile and Nusselt number

Figures 4.11(a) - 4.11(d) represent the variation of temperature profile and Nusselt number influence of the surface thickness parameter (s) when the stretching ratio parameter ϵ = 0.2, ϵ = 2.0, and also for air (Pr = 0.71), and water (Pr = 7.0) respectively. It shows that the temperature profile and thermal boundary layer thickness expand but Nusselt number squeeze with an increase of surface thickness parameter because the velocity profile increases for the effect of this parameter which tends to pass more fluid from the boundary layer region to the surrounding fluid. It is also observed that the variation of the Prandtl number has a significant effect on viscous fluid temperature in connection with the surface thickness parameter.

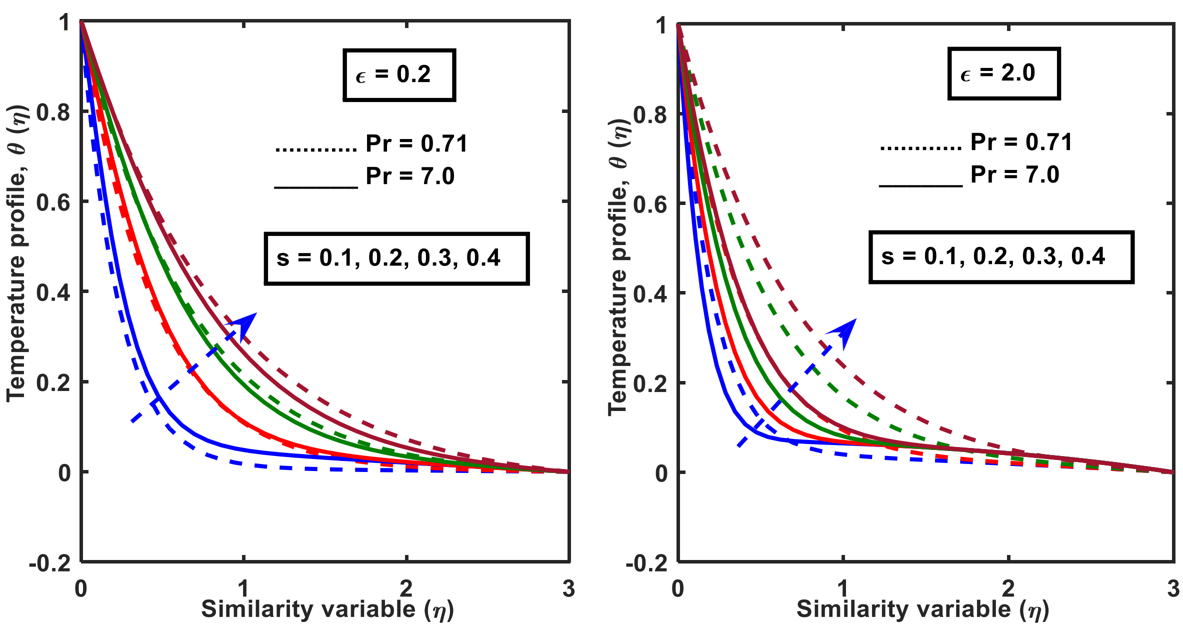

(a) (b)

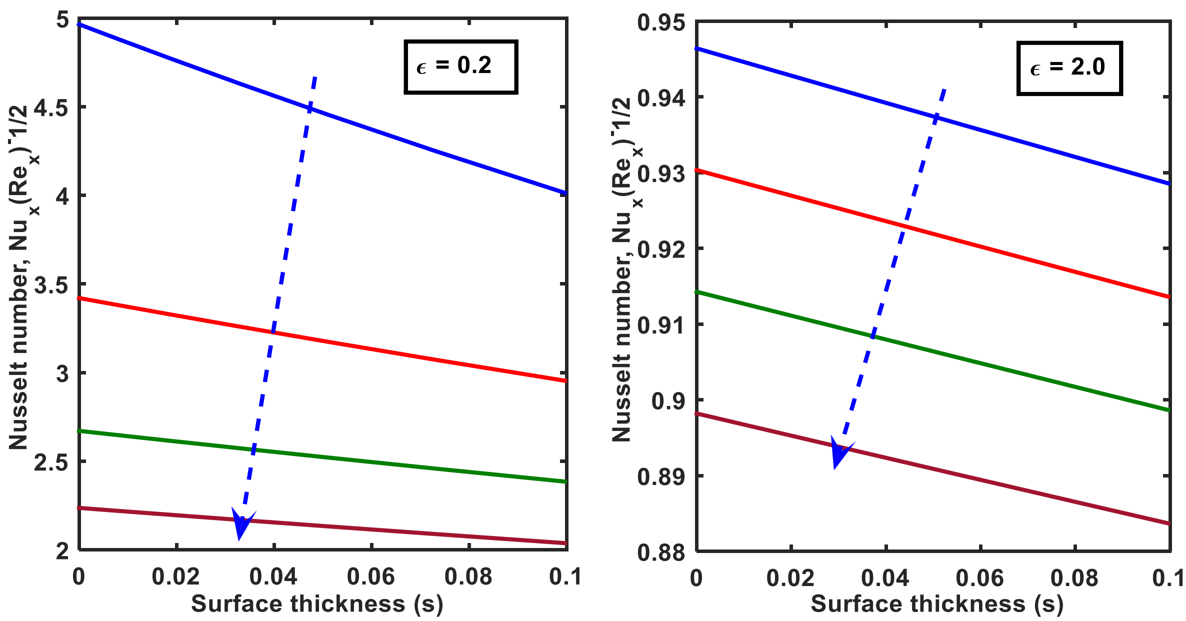

(c) (d)

Figure 4. 11 Effect of surface thickness parameter (s) on temperature profile (a) $s = 0.05$, Pr = 0.71, Pr = 7.0 (b) $s = 2.0$, Pr = 0.71, Pr = 7.0 and Nusselt number when (c) $\epsilon = 0.2$, Pr = 0.71 and (d) $\epsilon = 2.0$, Pr = 0.71

A higher Prandtl number has a greater decelerating effect than a lower Prandtl number. For air (Pr = 0.71) with increasing s, the accelerating effect is more prominent than for water (Pr = 7.0).

4.3.2.5 Effect of Eckert number (*Ec*) on temperature profile and Nusselt number

Figures 4.12 (a) - 4.12 (f) illustrate the effect of the Eckert number (*Ec*) on the temperature profile and Nusselt number when the stretching ratio parameter $\epsilon = 0.2$, $\epsilon = 2.0$, the surface thickness parameter $s = 0.05$, $s = 2.0$, and Pr = 0.71, 7.0 respectively. Figure 4.12 (a) and Figure 4.12 (b) depict the influence of Eckert number (Ec) on viscous fluid temperature for thinner surface ($s = 0.05$) and thicker surface ($s = 2.0$) when $\epsilon = 0.2$ and 2.0 respectively. These plots represent that the temperature profile of the viscous fluid and thermal boundary layer thickness affected significantly with increasing Eckert number (Ec). It is noticed from these figures that the variation of the Eckert number has a significant effect on fluid temperature in connection with the surface thickness parameter and the Prandtl number. A lower surface thickness parameter has a lower accelerating effect than a higher surface thickness parameter. For thicker surfaces (s = 2.0) with increasing Ec, the accelerating effect is more prominent than for thinner surfaces (s = 0.05). Therefore, the thermal boundary layer thickness is higher due to the thicker surface when compared with the thinner surface. Hence, the temperature profile and boundary layer thickness expand for both of the thicker (s = 2.0) and thinner (s = 0.05) surfaces of the bullet-shaped object whereas the Nusselt number decreases (Figure 3.12 (e) and Figure 3.12 (f)).

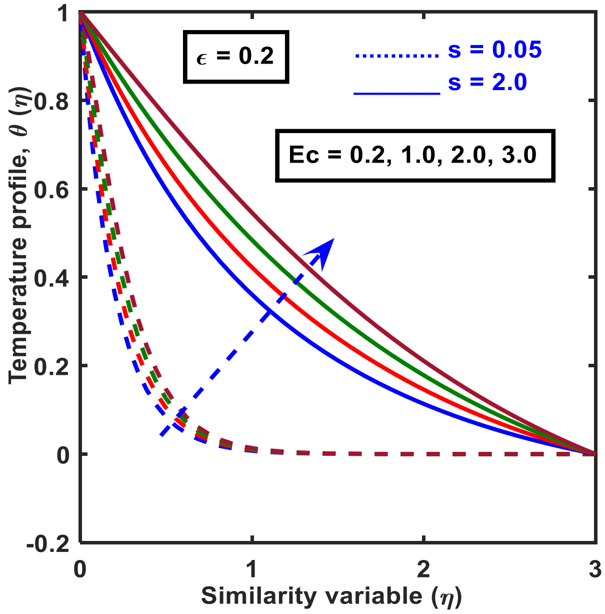

(a)

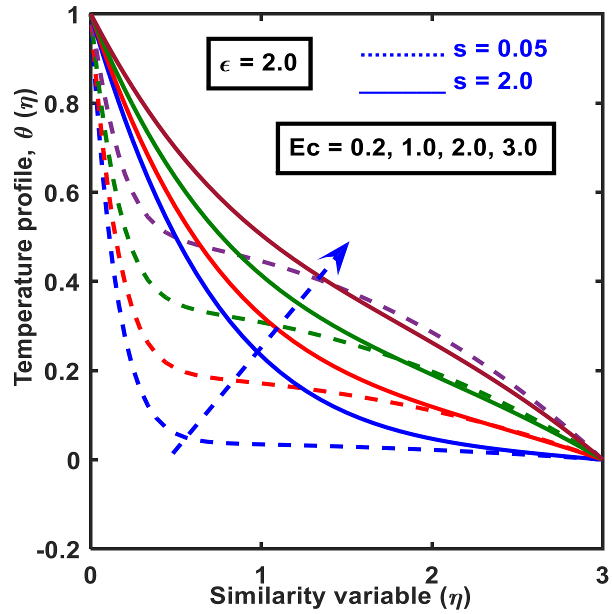

(b)

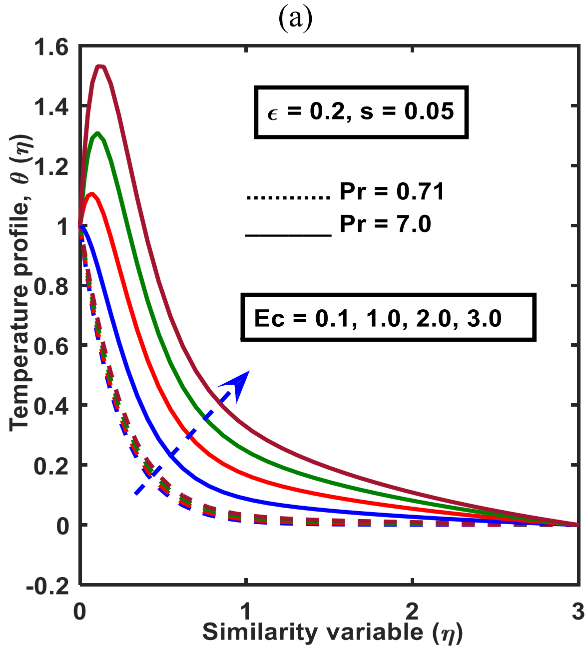

(c)

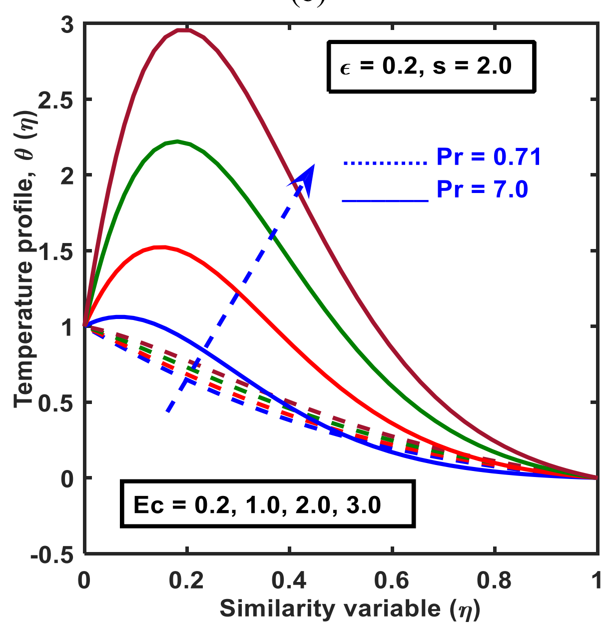

(d)

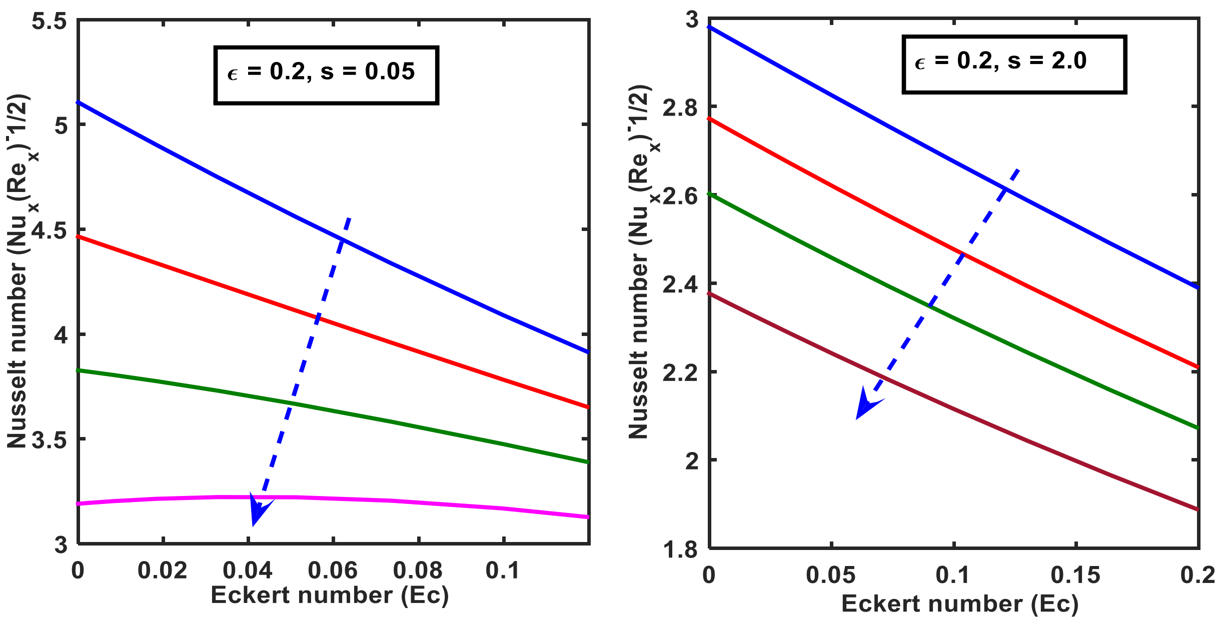

(e) (f)

Figure 4. 12 Effect of Eckert number (Ec) on temperature profile when (a) $\epsilon = 0.2$, $s = 0.05$, $s = 2.0$ (b) $\epsilon = 2.0$, $s = 0.05$, $s = 2.0$ (c) $s = 0.05$, Pr = 0.71, Pr = 7.0 (d) $s = 2.0$, Pr = 0.71, Pr = 7.0 and Nusselt number when (e) $\epsilon = 0.2$, $s = 0.05$, Pr = 0.71 and (f) $\epsilon = 0.2$, $s = 2.0$, Pr = 0.71

Again, Figure 3.12 (c) and Figure 3.12 (d) also represent the influence of Eckert number on viscous fluid temperature for air (Pr = 0.71) and water (Pr = 7.0) when s = 0.05 and 2.0, respectively. It is seen from these figures that the variation of the Prandtl number has a significant effect on viscous fluid temperature in connection with the Eckert number. A higher Prandtl number has a greater accelerating effect on the temperature profile. For water (Pr = 0.71) with increasing Ec, the accelerating effect is more prominent than for air (Pr = 0.71). Therefore, the thermal boundary layer thickness is higher for water when compared with air. From these figures, the temperature profile and thermal boundary layer thickness increase with the increase of Ec for all mentioned cases. These plots also represent that the temperature profile of the viscous fluid and thermal boundary layer thickness affected significantly with increasing Eckert number.

Therefore, it is seen that for higher values of surface thickness parameter, the maximum temperature shows in the thermal boundary layer compared to that of lower surface thickness parameter. Again, in the case of water (Pr = 7.0), the highest temperature shows in the thermal boundary layer compared to that of air (Pr = 0.71). Hence, the thermal boundary layer thickness is lower in the case of thinner surface ($s = 0.05$) than the thicker surface (s = 2.0) because the heat transfer rate is higher due to the thinner surface (s = 0.05) than the thicker surface (s = 2.0) for increasing effect of Ec. From these figures, it is revealed that the temperature profile and thermal boundary layer thickness increase but the Nusselt number decreases for both of the thicker (s = 2.0) and thinner (s = 0.05) bullet-shaped objects. This happens because raising values of Eckert number produces extra heat energy in the fluid because of frictional heating as a result the temperature within the boundary layer enhances at any given point which can be seen in Figures 4.12 (a) - 4.12 (d). From the numerical values of the temperature gradient, it is observed that when the Eckert number increases from 0.5 to 3.5 then there is a 37.5% decrease in the Nusselt number in the case of s = 0.05, whereas, in the case of s = 2.0, the corresponding decrease is 65.15%.

4.3.2.6 Effect of stretching ratio parameter (ϵ) on temperature profile and Nusselt number

Figures 4.13(a) – 4.13(d) exhibit the effect of stretching ratio parameter, $\left(0.2 \le \varepsilon \le 2.0\right)$ on the temperature profile and Nusselt number when the surface thickness parameter, s = 0.05, and s = 2.0, respectively. It is perceived from these figures that the temperature profile inside the boundary layer region squeezes but the Nusselt number enhances with the increase of stretching ratio parameter because the velocity profile increases for the effect of this parameter which tends to pass more fluid from the boundary layer region to the surrounding fluid. It is observed that in the case of a thinner surface the temperature profile within the boundary layer region reduces up to $\eta < 0.6$ then enhances. It is also noted that the stretching ratio is directly proportional to the temperature profile but adversely proportional to the Nusselt number. From the numerical values of the temperature gradient, it is observed that when ϵ increases from 0.2 to 2.0 there is a 12.5% increase in the Nusselt number in case of thinner surface (s = 0.05), whereas the corresponding increase is 49.5%, due to s = 2.0.

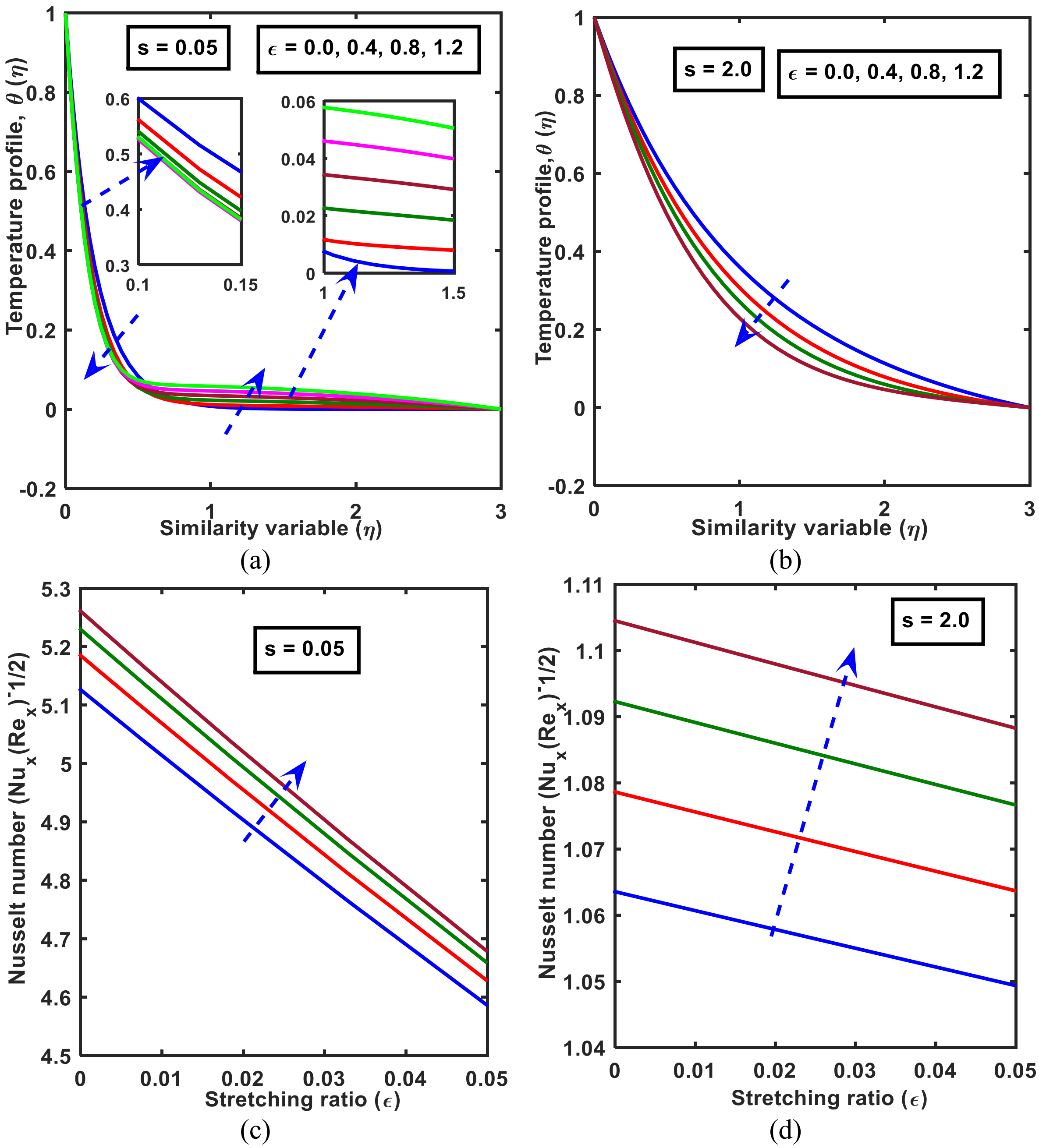

Figure 4. 13 Effect of stretching ratio(ϵ) on temperature profile and Nusselt number when (a) $s = 0.05$ (b) $s = 2.0$ (c) $s = 0.05$, and (d) $s = 2.0$

4.3.2.7 Effect of mixed convection parameter (λ) on temperature profile and Nusselt number

Figures 4.14(a) - 4.14(f) describes the influence of mixed convection parameter $(0.5 \le \lambda \le 3.5)$ on the temperature profile and Nusselt number when the stretching ratio parameter $\epsilon = 0.2$, $\epsilon = 2.0$, the surface thickness parameter $s = 0.05$, $s = 2.0$, and Pr = 0.71, 7.0 respectively. It is evident from these figures that the mixed convection parameter does not affect the temperature profile inside the boundary layer region and also the Nusselt number. Figure 3.14 (a) and Figure 3.14 (b) depict the influence of mixed convection parameter on viscous fluid temperature for thinner surface ($s = 0.05$) and thicker surface ($s = 2.0$) when $\epsilon = 0.2$ and 2.0 respectively. These plots represent that the temperature profile of the viscous fluid and thermal boundary layer thickness does not affect increasing mixed convection parameters. A lower surface thickness parameter has a lower effect than a higher surface thickness parameter. For thicker surfaces (s = 2.0) with increasing λ, the effect is more prominent than for thinner surfaces (s = 0.05). Therefore, the thermal boundary layer thickness is higher due to the thicker surface when compared with the thinner surface. Hence, the temperature profile and boundary layer thickness does not change for both of the thicker ($s = 2.0$) and thinner ($s = 0.05$) surfaces of the bullet-shaped object whereas the Nusselt number also (Figure 3.14 (e) and Figure 3.14 (f)). Again, Figure 3.14 (c) and Figure 3.14 (d) also represent the influence of mixed convection parameter on viscous fluid temperature for air (Pr = 0.71) and water (Pr = 7.0) when s = 0.05 and 2.0, respectively. It is seen from these figures that the variation of the Prandtl number has a significant effect on viscous fluid temperature in connection with the mixed convection parameter. A higher Prandtl number has a greater effect on the temperature profile. For water (Pr = 0.71) with increasing λ, the effect is more prominent than for air (Pr = 0.71). Therefore, the thermal boundary layer thickness is higher for water when compared with air. From these figures, the temperature profile and thermal boundary layer thickness are unchanged with the increase of λ for all mentioned cases. Therefore, it is seen that for higher values of surface thickness parameter, the maximum temperature shows in the thermal boundary layer compared to that of lower surface thickness parameter. Again, in the case of water (Pr = 7.0), the highest temperature shows in the thermal boundary layer compared to that of air (Pr = 0.71). Hence, the thermal boundary layer thickness is lower in the case of thinner surface ($s = 0.05$) than the thicker surface ($s = 2.0$) because the heat transfer rate is higher due to thinner surface ($s = 0.05$) than the thicker surface ($s = 2.0$) for increasing effect of λ.

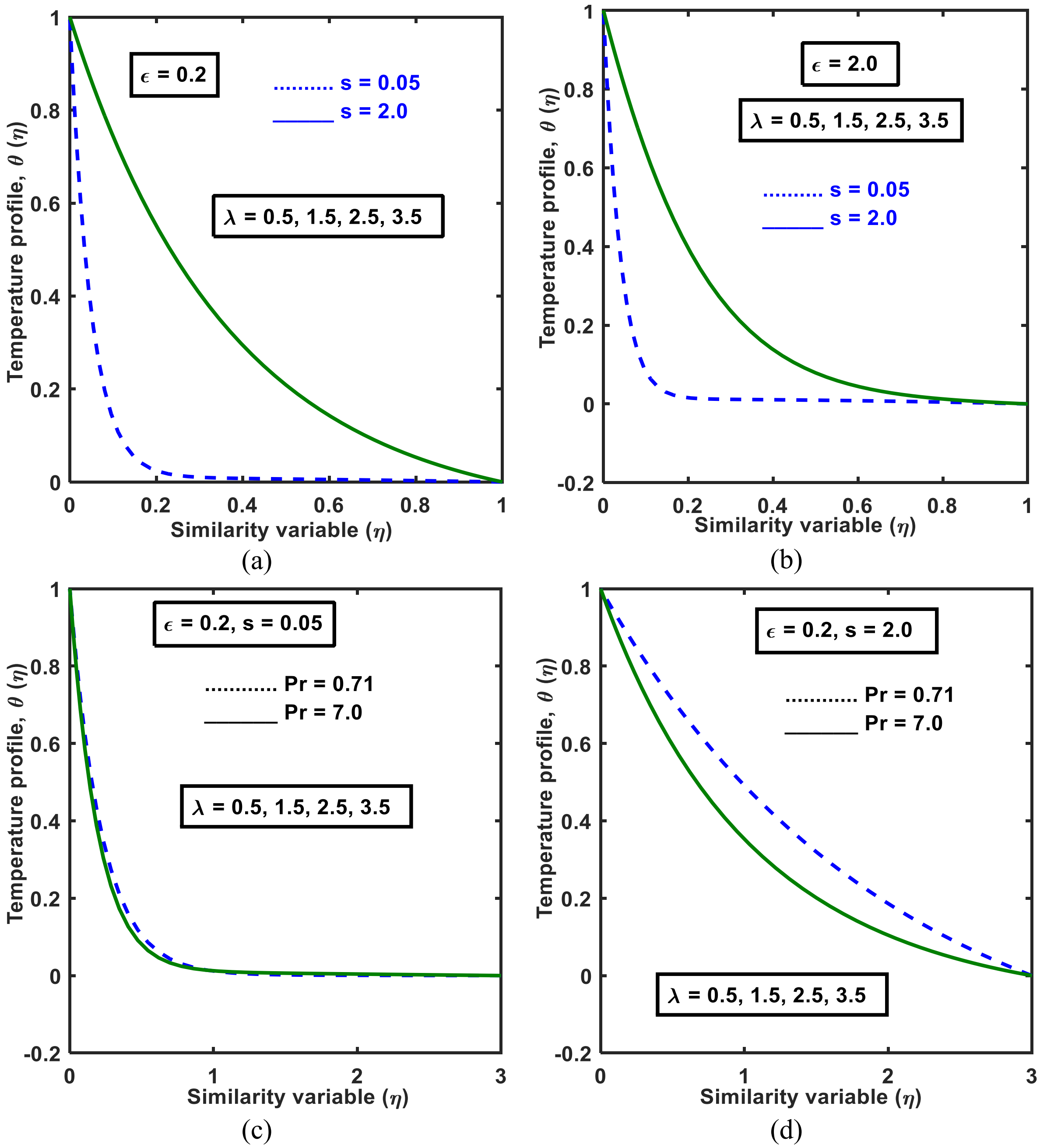

(a)
Temperature profile, θ (η)
Similarity variable (η)
ϵ = 0.2
.... s = 0.05
______ s = 2.0
λ = 0.5, 1.5, 2.5, 3.5
(b)
Temperature profile, θ (η)
Similarity variable (η)
ϵ = 2.0
λ = 0.5, 1.5, 2.5, 3.5
.... s = 0.05
______ s = 2.0
(c)
Temperature profile, θ (η)
Similarity variable (η)
ϵ = 0.2, s = 0.05
.... Pr = 0.71
_______ Pr = 7.0
λ = 0.5, 1.5, 2.5, 3.5
(d)
Temperature profile, θ (η)
Similarity variable (η)
ϵ = 0.2, s = 2.0
.... Pr = 0.71
_______ Pr = 7.0
λ = 0.5, 1.5, 2.5, 3.5

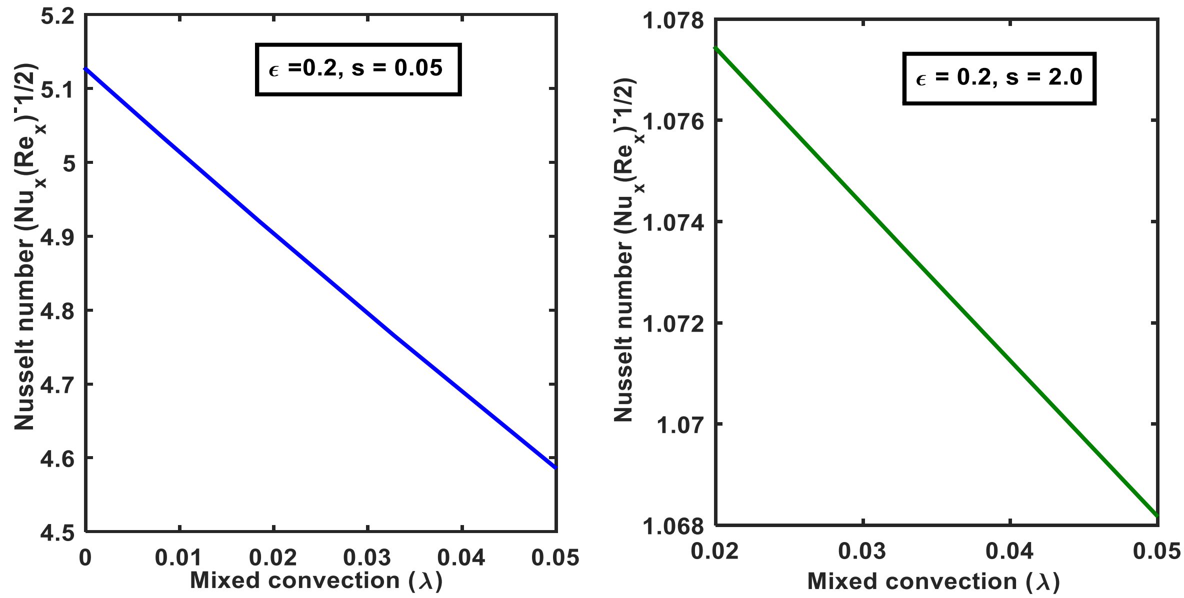

(e) (f)

Figure 4. 14 Effect of mixed convection (λ) on temperature profile and Nusselt number when (a) $s = 0.05$, $\epsilon = 0.2$ (b) $s = 2.0$, $\epsilon = 2.0$ (c) $s = 0.05$, $\epsilon = 0.2$, $\Pr = 0.71, 7.0$ (d) $s = 2.0$, $\epsilon = 0.2$, $\Pr = 0.71, 7.0$ (e) $s = 0.05$, $\epsilon = 0.2$ and (f) $s = 2.0$, $\epsilon = 0.2$

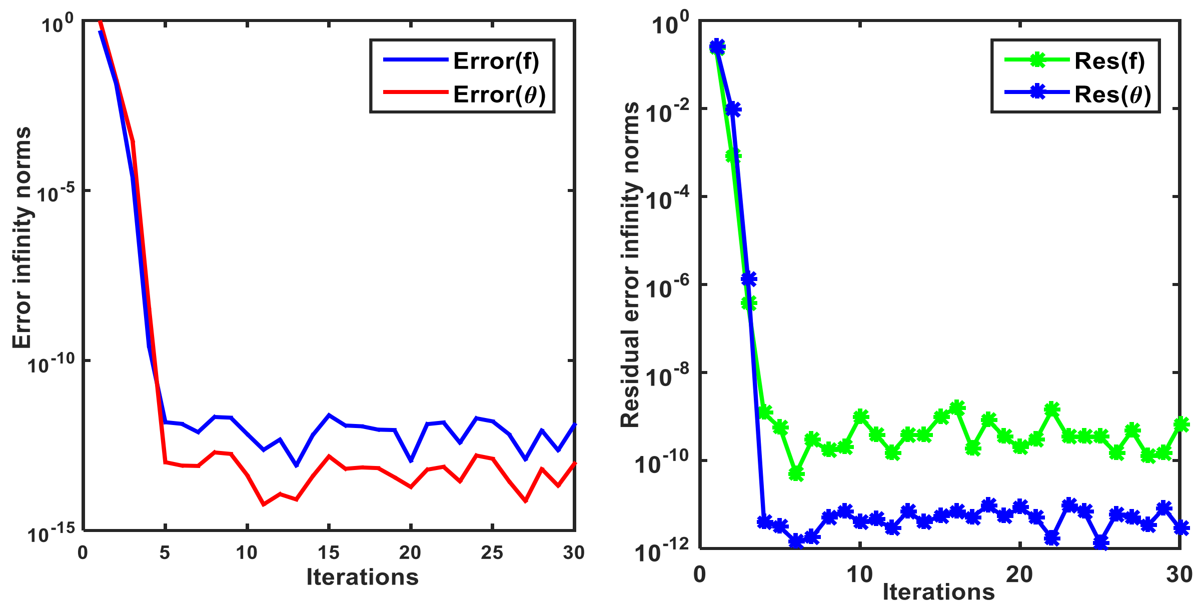

(a) (b)

Figure 4. 15 (a) Error infinity norms and (b) Residual error infinity norms for $f(\eta)$ and $\theta(\eta)$

Figure 4.15 denotes the convergence and accuracy of the SQLM. It is noticed that the error infinity norm decrease with an increase in the number of iterations, as a result, the method converges after only five iterations. Also, the decrease in residual error infinity norms ensures the accuracy of the numerical method. The SQLM achieves an accuracy of orders 10^{-8} and 10^{-13} after only five iterations which recommend the method is highly accurate.

The graph of temperature profile depicts that the fluid temperature within the boundary layer region is getting lower due to Prandtl number (Pr), stretching ratio parameter (ϵ), and mixed convection parameter (λ) whereas surface thickness parameter (s), magnetic parameter (M), heat generation parameter (Q^*) and Eckert number (Ec) have a reverse effect on it throughout the boundary layer region. From these figures, it is also revealed that in the case of a thicker bullet-shaped object (s = 2.0) the temperature profile does not approach the ambient condition asymptotically but intersects the vertical axis with a steep angle and the boundary layer structure has no definite shape whereas in the case of a thinner bullet-shaped object (s = 0.05) the temperature profile converge the ambient condition asymptotically and the boundary layer structure has a definite shape. It is also seen that the thinner bullet-shaped object represents a thinner thermal boundary layer because the heat transfer rate is higher than the thicker bullet-shaped object in both static and moving bullet-shaped objects.

Table 4.2 indicates the influence of magnetic parameter (M), power-law index parameter (m), Prandtl number (Pr), heat generation parameter (Q^*), Eckert number (Ec), surface thickness parameter (s), and mixed convection parameter (λ) on the Nusselt number when ϵ = 0.0, ϵ = 2.0 and s = 0.2, respectively. It is observed that the Prandtl number and power-law index parameter enhance the Nusselt number whereas the magnetic parameter, heat generation parameter, Eckert number, and surface thickness parameter reduces the Nusselt number for both of the cases. Therefore, heat transfer rate is high in ϵ = 2.0 case, when compared with ϵ = 0.0 case. At this point, it is highlighted that for enhancing the heat transfer rate we have to consider stretching (ϵ = 2.0) bullet-shaped object. On the other hand, the mixed convection parameter (λ) does not affect the Nusselt number.

Table 4. 2 Variation in Nusselt number which is directly proportional to the temperature gradient, $\theta'(\eta)$ for different values of *M,* Pr, λ, *Ec, s, Q*,* and *m* with $\epsilon = 0.0$, $\epsilon = 2.0$ and $s = 0.2$

M	Pr	λ	Ec	s	Q^*	m	$\lvert -\theta'(\eta) \rvert$ $\epsilon = 0.0,\ s = 0.2$	$\lvert -\theta'(\eta) \rvert$ $\epsilon = 2.0,\ s = 0.2$
1.0	1.0	0.2	0.2	0.2	0.2	2.0	**5.2632**	**5.4383**
5.0	1.0	0.2	0.2	0.2	0.2	2.0	**5.1402**	**3.3227**
10.0	1.0	0.2	0.2	0.2	0.2	2.0	**5.0176**	**0.6318**
1.0	**0.71**	0.2	0.2	0.2	0.2	2.0	**5.1904**	**5.3048**
1.0	**1.0**	0.2	0.2	0.2	0.2	2.0	**5.2632**	**5.4383**
1.0	**7.0**	0.2	0.2	0.2	0.2	2.0	**6.5379**	**7.4078**
1.0	1.0	**0.2**	0.2	0.2	0.2	2.0	**5.2632**	**5.4383**
1.0	1.0	**1.5**	0.2	0.2	0.2	2.0	**5.2632**	**5.4383**
1.0	1.0	**2.5**	0.2	0.2	0.2	2.0	**5.2632**	**5.4383**
1.0	1.0	0.2	**0.2**	0.2	0.2	2.0	**5.2632**	**5.4383**
1.0	1.0	0.2	**0.4**	0.2	0.2	2.0	**5.1071**	**4.7571**
1.0	1.0	0.2	**0.6**	0.2	0.2	2.0	**4.9511**	**4.0748**
1.0	1.0	0.2	0.2	**0.1**	0.2	2.0	**10.1482**	**9.8941**
1.0	1.0	0.2	0.2	**0.2**	0.2	2.0	**5.2632**	**5.4383**
1.0	1.0	0.2	0.2	**0.3**	0.2	2.0	**3.6482**	**3.9123**
1.0	1.0	0.2	0.2	0.2	**0.2**	2.0	**5.2632**	**5.4383**
1.0	1.0	0.2	0.2	0.2	**0.8**	2.0	**5.1225**	**5.3136**
1.0	1.0	0.2	0.2	0.2	**1.5**	2.0	**4.9483**	**5.1622**
1.0	1.0	0.2	0.2	0.2	0.2	**2.0**	**5.2632**	**5.4383**
1.0	1.0	0.2	0.2	0.2	0.2	**3.0**	**5.4816**	**6.0044**
1.0	1.0	0.2	0.2	0.2	0.2	**4.0**	**5.6919**	**6.4826**

4.4 Correlation Analysis of Velocity Gradient

A positive correlation means higher values of one variable tend to higher values of other variables but the reverse case arises for the negative correlation. The correlations are significant between the variables if the numerical value of 0.25 or above. Then we say that a 95% chance of a relationship between the parameters. So, from Table 4.3, the correlation is significant for the parameter, *M*, λ, and *s* with the velocity gradient which is highlighted in Table 4.3. Besides, it is also seen that the velocity gradient is negatively correlated with mixed convection parameter *(*λ*),* and surface thickness parameter (*s*) whereas positively correlated with the magnetic parameter.

Table 4. 3 Correlation coefficient of the velocity gradient and controlling parameters by taking 3rd order coefficient in the case of $\epsilon = 0.0$

	M	λ	s	$f''(\eta)$
M	1.00			
λ	-0.31	1.00		
s	-0.17	-0.12	1.00	
$f''(\eta)$	**0.45**	**-0.29**	**-0.57**	1.00

Table 4. 4 Correlation coefficient of the velocity gradient $f''(\eta)$ and controlling parameters by taking 3rd order coefficient in the case of $\epsilon = 2$

	M	λ	m	s	$f''(\eta)$
M	1.00				
λ	-0.31	1.00			
m	-0.17	-0.12	1.00		
s	-0.17	-0.12	-0.18	1.00	
$f''(\eta)$	0.31	0.13	0.25	-0.96	1.00

Table 4.4 represents that the velocity gradient is negatively correlated with surface thickness parameter (*s*) whereas positively correlated with mixed convection parameter *(*λ*),* power-law index parameter, and the magnetic parameter (*M*).

4.5 Correlation Analysis of Temperature Gradient

From Table 4.5 it is noticed that the correlation coefficient is statistically significant for the Prandtl number (Pr), surface thickness (*s*), and Eckert number (*Ec*) which are highlighted in the table. It is also noticed that the Prandtl number and power-law index parameter (*m*)are positively correlated with temperature gradient but magnetic parameter (M), surface thickness (*s*), heat generation parameter (Q^*), and Eckert number (*Ec*) are negatively correlated with a temperature gradient.

Table 4. 5 Correlation coefficient between the temperature gradient $\theta'(\eta)$ and controlling parameters by taking 1st order coefficient

	M	Pr	Ec	s	Q^*	m	$\theta'(\eta)$
M	1.00						
Pr	-0.06	1.00					
Ec	-0.09	-0.06	1.00				
s	0.00	0.00	0.00	1.00			
Q^*	-0.09	-0.06	-0.09	0.00	1.00		
m	-0.09	-0.06	-0.09	0.00	-0.09	1.00	
$\theta'(\eta)$	-0.22	0.64	-0.30	-0.44	-0.15	0.17	1.00

Table 4. 6 Correlation coefficient between the temperature gradient $\theta'(\eta)$ and controlling parameters by taking 2nd order coefficient

	M	Pr	Ec	s	Q^*	m	$\theta'(\eta)$
M	1.00						
Pr	-0.08	1.00					
Ec	-0.11	-0.08	1.00				
s	0.00	0.00	0.00	1.00			
Q^*	-0.11	-0.08	-0.11	0.00	1.00		
m	-0.11	-0.08	-0.11	0.00	-0.11	1.00	
$\theta'(\eta)$	**-0.63**	**0.27**	**-0.57**	**-0.26**	-0.14	**0.32**	1.00

From Table 4.6 it is observed that the temperature gradient is positively correlated with the Prandtl number and power-law index parameter (*m*) whereas negatively correlated with magnetic parameter (*M*), surface thickness parameter (*s*), heat generation parameter (Q^*), and Eckert number (*Ec*). Therefore, the temperature gradient is an increasing function of the Prandtl number and power-law index parameter but decreasing function of the magnetic parameter (*M*), surface thickness parameter, heat generation parameter, and Eckert number.

CHAPTER FIVE

MHD MIXED CONVECTION BOUNDARY LAYER FLOW WITH HEAT TRANSFER OVER AN EXPONENTIALLY STRETCHING BULLET-SHAPED OBJECT CONSIDERING THE EFFECTS OF HEAT GENERATION AND VISCOUS DISSIPATION

This chapter investigates the exponential stretching effect on the mixed convection magnetohydrodynamic boundary layer flow with heat transfer over a bullet-shaped object by applying SQLM due to viscous dissipation and heat generation. So, chapter five performs the velocity and temperature distribution, local skin friction coefficient, and local Nusselt number by considering two different cases of surface thickness parameter s (s = 0.05, s = 2.0) and also stretching ratio parameter such as (i) when stretching velocity is greater than the free stream velocity $(\varepsilon < 1)$ and (ii) when stretching velocity is less than the free stream velocity $(\varepsilon > 1)$. The numerical results of velocity profile, temperature profile, the local skin friction coefficient (velocity gradient), and the local Nusselt number (rate of heat transfer) have been displayed graphically.

5.1 Mathematical Formulation and Analysis of the Present Problem

Let us suppose the axisymmetric steady two-dimensional mixed convection MHD boundary layer flow and heat transfer over an exponentially stretching bullet-shaped object (Figure 2.2 in chapter two). For developing the mathematical model of the present problem the detailed assumptions are discussed in chapter three. Assume that the surface of the bullet-shaped objects has been stretched exponentially.

Therefore, the governing PDEs are as follows

Equation of continuity:

$$\frac{\partial}{\partial x}\left(ru\right)+\frac{\partial}{\partial y}\left(rv\right)=0 \tag{5.1.1}$$

Momentum equation:

$$\mathrm{u}\frac{\partial \mathrm{u}}{\partial \mathrm{x}}+\mathrm{v}\frac{\partial \mathrm{u}}{\partial r}=\mathrm{U}\frac{\partial \mathrm{U}}{\partial \mathrm{x}}+\frac{\nu}{r}\left(\frac{\partial \mathrm{u}}{\partial \mathrm{r}}+r\frac{\partial^2 \mathrm{u}}{\partial \mathrm{r}^2}\right)+\frac{\sigma \mathrm{B_0}^2}{\rho}\left(\mathrm{U}-\mathrm{u}\right)+g\beta\left(T-T_\infty\right) \tag{5.1.2}$$

Energy equation:

$$u\frac{\partial T}{\partial x}+v\frac{\partial T}{\partial r}=\frac{\alpha}{r}\left(\frac{\partial T}{\partial r}+r\frac{\partial^2 T}{\partial r^2}\right)+\frac{Q}{\rho C_p}\left(T-T_\infty\right)+\frac{\nu}{C_p}\left(\frac{\partial u}{\partial r}\right)^2+\frac{\sigma B_0{}^2u^2}{\rho C_p} \tag{5.1.3}$$

The boundary conditions of the above equations are subjected to the following form.

$$\begin{aligned}&u=U_w\left(x\right),\ v=0,\ T=T_w\ at\ \ r=R\left(x\right)\\ &\text{and } u\to U_\infty\left(x\right),T\to T_\infty,as\ \ \ r\to\infty\end{aligned} \tag{5.1.4}$$

Here $U_w\left(x\right)=ae^{\frac{x}{L}}$ is the stretching velocity, $U_\infty\left(x\right)=be^{\frac{x}{L}}$ is the free stream velocity, a and b are the reference velocity, and L is the reference length.

The following axisymmetric similarity transformations have been considered for finding the numerical solutions of the system of equation (5.1.1) – equation (5.1.3) according to the boundary conditions (5.1.4).

$$\eta=\frac{ar^2e^{\frac{x}{2L}}}{2\nu L},\ \ \psi=\nu Le^{e^{\frac{x}{2L}}}f\left(\eta\right),T=T_\infty e^{e^{\frac{x}{2L}}}\theta\left(\eta\right) \tag{5.1.5}$$

where ψ is called the stream function and is denoted by the velocity components $u=\frac{1}{r}\frac{\partial\psi}{\partial r}$ and $v=-\frac{1}{r}\frac{\partial\psi}{\partial x}$, respectively? The expression η denotes the shape and size of the bullet-shaped object and if we take η = s in the expression $\eta=\frac{ar^2e^{x/2L}}{2\nu L}$ then the dimensionless radius of the bullet-shaped object is $R\left(x\right)=\sqrt{\frac{2\nu Lse^{\frac{x}{2L}}}{a}}$. The continuity equation (5.1.1) is identically satisfied by the equation (5.1.5). By applying the equation (5.1.5) into the equations (5.1.2) and (5.1.3), we obtain the following reduced ODEs as

$$\begin{aligned}&\eta f'''\left(\eta\right)+f''\left(\eta\right)+e^{\frac{X}{2}}f\left(\eta\right)f''\left(\eta\right)+\ e^{\frac{X}{2}}\left(\varepsilon^2 - f'^2\left(\eta\right)\right)+\\ &Me^{\frac{-X}{2}}\left(\varepsilon - f'\left(\eta\right)\right)+e^{\frac{-3X}{2}}\lambda\theta\left(\eta\right)=0\end{aligned} \tag{5.1.6}$$

$$\eta\theta''(\eta)+\frac{1}{2}\theta'(\eta)+e^{\frac{X}{2}}\Pr\left[f(\eta)\ \theta'(\eta)-\ \frac{1}{2}f'(\eta)\ \theta(\eta)\right]$$
$$+e^{-2X}\Pr Q^{*}\theta(\eta)+2\eta Ecf''^{2}(\eta)+MEcf'^{2}(\eta)e^{\frac{-3X}{2}}=0 \tag{5.1.7}$$

The transformed boundary conditions are

$$f(\eta)\ =\ 0,\ f^{'}(\eta)=\ 1,\theta\ (\eta)=\ 1,\ at\ \eta\ =\ 0, and$$
$$f^{'}(\eta)\to\varepsilon,\theta\ (\eta)\to 0\ \ as\ \eta\to\infty \tag{5.1.8}$$

The conditions of the stretching ratio parameter (ϵ) have been discussed in the previous chapter.

The dimensionless parameters M, λ, ε, Pr, Ec, Gr, Re_x, X, and Q^* are defined as

$$M=\frac{\sigma B_0^2 L}{\rho a}, \lambda=\frac{Gr}{\mathrm{Re}_x^{2}}, \varepsilon=\frac{b}{a},\ \Pr=\frac{\nu}{\alpha},\ Ec=\frac{U_w^{2}}{C_p(T_w-T_\infty)},$$
$$Gr=\frac{g\beta(T_w-T_\infty)L^3}{\nu^2}, \mathrm{Re}_x=\frac{U_w L}{\nu}, Q^{*}\ =\ \frac{QL(T_w-T_\infty)}{\rho a c_p}, X=\frac{x}{L}$$

The skin friction coefficient and the local Nusselt number

The shear stress and the rate of heat transfer (local Nusselt number) can be expressed in the following way. The shear stress and the local skin friction coefficient are defined as $\tau_w=-\mu\left(\frac{\partial u}{\partial r}\right)_{r=\eta}$ and $C_f=\frac{-2\tau_w}{\rho U^2}$ respectively. After applying the equations (5.1.4) and (5.1.5), the local skin friction coefficient can be written as

$$C_f=\frac{-\mu}{\rho U^2}\left(\frac{\partial u}{\partial r}\right)_{r=\eta}=-\sqrt{\frac{2X}{\mathrm{Re}_x}}f''(\eta)\Rightarrow C_f\sqrt{\mathrm{Re}_x}=-\sqrt{2X}f''(\eta) \tag{5.1.9}$$

The local Nusselt number can be defined as $Nu_x = \dfrac{xq_w}{\kappa\left(T_w - T_\infty\right)}$. Where q_w is the wall heat flux and taken as $q_w = -\kappa\left(\dfrac{\partial T}{\partial r}\right)_{r=\eta}$? By using the equations (5.1.4) and (5.1.5), we obtain the local Nusselt number $Nu_x\left(\mathrm{Re}_x\right)^{-\frac{1}{2}} = -\sqrt{\dfrac{X}{2}}\theta'(\eta)$ (5.1.10)

5.2 The Procedure of Numerical Calculation

The system of equations (5.1.6) and (5.1.7) are converted into the following iterative sequence of linear differential equations after applying the SQLM [82].

$$a_{0,r}\frac{\partial^3 f_{r+1}}{\partial\eta^3} + a_{1,r}\frac{\partial^2 f_{r+1}}{\partial\eta^2} + a_{2,r}\frac{\partial f_{r+1}}{\partial\eta} + a_{3,r}f_{r+1} + a_{4,r}\theta_{r+1} = R_{1,r}$$

$$b_{0,r}\frac{\partial^2\theta_{r+1}}{\partial\eta^2} + b_{1,r}\frac{\partial\theta_{r+1}}{\partial\eta} + b_{2,r}\theta_{r+1} + b_{3,r}\frac{\partial^2 f_{r+1}}{\partial\eta^2} + b_{4,r}\frac{\partial f_{r+1}}{\partial\eta} + b_{5,r}f_{r+1} = R_{2,r}$$

This implies

$$\mathrm{a}_{0,\mathrm{r}}f'''_{r+1}(\eta) + \mathrm{a}_{1,\mathrm{r}}f''_{r+1}(\eta) + \mathrm{a}_{2,\mathrm{r}}f'_{r+1}(\eta) + \mathrm{a}_{3,\mathrm{r}}f_{r+1}(\eta) + \mathrm{a}_{4,\mathrm{r}}\theta_r(\eta) = R_{1,r}(\eta) \quad (5.1.11)$$

$$b_{0,r}\theta''_{r+1}(\eta) + b_{1,r}\theta'_{r+1}(\eta) + b_{2,r}\theta_r + b_{3,r}f''(\eta) + b_{4,r}f'_{r+1}(\eta) + b_{5,r}f_{r+1}(\eta) = R_{2,r}(\eta) \quad (5.1.12)$$

The variable coefficients obtained from the previous iteration are given by

$$a_{0,r} = \eta, a_{1,r} = 1 + e^{\frac{X}{2}}f_r, a_{2,r} = -2e^{\frac{X}{2}}f'_r - Me^{\frac{-X}{2}}, a_{3,r} = e^{\frac{X}{2}}f''_r, a_{4,r} = e^{\frac{-3X}{2}}\lambda,$$
$$b_{0,r} = \eta, b_{1,r} = \frac{1}{2} + \Pr e^{\frac{X}{2}}f_r, b_{2,r} = -\frac{1}{2}\Pr e^{\frac{X}{2}}f'_r + \Pr Q^* e^{-2X}, b_{3,r} = 4\eta Ecf''_r,$$
$$b_{4,r} = \frac{1}{2}\Pr e^{\frac{X}{2}}\theta_r + 2MEcf'_r e^{\frac{-3X}{2}}, b_{5,r} = \Pr e^{\frac{X}{2}}\theta'_r$$

The terms on the right side are defined as follows:

$$R_{1,r}(\eta) = a_{0,r}f'''_r + a_{1,r}f''_r + a_{2,r}f'_r + a_{3,r}f_r + a_{4,r}\theta_r - F\left[\eta, f, f', f''......f^n\right]$$
$$= e^{\frac{X}{2}}f_r f''_r - e^{\frac{X}{2}}f'^2_r - \varepsilon^2 e^{\frac{X}{2}} - M\varepsilon e^{\frac{-X}{2}}$$

$$R_{2,r}(\eta)=b_{0,r}\theta_r''+b_{1,r}\theta_r'+b_{2,r}\theta_r+b_{3,r}f_r''+b_{4,r}f_r'+b_{5,r}f_r-F\left[\eta,f,f',f''......f^n\right]$$
$$=e^{\frac{X}{2}}\Pr f_r\theta_r'-\frac{1}{2}\Pr e^{\frac{X}{2}}f_r'\theta_r+MEce^{\frac{-3X}{2}}f_r'^2+2\eta Ecf_r''^2$$

Evaluating Equations (5.1.10) and (5.1.12) at the collocation points and approximating derivatives with Chebyshev derivatives which provide in the vector-matrix form such as

$$\begin{bmatrix} A_{11} & A_{12} \\ A_{21} & A_{22} \end{bmatrix}\begin{bmatrix} F_{r+1} \\ \theta_{r+1} \end{bmatrix}=\begin{bmatrix} R_{1,r} \\ R_{2,r} \end{bmatrix}, \text{ here } \begin{array}{l} A_{11}=a_{0,r}D^3+a_{1,r}D^2+a_{2,r}D+a_{3,r}, A_{12}=a_{4,r}, \\ A_{2,1}=b_{3,r}D^2+b_{4,r}D+b_{5,r}, A_{2,2}=b_{0,r}D^2+b_{1,r}D+b_{2,r} \end{array}$$

The transformed boundary conditions

$$f_{r+1}(\eta_0)=0, f_{r+1}'(\eta_0)=1, \theta_{r+1}(\eta_0)=1, \mathrm{R_r}(\eta_N)=1 \text{ at } \eta=0$$
$$f_{r+1}(\eta_N)=0, f_{r+1}'(\eta_N)=\varepsilon, \theta_{r+1}(\eta_N)=0, \mathrm{R_r}(\eta_{N+1})=\varepsilon \text{ as } \eta\to\infty$$

5.3 Results and Discussion

The non-linear ODEs of the present problem are solved by applying SQLM. The convergence criteria of the solution are performed by the use of solution-based errors. These errors are defined by the differences between approximate solutions at the previous and current iteration levels t and t + 1, respectively. The error norms have been defined in section 3.4.

The infinity norms of the residual errors are defined by

$$\left\|\mathrm{Re}\,s(f)\right\|_\infty=\left\|\begin{array}{l}\eta f'''(\eta)+f''(\eta)+e^{\frac{X}{2}}f(\eta)f''(\eta)\ +\ e^{\frac{X}{2}}\left(\varepsilon^2\text{ - }f'^2(\eta)\right)\\ +Me^{\frac{-X}{2}}\left(\varepsilon\text{ - }f'(\eta)\right)+e^{\frac{-3X}{2}}\lambda\theta(\eta)\end{array}\right\|=0 \text{ and}$$

$$\left\|\mathrm{Re}\,s(\theta)\right\|_\infty=\left\|\begin{array}{l}\eta\theta''(\eta)+\frac{1}{2}\theta'(\eta)+e^{\frac{X}{2}}\Pr\left[f(\eta)\ \theta'(\eta)\text{- }\ \frac{1}{2}f'(\eta)\ \theta(\eta)\right]\\ +e^{-2X}\Pr Q^*\theta(\eta)+2\eta Ecf''^2(\eta)+MEcf'^2(\eta)e^{\frac{-3X}{2}}\end{array}\right\|=0$$

The impact of controlling parameters on velocity, temperature, skin friction, and the local Nusselt number has been represented graphically. The fluid velocity profile, skin friction, temperature profile, and Nusselt number depict graphically as a function of boundary layer coordinate (η) in Figures 5.1 – 5.15 for different values of the magnetic parameter (M), Eckert number (Ec), heat generation parameter (Q^*), mixed convection parameter (λ), stretching ratio parameter (ϵ), location parameter (X), and surface thickness parameter (s). The numerical values of skin friction and Nusselt number have been presented in Table 5.1 and Table 5.4 which are directly proportional to velocity gradient and temperature gradient, respectively. The numerical computation is done by taking N = 60 collocation points and solution-based errors are defined for the convergence of the numerical method. So, Figures 5.16(a) and 5.16(b) show the convergence and accuracy of the present problem. Figure 5.16(a) represents the infinity norms with iterations. The error infinity norm decreases with the increasing number of iterations that confirms the convergence of the present method. So the present method converges after five iterations. Figure 5.16 (b) represents the residual error norms of less than 10^{-14} for $f(\eta)$ and $\theta(\eta)$ against after five iterations. It is seen that the residual error decreases with increasing the iterations. This proves the validity of the present method. The errors show that the SQLM is accurate giving errors of less than 10^{-14} within the fifth iterations. In this chapter, the default parameters are taken as $\Pr(0.71 \le \Pr \le 10.0), M(0.5 \le M \le 15.5), Q^*(0.2 \le Q^* \le 3.5), X(0.5 \le X \le 3.5), \varepsilon(0.0 \le \varepsilon \le 2.0)$, $Ec(0.2 \le Ec \le 2.0), s(0.2 \le s \le 0.5), \lambda(0.2 \le \lambda \le 5.5)$.

5.3.1 Velocity profiles and skin friction coefficient with parameter variations

5.3.1.1 Effect of the magnetic parameter (*M*) on the velocity profile and skin friction

Figure 5.1(a) - 5.1(d) show the effect of the magnetic parameter (M) when stretching ratio parameter $\varepsilon > 1.0$, or < 1.0 and surface thickness parameter, s = 0.05, and 2.0 on the velocity profile and skin friction, respectively. From these figures, it is observed that the velocity profile and boundary layer thickness expand and the fluid flow forms an inverted boundary layer pattern when $0.0 \le \varepsilon < 1.0$ but in the case of $1.0 < \varepsilon \le 2.0$, the fluid flow forms a definite boundary layer pattern, and the velocity profile and boundary layer thickness squeeze for both of the thinner (s = 0.05) and thicker (s = 2.0) bullet-shaped objects. It is seen that the fluid velocity enhances just near the bullet-shaped object and reduces far from it when $\varepsilon < 1.0$ but an opposite trend is observed when $\varepsilon < 1.0$.

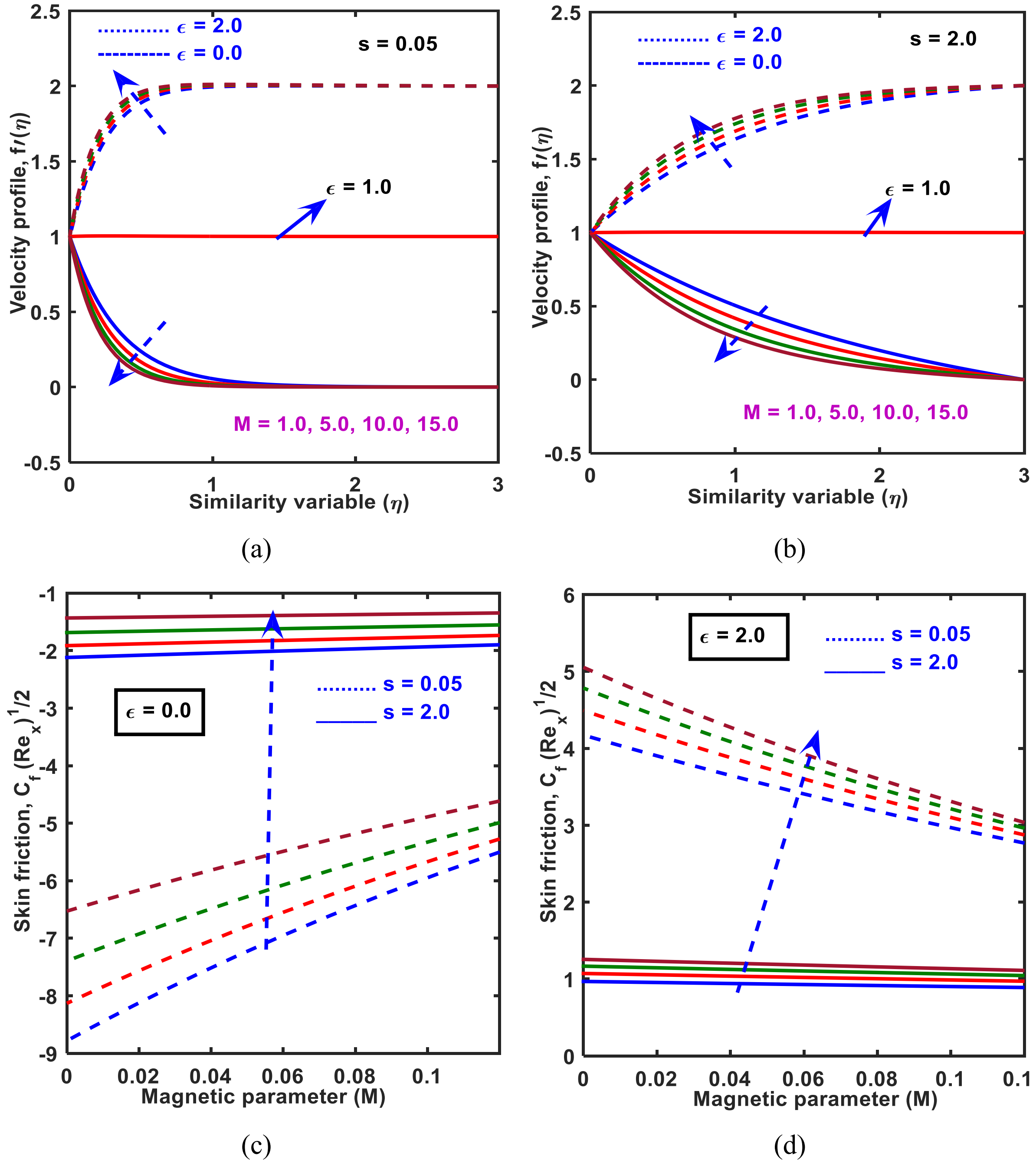

Figure 5. 1 Effect of magnetic parameter, *M* on velocity profile when (a) $\epsilon = 0.0, 1.0, 2.0$, $s = 0.05$ (b) $\epsilon = 0.0, 1.0, 2.0$, s = 2.0 and skin friction when (c) $\epsilon = 0.0$, s = 0.05, s = 2.0 and (d) $\epsilon = 2.0$, s = 0.05, s = 2.0

Therefore, when $\varepsilon < 1.0$, the surface velocity dominates the free stream velocity and if $\varepsilon > 1.0$, the free stream velocity dominates the surface velocity at the edge of the BL. From equation (5.1.9) it is seen that the skin friction coefficient is directly proportional to the dimensionless velocity gradient. Therefore, the velocity gradient at the surface is positive when $\varepsilon > 1.0$ and negative due to $\varepsilon < 1.0$ all values of the controlling parameters. On the other hand, the skin friction increases in both of the cases $\varepsilon > 1.0$ and $\varepsilon < 1.0$, respectively. It happens because M is defined as the hydromagnetic body force and viscous force, so larger values of M enhance the hydromagnetic body force which tends to reduce the fluid flow. But the reverse results arise in the case $\varepsilon > 1.0$ since in this case, viscous force dominates the hydromagnetic body force. The velocity profile is directly proportional to M when $\varepsilon > 1.0$ but inversely proportional when $\varepsilon < 1.0$. From the numerical values of the velocity gradient, it is observed that when M increases from 1.0 to 15.0, then there is a 67.4% increase of the skin friction in the case of thinner surface (s = 0.2) and in the case of thicker surface (s = 2.0) the corresponding increase is 97.93%.

5.3.1.2 Effect of Eckert number (*Ec*) on the velocity profile and skin friction

Figure 5.2(a) - 5.2(d) shows the variation of velocity profile and skin friction for different values of the Eckert number.

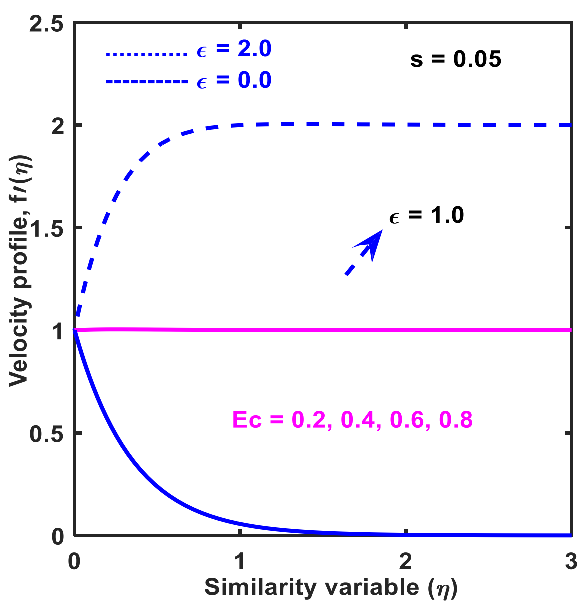

(a)

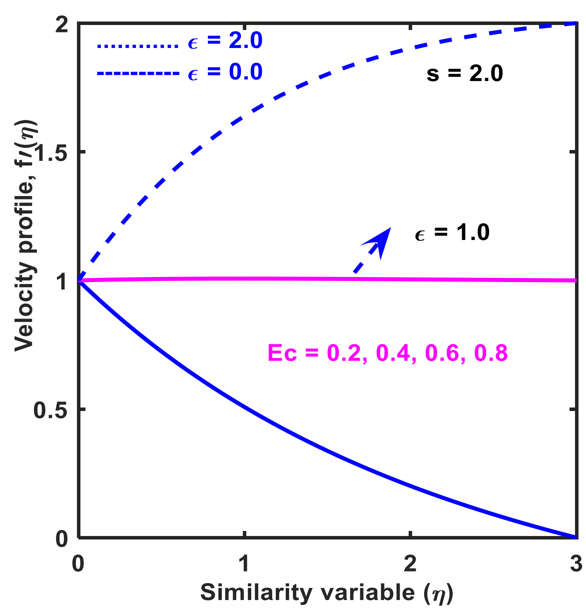

(b)

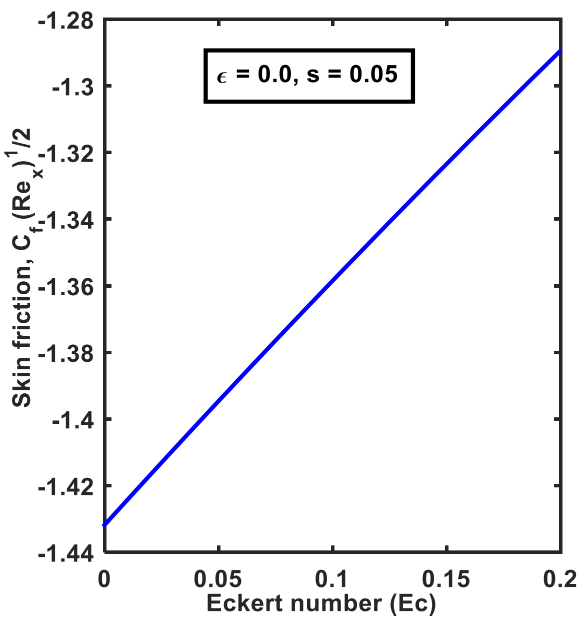

(c)

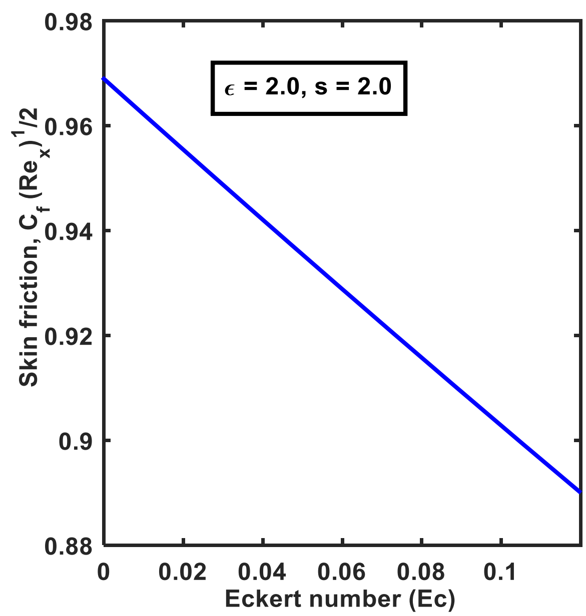

(d)

Figure 5. 2 Effect of Eckert number on velocity profile when (a) ϵ = 0.0, 1.0, 2.0, s = 0.05 (b) ϵ = 0.0, 1.0, 2.0, s = 2.0 and skin friction when (c) ϵ = 0.0, s = 0.05 and (d) ϵ = 2.0, s = 2.0

From these figures, it is observed that the Eckert number does not affect the velocity profile as well as the skin friction coefficient. Therefore, fluid velocity into the boundary layer region is constant for the increasing effect of the Ec.

5.3.1.3 Effect of heat generation parameter (Q*) on the velocity profile and skin friction

Figures 5.3(a) – 5.3(d) illustrate the effect of heat generation parameter when stretching ratio parameter $\varepsilon > 1.0$, or < 1.0 and surface thickness parameter, s = 0.05, and 2.0 on the velocity profile and skin friction, respectively. From these figures, it is observed that the heat generation parameter has no effect on the velocity profile as well as skin friction coefficient at the surface. From these figures, it is also observed that the fluid flow forms an inverted boundary layer pattern when $0.0 \le \varepsilon < 1.0$ but in the case of $1.0 < \varepsilon \le 2.0$, the fluid flow forms a definite boundary layer pattern. Therefore, the fluid velocity is a constant function of the parameter Q* within the boundary layer region and also the velocity gradient.

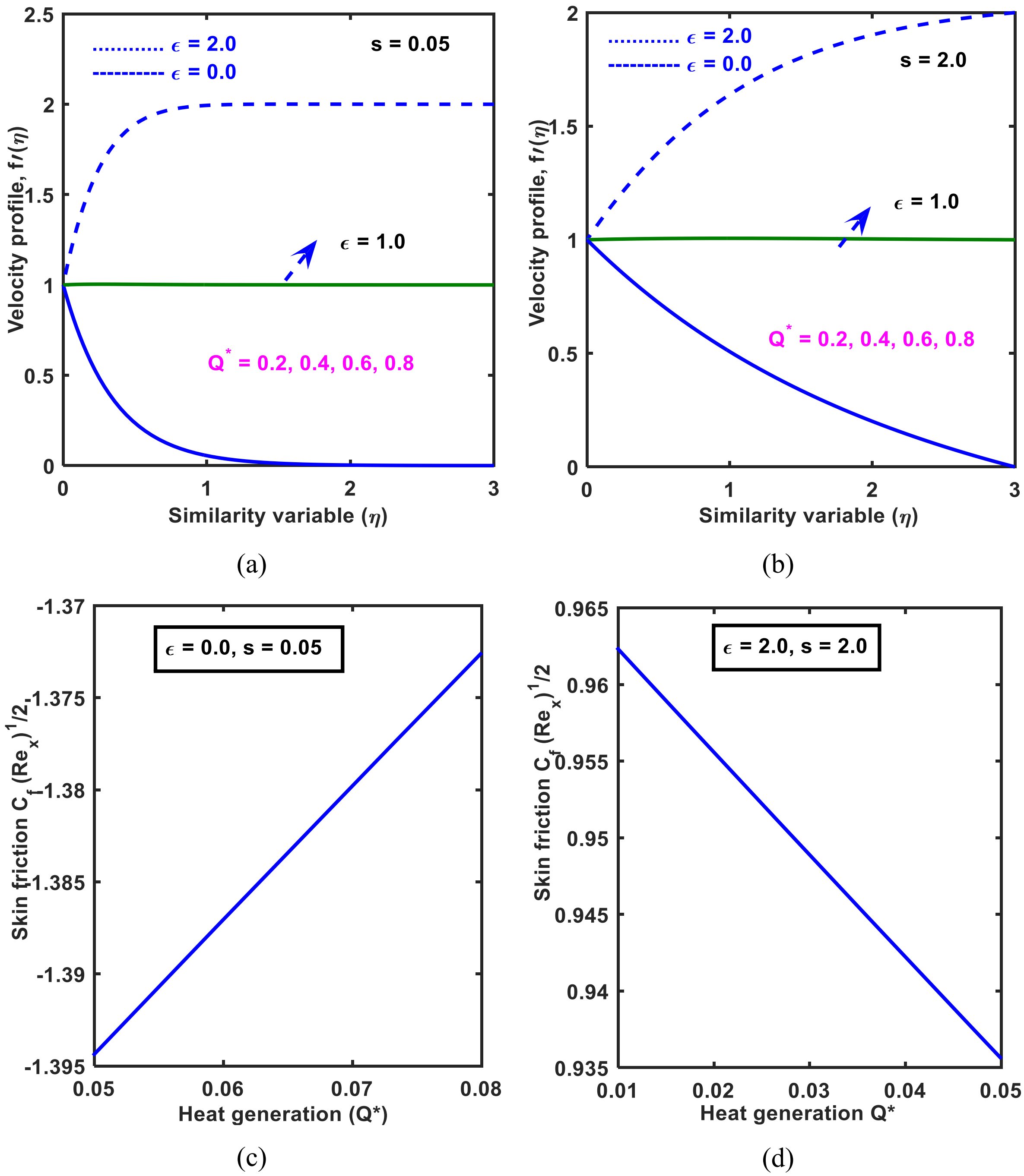

Figure 5. 3 Effect of heat generation on velocity profile when (a) $\epsilon = 0.0$, s = 0.05, s = 2.0 (b) $\epsilon = 0.0$, s = 0.2, s = 2.0 and skin friction when (c) $\epsilon = 0.0$, s = 0.05 and (d) $\epsilon = 2.0$ s = 2.0

5.3.1.4 Effect of mixed convection parameter (λ) on the velocity profile and skin friction

Figures 5.4(a) - 5.4(d) exhibit the influence of mixed convection parameter, λ on the velocity profile and skin friction in the case of the stretching ratio parameter $\varepsilon > 1.0$, or < 1.0 and surface thickness parameter, s = 0.05, and 2.0, respectively. From these figures, it is observed that the fluid velocity profile and boundary layer thickness expands both of the thinner and thicker surface (s = 0.05, 2.0). Also, it is seen that the fluid flow form an inverted boundary layer pattern when $0.0 \leq \varepsilon < 1.0$ but a definite boundary layer pattern in case of $1.0 < \varepsilon \leq 2.0$ both of the thinner and thicker bullet-shaped objects. Therefore, the velocity gradient at the surface is positive when $\varepsilon > 1.0$ and negative due to $\varepsilon < 1.0$ all values of the controlling parameters. So, the skin friction increase in both of the cases $\varepsilon > 1.0$ and $\varepsilon < 1.0$ also s = 0.05, s = 2.0 respectively. It is seen that the fluid velocity increases just near the bullet-shaped object and decreases far from it when $\varepsilon < 1.0$ but an opposite trend is observed when $\varepsilon < 1.0$. This is because of an increase in the mixed convection parameter the buoyancy force increases which, in turn, reduces the viscous force as a result the fluid velocity increases. Therefore, the boundary layer thickness and skin friction decrease with an increase of the mixed convection parameter λ.

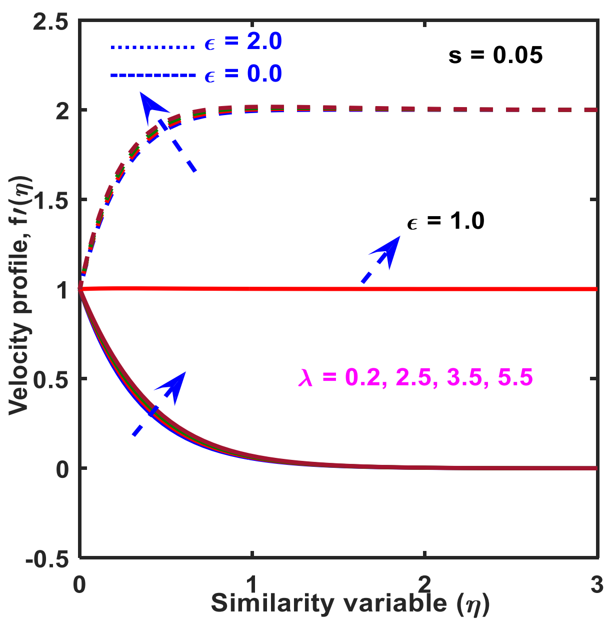

(a)

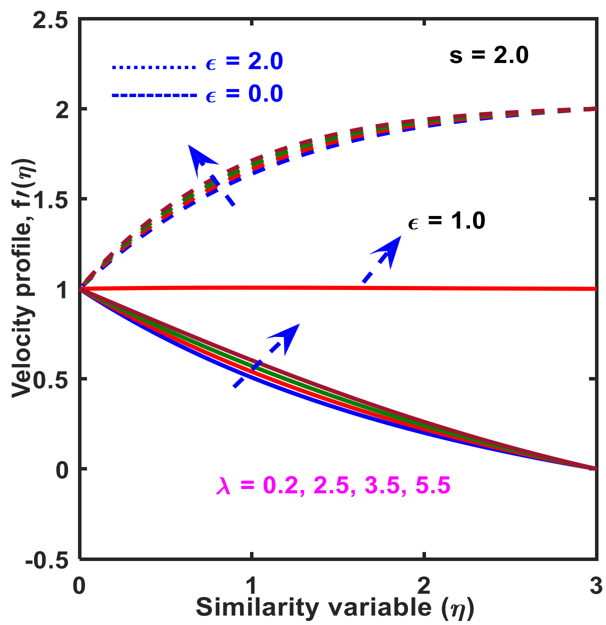

(b)

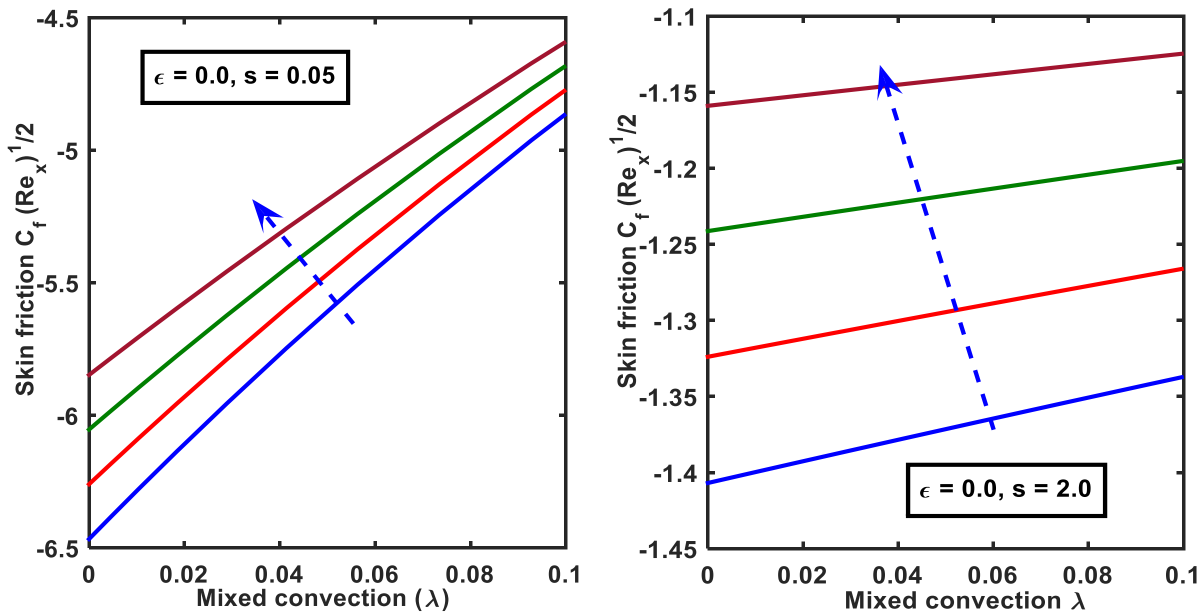

(c) (d)

Figure 5. 4 Effect of mixed convection on velocity profile when (a) $\epsilon = 0.0$, s = 0.05, s = 2.0 (b) $\epsilon = 0.0$, s = 0.05, s = 2.0 and skin friction when (c) $\epsilon = 0.0$, s = 0.05 and (d) $\epsilon = 0.0$ s = 2.0

From the numerical values of the velocity gradient, it is observed that when λ increases from 0.5 to 3.5 and $s = 0.2$ there is a 9.7% decrease in the skin friction and the corresponding decrease is 18% for $s = 2.0$.

5.3.1.5 Effect of stream-wise coordinate (*X*) on the velocity profile and skin friction

Figures 5.5(a) – 5.5(d) represent the variation of velocity distribution and skin friction coefficient for different values of stream-wise coordinate. It is seen from these figures that the velocity profile and boundary layer thickness enhance on increasing X when $\varepsilon < 1$ whereas opposite trend is observed in case of $\varepsilon > 1$. This is because the stream-wise coordinate acts as a favorable pressure gradient in the direction of flow velocity which in turn increases the flow rate as a result the momentum boundary layer thickness increases. Besides, increasing the dimensionless coordinate X from the leading edge leads to an enhancement of the fluid velocity within the boundary layer region. Also, it is seen that the fluid flow forms an inverted boundary layer pattern when $0.0 \le \varepsilon < 1.0$ but a definite boundary layer pattern in case of $1.0 < \varepsilon \le 2.0$ both of the thinner and thicker bullet-shaped objects. Therefore, the velocity gradient at the surface is positive when $\varepsilon > 1$ and negative due to $\varepsilon < 1$ all values of the controlling parameters.

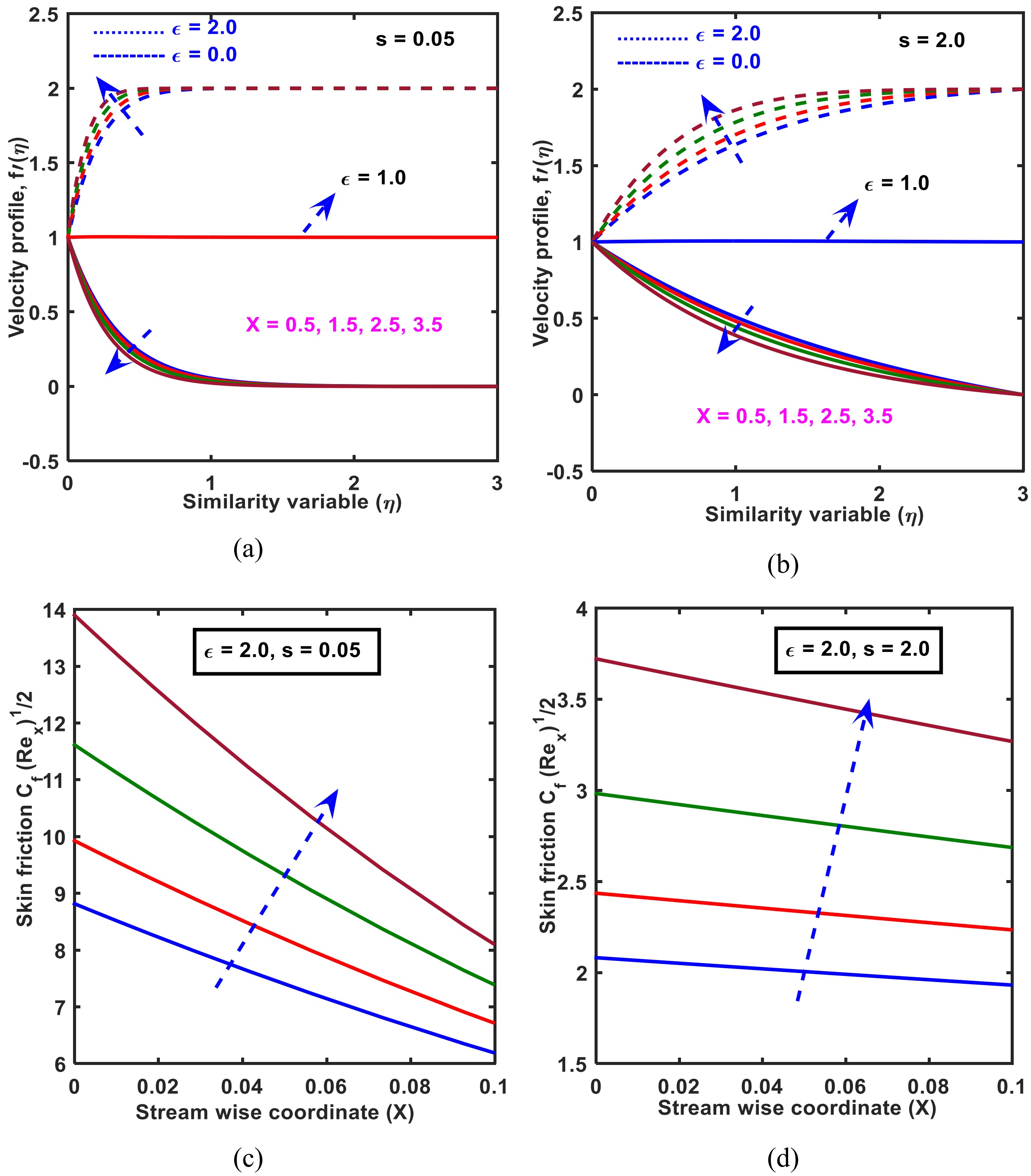

Figure 5. 5 Effect of Stream-wise coordinate on velocity profile when (a) $\epsilon = 0.0$, s = 0.05, s = 2.0 (b) $\epsilon = 0.0$, s = 0.05, s = 2.0 and skin friction when (c) $\epsilon = 2.0$, s = 0.05 and (d) $\epsilon = 2.0$, s = 2.0

So, the skin friction increases in both of the cases $\varepsilon > 1$ and $\varepsilon < 1$ also $s = 0.05$, $s = 2.0$, respectively. From the numerical values of the velocity gradient, it is observed that when X

increases from 0.5 to 3.5, there is a 31.3% increase in the skin friction and the corresponding increase is 45.4% when s = 0.2 and s = 2.0, respectively.

5.3.1.6 Effect of stretching ratio parameter (ϵ) on the velocity profile and skin friction

Figures 5.6(a) - 5.6(d) exhibit the variation of velocity profile and skin friction for different values of stretching ratio parameters. It is seen from these figures that the velocity profile and boundary layer thickness enhance on increasing ϵ when $\varepsilon < 1$ whereas opposite trend is observed in case of $\varepsilon > 1$. It is clear that the velocity profile and boundary layer thickness increases for raising the effect of stretching ratio parameter due to thinner (s = 0.05) and thicker (s = 2.0) surface. Therefore, ϵ is directly proportional to the velocity profile. From these figures, it is also observed that when the term, $\varepsilon > 1$ then the flow has a certain boundary layer structure and form a definite boundary layer pattern but

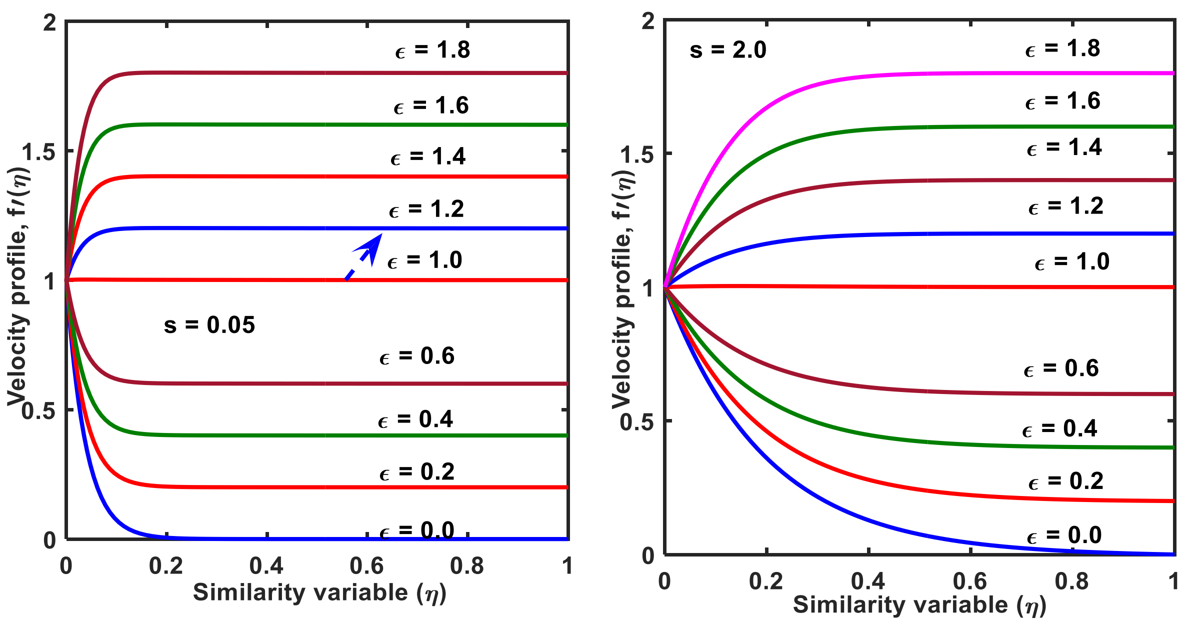

(a) (b)

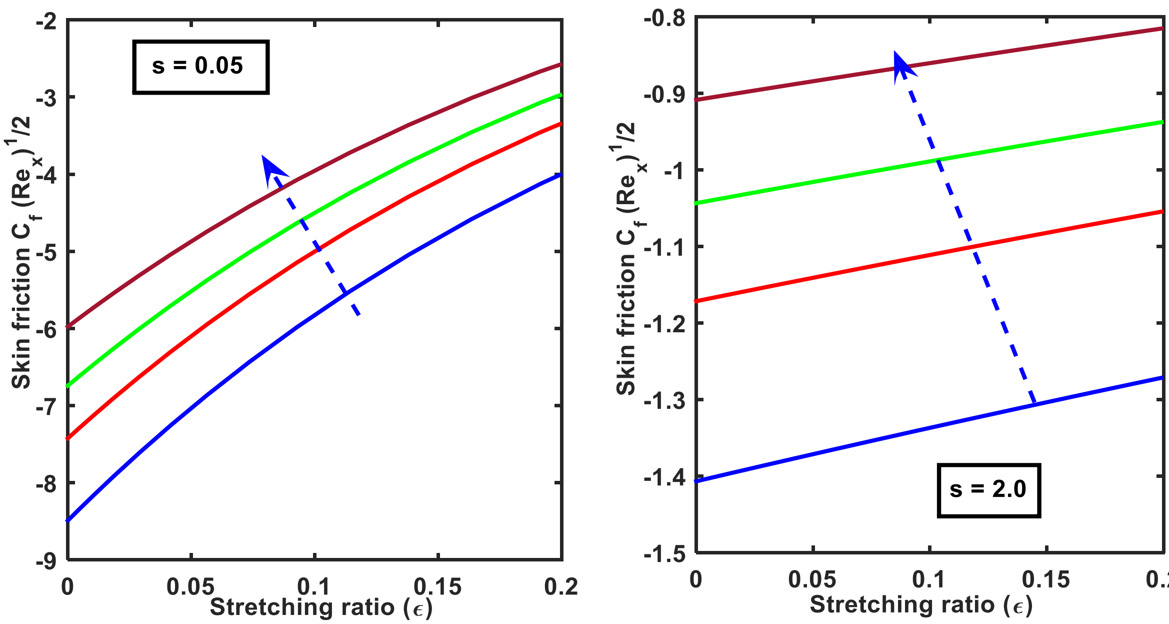

(c) (d)

Figure 5. 6 Effect of stretching ratio on velocity profile when (a) s = 0.05 (b) s = 2.0 and skin friction when (c) s = 0.05, $\varepsilon < 1$ and (d) s = 2.0, $\varepsilon < 1$

the term $\varepsilon < 1$, then the boundary layer flow has an inverse pattern and it becomes a reverse boundary layer. Again, the velocity gradient at the surface is positive when $\varepsilon > 1$ and negative due to $\varepsilon < 1$ for all values of the controlling parameters but the skin friction increases for both of the cases s = 0.05, s = 2.0, respectively. From the numerical values of the velocity gradient, it is observed that when ϵ increases from 0.0 to 0.4, there is a 35.6% increase of the skin friction and the corresponding increase is 35.43% when s = 0.2 and s = 2.0 respectively.

5.3.1.7 Effect of a surface thickness parameter (*s*) on the velocity profile and skin friction

Figure 5.7 (a) and Figure 5.7(b) illustrate the influence of surface thickness parameter on the velocity profile and skin friction by taking the stretching ratio parameter $\varepsilon > 1$, or < 1.0 , respectively. The velocity profile and boundary layer thickness enhance with increasing values of s in case of $\varepsilon < 1$ but in case of $\varepsilon > 1$ the velocity profile and boundary layer thickness decreases which is significant because an increase in s which enhances the surface area of the object that provides more resistance against the fluid motion, as a result, the fluid velocity decreases. Again, it is also seen that the velocity gradient at the surface is positive when $\varepsilon > 1$ and negative when $\varepsilon < 1$ for all values of the controlling parameters.

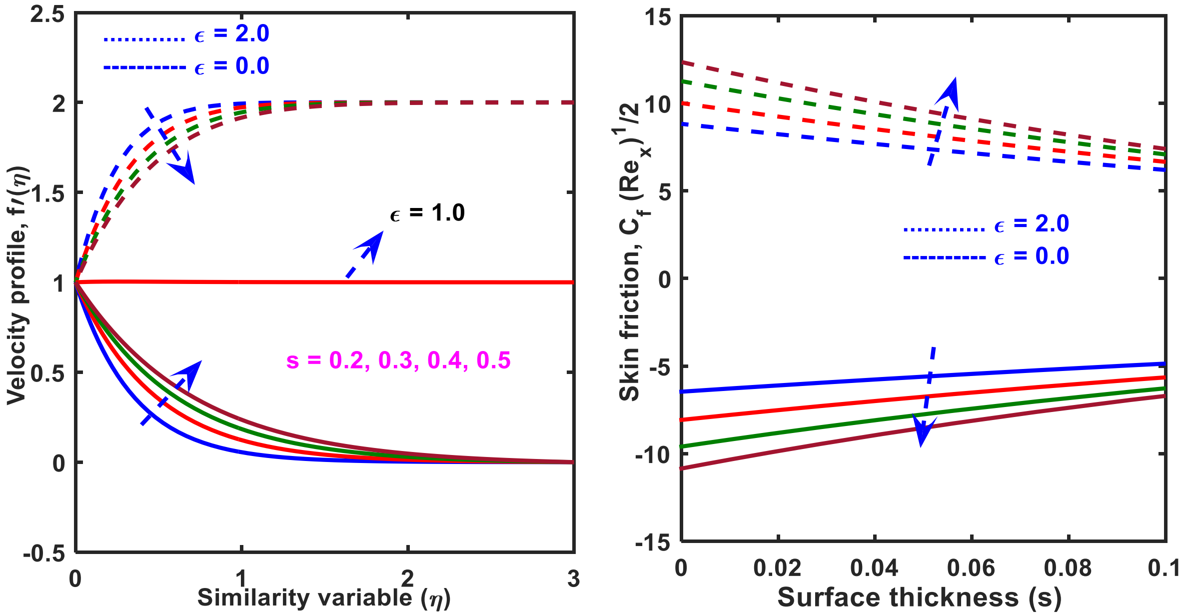

(a) (b)

Figure 5. 7 Effect of surface thickness (s) on velocity profile when (a) $\epsilon = 0.0, 1.0, 2.0$ and skin friction (b) $\epsilon = 0.0, 2.0$

It is revealed from Figure 5.7(b) that the skin friction increases in the case of $\varepsilon > 1$ and decreases in the case of $\varepsilon < 1$ on increasing surface thickness parameter. From the numerical values of the velocity gradient, it is observed that when s increases from 0.2 to 0.4, there is a 50.6% decrease of the skin friction and the corresponding decrease is 4.1% when $s = 0.2$ and $s = 2.0$ respectively.

From these velocity distribution figures, it is observed that the velocity profile and momentum boundary layer thickness is getting expand due to magnetic parameter (M), mixed convection parameter (λ), location parameter (X), and stretching ratio parameter (ϵ) whereas surface thickness parameter (s) has a reverse effect on it in the case of $\epsilon > 1$ for both of the thicker ($s = 2.0$) and the thinner ($s = 0.05$) surfaces. On the other hand, in the case of $\epsilon < 1$ the velocity profile and momentum boundary layer thickness are getting squeezes due to magnetic parameter (M), and location parameter (X) whereas surface thickness parameter (s) and mixed convection parameter (λ) have a reverse effect on it. On the other hand, Eckert number (Ec) and heat generation parameter (Q^*) have no effect on the velocity profile for both of the thicker (s = 2.0) and the thinner (s = 0.05) surfaces. Therefore, in the case of a thicker bullet-shaped object (s = 2.0), the velocity profile does not approach the ambient condition asymptotically but intersects the vertical axis with a steep angle and the boundary layer structure has no definite shape whereas in the case of a thinner bullet-shaped object (s = 0.05) the velocity profile converge the ambient condition asymptotically and the boundary layer structure has a definite shape. It is also noticed that the thinner bullet-shaped object represents a thinner momentum boundary layer than the thicker bullet-shaped object in both static and moving bullet-shaped objects.

Table 5.1 shows the influence of magnetic parameter (M), location parameter (X), Prandtl number (Pr), heat generation parameter (Q^*), Eckert number (Ec), mixed convection parameter (λ) and surface thickness parameter (s) on the skin friction coefficient when ϵ = 0.0, ϵ = 2.0 and s = 0.2. It is observed that the Prandtl number, heat generation parameter, and Eckert number do not affect the skin friction coefficient whereas the magnetic parameter and location parameter enhances the skin friction coefficient in the case of $\varepsilon < 1.0$ but reduce the skin friction in the case of $\varepsilon > 1.0$. A precisely reverse trend is observed for the surface thickness parameter. On the other hand, the skin friction reduces for the increasing effect of the mixed convection parameter either $\varepsilon >$ or < 1. It is interesting to note that the friction factor coefficient is less in ϵ = 0.0 case when compared with ϵ = 2.0 case. At this point, it is highlighted that for reducing the friction between the particles we have to consider the ϵ = 0.0 case. It is evident from this table that the skin friction coefficient is higher in the ϵ = 2.0 case when comparing with ϵ = 0.0. It is worth mentioning that the skin friction is negative for all values of the mentioned parameters in the case of $\varepsilon < 1$ but positive in the case of $\varepsilon > 1$. Physically, the negative value means that the bullet-shaped object applies a drag force on fluid and positive values of skin friction coefficient mean that the fluid exerts a drag force on the bullet-shaped object. Therefore, skin friction is an increasing function of the magnetic parameter and location parameter in the case of $\varepsilon < 1.0$ but decreasing function in the case of $\varepsilon > 1.0$ whereas it is constant for the effect of the Prandtl number, heat generation parameter, and Eckert number.

Table 5. 1 Variation in skin friction coefficient for different values of *M, X,* Pr, *Q*,* *Ec, λ,* and *s* with $\epsilon = 0.0$, $\epsilon = 2.0$, and $s = 0.2$

M	X	Pr	Q^*	Ec	λ	s	$\left\|-C_f\sqrt{\mathrm{Re}_x}\right\|$ $\epsilon = 0.0$, s = 0.2	$-C_f\sqrt{\mathrm{Re}_x}$ $\epsilon = 2.0$, s = 0.2
1.0	0.5	0.71	0.5	0.2	0.5	0.2	**6.3868**	**8.8939**
5.0	0.5	0.71	0.5	0.2	0.5	0.2	**8.0175**	**10.1511**
10.0	0.5	0.71	0.5	0.2	0.5	0.2	**9.5543**	**11.4398**
1.0	**0.5**	0.71	0.5	0.2	0.5	0.2	**6.3868**	**8.8939**
1.0	**1.5**	0.71	0.5	0.2	0.5	0.2	**6.8445**	**9.9342**
1.0	**2.5**	0.71	0.5	0.2	0.5	0.2	**7.5062**	**11.6172**
1.0	0.5	**0.71**	0.5	0.2	0.5	0.2	**6.3868**	**8.8939**
1.0	0.5	**1.0**	0.5	0.2	0.5	0.2	**6.3868**	**8.8939**
1.0	0.5	**7.0**	0.5	0.2	0.5	0.2	**6.3868**	**8.8939**
1.0	0.5	0.71	**0.5**	0.2	0.5	0.2	**6.3868**	**8.8939**
1.0	0.5	0.71	**1.5**	0.2	0.5	0.2	**6.3868**	**8.8939**
1.0	0.5	0.71	**2.0**	0.2	0.5	0.2	**6.3868**	**8.8939**
1.0	0.5	0.71	0.5	**0.2**	0.5	0.2	**6.3868**	**8.8939**
1.0	0.5	0.71	0.5	**0.4**	0.5	0.2	**6.3868**	**8.8939**
1.0	0.5	0.71	0.5	**0.6**	0.5	0.2	**6.3868**	**8.8939**
1.0	0.5	0.71	0.5	0.2	**0.5**	0.2	**6.3868**	**8.8939**
1.0	0.5	0.71	0.5	0.2	**1.5**	0.2	**6.0251**	**9.2584**
1.0	0.5	0.71	0.5	0.2	**2.5**	0.2	**5.6691**	**9.6234**
1.0	0.5	0.71	0.5	0.2	0.5	**0.1**	**11.5445**	**14.8115**
1.0	0.5	0.71	0.5	0.2	0.5	**0.2**	**6.3868**	**8.8939**
1.0	0.5	0.71	0.5	0.2	0.5	**0.3**	**4.6087**	**6.7212**

5.3.2 Temperature profiles and Nusselt number with parameter variations

5.3.2.1 Effect of Prandtl number (Pr) on temperature profile and Nusselt number

Figures 5.8(a) - 5.8(d) show the influence of Prandtl number (Pr) on temperature profile and Nusselt number in case of the stretching ratio parameter $\varepsilon > 1.0$ or < 1 and surface thickness parameter, s = 0.05, and 2.0, respectively. These plots depict that the temperature profile of the viscous fluid and thermal boundary layer thickness affected significantly with increasing Prandtl number. It is noticed from these figures that the variation of surface thickness parameter has a significant effect on fluid temperature in connection with the Prandtl number. It is also seen that the temperature profile and boundary layer thickness squeezes for both of the thicker (s = 2.0, and thinner (s = 0.05) surfaces of the bullet-shaped object but the Nusselt number increases. It is also observed that the thermal boundary layer thickness is higher in the case of the thicker surface (s = 2.0) than the thinner surface (s = 0.05). Because raising the Pr tends to decrease the thermal diffusivity of the fluid and causes a weak entrance of heat inside the fluid. In the case of smaller Prandtl number heat is quickly diffuse from the heated surface than for higher values of Pr. So, for the cooling purpose, we can use the higher the Prandtl number.

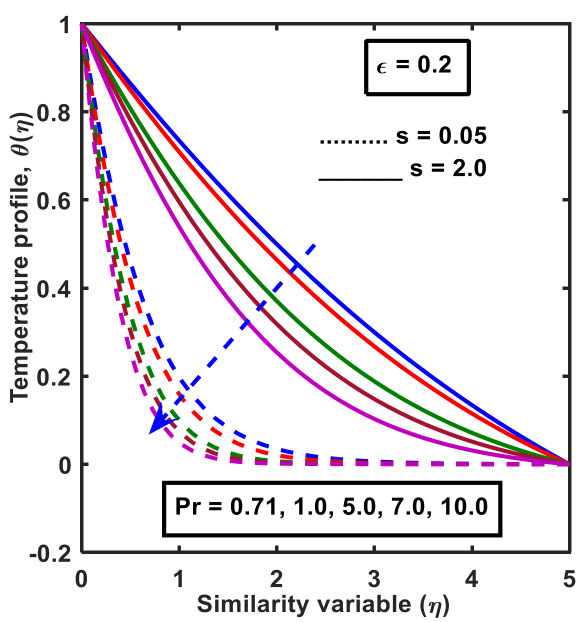

(a)

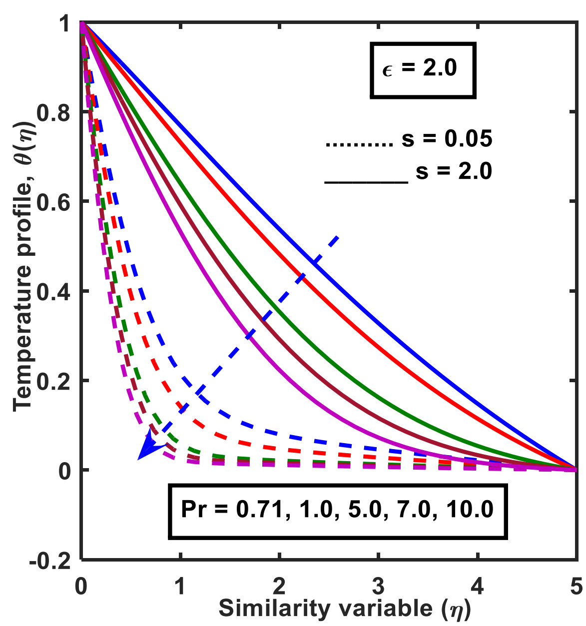

(b)

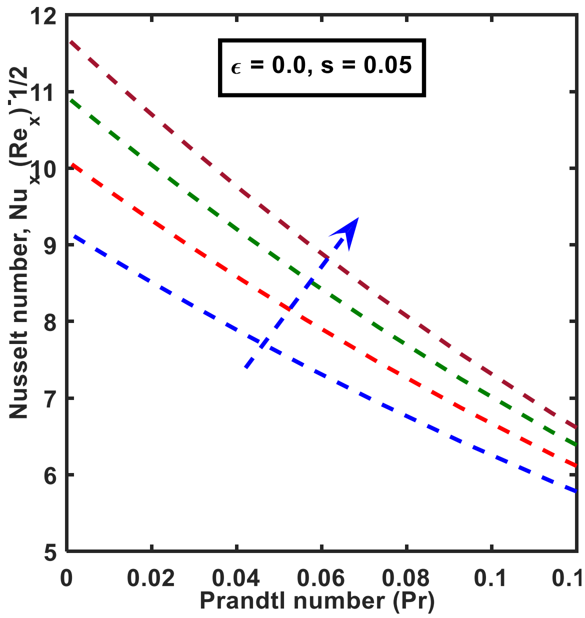

(c)

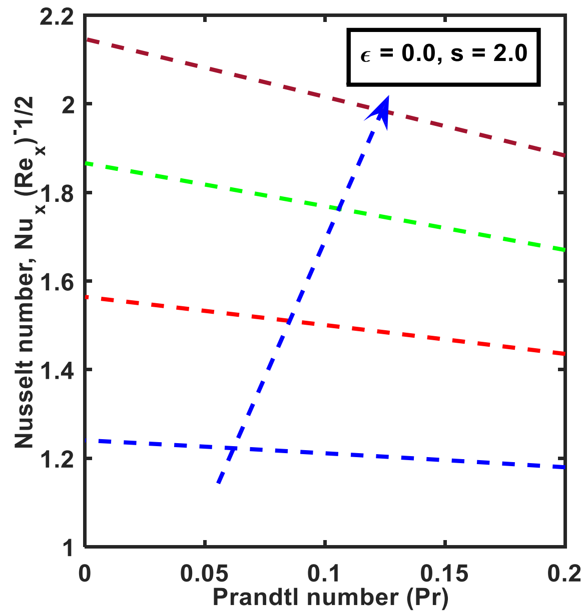

(d)

Figure 5. 8 Effect of Prandtl number (Pr) on temperature profile when (a) $\epsilon = 0.0$, s = 0.05, 2.0 (b) $\epsilon = 0.0$, s = 0.05, 2.0 and Nusselt number when (c) $\epsilon = 0.0$, s = 0.05 and (d) $\epsilon = 0.0$, s = 2.0

A smaller surface thickness has a greater decelerating effect than a thicker surface. Therefore, it is noticed that for higher values of surface thickness parameter, the maximum temperature shows in the thermal boundary layer compared to that of lower surface thickness parameter. Again, the dimensionless numerical values of the Nusselt number show that the rate of heat transfer is about 65 % higher in the case of a thinner surface than a thicker surface. From the numerical values of the temperature gradient, it is observed that when Pr increases from 0.71 to 7.0, there is a 29.56% increase of the Nusselt number and the corresponding increase is 80.1% when $s = 0.2$ and $s = 2.0$ respectively.

5.3.2.2 Effect of heat generation parameter (Q^*) on temperature profile and Nusselt number

Figures 5.9(a) - 5.9(d) illustrate the variation of temperature profile and Nusselt number for the effect of heat generation parameter when the stretching ratio parameter $\epsilon = 0.2$, $\epsilon = 2.0$, the surface thickness parameter $s = 0.05$, $s = 2.0$, and Pr = 0.71, 7.0 respectively. The positive values of Q^* mean source i.e. heat generation in the fluid.

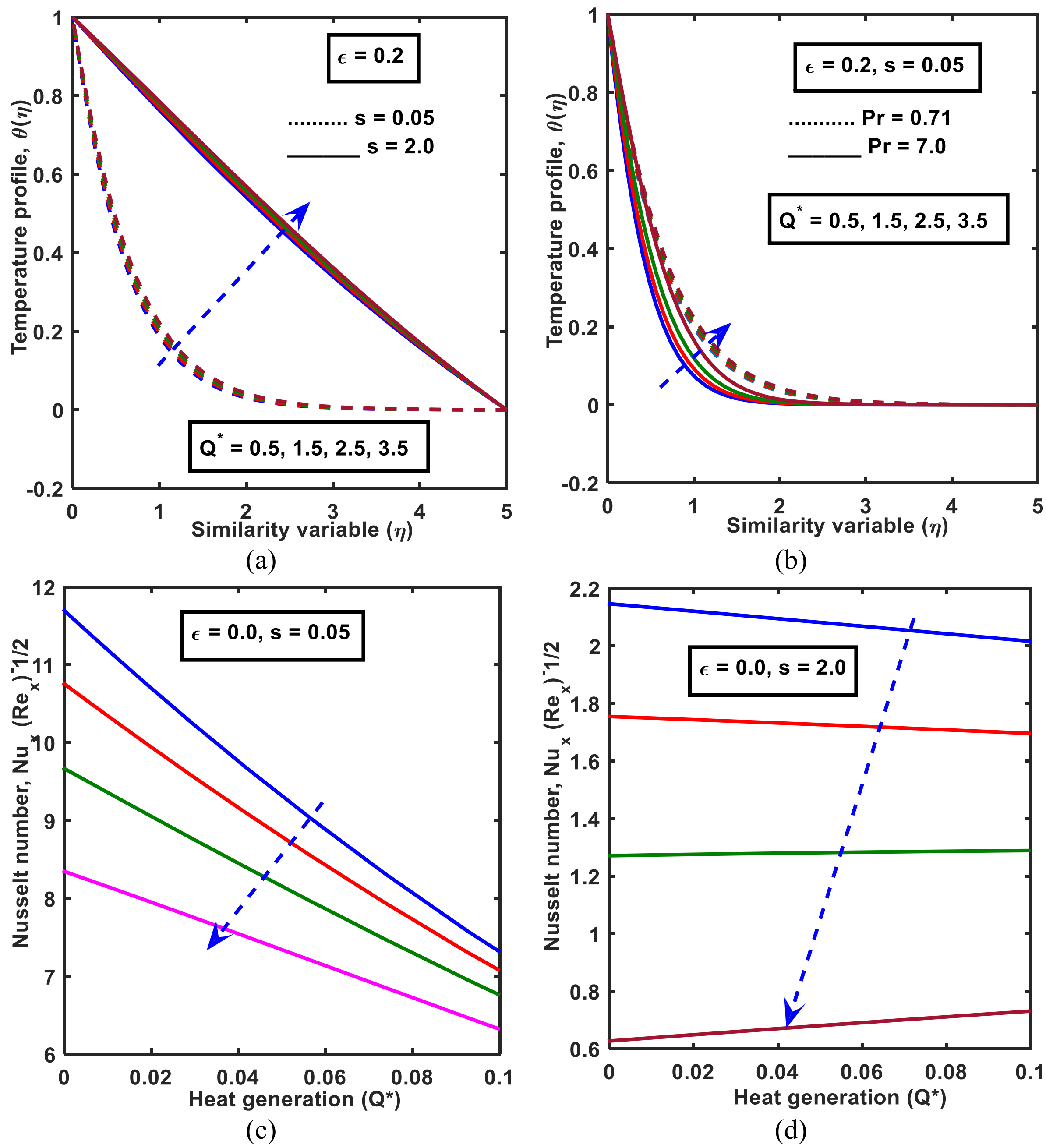

Figure 5. 9 Effect of heat generation (Q^*) on temperature profile when (a) $\epsilon = 0.2$, s = 0.05, 2.0 (b) $\epsilon = 0.2$, s = 0.05, Pr = 0.71, 7.0 and Nusselt number when (c) $\epsilon = 0.0$, s = 0.05, and (d) $\epsilon = 0.0$, s = 2.0

Figure 5.9 (a) depicts the influence of heat generation parameter on viscous fluid temperature for thinner surface (s = 0.05) and thicker surface (s = 2.0) when $\epsilon = 0.2$ respectively. This plot represents that the variation of heat generation parameter has an insignificant effect on fluid temperature in connection with the surface thickness parameter and the Prandtl number. A lower surface thickness parameter has a lower accelerating effect. For thicker surfaces (s = 2.0) with increasing Q*, the accelerating effect is more prominent than for thinner surfaces (s = 0.05). Therefore, the thermal boundary layer thickness is higher due to the thicker surface when compared with the thinner surface. Hence, the temperature profile and boundary layer thickness expand for both of the thicker (s = 2.0) and thinner (s = 0.05) surfaces of the bullet-shaped object whereas the Nusselt number decreases (Figures 5.9 (c) and (d)). Figure 5.9 (b) also represent the influence of heat generation parameter on viscous fluid temperature for air (Pr = 0.71) and water (Pr = 7.0) when s = 0.05 and 2.0 respectively. It is seen from these figures that the variation of the Prandtl number has a significant effect on viscous fluid temperature in connection with the heat generation parameter. A higher Prandtl number has a greater accelerating effect on the temperature profile. For air (Pr = 0.71) with increasing Q*, the accelerating effect is more prominent than for water (Pr = 0.71). Therefore, the thermal boundary layer thickness is higher in the case of air when compared with water. However, the temperature attains its minimum in connection with the heat generation parameter and then the profile decreases sharply to meet the boundary condition as well. From these figures, the temperature profile and thermal boundary layer thickness increase with the increase of Q^* for all mentioned cases. Therefore, it is seen that for higher values of surface thickness parameter, the maximum temperature shows in the thermal boundary layer compared to that of lower surface thickness parameter. Again, in the case of air (Pr = 0.71), the highest temperature shows in the thermal boundary layer compared to that of water (Pr = 7.0). From the numerical values of the temperature gradient, it is observed that when Q^* increases from 0.5 to 6.5, there is a 4.66% decrease of the Nusselt number when s = 0.05 and the corresponding decrease is 14.63% when s = 2.0.

5.3.2.3 Effect of the magnetic parameter (*M*) on temperature profile and Nusselt number

Figures 5.10(a) - Figure 5.10(d) show the effect of the magnetic parameter (M) on temperature profile and Nusselt number when the stretching ratio parameter $\epsilon = 0.2$, $\epsilon = 2.0$, the surface thickness parameter s = 0.05, s = 2.0, and Pr = 0.71, 7.0 respectively.

Figure 5.10 (a) depicts the influence of magnetic parameter on viscous fluid temperature for thinner surface (s = 0.05) and thicker surface (s = 2.0) when ϵ = 0.2 respectively. It is noticed from these figures that the variation of the magnetic parameter has a significant effect on fluid temperature in connection with the surface thickness parameter and the Prandtl number. A lower surface thickness parameter has a lower accelerating effect. For thicker surfaces (s = 2.0) with increasing M, the accelerating effect is more prominent than for thinner surfaces (s = 0.05). Therefore, the thermal boundary layer thickness is higher due to the thicker surface when compared with the thinner surface. Hence, the temperature profile and boundary layer thickness expand for both of the thicker (s = 2.0) and thinner (s = 0.05) surfaces of the bullet-shaped object whereas the Nusselt number decreases (Figures 5.10 (c) and (d)). Figure 5.10 (b) also represents the influence of magnetic parameter on viscous fluid temperature for air (Pr = 0.71) and water (Pr = 7.0) when s = 0.05 and 2.0 respectively. It is seen from these figures that the variation of the Prandtl number has a significant effect on viscous fluid temperature in connection with the magnetic parameter. A higher Prandtl number has a greater accelerating effect on the temperature profile. For air (Pr = 0.71) with increasing M, the accelerating effect is more prominent than for water (Pr = 7.0).

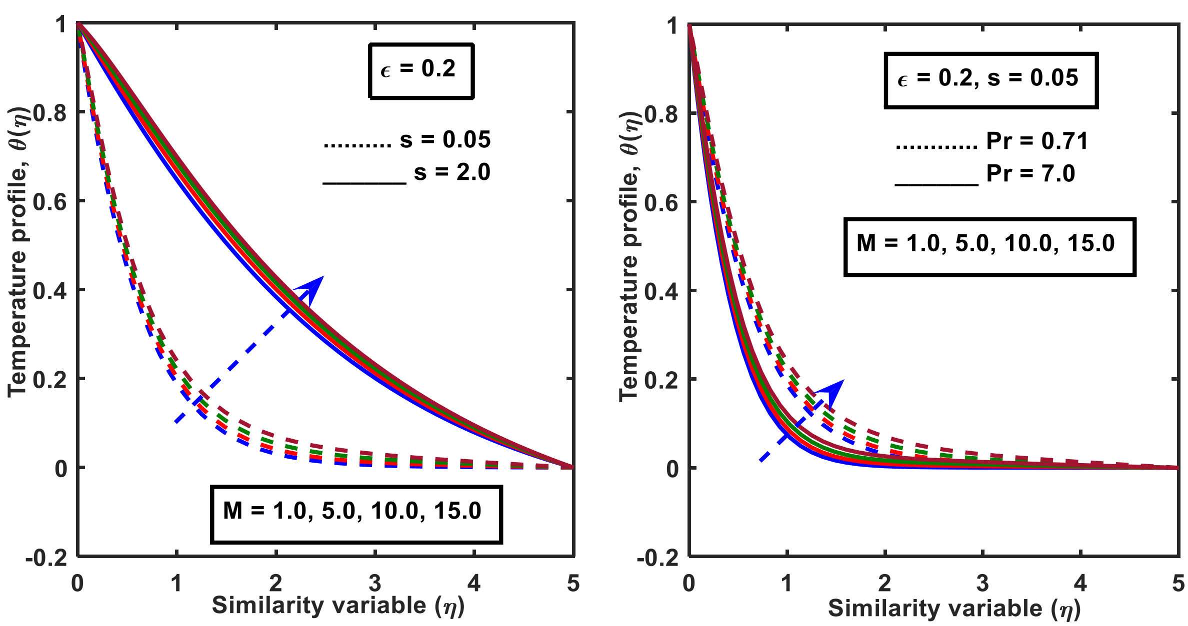

(a) (b)

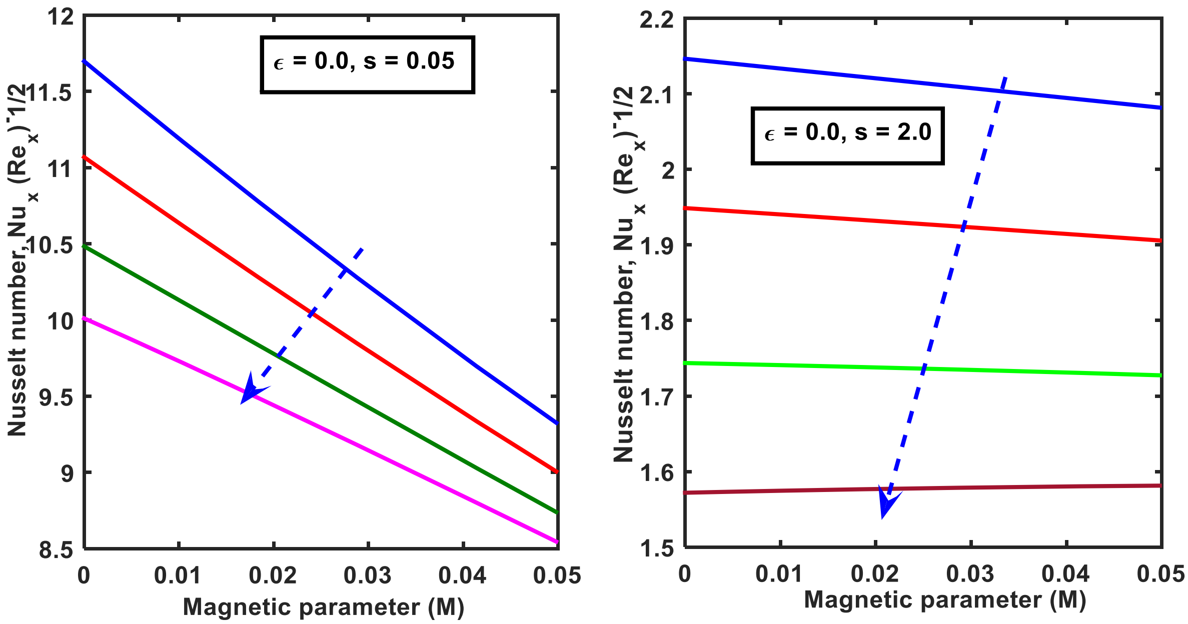

(c) (d)

Figure 5. 10 Effect of magnetic parameter on temperature profile when (a) ϵ = 0.0, s = 0.05, 2.0 (b) ϵ = 0.0, s = 0.05, Pr = 0.71, 7.0 and Nusselt number when (c) ϵ = 0.0, s = 0.05 and (d) ϵ = 0.0, s = 2.0

Therefore, the thermal boundary layer thickness is higher for air when compared with water. However, the temperature attains its minimum in connection with the magnetic parameter and then the profile decreases sharply to meet the boundary condition as well. From these figures, the temperature distribution and the thickness of the thermal boundary layer increase with the increase of M for all mentioned cases. Therefore, it is seen that for higher values of surface thickness parameter, the maximum temperature shows in the thermal boundary layer compared to that of lower surface thickness parameter. Again, in the case of air (Pr = 0.71), the highest temperature shows in the thermal boundary layer compared to that of water (Pr = 7.0). Because, in an electrically conducting fluid if the magnetic field is applied a resistive type force like a drag force is produced, which is called Lorentz force? The nature of this force retards the fluid velocity, and therefore, the magnetic field effects decelerate the velocity profiles. This Lorentz force tends to slow down the fluid motion and the resistance offered to the flow. Therefore, it is possible for the increase in the temperature. From the numerical values of the temperature gradient, it is observed that when M increases from 1.0 to 15.0, there is a 13.82% decrease of the Nusselt number when $s = 0.05$ and the corresponding decrease is 31.77% when $s = 2.0$.

5.3.2.4 Effect of Eckert number (*Ec*) on temperature profile and Nusselt number

Figures 5.11 (a) - 5.11 (d) represent the effect of the Eckert number (Ec) on temperature profile and Nusselt number when the stretching ratio parameter $\epsilon = 0.2$, $\epsilon = 2.0$, the surface thickness parameter $s = 0.05$, $s = 2.0$, and Pr = 0.71, 7.0 respectively. Figure 5.11 (a) reveals the influence of Eckert number (Ec) on viscous fluid temperature for thinner surface ($s = 0.05$) and thicker surface ($s = 2.0$) when $\epsilon = 0.2$ respectively. It is noticed from these figures that the variation of the Eckert number (Ec) has a significant effect on fluid temperature in connection with the surface thickness parameter and the Prandtl number. A lower surface thickness parameter has a lower accelerating effect. For thicker surface ($s = 2.0$) with increasing Eckert number (Ec), the accelerating effect is more prominent than for thinner surface ($s = 0.05$). Therefore, the thermal boundary layer thickness is higher due to the thicker surface when compared with the thinner surface. Hence, the temperature profile and boundary layer thickness expand for both of the thicker ($s = 2.0$) and thinner ($s = 0.05$) surfaces of the bullet-shaped object whereas the Nusselt number decreases (Figures 5.11 (c) and (d)). Figure 5.11 (b) also represents the influence of Eckert number (Ec) on viscous fluid temperature for air (Pr = 0.71) and water (Pr = 7.0) when s = 0.05 and $\epsilon = 0.2$ respectively. It is seen from these figures that the variation of the Prandtl number has a significant effect on viscous fluid temperature in connection with the Eckert number (Ec). A lower Prandtl number has a greater accelerating effect on the temperature profile. For air (Pr = 0.71) with an increasing Eckert number, the accelerating effect is more prominent than for water (Pr = 7.0). Therefore, the thermal boundary layer thickness is higher for air when compared with water. However, the temperature attains its minimum in connection with the Eckert number for a low value of $Ec \leq 1$ but the higher value of $Ec > 1$ shooting up the profiles near the surface of the bullet-shaped object within the region $\eta < 0.2$ and then the profile decreases sharply to meet the boundary condition as well for both of air (Pr = 0.71) and water (Pr = 7.0).

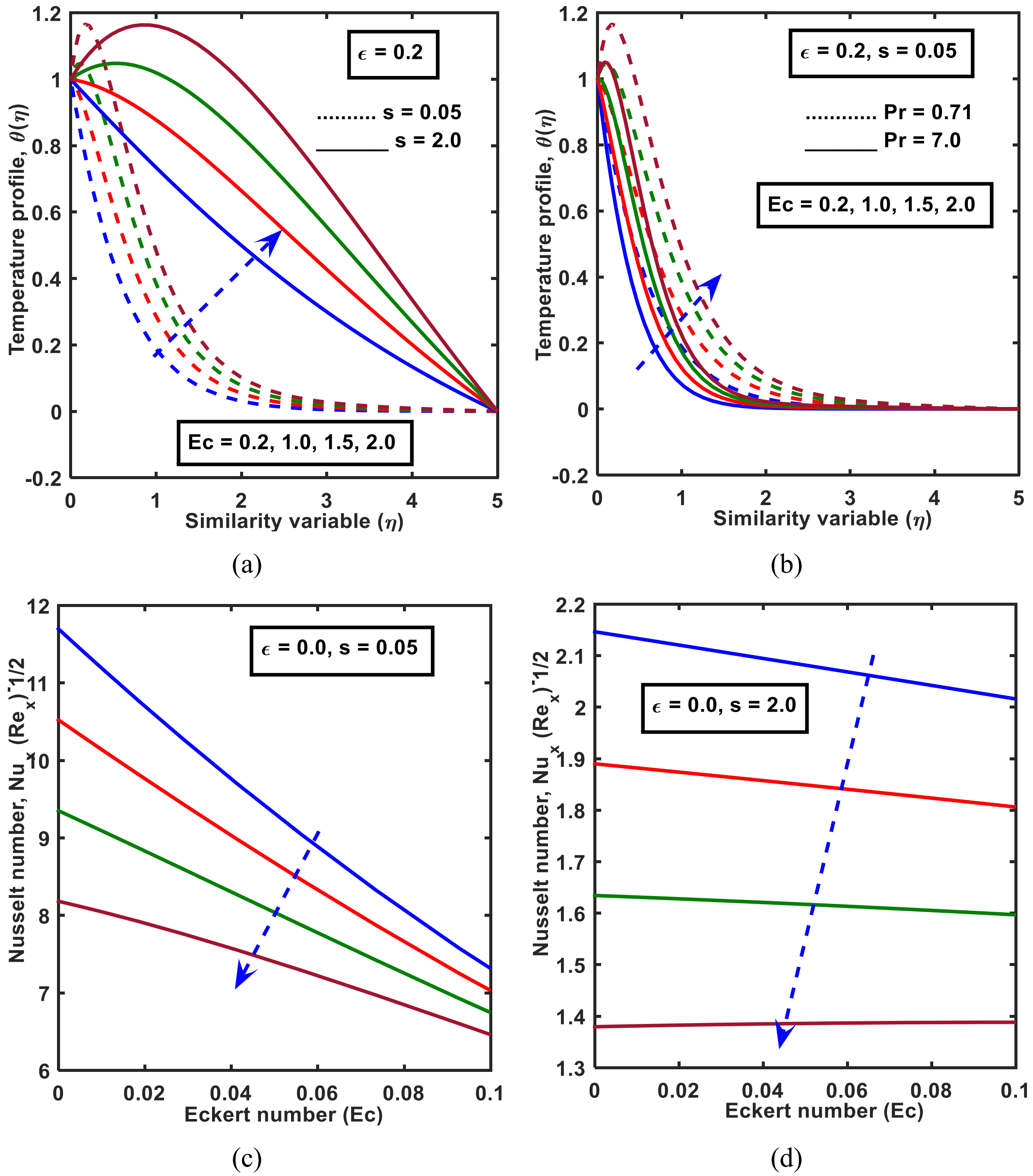

Figure 5. 11 Effect of Eckert number on temperature profile when (a) $\epsilon = 0.2$, s = 0.05, s = 2.0 (b) $\epsilon = 0.0$, s = 0.05, Pr = 0.71, 7.0 and Nusselt number when (c) $\epsilon = 0.0$, s = 0.05, and (d) $\epsilon = 0.0$, s = 2.0**.**

From these figures, the temperature distribution and the thickness of the thermal boundary layer increase with the increase of Ec for all mentioned cases. Therefore, it is seen that for higher values of surface thickness parameter, the maximum temperature shows in the thermal boundary layer compared to that of lower surface thickness parameter. Again, in the case of air (Pr = 0.71), the highest temperature shows in the thermal boundary layer compared to that of water (Pr = 7.0). It happens because increasing values of *Ec* produce extra heat energy in the fluid because of frictional heating as a result the temperature enhances at any given point within the boundary layer region. From the numerical values of the temperature gradient, it is observed that when Ec changes from 0.2 to 0.6, there is a 42.77% decrease of the Nusselt number when s = 0.2 and the corresponding decrease is 70.96% when s = 2.0.

5.3.2.5 Effect of mixed convection parameter (*λ*) on temperature profile and Nusselt number

Figures 5.12(a) - 5.12(b) describe the mixed convection parameter on the temperature profile and Nusselt number when $\varepsilon > 1.0$ or < 1. It is observed that the mixed convection parameter does not affect the temperature profile and also temperature gradient both of s = 0.05 and s = 2.0 within the boundary layer.

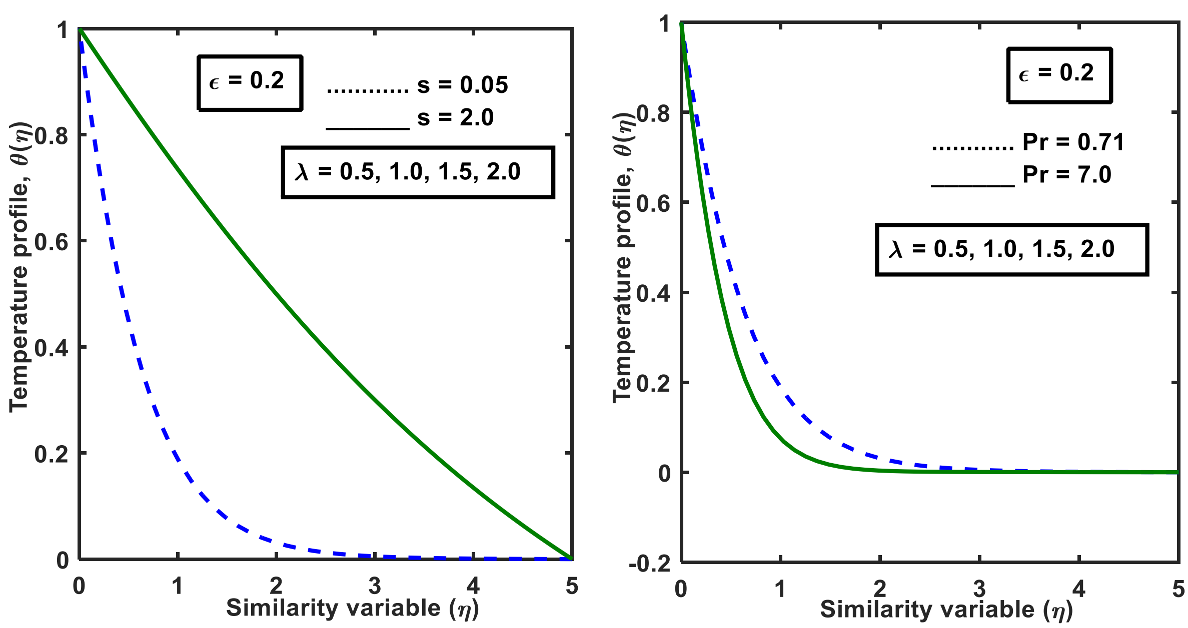

(a) (b)

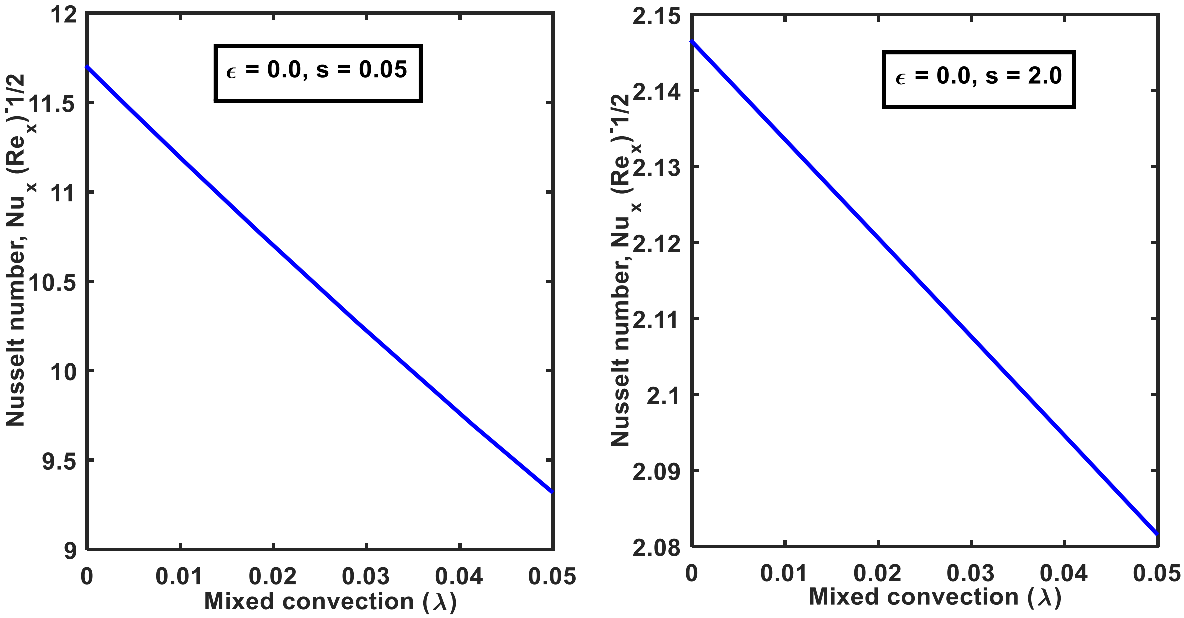

(c) (d)

Figure 5. 12 Effect of mixed convection on temperature profile when (a) $\epsilon = 0.0$, s = 0.05, 2.0 (b) $\epsilon = 0.2$, s = 0.05, Pr = 0.71, 7.0 and Nusselt number when (c) $\epsilon = 0.0$, s = 0.2 and (d) $\epsilon = 0.0$, s = 2.0

5.3.2.6 Effect of stretching ratio parameter (ϵ) on temperature profile and Nusselt number

Figures 5.13(a) – 5.13(d) display the influence of the stretching ratio parameter ($-0.5 \leq \varepsilon \leq 1.5$) on the temperature profile and Nusselt number when the surface thickness parameter s = 0.05, s = 2.0, and Pr = 0.71, Pr = 7.0 respectively. Figure 5.13 (a) displays the influence of stretching ratio parameter on viscous fluid temperature for thinner surface (s = 0.05) and thicker surface (s = 2.0) respectively. It is noticed from these figures that the variation of stretching ratio parameters has a significant effect on fluid temperature in connection with the surface thickness parameter and the Prandtl number. A lower surface thickness parameter has a lower accelerating effect. For thicker surfaces (s = 2.0) with increasing stretching ratio parameters, the accelerating effect is more prominent than for thinner surfaces (s = 0.05). Therefore, the thermal boundary layer thickness is higher due to the thicker surface when compared with the thinner surface. Hence, the temperature variation and the thickness of the thermal boundary layer expand for both of the thicker (s

= 2.0) and thinner (s = 0.05) surfaces of the bullet-shaped object whereas the Nusselt number decreases (Figures 5.13 (c) and (d)).

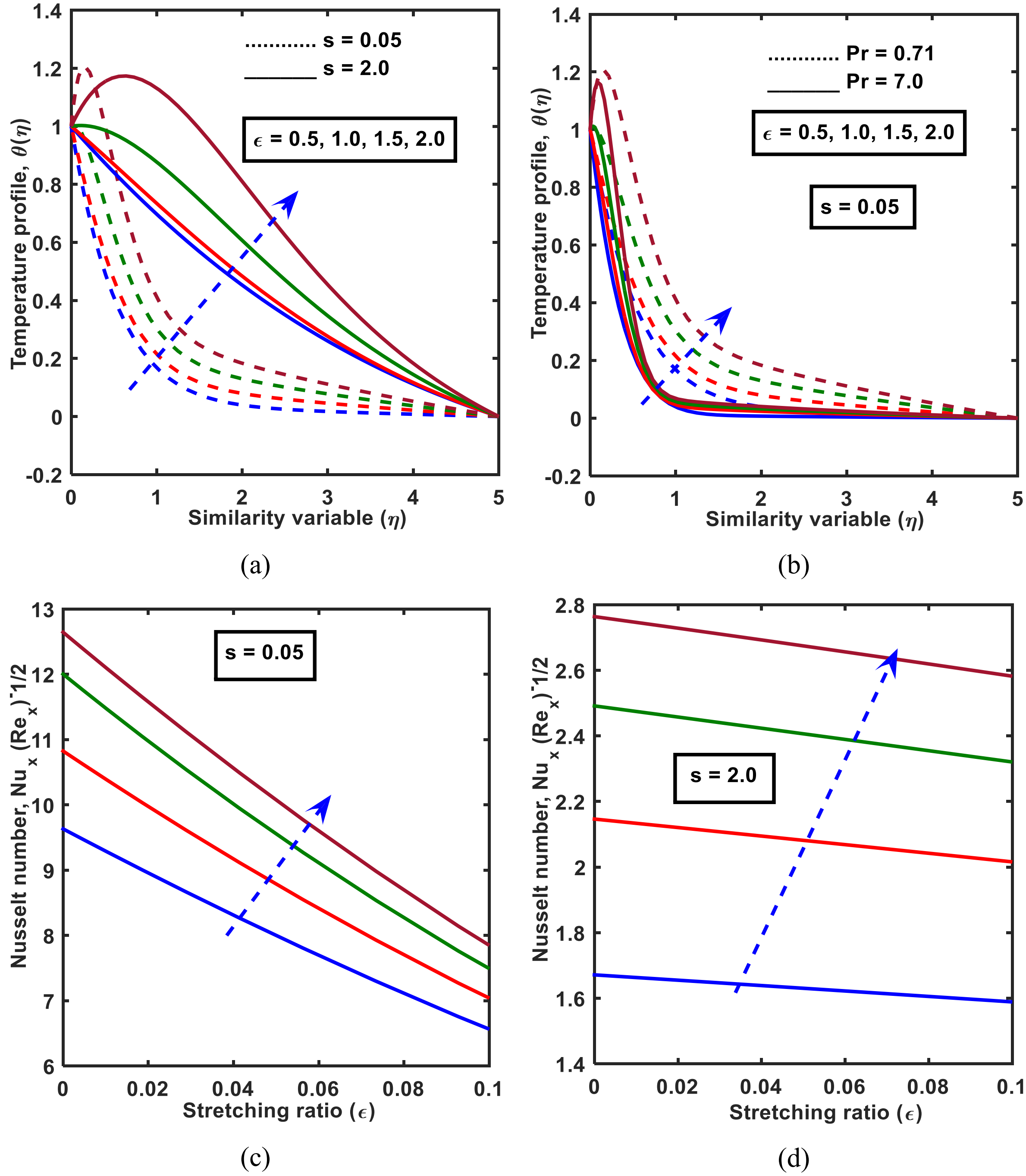

Figure 5. 13 Effect of stretching ratio (ϵ) on temperature profile when (a) ϵ = 0.2, s = 0.05, s = 2.0 (b) ϵ = 0.2, s = 0.05, Pr = 0.71, Pr = 7.0 and Nusselt number when (c) ϵ = 0.0, s = 0.05 and (d) ϵ = 0.0, s = 2.0

Figure 5.13 (b) also represents the influence of the stretching ratio parameter on viscous fluid temperature for air (Pr = 0.71) and water (Pr = 7.0) respectively. It is seen from this figure that the variation of the Prandtl number has a significant effect on viscous fluid temperature in connection with the stretching ratio parameter. For air (Pr = 0.71) with an increasing stretching ratio parameter, the accelerating effect is more prominent than for water (Pr = 7.0).

However, the temperature attains its minimum in connection with the stretching ratio parameter for a low value of $\varepsilon \leq 1.0$ but the higher value of $\varepsilon > 1$ shooting up the profiles near the surface of the bullet-shaped object within the region $\eta < 0.1$ and then the profile decreases sharply to meet the boundary condition as well for both of air (Pr = 0.71) and water (Pr = 7.0). From these figures, the temperature profile and thermal boundary layer thickness increase with the increase of stretching ratio parameter for all mentioned cases. Therefore, it is seen that for higher values of surface thickness parameter, the maximum temperature shows in the thermal boundary layer compared to that of lower surface thickness parameter. Again, in the case of air (Pr = 0.71), the highest temperature shows in the thermal boundary layer compared to that of water (Pr = 7.0). Therefore, the thermal boundary layer thickness is higher for air when compared with water. From the numerical values of the temperature gradient, it is observed that when ϵ increases from 0.0 to 0.4, there is an 8.58% increase of the Nusselt number when s = 0.2 and the corresponding increase is 15.65% when s = 2.0.

5.3.2.7 Effect of location parameter (X) on temperature profile and Nusselt number

Figures 5.14(a) – 5.14(d) depict the location parameter with η on dimensionless temperature and local Nusselt number. It is observed that an increase of location parameter leads to a decrease of the temperature profile within the boundary layer but the Nusselt number increases for both of the thinner surface (s = 0.05) and thicker surface (s = 2.0) and Pr = 0.71, Pr = 7.0 respectively. Figure 5.14 (a) displays the influence of location parameter on viscous fluid temperature for thinner surface (s = 0.05) and thicker surface (s = 2.0) respectively. It is noticed from these figures that the variation of location parameter has a significant effect on fluid temperature in connection with surface thickness parameter and the Prandtl number. A lower surface thickness parameter has a lower decelerating effect. For thicker surfaces ($s = 2.0$) with increasing location parameters, the decelerating effect is more prominent than for thinner surfaces ($s = 0.05$).

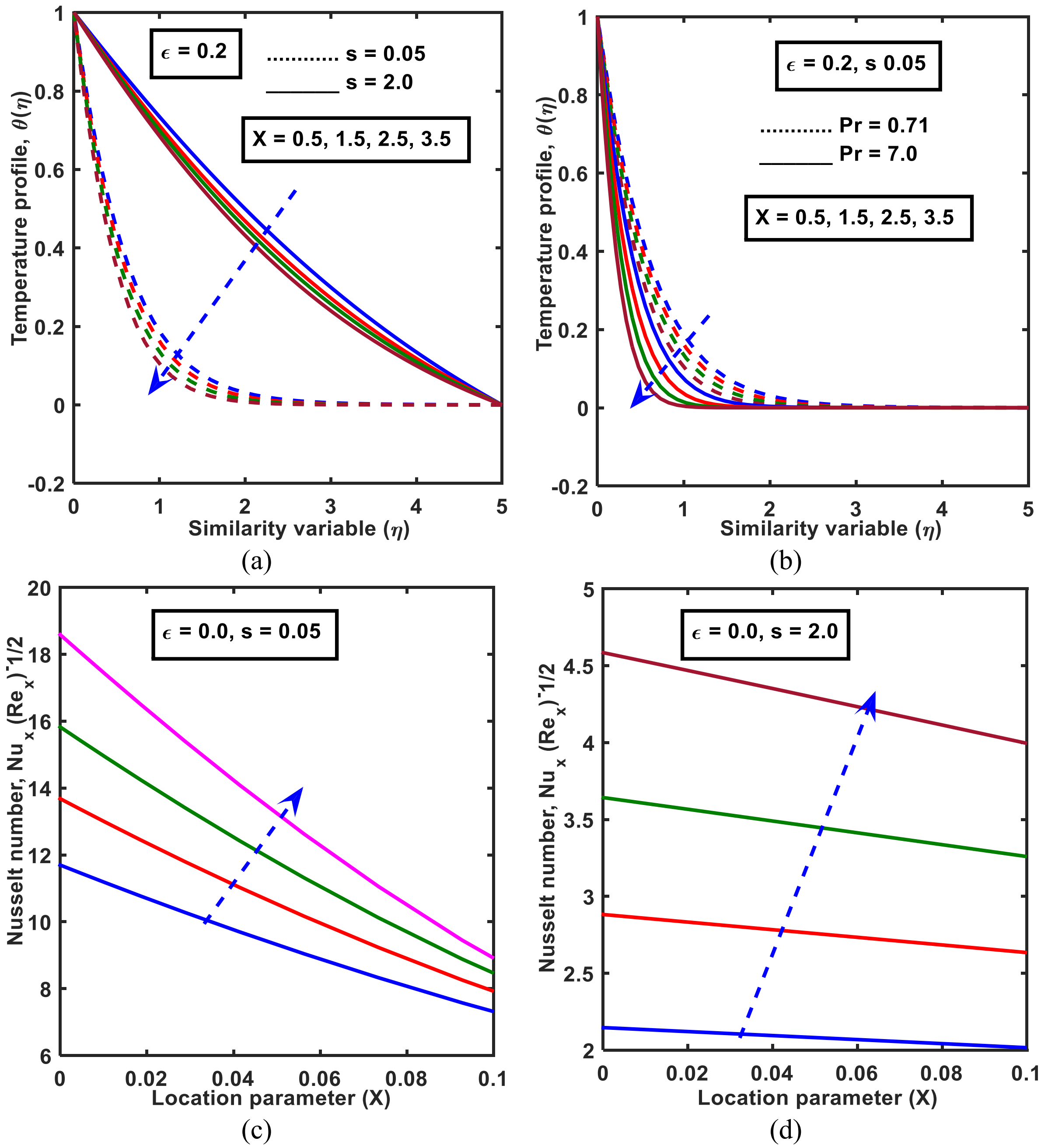

Figure 5. 14 Effect of location parameter (X) on temperature profile when (a) $\epsilon = 0.2$, s = 0.05, 2.0 (b) $\epsilon = 0.2$, s = 0.05, Pr = 0.71, Pr = 7.0 and Nusselt number when (c) $\epsilon = 0.0$, s = 0.05, and (d) $\epsilon = 0.0$, s = 2.0

Therefore, the thermal boundary layer thickness is higher due to the thicker surface when compared with the thinner surface. Hence, the temperature profile and boundary layer thickness squeeze for both of the thicker (s = 2.0) and thinner (s = 0.05) surfaces of the bullet-shaped object whereas the Nusselt number increases (Figures 5.14 (c) and (d)). Figure 5.14 (b) also represents the influence of location parameter on viscous fluid temperature for air (Pr = 0.71) and water (Pr = 7.0) respectively. It is seen from these figures that the variation of the Prandtl number has a significant effect on viscous fluid temperature in connection with the location parameter. A higher Prandtl number has a greater accelerating effect on the temperature profile. For air (Pr = 0.71) with increasing location parameters, the decelerating effect is more prominent than for water (Pr = 7.0). Therefore, the thermal boundary layer thickness is higher for air when compared with water. However, the temperature attains its minimum in connection with the location parameter and then the profile decreases sharply to meet the boundary condition as well for both air (Pr = 0.71) and water (Pr = 7.0) respectively.

From these figures, the profile of temperature and thickness of the thermal boundary layer decrease with the increase of stretching ratio parameter for all mentioned cases. Therefore, it is seen that for higher values of surface thickness parameter, the maximum temperature shows in the thermal boundary layer compared to that of lower surface thickness parameter. Again, in the case of air (Pr = 0.71), the highest temperature shows in the thermal boundary layer compared to that of water (Pr = 7). From the numerical values of the temperature gradient, it is observed that when X increases from 0.5 to 3.5, there is a 9.77% increase of the Nusselt number when s = 0.05 and the corresponding increase is 28.75% when s = 2.0.

5.3.2.8 Effect of surface thickness parameter (s) on temperature profile and Nusselt number

Figures 5.15 (a) - 5.15(d) depict the effect of the surface thickness parameter on the temperature profile and Nusselt number when the stretching ratio parameter $\varepsilon > 1.0$ or < 1 and Pr = 0.71, Pr = 7.0 respectively. Figure 5.15 (a) exhibits the influence of surface thickness parameter on viscous fluid temperature for ϵ = 0.2 and ϵ = 2.0 respectively. It is noticed from this figure that the variation of surface thickness parameter has a significant effect on fluid temperature in connection with the stretching ratio parameter and the Prandtl number. A lower stretching parameter has a lower accelerating effect. For ϵ = 2.0 with increasing surface thickness parameter, the accelerating effect is more prominent than for ϵ = 0.2. Therefore, the thermal boundary layer thickness is higher due to ϵ = 2.0 case when compared with ϵ = 0.2 case. Hence, the temperature profile and thickness of the thermal boundary layer expand for both of the ϵ = 0.2 and ϵ = 2.0 cases whereas the Nusselt number decreases (Figures 5.15 (c) and (d)). Figure 5.15 (b) also represents the influence of surface thickness parameter on viscous fluid temperature for air (Pr = 0.71) and water (Pr = 7.0) respectively. It is seen from this figure that the variation of the Prandtl number has a significant effect on viscous fluid temperature in connection with the surface thickness parameter. A higher Prandtl number has a greater accelerating effect on the temperature profile. For air (Pr = 0.71) with an increasing surface thickness parameter, the accelerating effect is more prominent than for water (Pr = 7.0). Therefore, the thermal boundary layer thickness is higher for air when compared with water. However, the temperature attains its minimum in connection with the surface thickness parameter and then the profile decreases sharply to meet the boundary condition as well for both air (Pr = 0.71) and water (Pr = 7.0). From these figures, the temperature profile and thermal boundary layer thickness increase with the increase of surface thickness parameter for all mentioned cases. Therefore, it is seen that for higher values of surface thickness parameter, the maximum temperature shows in the thermal boundary layer compared to that of lower surface thickness parameter. Again, in the case of air (Pr = 0.71), the highest temperature shows in the thermal boundary layer compared to that of water (Pr = 7.0). This is because an increase in surface thickness parameter enhances the surface area of the object which provides more resistance against the fluid motion, as a result, more fluid particles are stored within the boundary layer that causes the temperature increase. From the numerical values of the temperature gradient, it is observed that when s change from 0.2 to 0.4, there is a 595% increase of the Nusselt number when s = 0.2 and the corresponding increase is 5.2% when s = 2.0.

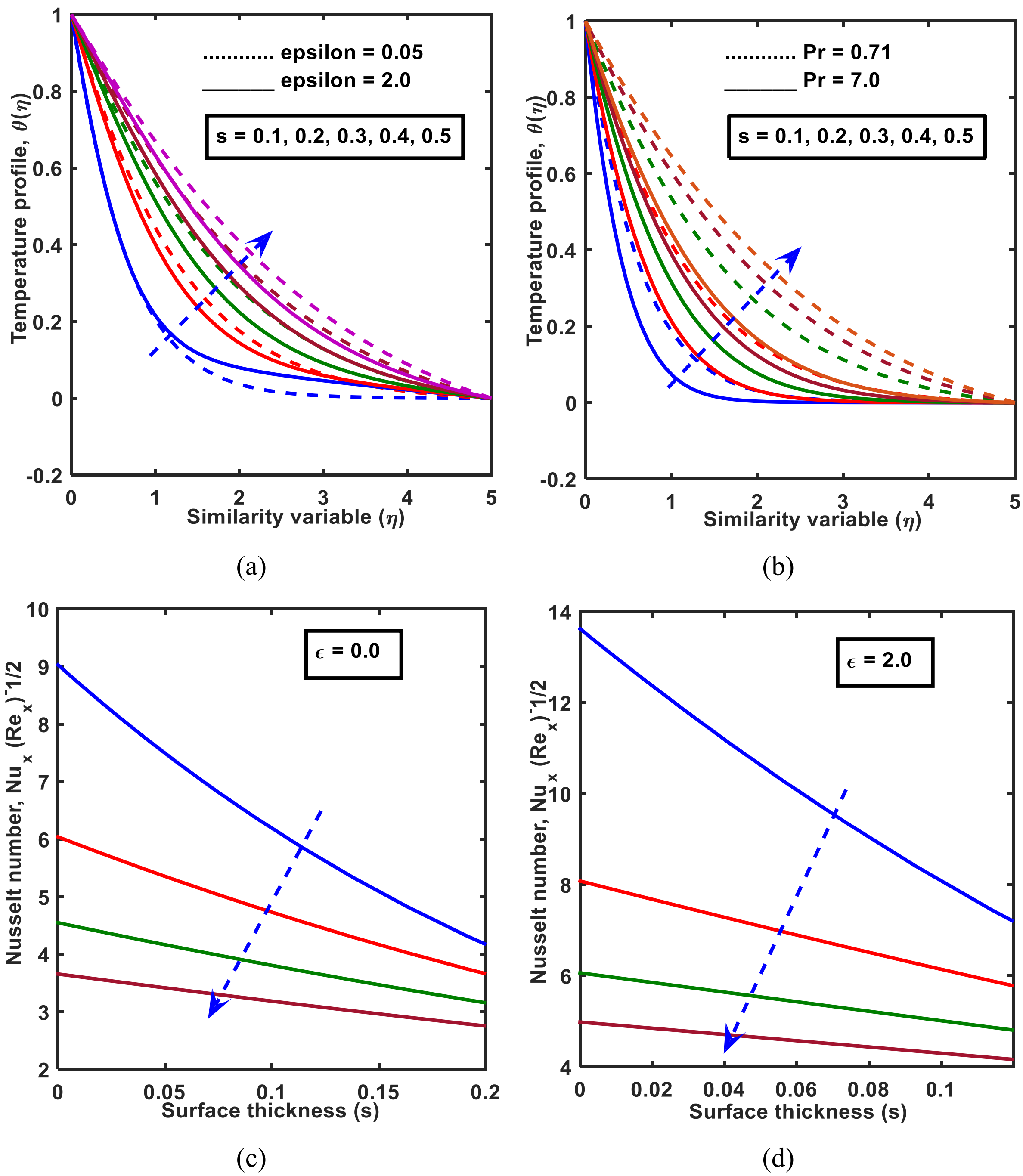

Figure 5. 15 Effect of surface thickness parameter (s) on temperature profile when (a) $\epsilon = 0.2$, $\epsilon = 2.0$ (b) $\epsilon = 0.2$, Pr = 0.71, Pr = 7.0 and Nusselt number when (c) $\epsilon = 0.0$ and (d) $\epsilon = 2.0$

The graph of temperature profile depicts that the fluid temperature within the boundary layer region is getting lower due to Prandtl number (Pr), stretching ratio parameter (ϵ), location parameter (X), and mixed convection parameter (λ) whereas surface thickness parameter (s), magnetic parameter (M), heat generation parameter (Q^*) and Eckert number (Ec) have a reverse effect on it throughout the boundary layer region. From these figures, it is revealed that in the case of a thicker bullet-shaped object (s = 2.0) the temperature profile does not approach the ambient condition asymptotically but intersects the axis with a steep angle and the thermal boundary layer structure has no definite shape whereas in the case of a thinner bullet-shaped object (s = 0.05) the temperature profile converge the ambient condition asymptotically and the boundary layer structure has a definite shape. It is also observed that the thinner bullet-shaped object represents a thinner thermal boundary layer because the heat transfer rate is higher than the thicker bullet-shaped object in both static and moving bullet-shaped objects.

Figure 5.16 denotes the convergence criteria and accuracy of the present numerical method.

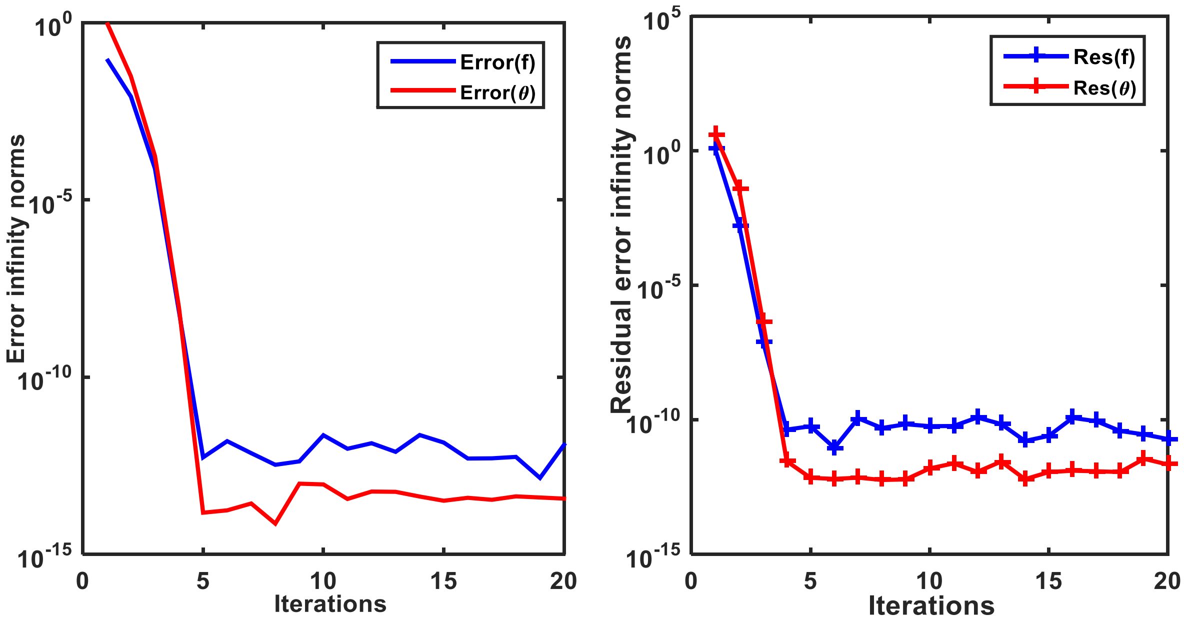

(a) (b)

Figure 5. 16 (a) Error infinity norms and (b) Residual error infinity norms for $f(\eta)$ and $\theta(\eta)$

This implies that the error infinity norm decrease with an increase in the number of iterations and the method converges after only six iterations. Also, the residual error infinity norms decrease against the number of iterations which confirms the accuracy of the numerical method. Therefore, the numerical method (SQLM) achieves an accuracy of 10^{-13} after only five iterations which means the method is highly accurate.

Table 5. 2 Variation in Nusselt number which is directly proportional to the temperature gradient for different values of *M, X,* Pr, *Q*, Ec, λ,* and *s* with ϵ = 0.0, ϵ = 2.0 and *s* = 0.2

M	X	Pr	Q^*	Ec	λ	s	$\lvert -\theta'(0) \rvert$ ϵ = 0.0, s = 0.2	$\lvert -\theta'(0) \rvert$ ϵ = 2.0, s = 0.2
1.0	0.5	0.71	0.5	0.2	0.5	0.2	**4.1743**	**2.9254**
5.0	0.5	0.71	0.5	0.2	0.5	0.2	**3.6699**	**- 4.1791**
10.0	0.5	0.71	0.5	0.2	0.5	0.2	**3.2087**	**- 13.1528**
1.0	**0.5**	0.71	0.5	0.2	0.5	0.2	**4.1743**	**2.9254**
1.0	**1.5**	0.71	0.5	0.2	0.5	0.2	**4.5471**	**4.8975**
1.0	**2.5**	0.71	0.5	0.2	0.5	0.2	**4.9131**	**5.7091**
1.0	0.5	**0.71**	0.5	0.2	0.5	0.2	**4.1743**	**2.9254**
1.0	0.5	**1.0**	0.5	0.2	0.5	0.2	**4.3618**	**3.6715**
1.0	0.5	**7.0**	0.5	0.2	0.5	0.2	**7.4634**	**9.1876**
1.0	0.5	0.71	**0.5**	0.2	0.5	0.2	**4.1743**	**2.9254**
1.0	0.5	0.71	**1.5**	0.2	0.5	0.2	**3.9126**	**2.5471**
1.0	0.5	0.71	**2.5**	0.2	0.5	0.2	**3.7716**	**2.3411**
1.0	0.5	0.71	0.5	**0.2**	0.5	0.2	**4.1743**	**2.9254**
1.0	0.5	0.71	0.5	**0.4**	0.5	0.2	**2.9006**	**0.5816**
1.0	0.5	0.71	0.5	**0.6**	0.5	0.2	**1.6356**	**- 4.1579**
1.0	0.5	0.71	0.5	0.2	**0.5**	0.2	**4.1743**	**2.9254**
1.0	0.5	0.71	0.5	0.2	**1.5**	0.2	**4.2678**	**2.8158**
1.0	0.5	0.71	0.5	0.2	**2.5**	0.2	**4.3544**	**2.7025**
1.0	0.5	0.71	0.5	0.2	0.5	**0.1**	**8.1784**	**5.4341**
1.0	0.5	0.71	0.5	0.2	0.5	**0.2**	**4.1743**	**2.9254**
1.0	0.5	0.71	0.5	0.2	0.5	**0.3**	**2.8365**	**2.0792**

Table 5.2 depicts the influence of magnetic parameter (M), location parameter (X), Prandtl number (Pr), heat generation parameter (Q^*), Eckert number (Ec), mixed convection parameter (λ), and surface thickness parameter (s) on the Nusselt number when ϵ = 0.0, ϵ

= 2.0 and s = 0.2, respectively. It is observed that location parameter, Prandtl number, and mixed convection parameter (λ) enhance the Nusselt number whereas magnetic parameter, heat generation parameter, Eckert number, and surface thickness parameter reduces the Nusselt number for both of the static and moving bullet-shaped objects. Therefore, the heat transfer rate is high in the static (ϵ = 0.0) case, when compared with the moving (ϵ = 2.0) case. At this point, it is highlighted that for enhancing the heat transfer rate we have to consider the non-stretching (ϵ = 0.0) bullet-shaped object.

5.4 Correlation Analysis for Velocity Gradient

The correlation coefficient and multiple regression model have been established for the thinner bullet-shaped object (s = 0.05) and $\epsilon < 1$. Therefore, from Table 5.3 it is observed that the skin friction which is equivalent to velocity gradient is positively correlated with magnetic parameter (M), and location parameter (X) but negatively correlated with mixed convection parameter (λ) and surface thickness parameter (s). Again, Prandtl number (Pr), heat generation parameter (Q^*), and Eckert number (Ec) do not correlate with velocity gradient. A positive correlation indicates that higher values of one variable tend to be related to higher values for the other variable. A negative correlation indicates that higher values for one variable tend to be related to lower values for the other variable.

Table 5. 3 Correlation coefficient between the velocity gradient and controlling parameters by taking 2nd order coefficient

	M	X	Q^*	Ec	λ	s	$f''(\eta)$
M	1.00						
X	-0.30	1.00					
Q^*	-0.10	-0.04	1.00				
Ec	-0.10	-0.04	-0.10	1.00			
λ	-0.10	-0.04	-0.10	-0.10	1.00		
s	-0.10	-0.04	-0.10	-0.10	-0.10	1.00	
$f''(\eta)$	**0.48**	0.19	0.0	0.0	**-0.46**	**-0.36**	1.00

5.5 Correlation Analysis for Temperature Gradient

The correlation coefficient and multiple regression model have been established by considering the thinner bullet-shaped object (s = 0.05) and $\varepsilon < 1$. Therefore, from Table

5.4 it is observed that the temperature gradient, $\theta'(\eta)$ are positively correlated with Prandtl number (Pr), location parameter (X), and mixed convection parameter (λ), but negatively correlated with magnetic parameter (M), surface thickness parameter (s), heat generation parameter ($Q*$), and Eckert number (Ec). A positive correlation indicates that higher values of one parameter tend to be related to higher values for the other parameter. A negative correlation indicates that higher values for one parameter tend to be related to lower values for the other parameter.

Table 5. 4 Correlation coefficient between the temperature gradient and controlling parameters by taking 1st order coefficient

	M	X	Pr	$Q*$	Ec	λ	s	$\theta'(\eta)$
M	1.00							
X	-0.30	1.00						
Pr	0.10	0.04	1.00					
$Q*$	-0.10	-0.04	0.10	1.00				
Ec	-0.10	-0.04	0.10	-0.10	1.00			
λ	-0.10	-0.04	0.10	-0.10	-0.10	1.00		
s	-0.10	-0.04	0.10	-0.10	-0.10	-0.10	1.00	
$\theta'(\eta)$	-0.14	**0.61**	0.28	-0.27	-0.23	0.13	**-0.66**	1.00

CHAPTER SIX

UNSTEADY MHD MIXED CONVECTION BOUNDARY LAYER FLOW AND HEAT TRANSFER OVER AN EXPONENTIALLY STRETCHING BULLET-SHAPED OBJECT IN POROUS MEDIA WITH HEAT GENERATION AND VISCOUS DISSIPATION

The present chapter deals with the unsteady mixed convection magnetohydrodynamic boundary layer flow and heat transfer over an exponentially stretching permeable bullet-shaped object. The porous medium consists of pores, cavities, and void spaces. The flow-through porous medium was described by Henry Darcy in Darcy law as the velocity is linearly proportional to the pressure gradient. It is valid only for low velocity and small porosity. The Darcy law is not applicable in the case of high velocities and nonlinear porosity. Therefore, to explain the high velocity of the flow and nonlinear porosity are used non-Darcy or inertial effects. Therefore, it is necessary to incorporate the non-Darcian terms in the study of convective transport in a porous medium. The Industrial sectors and the environmental setups involve with the heat and a mass flux such as geological setups, chemical reactions, and other heating systems are the main focus in convection through the porous medium. The porosity factor is involved in such systems which induce the incremental inertial influence that results in the variation of skin friction. These types of formulations help build heat insulation mechanisms, energy storage systems, fossil fuel beds, disposal reactors for nuclear wastes, and many more. This concept was first introduced by Darcy and the law which is known as Darcy’s law. This law is valid for a restricted range of velocity. In the case of porous media, it does not possible to ignore the high effects of inertial force and resistance given by the porosity term. Thus, a velocity squared term is added in the momentum equation to analyze the inertial influences which are known as the Forchheimer drag parameter or inertia term. The heat transfer through exponentially stretching sheet has many applications in science and technology such as annealing and thinning of copper wires and many more. The present chapter aims to explore the study of unsteady MHD mixed convection flow over an exponentially stretching bullet-shaped object in presence of viscous dissipation, heat generation, and Darcy Forchheimer's porous medium. So, this chapter performs the velocity and temperature distributions, local skin friction coefficient, and local Nusselt number by considering two distinct cases of thinner surface and thicker surface.

6.1 Mathematical Formulation and Analysis of the Present Problem

Let us assume that the unsteady two-dimensional mixed convection MHD axisymmetric boundary layer flow with heat transfer over an exponentially stretching bullet-shaped object (Figure 2.2 in chapter two). For developing the mathematical model of the present problem the detailed assumptions have been discussed in chapter three.

Therefore, the governing PDEs are as follows [78]

Equation of continuity:

$$\frac{\partial}{\partial x}(ru)+\frac{\partial}{\partial y}(rv)=0 \tag{6.1.1}$$

Momentum equation:

$$\frac{\partial u}{\partial t}+u\frac{\partial u}{\partial x}+v\frac{\partial u}{\partial r}=\frac{\partial T}{\partial t}+U\frac{\partial U}{\partial x}+\frac{\nu}{r}\left(\frac{\partial u}{\partial r}+r\frac{\partial^2 u}{\partial r^2}\right)+\left(\frac{\sigma B_0{}^2}{\rho}+\frac{\nu}{K}\right)(U-u)+ g\beta\left(T-T_\infty\right)-C_1u^2 \tag{6.1.2}$$

Energy equation:

$$\frac{\partial T}{\partial t}+u\frac{\partial T}{\partial x}+v\frac{\partial T}{\partial r}=\frac{\alpha}{r}\left(\frac{\partial T}{\partial r}+r\frac{\partial^2 T}{\partial r^2}\right)+\frac{Q}{\rho C_p}\left(T-T_\infty\right)+\frac{\nu}{C_p}\left(\frac{\partial u}{\partial r}\right)^2+\frac{\sigma B_0{}^2u^2}{\rho C_p} \tag{6.1.3}$$

The fluid and the surface are at rest when t = 0. Therefore, the no-slip boundary conditions at the surface of the body for the above problem (t > 0) are

$$\begin{aligned} &u=U_w(x,t),\ v=-v_w(x),\ T=T_w(x,t)\ at\ \ r=R(x)\\ &u\to U_\infty(x,t), T\to T_\infty, as\ \ r\to\infty \end{aligned} \tag{6.1.4}$$

Here $U_w(x,t)=\dfrac{ae^{\frac{x}{L}}}{1+dt}$ is the stretching velocity, $U_\infty(x,t)=\dfrac{be^{\frac{x}{L}}}{1+dt}$ is the free stream velocity, $v_w=-\sqrt{\dfrac{\nu U_w}{x}}f_w$ is a special class of velocity which $v_w(x)>0$ represents suction and $v_w(x)<0$ represents blowing, $B(x)=B_0e^{\frac{x}{2L}}$ is the magnetic field which is applied normal to the flow direction, and $T_w(x,t)=T_\infty+\dfrac{e^{\frac{x}{2L}}}{1+dt}$ is the surface temperature of the bullet-shaped object, a, b, and d is constants with dt > 0, and both a, b, and d have dimension time^{-1}, v_w is the suction/injection parameter.

To obtain the similarity solutions for the system of equation (6.1.1) – equation (6.1.3) subject to the boundary conditions (6.1.4), we use the following axisymmetric similarity transformation:

$$\eta=\frac{ar^2e^{\frac{x}{2L}}}{2\nu L(1+dt)},\ \psi=\frac{\nu Le^{\frac{x}{2L}}f(\eta)}{(1+dt)},T=T_\infty+\frac{e^{\frac{x}{2L}}}{(1+dt)}\theta(\eta),\theta(\eta)=\frac{T-T_\infty}{T_w-T_\infty} \tag{6.1.5}$$

where ψ is the stream function and is denoted by the horizontal and vertical velocity components are $u=\dfrac{1}{r}\dfrac{\partial\psi}{\partial r}$ and $v=-\dfrac{1}{r}\dfrac{\partial\psi}{\partial x}$, η is the similarity variable. The expression η represents the shape and size of the bullet-shaped object, if we take η = s in the expression $\eta=\dfrac{ar^2e^{\frac{x}{2L}}}{2\nu L(1-dt)}$, then the dimensionless radius is $R(x)=\sqrt{\dfrac{2\nu Ls(1-dt)e^{\frac{x}{2L}}}{a}}$. The continuity equation (6.1.1) is satisfied by the similarity transformation (6.1.5) and after applying the similarity transformations then the equations (6.1.2) and (6.1.3) are transformed as

$$\begin{aligned}&\eta f'''(\eta)+e^{\frac{X}{2}}\left[f(\eta)f''(\eta)-\gamma f'^2(\eta)+\varepsilon^2-f'^2(\eta)\right]+e^{\frac{-3X}{2}}\lambda\theta(\eta)\\&+f''(\eta)+e^{\frac{-X}{2}}\left[(M+Da)(\varepsilon-f'(\eta))-A\left(\varepsilon+f'(\eta)+\eta f''(\eta)\right)\right]=0\end{aligned} \tag{6.1.6}$$

$$\theta''(\eta)+\frac{1}{2}\theta'(\eta)+e^{\frac{X}{2}}\Pr\left[f(\eta)\ \theta'(\eta)-\ \frac{1}{2}f'(\eta)\ \theta(\eta)+MEcf'^2(\eta)e^{-X}\right]$$
$$+2\eta Ecf''^2(\eta)+\Pr\left[e^{-2X}Q^*\theta(\eta)+Ae^{\frac{X}{2}}\{\theta(\eta)+\eta\theta'(\eta)\}\right]=0 \tag{6.1.7}$$

Where prime denotes differentiation concerning η, $f_w = -v_0\left(\frac{\mu a}{2\rho L}\right)^{\frac{-1}{2}}$ is the suction /blowing velocity such that $f_w > 0$ indicates suction and $f_w < 0$ indicates blowing at the surface.

The dimensionless parameters are defined as

$$M=\frac{\sigma B_0^2 L}{\rho a},\lambda=\frac{Gr}{Re_x^2},\varepsilon=\frac{b}{a},\ \Pr=\frac{\nu}{\alpha},\ Ec=\frac{U_w^2}{C_p(T_w-T_\infty)},X=\frac{x}{L},A=\frac{d}{a},$$
$$Gr=\frac{g\beta(T_w-T_\infty)L^3}{\nu^2},Re_x=\frac{U_wL}{\nu},Q^*=\frac{QL(T_w-T_\infty)}{\rho ac_p},Da=\frac{Ka}{\nu L},\gamma=\frac{C_1L}{a}$$

The transformed boundary conditions for t > 0 are obtained as:

$$f(\eta)=f_w,\ f'(\eta)=1,\theta(\eta)=1,\ at\ \eta=0$$
$$f'(\eta)\to\varepsilon,\theta(\eta)\to 0\ \ as\ \eta\to\infty \tag{6.1.8}$$

Here, $\epsilon = 0$ is for the static bullet-shaped object, $\varepsilon < 1$ represents the free stream velocity is less than the object velocity, $\varepsilon > 1$ means the object velocity is greater than the free stream velocity, and $\epsilon = 1$ depicts the equal velocities of the bullet-shaped object and the free stream.

The skin friction coefficient and the local Nusselt number

The skin friction and the local Nusselt number have been discussed in section 5.1 (Chapter five).

6.2 Numerical Procedure

The system of equations (6.1.6) and (6.1.7) are converted into the following iterative sequence of linear differential equations after applying the SQLM [83].

$$a_{0,r}\frac{\partial^3 f_{r+1}}{\partial\eta^3}+a_{1,r}\frac{\partial^2 f_{r+1}}{\partial\eta^2}+a_{2,r}\frac{\partial f_{r+1}}{\partial\eta}+a_{3,r}f_{r+1}+a_{4,r}\theta_{r+1}=R_{1,r} \tag{6.1.9}$$

$$b_{0,r}\frac{\partial^2\theta_{r+1}}{\partial\eta^2}+b_{1,r}\frac{\partial\theta_{r+1}}{\partial\eta}+b_{2,r}\theta_{r+1}+b_{3,r}\frac{\partial^2 f_{r+1}}{\partial\eta^2}+b_{4,r}\frac{\partial f_{r+1}}{\partial\eta}+b_{5,r}f_{r+1}=R_{2,r} \tag{6.1.10}$$

The variable coefficients obtained from the previous iteration are given by

$$\begin{aligned}
&a_{0,r}=\eta, a_{1,r}=1+e^{\frac{X}{2}}f_r-A\eta e^{\frac{-X}{2}}, a_{2,r}=-2e^{\frac{X}{2}}f_r'-\left(M+Da\right)e^{\frac{-X}{2}}-Ae^{\frac{-X}{2}}, a_{3,r}=e^{\frac{X}{2}}f_r'',\\
&b_{0,r}=\eta, b_{1,r}=\frac{1}{2}+\Pr e^{\frac{X}{2}}f_r+A\Pr\eta e^{\frac{X}{2}}, b_{2,r}=-\frac{1}{2}\Pr e^{\frac{X}{2}}f_r'+\Pr Q^*e^{-2X}+A\Pr e^{\frac{X}{2}},\\
&a_{4,r}=e^{\frac{-3X}{2}}\lambda, b_{3,r}=4\eta\Pr Ecf_r'', b_{4,r}=-\frac{1}{2}\Pr e^{\frac{X}{2}}\theta_r+2MEce^{\frac{-3X}{2}}f', b_{5,r}=\Pr e^{\frac{X}{2}}\theta_r'
\end{aligned}$$

The terms on the right are defined as follows

$$\begin{aligned}
R_{1,r}\left(\eta\right)&=a_{0,r}f_r'''+a_{1,r}f_r''+a_{2,r}f_r'+a_{3,r}f_r+a_{4,r}\theta_r-F\left[\eta,f,f',f''......f^n\right]\\
&=e^{\frac{X}{2}}f_rf_r''-e^{\frac{X}{2}}f_r'^2-\gamma e^{\frac{X}{2}}f_r''^2-\varepsilon^2e^{\frac{X}{2}}-\left(M+Da\right)\varepsilon e^{\frac{-X}{2}}+A\varepsilon e^{\frac{-X}{2}}
\end{aligned}$$

$$\begin{aligned}
R_{2,r}\left(\eta\right)&=b_{0,r}\theta_r''+b_{1,r}\theta_r'+b_{2,r}\theta_r+b_{3,r}f_r''+b_{4,r}f_r'+b_{5,r}f_r-F\left[\eta,f,f',f''......f^n\right]\\
&=e^{\frac{X}{2}}\Pr f_r\theta_r'-\frac{1}{2}\Pr e^{\frac{X}{2}}f_r'\theta_r+Je^{\frac{-3X}{2}}\Pr f_r'+2\eta Ecf_r''^2
\end{aligned}$$

Evaluating Equations (6.1.9) and (6.1.10) at the collocation points and approximating derivatives with Chebyshev derivatives which provide in a vector-matrix form such as

$$\begin{bmatrix}A_{11} & A_{12}\\ A_{21} & A_{22}\end{bmatrix}\begin{bmatrix}F_{r+1}\\ \theta_{r+1}\end{bmatrix}=\begin{bmatrix}R_{1,r}\\ R_{2,r}\end{bmatrix}, \text{ here } \begin{aligned}&A_{11}=a_{0,r}D^3+a_{1,r}D^2+a_{2,r}D+a_{3,r}, A_{12}=a_{4,r},\\ &A_{2,1}=b_{3,r}D^2+b_{4,r}D+b_{5,r}, A_{2,2}=b_{0,r}D^2+b_{1,r}D+b_{2,r}\end{aligned}$$

The transformed boundary conditions

$$\begin{aligned}
&f_{r+1}\left(\eta_0\right)=f_w, f_{r+1}'\left(\eta_0\right)=1, \theta_{r+1}\left(\eta_0\right)=1, \mathrm{R_r}\left(\eta_N\right)=1 \text{ at } \eta=0\\
&f_{r+1}\left(\eta_N\right)=f_w, f_{r+1}'\left(\eta_N\right)=\varepsilon, \theta_{r+1}\left(\eta_N\right)=0, \mathrm{R_r}\left(\eta_{N+1}\right)=\varepsilon \text{ as } \eta\to\infty
\end{aligned}$$

6.3 Results and discussion

The results have been discussed for both the cases of thinner (s = 0.05) and thicker (s = 2.0) bullet-shaped objects and also three values of stretching ratio parameter (ϵ = 0.0, 1.0 2.0). It is mentioned that a fixed object in a moving fluid represents when ϵ = 0.0, and while a moving object in a fixed fluid represents when ϵ = 0.2. On the other hand, ϵ = 1.0 represents equal velocities of the bullet-shaped object and free stream fluid. Numerical simulations are carried out for different values of the magnetic parameter (M) ranging from 0.5 to 15.5, Eckert number (Ec) in the range 0.2 to 0.8, heat generation parameter (Q^*) ranging from 0.2 to 0.8, mixed convection parameter (λ) in the range 0.1 to 3.0, Darcy number (Da) ranging from 5.0 to 20.0, drag coefficient (γ) in the range 0.1 to 3.0, stream-wise coordinate (X) ranging from 0.5 to 3.5, two values of the surface thickness parameter (s = 0.05 and 2.0), unsteady parameter (A) in the range 0.5 to 4.5, and suction/injection parameter (f_w) ranging from -1.0 to 1.0 respectively. The velocity and temperature distributions, skin friction coefficient, and Nusselt number have been discussed in the following sub-sections. The non-linear ODEs of the present problem are solved by applying SQLM. The convergence criteria of the solution are performed by the use of solution-based errors. The impact of physical parameters on velocity, temperature, skin friction, and the local Nusselt number is shown graphically. In this chapter, the default parameters have been taken as

$$\Pr\left(0.71 \le \Pr \le 10.0\right), M\left(0.5 \le M \le 15.5\right), Q^*\left(0.2 \le Q^* \le 3.5\right), Ec\left(0.2 \le Ec \le 0.8\right),$$
$$X\left(0.5 \le X \le 4.5\right), A\left(0.2 \le A \le 6.0\right), Da\left(5.0 \le Da \le 20.0\right), \varepsilon\left(0.0 \le \varepsilon \le 2.0\right),$$
$$\gamma\left(0.1 \le \gamma \le 3.0\right), s\left(0.1 \le s \le 0.9\right), f_w\left(-1.0 \le f_w \le 1.0\right), \lambda\left(0.1 \le \lambda \le 3.0\right).$$

The numerical values of skin friction and Nusselt number which are equivalent to velocity gradient and rate of heat transfer have been shown in Table 6.1 and Table 6.2 respectively. These errors are defined by the differences between approximate solutions at the previous and current iteration levels t and t + 1, respectively. The error norms have been defined in chapter three.

The infinity norms of the residual errors are defined as

$$\left\|\mathrm{Re}\,s\left(f\right)\right\|_{\infty} = \left\| \begin{matrix} \eta f'''\left(\eta\right) + e^{\frac{X}{2}}\left[f\left(\eta\right) f''\left(\eta\right) - \gamma f'^{2}\left(\eta\right) + \varepsilon^{2} - f'^{2}\left(\eta\right)\right] + e^{\frac{-3X}{2}} \lambda \theta\left(\eta\right) \\ + f''\left(\eta\right) + e^{\frac{-X}{2}}\left[\left(M + Da\right)\left(\varepsilon - f'\left(\eta\right)\right) - A\left(\varepsilon + f'\left(\eta\right) + \eta f''\left(\eta\right)\right)\right] \end{matrix} \right\| = 0$$

$$\left\|\mathrm{Re}\,s\left(\theta\right)\right\|_{\infty} = \left\| \begin{matrix} \eta\theta''\left(\eta\right) + \frac{1}{2}\theta'\left(\eta\right) + e^{\frac{X}{2}} \Pr\left[f\left(\eta\right)\ \theta'\left(\eta\right) - \frac{1}{2} f'\left(\eta\right)\ \theta\left(\eta\right) + MEcf'^{2}\left(\eta\right) e^{-X} \right] \\ + 2\eta Ecf''^{2}\left(\eta\right) + \Pr\left[e^{-2X} Q^{*}\theta\left(\eta\right) + Ae^{\frac{X}{2}}\left\{\theta\left(\eta\right) + \eta\theta'\left(\eta\right)\right\} \right] \end{matrix} \right\| = 0$$

The computations have been done by taking N = 60 collocation points and solution-based errors are defined for the convergence of the numerical method. So, Figures 6.1 (a) and 6.1 (b) are show the convergence and accuracy of the present problem.

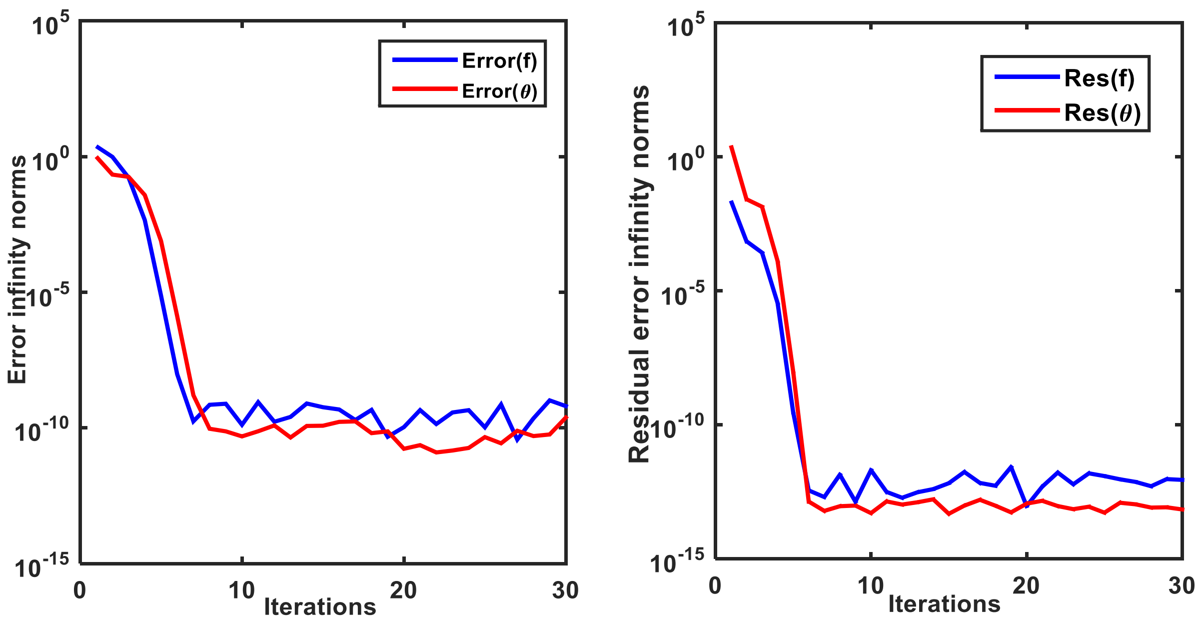

(a) (b)

Figure 6. 1 (a) Error infinity norms, and (b) Residual error infinity norms for $f\left(\eta\right)$ and $\theta\left(\eta\right)$

Figure 6.1 (a) represents the infinity norms with iterations. The error infinity norm decreases with the increasing number of iterations that confirms the convergence of the present method. So, the present method converges after five iterations. Figure 6.1 (b) represents the residual error norms of less than 10^{-14} for $f\left(\eta\right)$ and $\theta\left(\eta\right)$ against after five iterations. It is seen that the residual error decreases with increasing the iterations. This proves the validity of the present method. Also, the residual error infinity norms decrease against the number of iterations which confirms the accuracy of the numerical method. Therefore, the numerical method (SQLM) achieves an accuracy of 10^{-11} after only five iterations and orders 10^{-14} after the fourth iterations which means the method is highly accurate.

6.3.1 Velocity profiles and skin friction coefficient with parameter variations

6.3.1.1 Effect of the magnetic parameter (*M*) on the velocity profile and skin friction coefficient

Figures 6.2(a) - 6.2(d) show the effects of the magnetic parameter on the velocity field and local skin friction coefficient when other parameters are fixed for both the cases of thinner ($s = 0.05$) and thicker ($s = 2.0$) bullet-shaped objects. It is clear that the velocity profile, skin friction coefficient, and boundary layer thickness increases in the case of $\epsilon > 1$ for raising the effect of magnetic parameter due to both thinner and thicker bullet-shaped object whereas, the reverse results arise in the case of $\epsilon < 1$. From these figures, it is also observed that when the term $\epsilon > 1$, the flow has a certain structure and form a definite boundary layer pattern but the term $\epsilon < 1$, the boundary layer flow has an inverse pattern and it becomes a reverse boundary layer. This is expected as the application of the transverse magnetic field always results in a resistance-type force called Lorentz force. This force is similar to a drag force, and increasing M means the drag force increases that tend to resist the fluid flow, thus reducing the fluid motion significantly but opposite results arise when $\epsilon > 1$ because the free stream velocity dominates on surface velocity. Therefore, for controlling the flow of fluid during physical problems then one can regulate the intensity of the external magnetic field to obtain the desired flow rate. That is magnetic parameter is inversely proportional to velocity profiles and skin friction coefficient in case of $\epsilon < 1$ but opposite trends arise in case of $\epsilon > 1$. From equation (5.1.9) it is seen that the skin friction coefficient is directly proportional to the dimensionless velocity gradient.

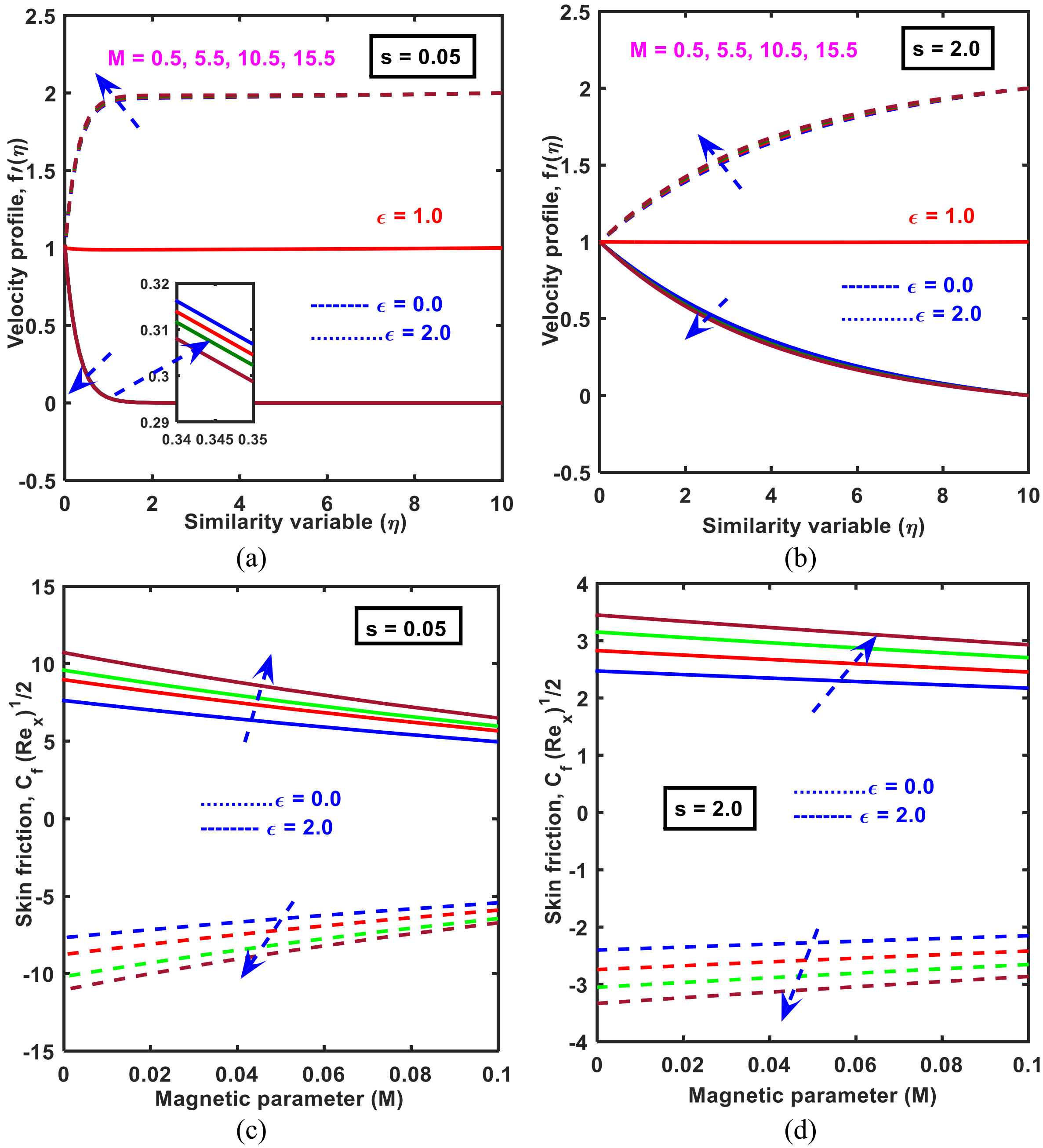

Figure 6. 2 Effects of magnetic parameter on velocity profile, and skin friction coefficient when (a) $\epsilon = 0.0, 1.0, 2.0, s = 0.05$ (b) $\epsilon = 0.0, 1.0, 2.0, s = 2.05$ (c) $\epsilon = 0.0, 2.0, s = 0.05$, and (d) $\epsilon = 0.0, 2.0, s = 2.0$

Therefore, the velocity gradient at the surface is positive when $\epsilon > 1.0$ and negative due to $\epsilon < 1.0$ for all values of the controlling parameters. Therefore, when M changes from 1.0 to 15.0, there is a 35.2% increase of the skin friction coefficient and the corresponding increase is 186.3% when $s = 0.2$ and $s = 2.0$ respectively.

6.3.1.2 Effect of Eckert number (*Ec*) on the velocity profile and skin friction coefficient

Figures 6.3(a) - 6.3(d) describe the effect of the Eckert number (*Ec*) on the velocity profile and local skin friction coefficient for the case of thinner surface (s = 0.05) and thicker surface (s = 2.0). It is seen from these figures that the velocity profile and boundary layer thickness decrease slightly but skin friction increase monotonically with an increase of Eckert number in the case of $\epsilon > 2.0$ and s = 0.05, respectively. That is Eckert's number is inversely proportional to the velocity profile and boundary layer thickness but directly proportional to skin friction coefficient for both thinner and thicker surfaces. The positive Eckert number implies cooling of the surface i.e., loss of heat from the surface to the fluid. Hence, greater viscous dissipative heat causes a rise in the temperature as well as the velocity. From the numerical values, it is noticed that when *Ec* increases from 0.2 to 0.8 then the skin friction coefficient increases 0.9 % in the case of thinner surface (s = 0.5) and ϵ = 2.0, respectively.

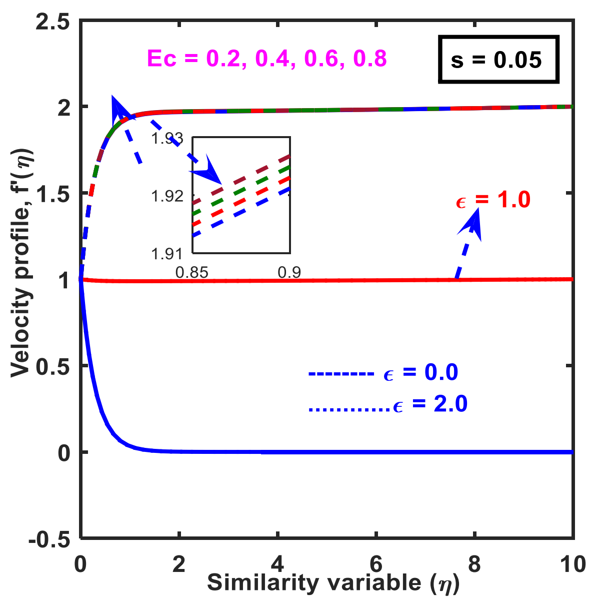

(a)

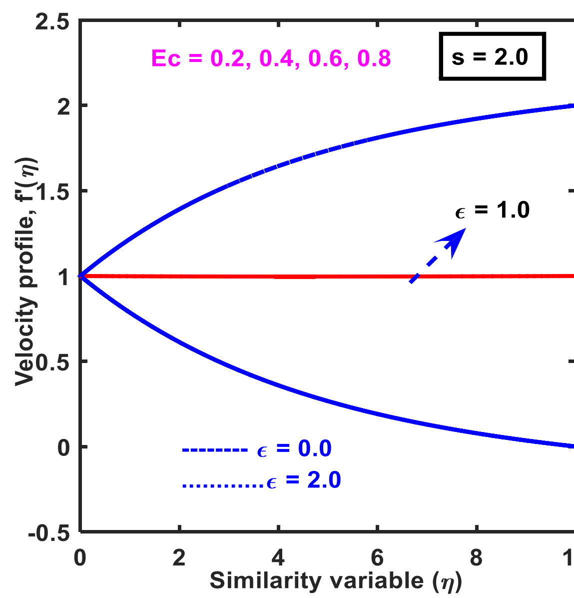

(b)

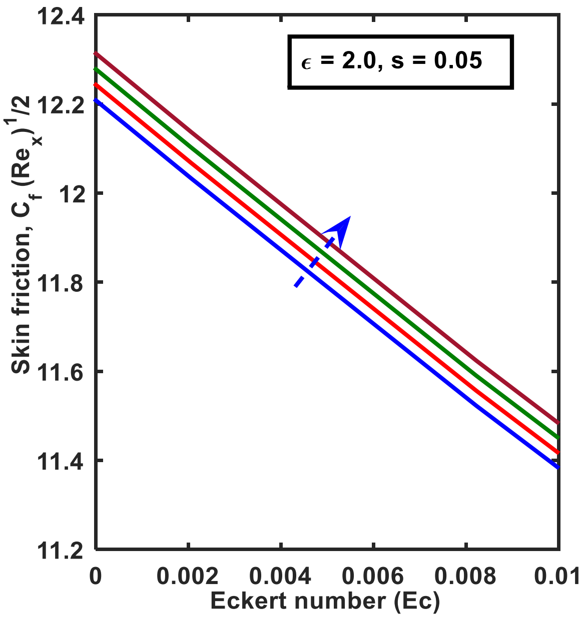

(c)

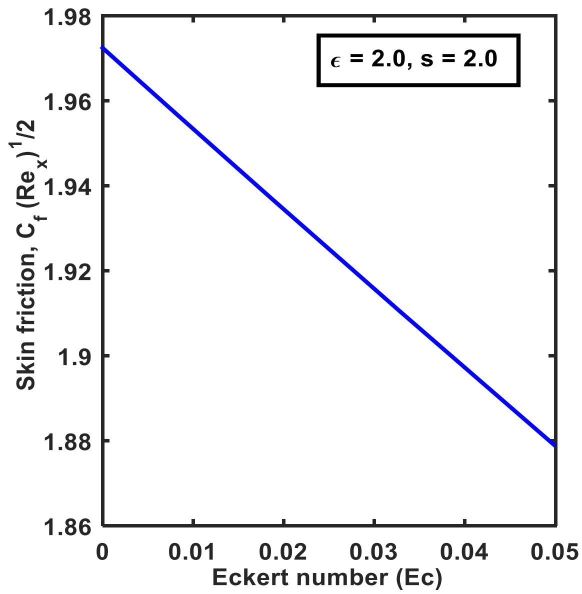

(d)

Figure 6. 3 Effects of Eckert number on velocity profile and skin friction coefficient when (a) $\epsilon = 0.0, 1.0, 2.0$, $s = 0.05$ (b) $\epsilon = 0.0, 1.0, 2.0$, $s = 2.0$ (c) $\epsilon = 2.0$, $s = 0.05$ and (d) $\epsilon = 2.0$, $s = 2.0$.

6.3.1.3 Effect of heat generation (Q^*) on the velocity profile and skin friction coefficient

Figures 6.4(a) - 6.4(d) represent the effect of the heat generation parameter (Q^*) on the velocity profile and skin friction coefficient for the case of thinner surface (s = 0.05) and thicker surface (s = 2.0). From these figures, it is observed that the fluid flow forms an inverted boundary layer pattern when $0.0 \le \varepsilon < 1.0$ but in case of $1.0 < \varepsilon \le 2.0$, the fluid flow forms a definite boundary layer pattern and the velocity profile and skin friction remain unchanged for both of the thinner (s = 0.05) and thicker (s = 2.0) bullet-shaped object.

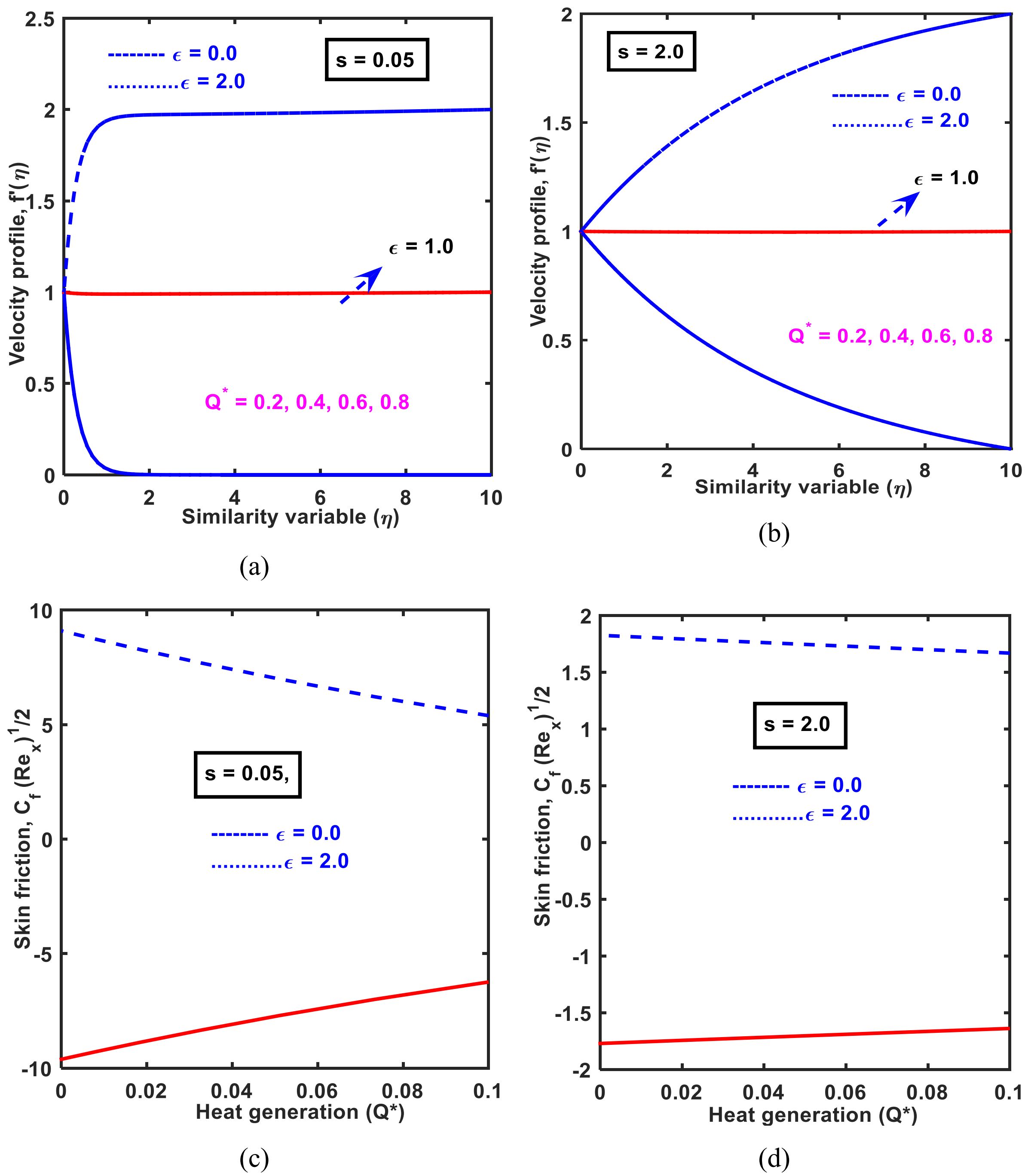

Figure 6. 4 Effects of heat generation on velocity profile and skin friction coefficient when (a) $\epsilon = 0.0, 1.0, 2.0$, $s = 0.05$ (b) $\epsilon = 0.0, 1.0, 2.0$, $s = 2.0$ (c) $\epsilon = 2.0$, $s = 0.05$ and (d) $\epsilon = 2.0$, $s = 2.0$

6.3.1.4 Effect of mixed convection parameter (λ) on the velocity profile and skin friction coefficient

Figures 6.5(a) - 6.5(d) display the plot of velocity profile and skin friction coefficient for studying the effects of mixed convection parameter (λ). It is seen that $\lambda = 0$ means pure forced convection. An increasing λ means the buoyancy force becomes stronger, as a result, the velocity distribution and thickness of the boundary layer increase but the skin friction coefficient decrease in the region near the solid surface for both of the thinner and thicker surfaces. From these figures, it is also observed that the fluid flow forms an inverted boundary layer pattern when $0.0 \le \varepsilon < 1.0$ but in the case of $1.0 < \varepsilon \le 2.0$, the fluid flow forms a definite boundary layer pattern. The velocity gradient at the surface is positive when $\varepsilon > 1.0$ and negative due to $\varepsilon < 1.0$ all values of the controlling parameters. On the other hand, the magnitude of the skin friction increases in both of the cases $\varepsilon > 1.0$ and $\varepsilon < 1.0$, respectively. It is observed that when λ increases from 0.5 to 15.5, there is an 8.2 % increase in the skin friction coefficient in the case of a thinner surface, whereas the corresponding increase is 15.5% in the case of a thicker surface.

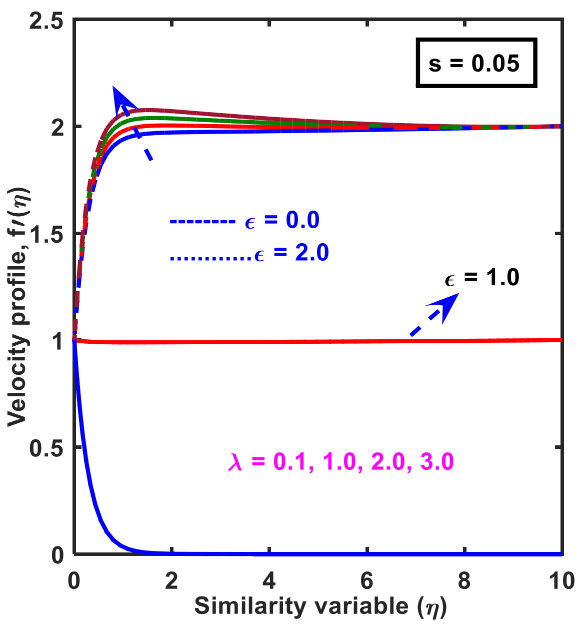

(a)

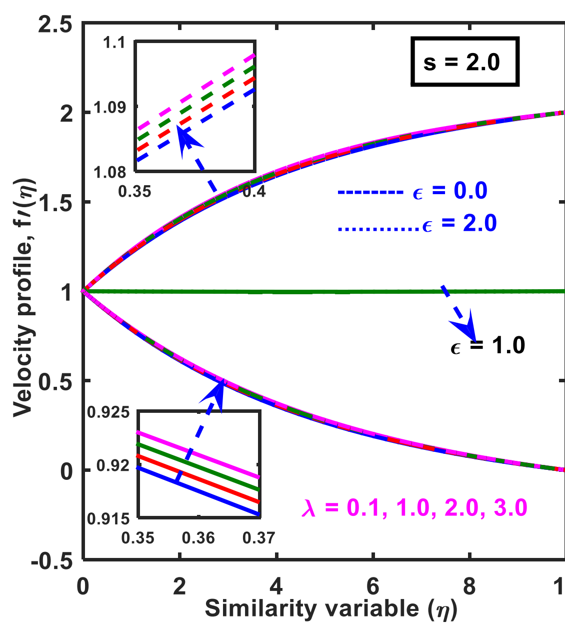

(b)

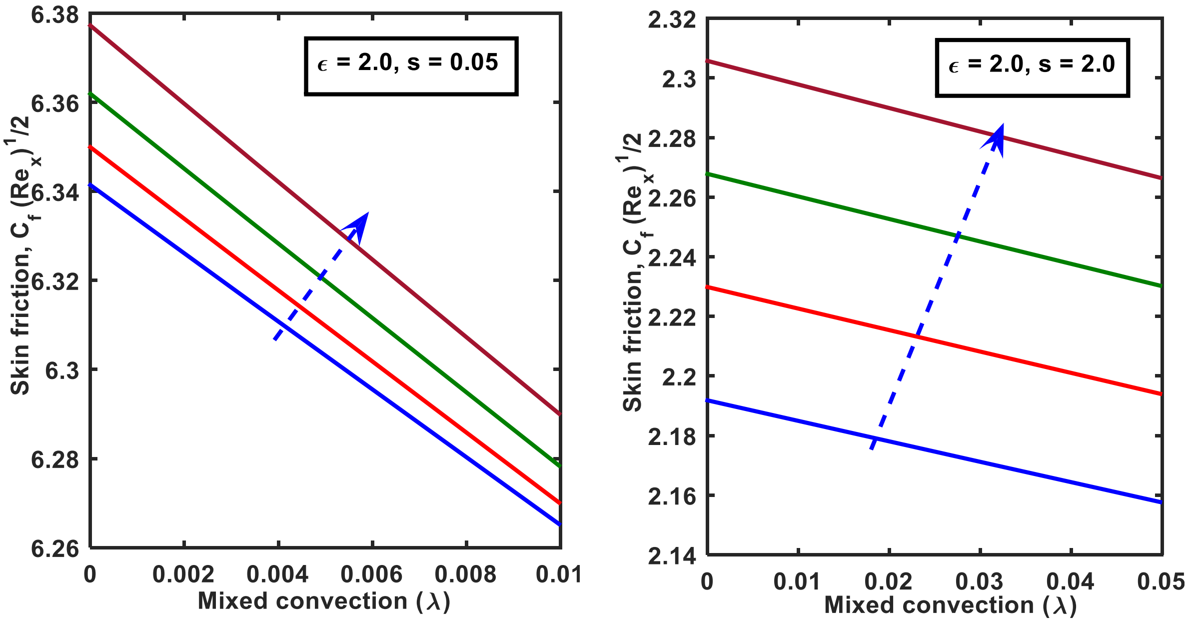

(c) (d)

Figure 6. 5 Effects of mixed convection parameter (λ) on velocity profile and skin friction coefficient when (a) $\epsilon = 0.0, 1.0, 2.0$, $s = 0.05$ (b) $\epsilon = 2.0, 1.0, 2.0$, $s = 2.0$ (c) $\epsilon = 2.0$, $s = 0.05$ and (d) $\epsilon = 2.0$, $s = 2.0$

6.3.1.5 Effect of Darcy number (*Da*) on the velocity profile and skin friction coefficient

Figures 6.6(a) – 6.6(d) illustrate the effect of the Darcy number (*Da*) on the velocity profile and skin friction coefficient. These figures show that the velocity profile and boundary layer thickness increase in the case of $\varepsilon > 1.0$ but reverse results arise in the case of $\varepsilon < 1.0$ both thinner and thicker surfaces. From these figures, it is also observed that the fluid flow forms an inverted boundary layer pattern when $0.0 \le \varepsilon < 1.0$ but in the case of $1.0 < \varepsilon \le 2.0$, the fluid flow forms a definite boundary layer pattern. With a porous medium (Da = 1) the movement of the fluid increases which results in a reduced velocity profile while in absence of a porous medium $(Da \to \infty)$ the velocity profile is enhanced. The presence of a porous medium in the flow presents the resistance to the flow, and in the limiting case, $(Da \to \infty)$ the porosity disappears. The Darcy number (*Da*) is inversely proportional to the actual permeability of the porous medium. An increase in *Da* leads to enhance deceleration of the flow, and hence the velocity decreases.

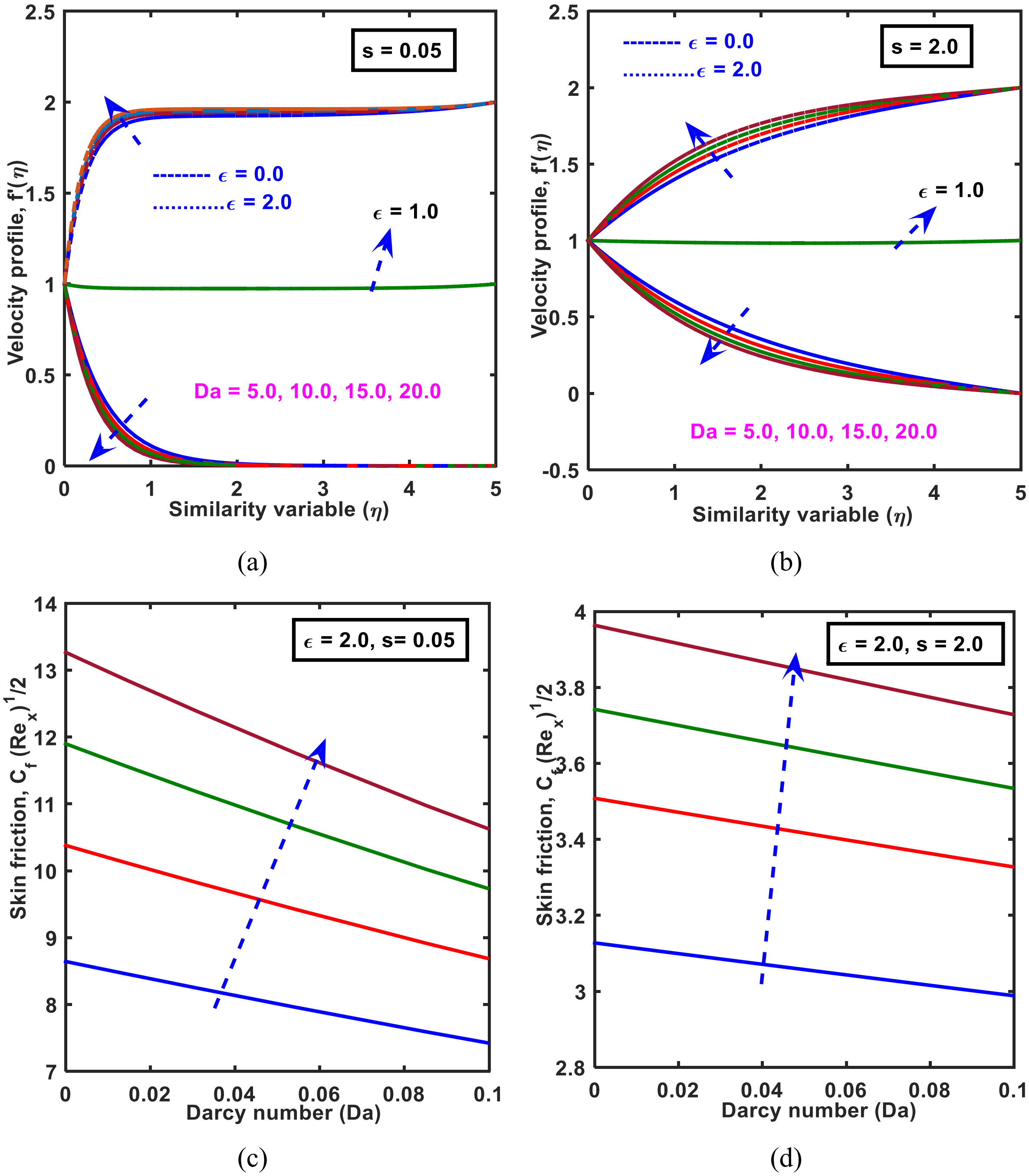

Figure 6. 6 Effect of Darcy number on velocity profile and skin friction coefficient when (a) $\epsilon = 0.0, 1.0, 2.0$, $s = 0.05$ (b) $\epsilon = 0.0, 1.0, 2.0$, $s = 2.0$ (c) $\epsilon = 2.0$, $s = 0.05$ and (d) $\epsilon = 2.0$, $s = 2.0$

Increasing *Da* increases the resistance of the porous medium (as the permeability physically becomes less with increasing). This decelerates the flow and reduces the magnitudes of the velocity. This is explained by the fact that an increase in *Da* means a decrease in the size of the pores of the porous medium, and this causes increased resistance to the flow, leading to lower velocity, and consequently to a decrease in two respective coefficients of friction. Physically, it must be noted that as *Da* increases, the porous medium becomes tighter, therefore the resistance against the flow increases. The velocity gradient at the surface is positive when $\varepsilon > 1.0$ and negative due to $\varepsilon < 1.0$ all values of the controlling parameters. Therefore, the magnitude of the skin friction increases in both of the cases $\varepsilon > 1.0$ and $\varepsilon < 1.0$, respectively. It is also observed that when *Da* changes from 5.0 to 20.0 there is a 13.4 % increase in the skin friction coefficient in the case of a thinner surface, whereas the corresponding increase is 21.3%, in the case of a thicker surface.

6.3.1.6 Effect of Forchheimer's drag coefficient (γ) on the velocity profile and skin friction coefficient

Figures 6.7(a) – 6.7(d) demonstrate the velocity profile, and skin friction coefficient for different values of Forchheimer's drag coefficient as the other flow parameters are kept fixed. It is noted that the velocity profile and skin friction decrease for both the thinner and thicker surface by increasing the value of Forchheimer's drag coefficient because the porous medium characterizes the fluid not to move freely through the boundary layer. Besides, the porous medium constitutes resistance to the flow. Thus, as the inertia coefficient increases, the resistance to the flow increases, causing the fluid flow in the porous medium to slow down. Therefore, the momentum boundary layer thickness also decreases for both surfaces. So, it is confirmed from this graph that porosity has an important role in the present analysis. From these figures, it is also noticed that the fluid flow forms an inverted boundary layer pattern when $0.0 \le \varepsilon < 1.0$ but in the case of $1.0 < \varepsilon \le 2.0$, the fluid flow forms a definite boundary layer pattern. It is observed that when γ increases from 0.5 to 4.5 there is an 18.5 % decrease in the skin friction coefficient in the case of a thinner surface, whereas the corresponding decrease is 28%, in the case of a thicker surface.

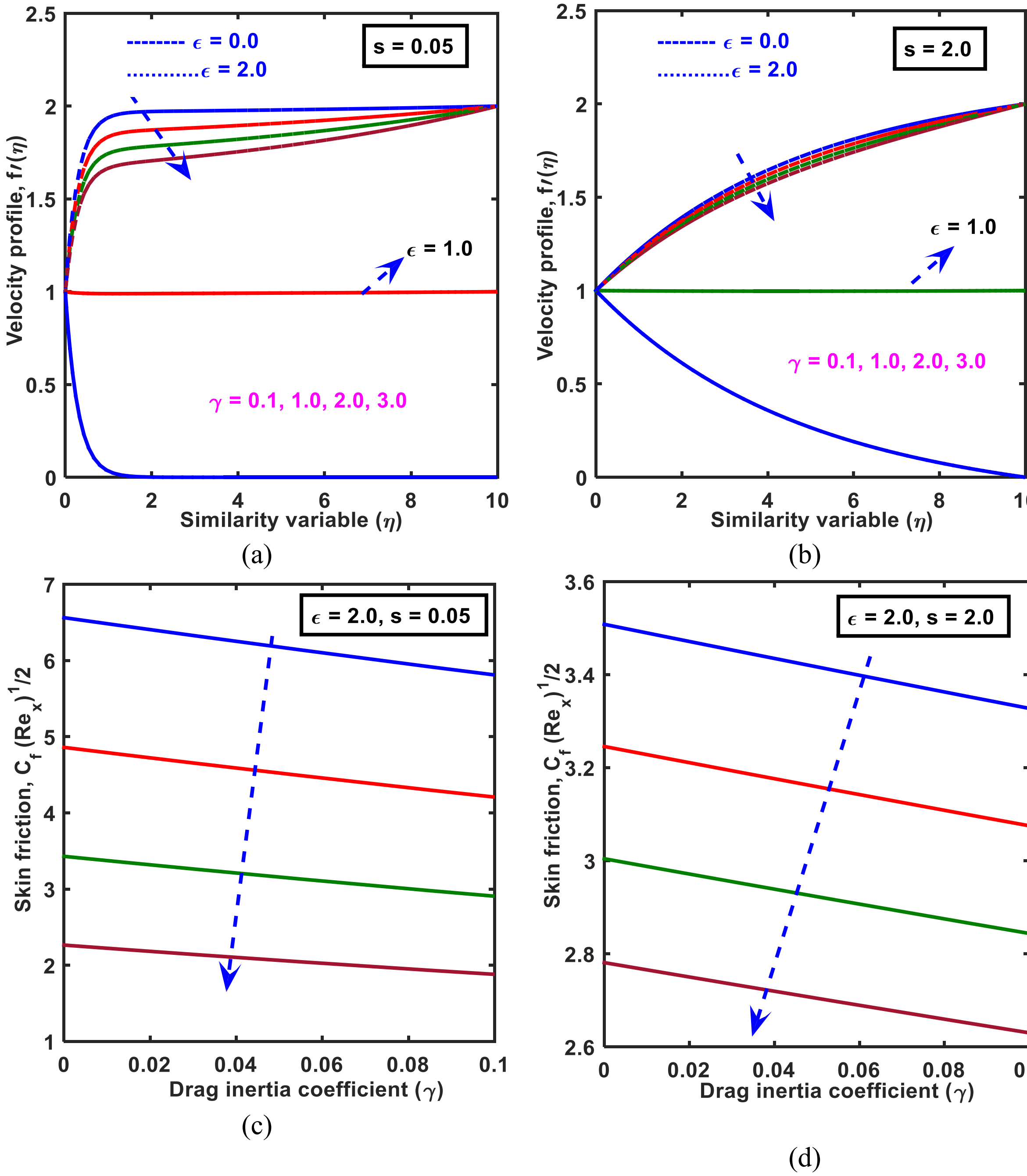

Figure 6. 7 Effects of drag inertia coefficient on velocity profile and skin friction coefficient when (a) $\epsilon = 0.0, 1.0, 2.0$, $s = 0.05$ (b) $\epsilon = 0.0, 1.0, 2.0$, $s = 2.0$ (c) $\epsilon = 2.0$, $s = 0.05$, and (d) $\epsilon = 2.0$, $s = 2.0$

6.3.1.7 Effect of stream-wise coordinate (*X*) on the velocity profile and skin friction

Figures 6.8(a) – 6.8(d) show the effects of the stream-wise coordinate on the velocity profile and skin friction for both thinner and thicker surfaces. From these figures, it is noticed that the velocity profile, boundary layer thickness, and skin friction increase in the case of $\varepsilon > 1$ both thinner and thicker surfaces.

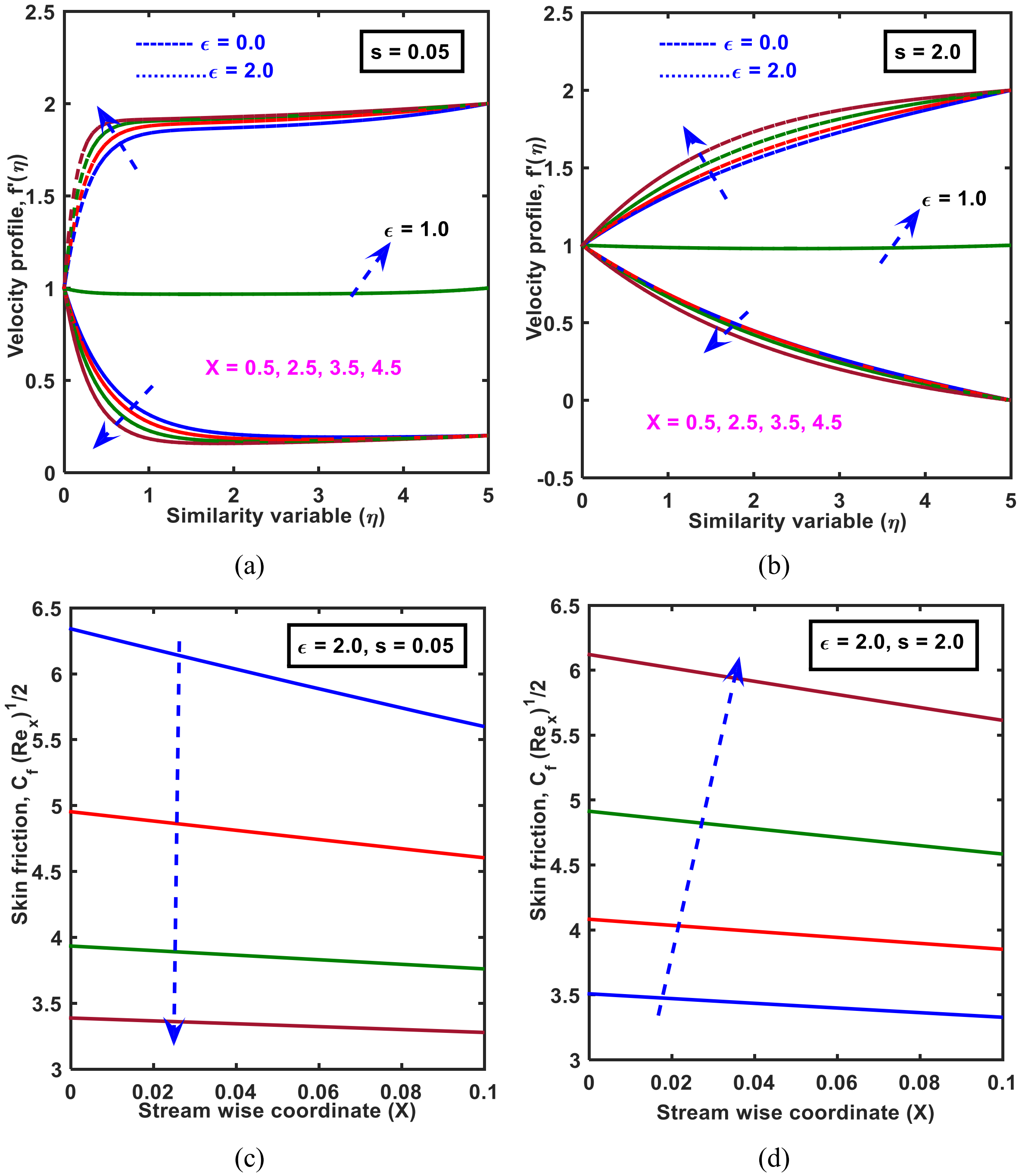

Figure 6. 8 Effects of stream wise coordinate on velocity profile and skin friction coefficient when (a) $\epsilon = 0.0, 1.0, 2.0, s = 0.05$ (b) $\epsilon = 0.0, 1.0, 2.0, s = 2.0$ (c) $\epsilon = 2.0, s = 0.05$, and (d) $\epsilon = 2.0, s = 2.0$

From these figures, it is also observed that the fluid flow forms an inverted boundary layer pattern when $0.0 \le \varepsilon < 1.0$ but in the case of $1.0 < \varepsilon \le 2.0$, the fluid flow forms a definite boundary layer pattern. This is because the stream-wise coordinate acts as the adverse pressure gradient in the direction of flow velocity which decreases the flow rate while increases the thickness of the momentum boundary layer. On the other hand, the opposite results arise in the case of $\varepsilon > 1$. It is observed that when X increases from 0.5 to 3.5 there is 53.9 % (s = 0.05) increase in the skin friction coefficient value, whereas the corresponding increase is 42.6%, (s = 1.0).

6.3.1.8 Effect of stretching ratio parameter (ϵ) on the velocity profile and skin friction coefficient

Figure 6.9(a) - 6.9(d) illustrate the effects of the stretching ratio parameter (ϵ) on the velocity profile and skin friction coefficient. It is observed that increasing the stretching ratio enhances the velocity and the skin friction coefficient for both the cases s = 0.05 and s = 2.0 because free stream velocity (U_∞) dominates over the reference velocity (U_w).

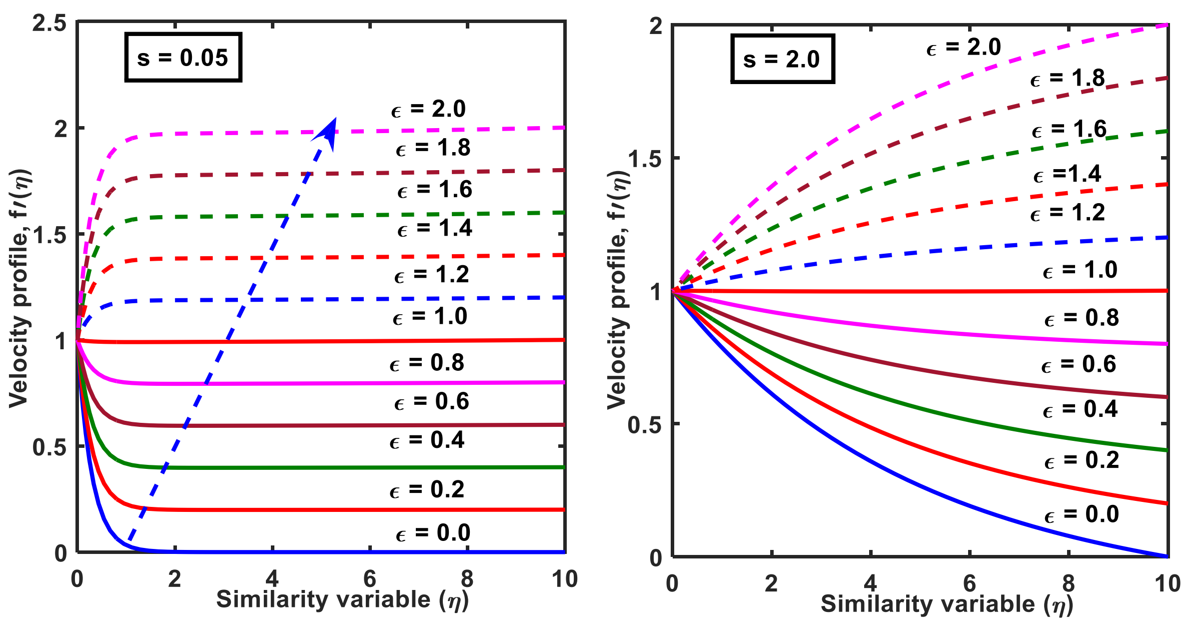

(a) (b)

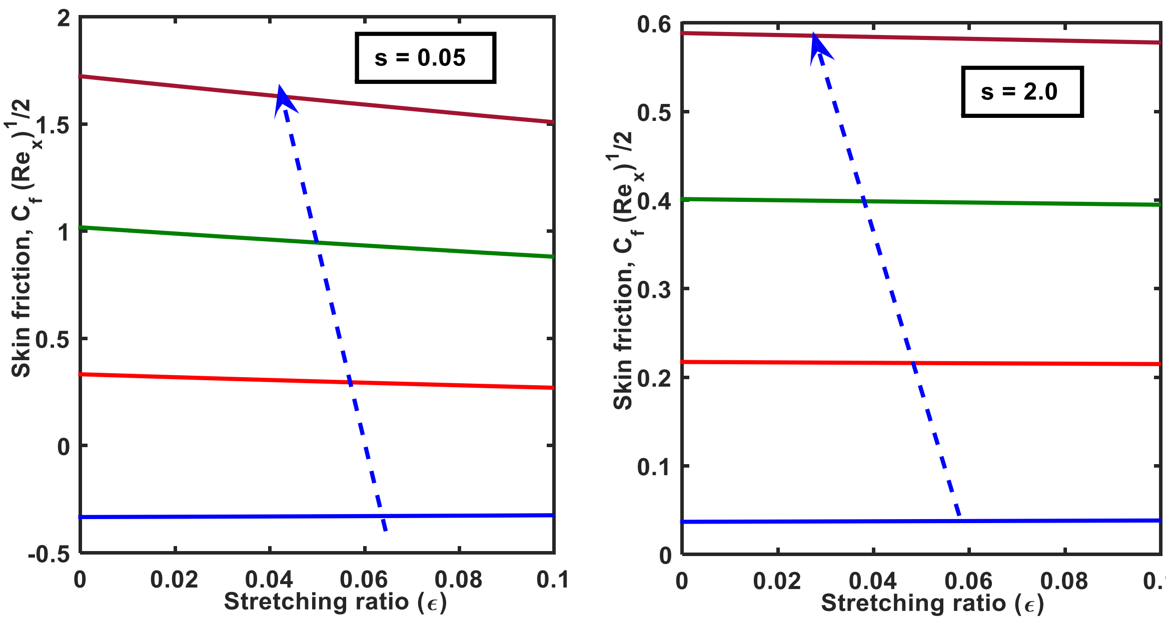

(c) (d)

Figure 6. 9 Effect of stretching ratio on velocity profile and skin friction coefficient when (a) $\epsilon = 0.0, 1.0, 2.0, s = 0.05$ (b) $\epsilon = 0.0, 1.0, 2.0, s = 2.0$ (c) $\epsilon = 2.0, s = 0.05$, and (d) $\epsilon = 2.0, s = 2.0$

From these figures, it is also observed that the fluid flow forms an inverted boundary layer pattern when $0.0 \le \varepsilon < 1.0$ but in the case of $1.0 < \varepsilon \le 2.0$, the fluid flow forms a definite boundary layer pattern. Again, when ϵ changes from 0.2 to 0.8 there is 63% (s = 0.05) increase in the skin friction coefficient value, whereas the corresponding increase is 65%, (s = 2.0).

6.3.1.9 Effect of surface thickness parameter (s) on the velocity profile and skin friction coefficient

Figure 6.10(a) and Figure 6.10(b) illustrate the effects of surface thickness parameter (s) on the velocity profile and skin friction coefficient. It is revealed from Figure 6.10(a) that the surface thickness parameter leads to an increase in the fluid velocity profile and boundary layer thickness when $\epsilon = 0.0$ whereas, in the case of $\varepsilon > 1$, the surface thickness parameter has a reverse effect on it. Physically, the surface of the object in contact with the fluid particles decreases when the surface thickness is getting smaller. This causes the friction force that occurs on the surface and the fluid flow will be reduced and this phenomenon leads to an increase in the skin friction coefficient.

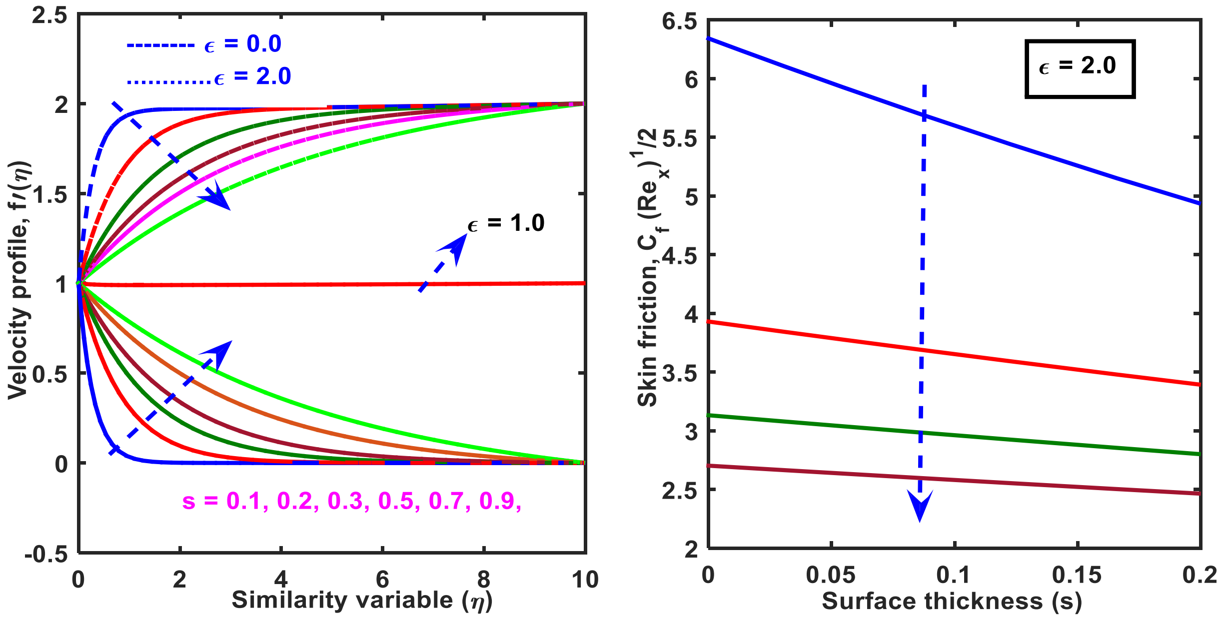

(a) (b)

Figure 6. 10 Effect of surface thickness parameter (*s*) on velocity profile when (a) $\epsilon = 0.0, 2.0$ and skin friction coefficient when (b) $\epsilon = 2.0$

From Figure 6.10(b) it is seen that the skin friction decreases in the case of $\epsilon = 2.0$. The result is significant when $\epsilon = 2.0$ and the flow forms a certain boundary layer pattern. It is also observed that when s increases from 0.10 to 1.0 there is a 4.8 % ($\varepsilon > 1$) decrease in the skin friction coefficient.

6.3.1.10 Effect of the unsteady parameter (*A*) on the velocity profile and skin friction coefficient

Figures 6.11(a) - 6.11(d) show that an increase in time t causes a decrease in the velocity profile, boundary layer thickness, and skin friction in case of $\epsilon = 2.0$ for both the thinner and thicker surfaces. In the case of $\epsilon = 0.0$ and $s = 0.05$, the unsteady parameter does not affect the velocity profile within the boundary layer region. In the case of $\epsilon = 0.0$ and $s = 2.0$, the velocity profile increases for increasing the within the region of the boundary layer.

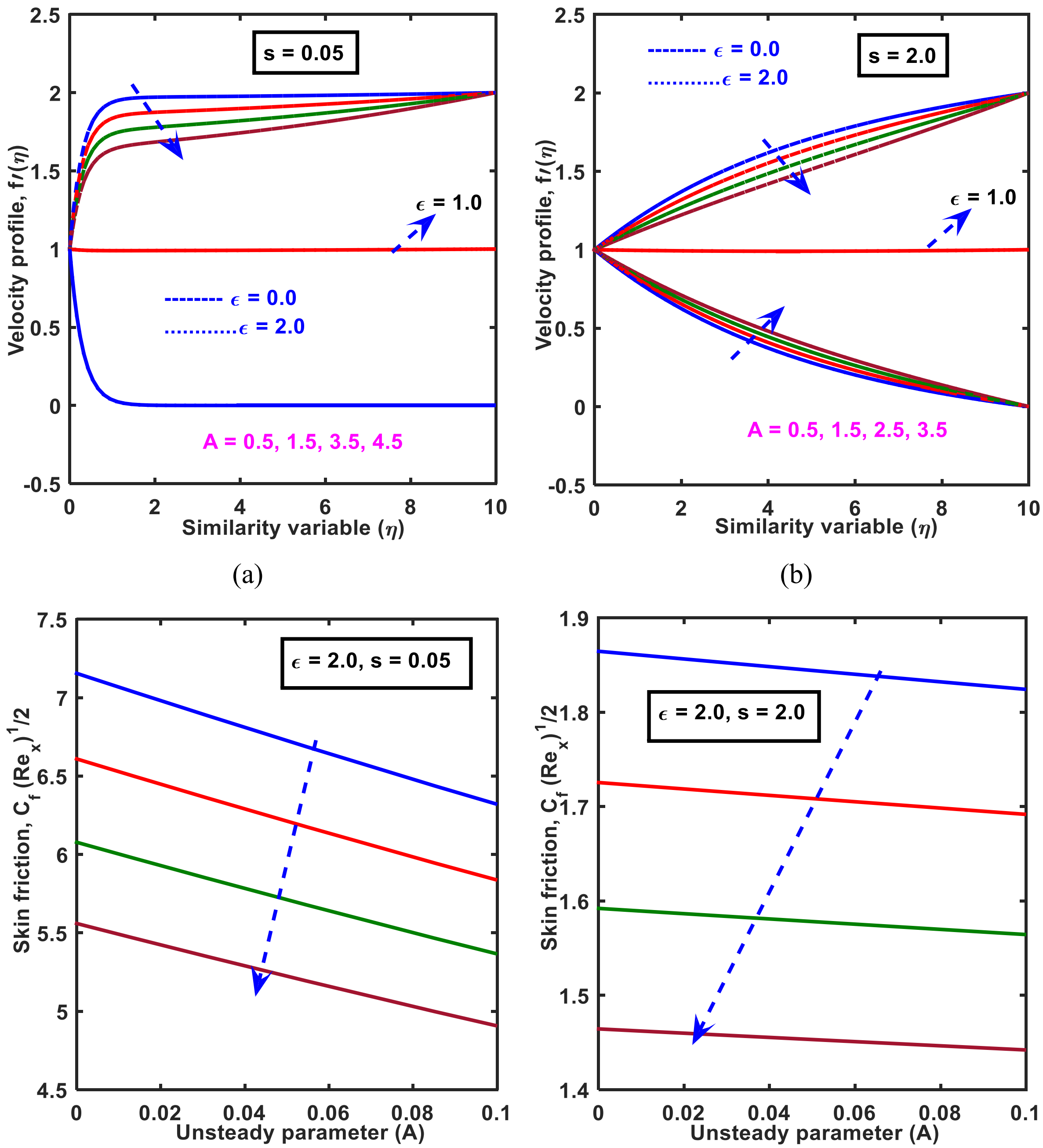

Figure 6. 11 Effect of unsteady parameter on velocity profile and skin friction coefficient when (a) $\epsilon = 0.0, 1.0, 2.0$, $s = 0.05$ (b) $\epsilon = 0.0, 1.0, 2.0$, $s = 2.0$ (c) $\epsilon = 2.0$, $s = 0.05$, and (d) $\epsilon = 2.0$, $s = 2.0$

This is because as time t enhances, the fluid velocity falls steeply near the fixed end of the stretching object, and the gradient decreases gradually as the distance from the fixed end of the stretching surface increases. From Figures 6.11(c) and 6.11(d) it is noticed that the skin friction decreases for raising the unsteady parameter. It is also seen that when unsteady parameter *(A)* increases from 0.2 to 4.5 there is 8.7 % (s = 0.05) decrease in the skin friction coefficient, whereas the corresponding decrease is 23.9%, (s = 2.0).

6.3.1.11 Effect of suction/injection parameter (f_w) on the velocity profile and skin friction coefficient

Figures 6.12(a) - 6.12(d) depict the effect of suction/injection parameter on velocity profile, and skin friction coefficient within the boundary layer. It is observed that the suction parameter decreases the velocity profile and the injection parameter increases the profile in the case of the thinner bullet-shaped object but the reverse trend happens in the case of thicker bullet-shaped object. The physical reason behind this behavior is that when the stronger injection is used, the heated fluid is pushed far from the surface where the buoyancy forces accelerate the flow with less influence on the viscosity. This effect tends to increase the shear by increasing the maximum velocity in the boundary layer. On the other hand, when suction increases, fluid comes near the surface, which decreases the velocity and temperature profiles.

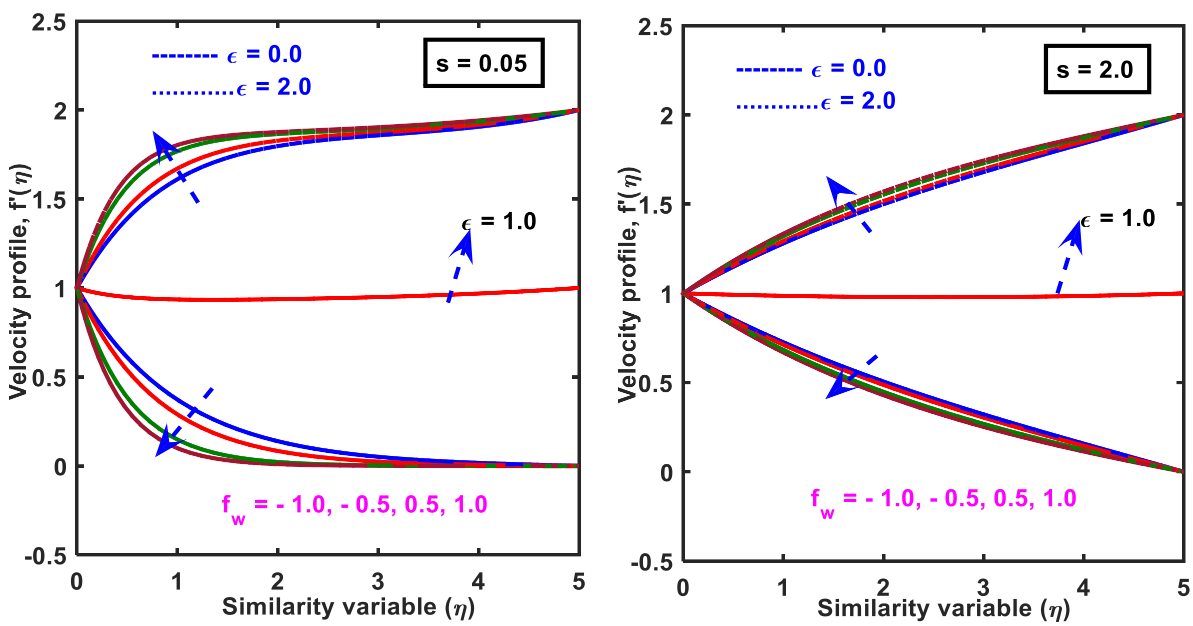

(a) (b)

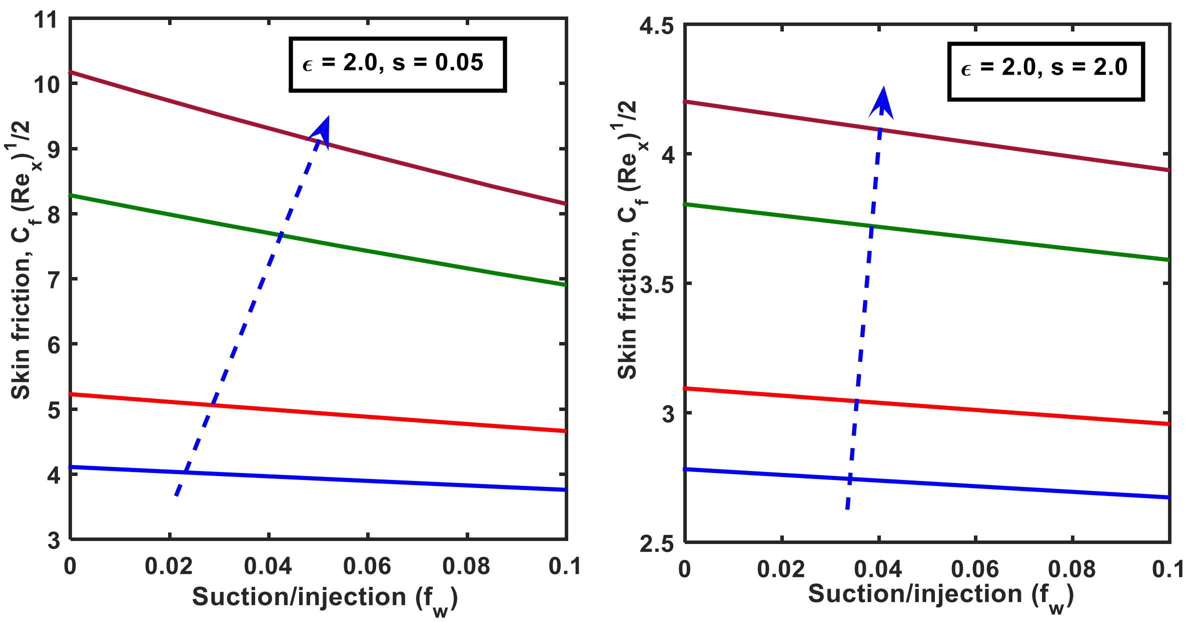

(c) (d)

Figure 6. 12 Effect of suction/injection parameter on velocity profile and skin friction coefficient when (a) $\epsilon = 0.0, 1.0, 2.0$, $s = 0.05$ (b) $\epsilon = 0.0, 1.0, 2.0$, $s = 2.0$ (c) $\epsilon = 2.0$, $s = 0.05$, and (d) $\epsilon = 2.0$, $s = 2.0$

Therefore, an increase in porosity parameter causes greater obstruction to the fluid flow, thus reducing the velocity and temperature. So that the fluid velocity can be controlled by suction or injection parameters. The same behavior has been shown in the study of Khadijah [84]. This gives the accuracy of the present study. It is noticed that when f_w changes from 0.2 to 0.4 there is a 165.6 % (s = 0.05) increase in the skin friction coefficient, whereas the corresponding increase is 57.5%, (s = 2.0) in the case of $\varepsilon > 1$.

From these figures, it is observed that the velocity profile and momentum boundary layer thickness is getting expand due to magnetic parameter (M), mixed convection parameter (λ), location parameter (X), Darcy number (Da), suction parameter (f_w), and stretching ratio parameter (ϵ) whereas surface thickness parameter (s), unsteady parameter (A), drag inertia coefficient (γ), and Eckert number (Ec) have a reverse effect on it in the case of $\varepsilon > 1$ for both of the thicker (s = 2.0) and the thinner (s = 0.05) surfaces of the bullet-shaped object. On the other hand, in the case of $\varepsilon < 1$ the velocity profile and momentum boundary layer thickness are getting squeezes due to magnetic parameter (M), Darcy number (Da), suction parameter (f_w), and location parameter (X) whereas surface thickness parameter (s), and unsteady parameter (A) have a reverse effect on it. On the other hand, Eckert number (Ec), mixed convection parameter (λ), drag inertia coefficient (γ), and heat generation parameter (Q^*) have no effect on the velocity profile for both of the thicker (s = 2.0) and the thinner (s = 0.05) surfaces. Therefore, in the case of a thicker bullet-shaped object (s = 2.0), the velocity profile does not approach the ambient condition asymptotically but intersects the vertical axis with a steep angle and the boundary layer structure has no definite shape whereas in the case of a thinner bullet-shaped object (s = 0.05) the velocity profile converge to the ambient condition asymptotically and the boundary layer structure has a definite shape. It is also mentioned that the thinner bullet-shaped object represents a thinner momentum boundary layer than the thicker bullet-shaped object in both static and moving bullet-shaped objects.

Table 6.1 depicts the variation in skin friction coefficient for various values of the controlling parameters such as the magnetic parameter (M), unsteady parameter (A), heat generation parameter (Q^*), surface thickness parameter (s), mixed convection parameter (λ), drag inertia coefficient (γ), Eckert number (Ec), location parameter (X), suction parameter (f_w), Darcy number (Da), and Prandtl number (Pr) for various movement of the bullet-shaped object. From Table 6.1, it is noticed that the magnetic parameter (M), location parameter (X), suction parameter (f_w), and Darcy number (Da) boosting the friction factor coefficient in the case of $\varepsilon < 1$ but reverse results arise in the case of $\varepsilon > 1$. The mixed convection parameter and surface thickness parameter reduce the friction factor in either of the cases $\left(\varepsilon < 1 \text{ or} > 1\right)$. On the other hand, unsteady parameter and drag inertia coefficient do not affect the friction factor in the case of $\varepsilon < 1$ but in the case of $\varepsilon > 1$ the friction factor enhances. It is interesting to note that the friction factor coefficient is less in ϵ = 0.2 case when compared with ϵ = 2.0 case. At this point, it is highlighted that for reducing the friction between the fluid particles we have to apply ϵ = 0.2 cases. It is evident from this table that the skin friction coefficient is higher in ϵ = 2.0 cases when comparing with ϵ = 0.2 cases.

Table 6. 1 Values of skin friction coefficient which is equivalent to velocity gradient for different values of *M, A,* ϵ, λ, Pr, γ, *X*, f_w, *Da* and *s* respectively

M	A	s	λ	γ	X	f_w	Da	Pr	$\lvert -f''(\eta)\rvert$ $\epsilon = 0.2$	$-f''(\eta)$ $\epsilon = 2.0$
0.5	0.2	0.2	0.5	0.5	0.5	0.2	5.0	0.71	**7.7666**	**8.9674**
5.5	0.2	0.2	0.5	0.5	0.5	0.2	5.0	0.71	**8.7991**	**10.3515**
10.5	0.2	0.2	0.5	0.5	0.5	0.2	5.0	0.71	**9.6984**	**11.5581**
0.5	**0.4**	0.2	0.5	0.5	0.5	0.2	5.0	0.71	**7.7817**	**8.4263**
0.5	**0.6**	0.2	0.5	0.5	0.5	0.2	5.0	0.71	**7.7817**	**7.8949**
0.5	**0.8**	0.2	0.5	0.5	0.5	0.2	5.0	0.71	**7.7817**	**7.3733**
0.5	0.2	**0.2**	0.5	0.5	0.5	0.2	5.0	0.71	**7.7666**	**8.9674**
0.5	0.2	**0.3**	0.5	0.5	0.5	0.2	5.0	0.71	**5.8671**	**6.9819**
0.5	0.2	**0.4**	0.5	0.5	0.5	0.2	5.0	0.71	**4.9026**	**5.9328**
0.5	0.2	0.2	**0.5**	0.5	0.5	0.2	5.0	0.71	**7.7666**	**8.9674**
0.5	0.2	0.2	**1.5**	0.5	0.5	0.2	5.0	0.71	**7.2813**	**9.1121**
0.5	0.2	0.2	**2.5**	0.5	0.5	0.2	5.0	0.71	**7.1224**	**9.2565**
0.5	0.2	0.2	0.5	**0.5**	0.5	0.2	5.0	0.71	**7.7666**	**8.9674**
0.5	0.2	0.2	0.5	**1.5**	0.5	0.2	5.0	0.71	**7.7666**	**6.7502**
0.5	0.2	0.2	0.5	**2.5**	0.5	0.2	5.0	0.71	**7.7666**	**5.0271**
0.5	0.2	0.2	0.5	0.5	**0.5**	0.2	5.0	0.71	**7.7666**	**8.9674**
0.5	0.2	0.2	0.5	0.5	**1.0**	0.2	5.0	0.71	**7.9431**	**9.1254**
0.5	0.2	0.2	0.5	0.5	**1.5**	0.2	5.0	0.71	**8.2801**	**9.4762**
0.5	0.2	0.2	0.5	0.5	0.5	**0.2**	5.0	0.71	**7.7666**	**8.9674**
0.5	0.2	0.2	0.5	0.5	0.5	**0.3**	5.0	0.71	**8.1461**	**9.3621**
0.5	0.2	0.2	0.5	0.5	0.5	**0.4**	5.0	0.71	**8.5346**	**9.7668**
0.5	0.2	0.2	0.5	0.5	0.5	0.2	**5.0**	0.71	**7.7666**	**8.9674**
0.5	0.2	0.2	0.5	0.5	0.5	0.2	**7.0**	0.71	**8.1995**	**9.5375**
0.5	0.2	0.2	0.5	0.5	0.5	0.2	**10.0**	0.71	**8.8001**	**10.3304**

6.3.2 Temperature profiles and Nusselt number with parameter variations

6.3.2.1 Effect of Pr, *M, X, A* on temperature profile and Nusselt number

The influences of Prandtl number (Pr), magnetic parameter (*M*), stream-wise location coordinate (*X*), and unsteady parameter (*A*) on the non-dimensional temperature $\theta(\eta)$ and corresponding variations have been plotted in Figures 6.1 3(a) – 6.13(d), respectively in the case of air (Pr = 0.71) and water (Pr = 7.0) with the thinner surface (*s* = 0.05). These plots depict that the temperature profile of the viscous fluid and thermal boundary layer thickness affected significantly with increasing the mentioned parameters. From Figure 6.13(a) it is observed that the temperature profile and boundary layer thickness squeezes for thinner (*s* = 0.05) surface of the bullet-shaped object but the Nusselt number increases. It is also observed that the thermal boundary layer thickness is higher in the case $f_w < 0.6$ than in the $f_w > 0.6$ case. Therefore, in the case of smaller Prandtl number heat is quickly diffuse from the heated surface than for higher values of Pr. So, for the cooling purpose, we can use the higher the Prandtl number. Temperature is seen to be squeezed and very close to the surface of the bullet-shaped object as Pr increases. In the case of Pr $\ll$ 1, the fluid is highly conductive so that heat diffuses faster than for larger values of Pr. It is seen from Figure 6.13 (b) that the variation of the Prandtl number has a significant effect on viscous fluid temperature in connection with the magnetic parameter. A higher Prandtl number has a greater accelerating effect on the temperature profile. For water (Pr = 7.0) with increasing *M*, the accelerating effect is more prominent than for air (Pr = 0.71). Therefore, the thermal boundary layer thickness is higher for water when compared with air. The temperature attains its minimum in connection with the magnetic parameter in the case of air but shooting up the profiles near the surface of the bullet-shaped object within the region $\eta < 0.1$ and then the profile decreases sharply to meet the boundary condition asymptotically. A similar behavior arises for the location parameter depicts in Figure 6.13 (c). The temperature profile increase but Nusselt number decrease within the boundary layer for increasing the magnetic strength because in an electrically conducting fluid if the magnetic field is applied a resistive type force like a drag force is produced. The nature of this force retards the fluid velocity, and therefore, the magnetic field effects decelerate the velocity profiles. This Lorentz force tends to slow down the fluid motion and the resistance offered to the flow.

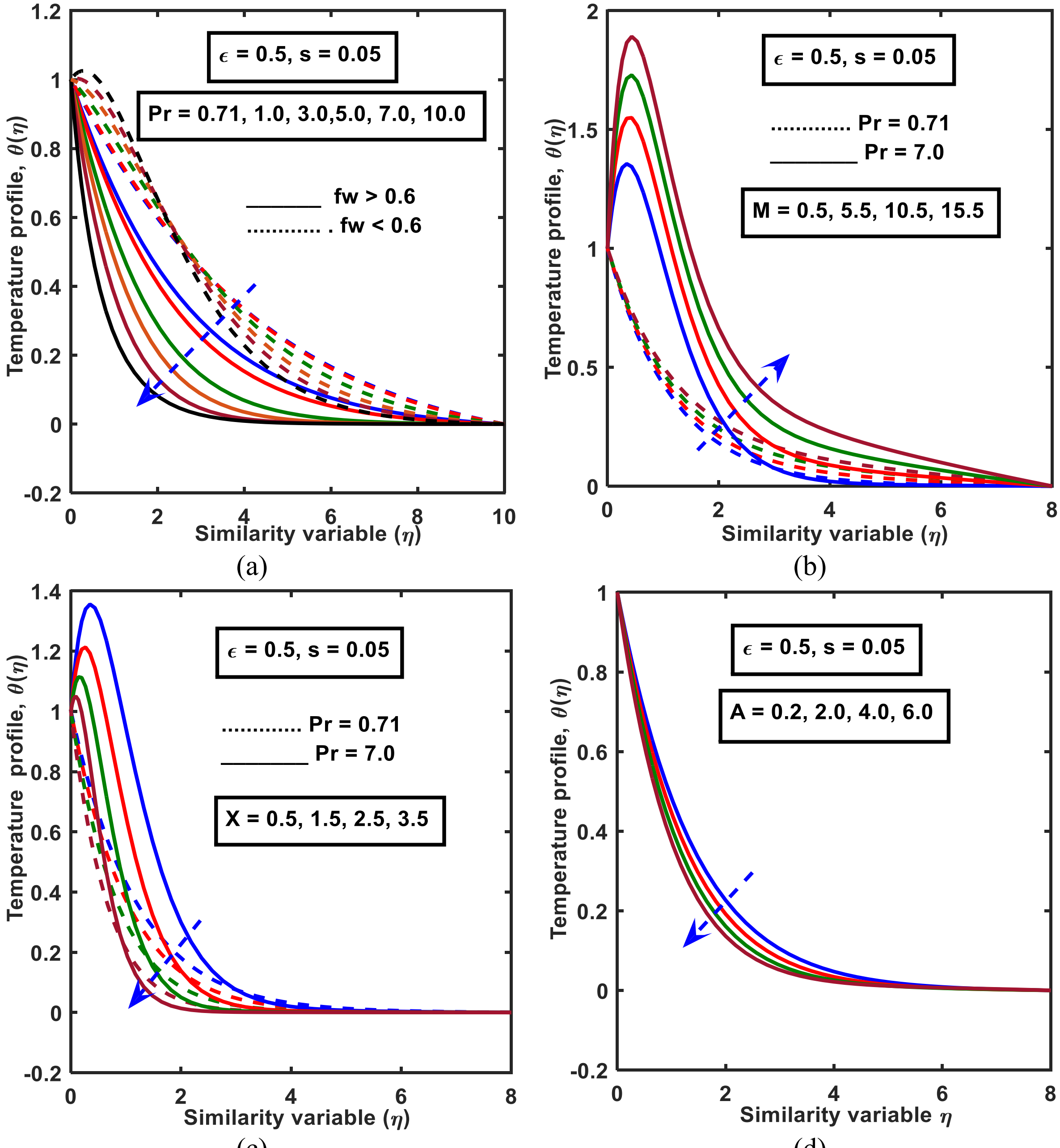

Figure 6. 13 Effect of Pr, M, X, and A on temperature profile when (a) $\varepsilon = 0.2$, $s = 0.05$, $f_w < 0.6$, $f_w > 0.6$ (b) $\varepsilon = 0.2$, $s = 0.05$, Pr = 0.71, 7.0 (c) $\varepsilon = 0.2$, $s = 0.05$, Pr = 0.71, 7.0, and (d) $\varepsilon = 0.2$, $s = 0.05$

Therefore, it is possible for the increase in the temperature. It is observed that the increase of location parameter X leads to a decrease in the temperature profile and an increase in the

Nusselt number within the boundary layer. We observe that the effect of increasing the values of location parameters *X* and *A* is to decrease the temperature profile and increase the rate of heat transfer as a result the thermal boundary layer thickness reduces. Physically, when *A* increases the surface of the bullet-shaped object loses more heat that causes the temperature profile to decrease. Therefore, the parameters Pr, *X*, and *A* are adversely proportional to the temperature profile and thermal boundary layer thickness.

6.3.2.2 Effect of Pr, *M, X,* and *A* on Nusselt number

Figures 6.14(a) - 6.14(d) depict the Nusselt number for the variations of the parameters Pr, *M, X,* and *A* respectively. From these figures, it is noticed that the Nusselt number increases with an increase of Prandtl number, location parameter, and unsteady parameter but decreases for the magnetic parameter. It is also mentioned that when Pr increases from 0.71 to 7.0, X increases from 0.5 to 3.5, and A increases from 0.2 to 6.0 then there are 36 %, 51.6%, and 17.7% increase in the Nusselt number in case of s = 0.2, whereas the corresponding increase is 20.7%, 91.5%, and 19.5% in case of s = 2.0.

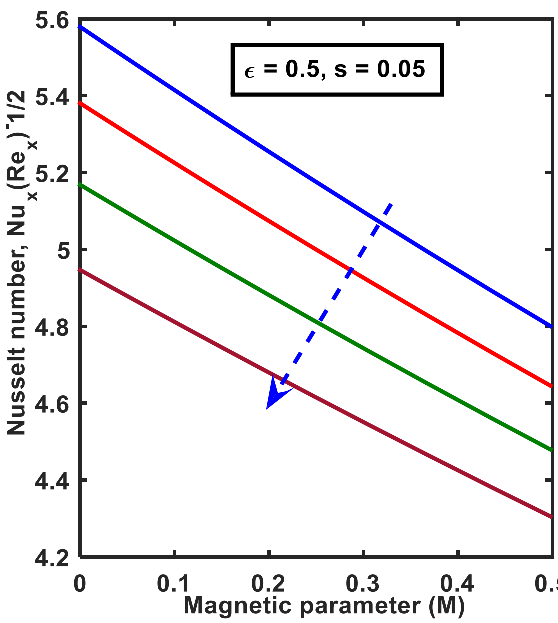

(a)

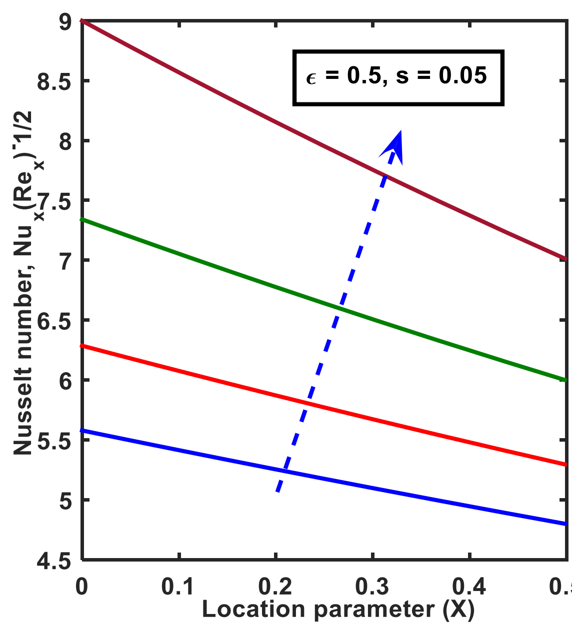

(b)

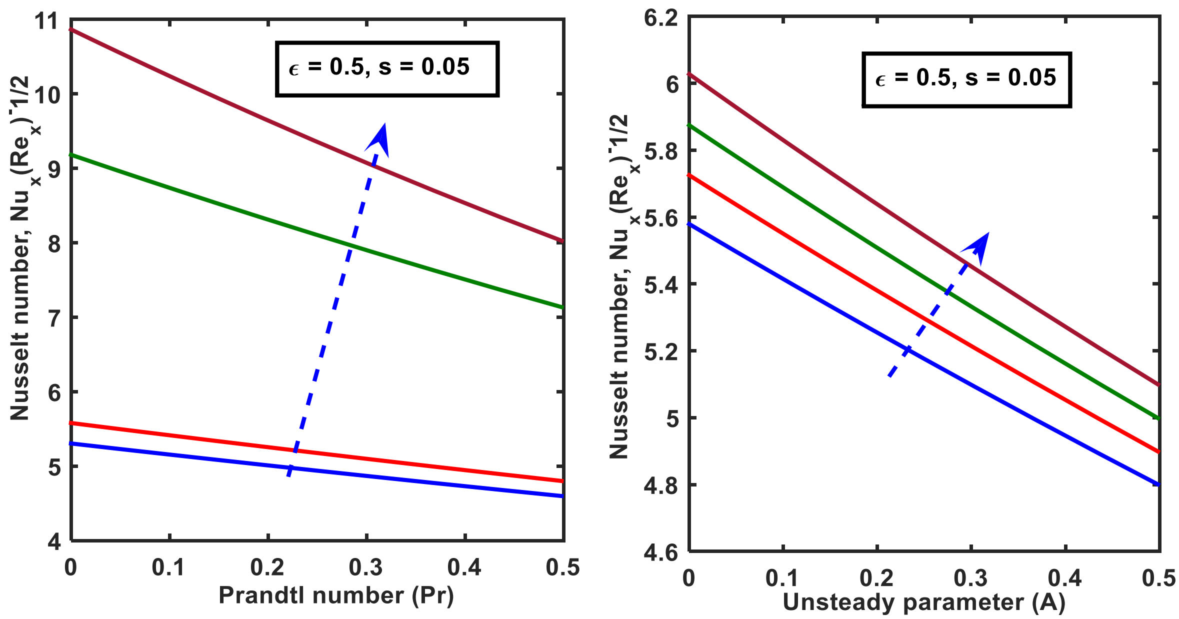

(c) (d)

Figure 6. 14 Effect of Pr, M , X , and A on Nusselt number when (a) $\varepsilon = 0.5,\ s = 0.05$ (b) $\varepsilon = 0.5,\ s = 0.05$ (c) $\varepsilon = 0.5,\ s = 0.05$, and (d) $\varepsilon = 0.5,\ s = 0.05$.

Again, when M increases from 0.5 to 15.5, there is a 25.6 % decrease of Nusselt number in the case of s = 0.2, whereas the corresponding decrease is 43.8% in the case of s = 2.0.

6.3.2.3 Effect of Q^*, f_w, Da, and γ on the temperature profile

The effects of heat generation parameter (Q*), suction/injection parameter (f_w), Darcy number (Da), and drag inertia coefficient (γ) on the non-dimensional temperature $\theta(\eta)$ and corresponding variations have been plotted in Figures 6.1 5(a) – 6.15(d), respectively in the case of air (Pr = 0.71) and water (Pr = 7.0). These plots depict that the temperature profile of the viscous fluid and thermal boundary layer thickness affected significantly with increasing the mentioned parameters. It is seen from Figure 6.15 (a) that the variation of the Prandtl number has a significant effect on viscous fluid temperature in connection with the heat generation parameter. A higher Prandtl number has a greater accelerating effect on the temperature profile. In the case of water (Pr = 7.0) with increasing Q^*, the accelerating effect is more prominent than for air (Pr = 0.71). Therefore, the thermal boundary layer thickness is higher for water when compared with air. The temperature attains its minimum in connection with the magnetic parameter in the case of air but shooting up the profiles near the surface of the bullet-shaped object within the region $\eta < 0.1$ and then the profile decreases sharply to meet the boundary condition asymptotically. A similar behavior arises for the Darcy number (*Da*), and drag inertia coefficient (γ) that depicts in Figures 6.15 (c) and 6.15(d), respectively whereas a reverse trend arises for the suction/injection parameter. As expected, increasing the value of heat generation leads to higher temperatures but a lower Nusselt number. It has happened because heat sources produce more heat energy near the surface as a result the temperature of the fluid increases. Again, it is seen that the temperature profiles also increase but the Nusselt number decrease as *Da*, and γ increase. The Darcy number enhances means the convective mode is stronger due to an increase in the permeability of the medium. Hence, the heat transfer over the hot wall increases with the increase of the Darcy number. The suction parameter tends to decrease the temperature of the flow field. Therefore, thermal boundary layer thickness reduces when the suction parameter is applied but the opposite trend is observed due to the injection parameter.

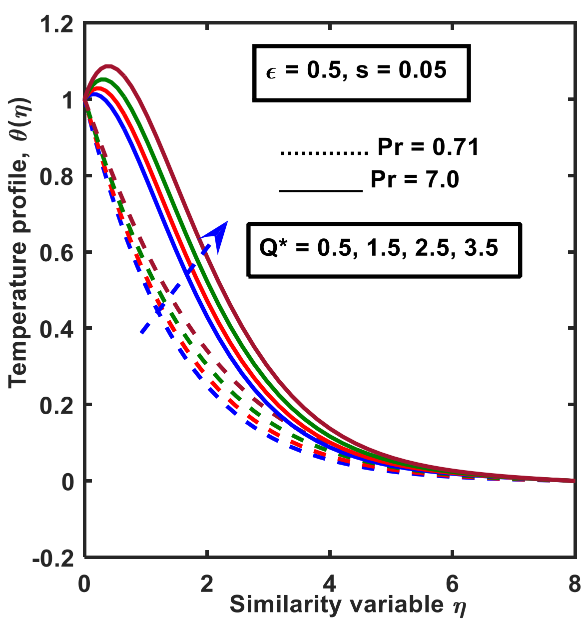

(a)

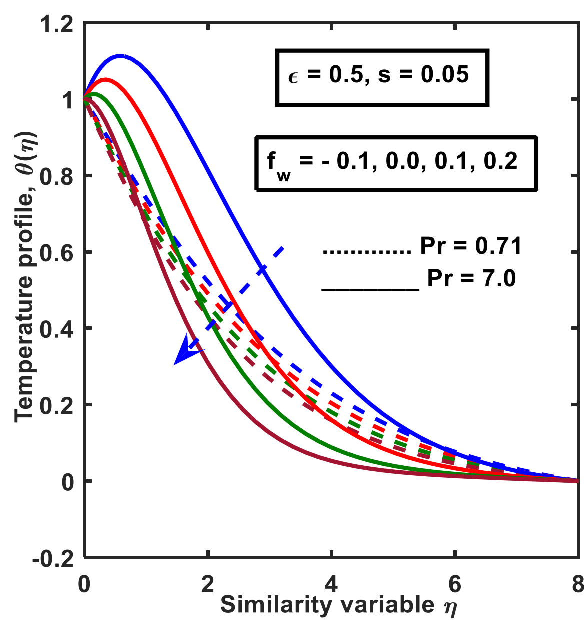

(b)

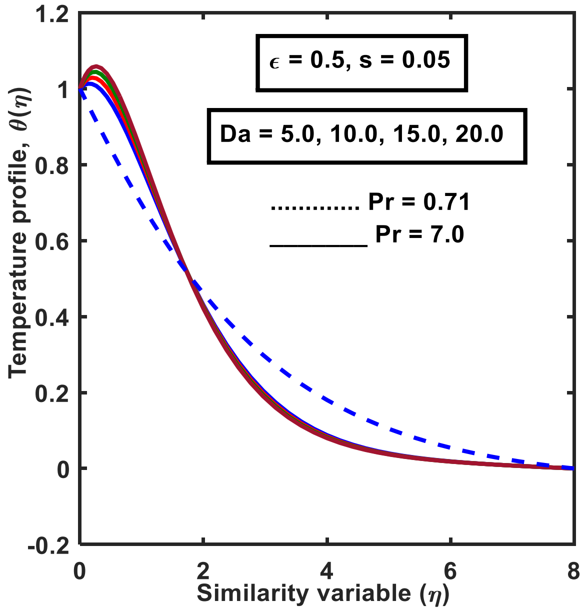

(c)

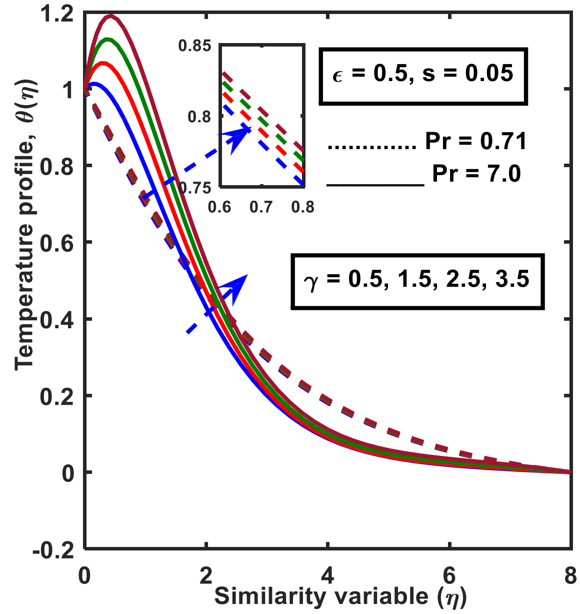

(d)

Figure 6. 15 Effect of Q^*, f_w, Da, and γ on temperature profile $\theta(\eta)$ when (a) ε = 0.5, s = 0.05, Pr = 0.71, Pr = 7.0 (b) ε = 0.5, s = 0.05, Pr = 0.71, Pr = 7.0 (c) ε = 0.5, s = 0.05, Pr = 0.71, Pr = 7.0, and (d) ε = 0.5, s = 0.05, Pr = 0.71, Pr = 7.0

Therefore, the temperature profile and thermal boundary layer thickness are directly proportional to these parameters but inversely proportional to the suction parameter.

6.3.2.4 Effect of Q^*, f_w, Da, and γ on Nusselt number

Figures 6.16(a) - 6.16(d) display the Nusselt number for the variations of the parameters Q^*, f_w,,Da, and γ respectively. From these figures, it is noticed that the Nusselt number increases with an increase of Injection parameter, and Darcy number but decreases for heat generation and drag inertia parameter. It is also mentioned that when Q^* increases from 0.5 to 9.5 and γ increases from 0.5 to 5.5, there are 15 %, and 2.6%, decrease in the Nusselt number in the case of s = 0.05, whereas the corresponding decrease is 52.4%, and 5.2% in case of s = 2.0. Again, when f_w increases from 0.2 to 3, and Da increases from 5.0 to 10.0, there are 147% and 1.7% increase of Nusselt number in the case of s = 0.05, whereas the corresponding increase is 91.5% and 0.4% in the case of s = 2.0.

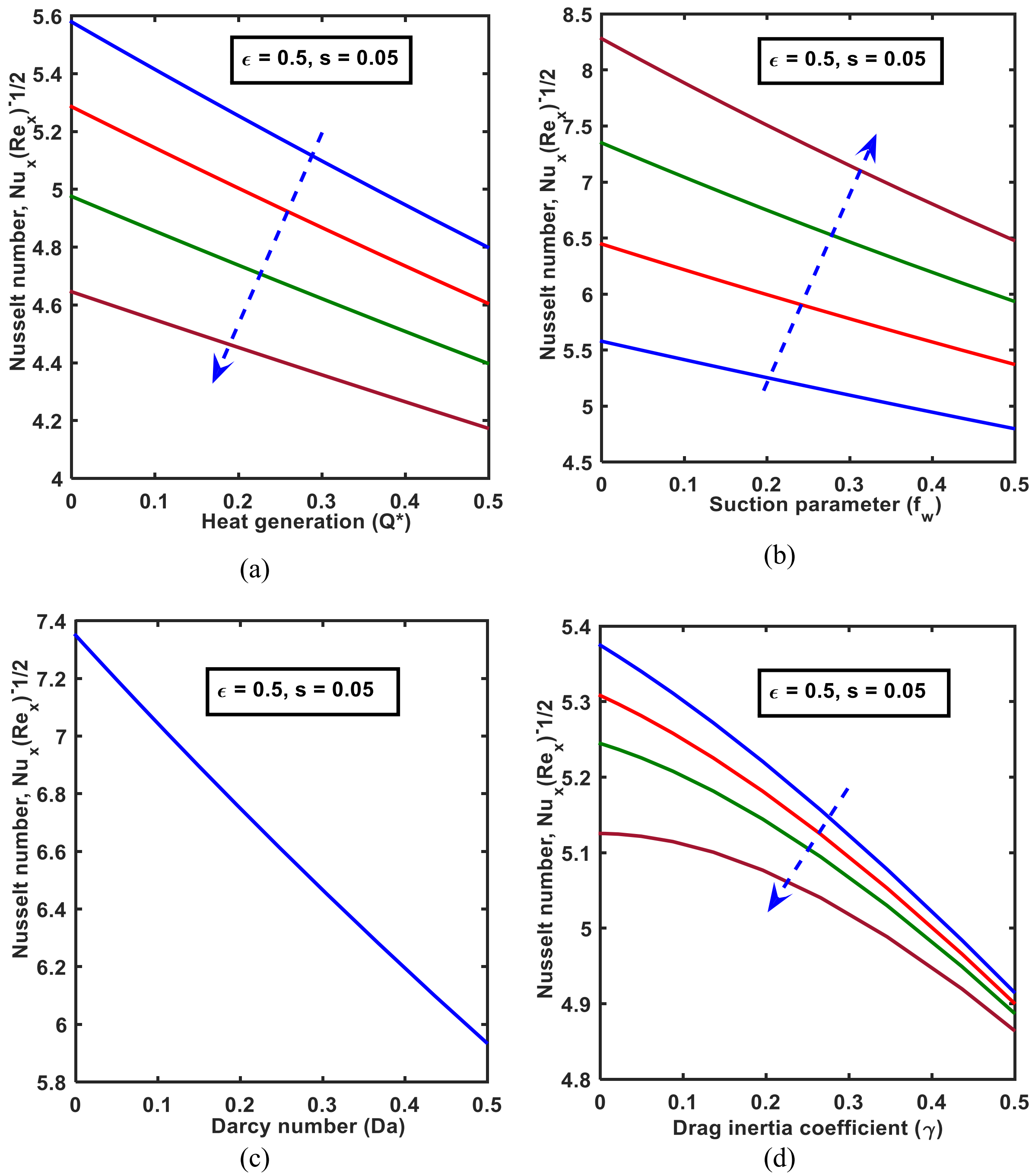

Figure 6. 16 Effect of Q^*, f_w , Da , and γ on Nusselt number when (a) $\varepsilon = 0.5, s = 0.05$ (b) $\varepsilon = 0.5, s = 0.05$ (c) $\varepsilon = 0.5, s = 0.05$, and (d) $\varepsilon = 0.5, s = 0.05$

6.3.2.5 Effect of ϵ, Ec, s, and λ on the temperature profile

Figures 6.17(a) – 6.17(d) exhibits the behavior of velocity profile for various values of the stretching ratio parameter (ϵ), Eckert number (Ec), surface thickness parameter(s), and mixed convection parameter (λ) in the case of air (Pr = 0.71) and water (Pr = 7.0). These plots depict that the temperature profile of the viscous fluid and thermal boundary layer thickness affected significantly with raising the mentioned parameters except for the mixed convection parameter. From Figure 6.17(a), it is observed that in the case of air (Pr = 0.71), an increase in λ the velocity profile remains constant, that is, there is no change in the velocity profile is noticed throughout the boundary layer, whereas, for the case of water, the changes are insignificant. In the case of water (Pr = 7.0) with increasing stretching ratio parameter (ϵ), Eckert number (Ec), and surface thickness parameter(s), the accelerating effect is more prominent than for air (Pr = 0.71). Therefore, the thermal boundary layer thickness is higher for water when compared with air. The temperature attains its minimum in connection with the stretching ratio parameter, Eckert number, and surface thickness parameter in the case of air but shooting up the profiles near the surface of the bullet-shaped object within the region $\eta < 0.1$ and then the profile decreases sharply to meet the boundary condition asymptotically.

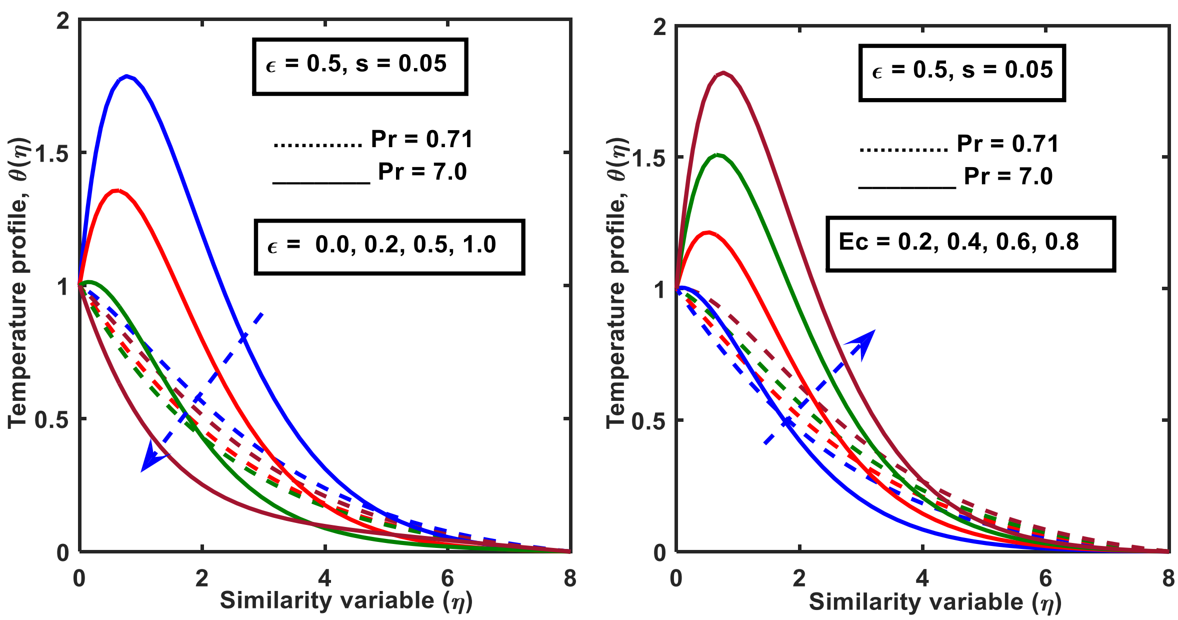

(a) (b)

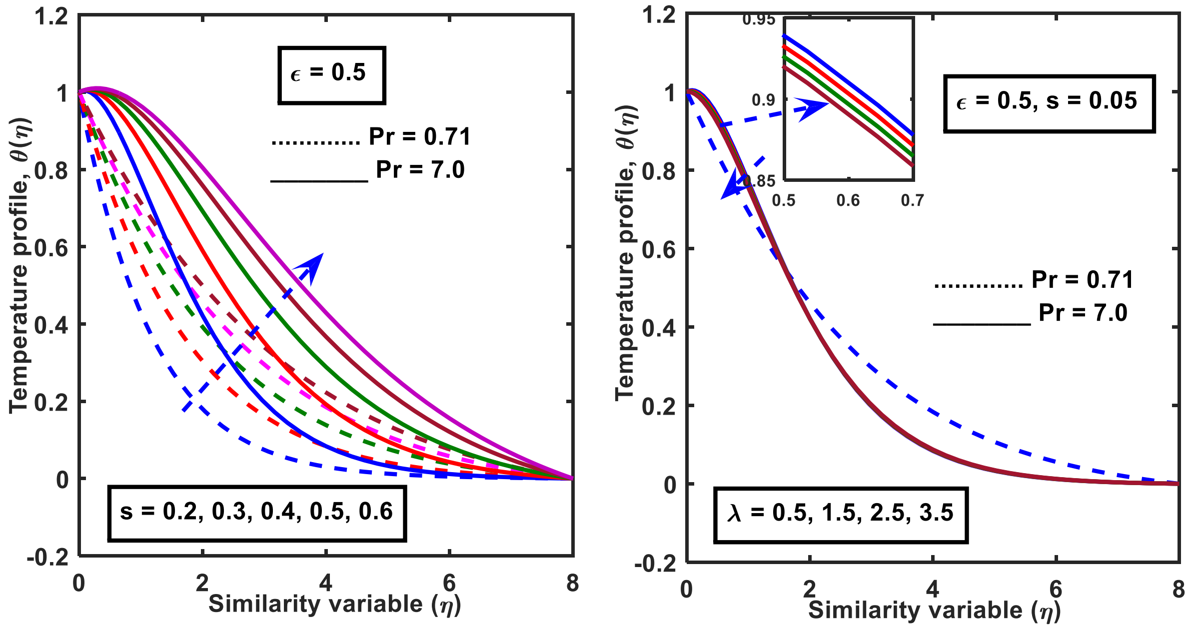

(c) (d)

Figure 6. 17 Effect of ϵ, Ec, s, and λ on temperature profile when (a) $\varepsilon = 0.5$, $s = 0.05$, Pr = 0.71, Pr = 7.0 (b) $\varepsilon = 0.5$, $s = 0.05$, Pr = 0.71, Pr = 7.0 (c) $\varepsilon = 0.5$, $s = 0.05$, Pr = 0.71, Pr = 7.0, and (d) $\varepsilon = 0.5$, $s = 0.05$, Pr = 0.71, Pr = 7.0

The temperature profile inside the boundary layer region enhances with the increase of stretching ratio parameter because the velocity profiles decrease for the effect of this parameter which tends to store more fluid inside the boundary layer region. Again, raising the values of Ec produce extra heat energy in the fluid because of frictional heating as a result the temperature enhances at any given point. On the other hand, an increase in s enhances the surface area of the object which provides more resistance against the fluid motion as a result more fluid particles are stored within the boundary layer that cases the temperature increases.

6.3.2.6 Effect of ϵ, Ec, s, and λ on Nusselt number

Figures 6.18(a) - 6.18(d) depict the variations of Nusselt number for the effect of ϵ, Ec, s, and λ respectively. From these figures, it is noticed that the Nusselt number decreases with an increase of Eckert number (Ec), and surface thickness parameter (s) but increases for stretching ratio parameter whereas mixed convection parameter has no effect.

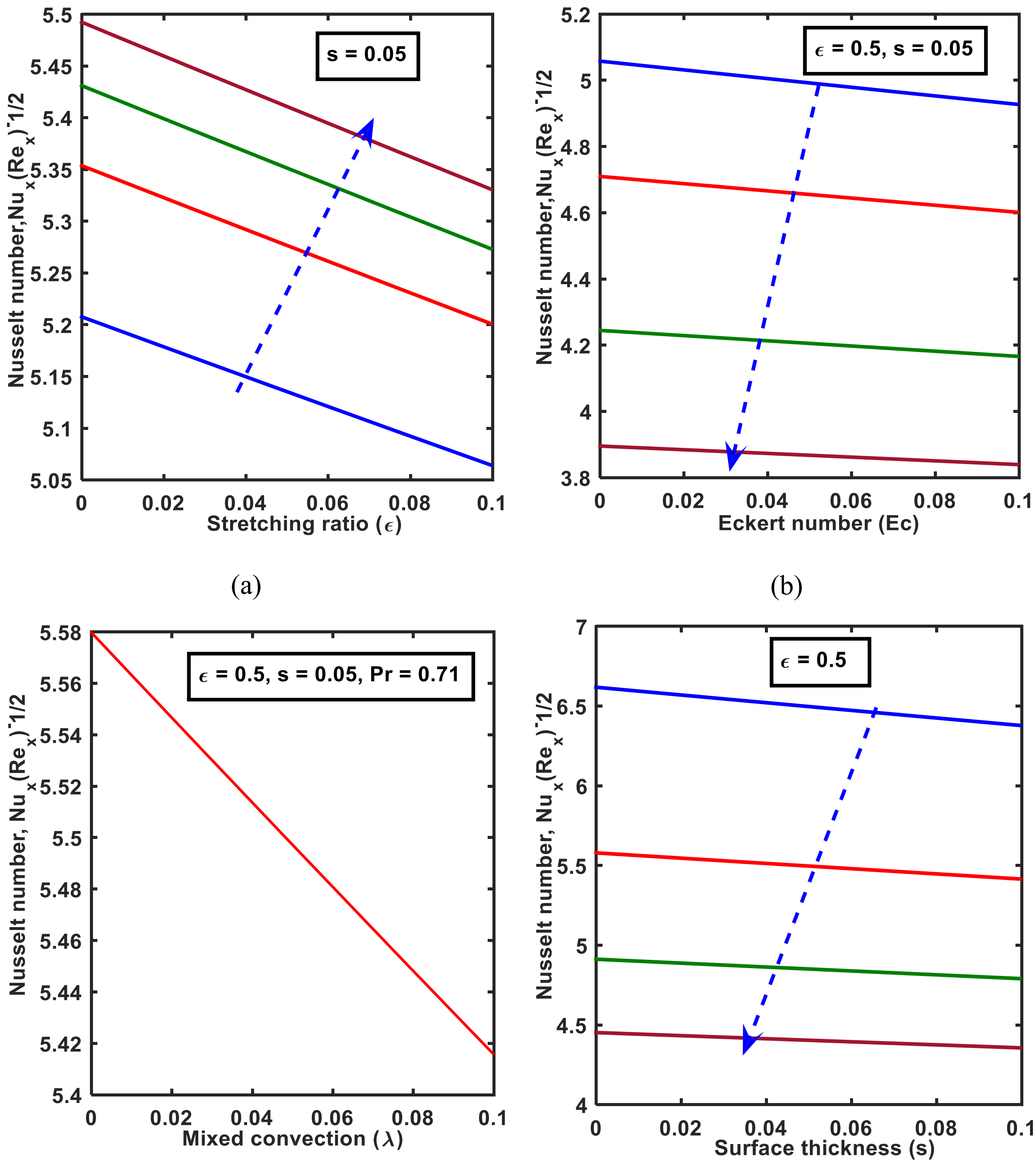

Figure 6. 18 Effect of ϵ, Ec, s, and λ on Nusselt number when (a) $\varepsilon = 0.5$, $s = 0.05$ (b) $\varepsilon = 0.5$, $s = 0.05$ (c) $\varepsilon = 0.5$, $s = 0.05$, and (d) $\varepsilon = 0.5$, $s = 0.05$

It is also seen that ϵ increases from 0.2 to 0.8, and Ec increases from 0.2 to 3.0, there are 13.6 %, and 173.6%, decrease in the Nusselt number in case of s = 0.05, whereas the corresponding decrease is 20% and 249.7% in case of s = 2.0. On the other hand, when s increases from 0.2 to 1.0, there is a 64.8% increase in the Nusselt number in the case of s = 0.05 and the corresponding increase is 25.6% in the case of s = 2.0.

The graph of temperature profile represents that the fluid temperature within the boundary layer region is getting lower due to Prandtl number (Pr), stretching ratio parameter (ϵ), location parameter (X), unsteady parameter (A), and suction parameter (f_w) whereas surface thickness parameter (s), magnetic parameter (M), heat generation parameter (Q^*), Darcy number (Da), drag inertia coefficient (γ) and Eckert number (Ec) have a reverse effect on it throughout the boundary layer region. From these figures, it is also revealed that in the case of a thicker bullet-shaped object (s = 2.0) the temperature profile does not approach the ambient condition asymptotically but intersects the vertical axis with a steep angle and the thermal boundary layer structure has no definite shape whereas in the case of a thinner bullet-shaped object (s = 0.05) the temperature profile converge the ambient condition asymptotically and the boundary layer structure has a definite shape. It is also mentioned that the thinner bullet-shaped object shows a thinner thermal boundary layer because the heat transfer rate is higher than the thicker bullet-shaped object in both static and moving bullet-shaped objects.

6.3.3 Stream function

Figure 6.19 (a) – (d) portrays the streamline plotting for both the thinner and thicker bullet-shaped objects. The streamlines are like a bunch of rays and later on, the branch grows, significant growth is observed. It is noticed that the fluid particle traces a definite curve along x-direction past fixed a bullet-shaped object. From Figures (a) - (d) it is revealed that the flow pattern growth ascends as the starching ratio parameter effect ascends whereas the reverse trend happens for stream-wise coordinates. It is also noticed that the isotherms look reduced in thinner bullet-shaped objects and the stream plots are less shaded than the thicker bullet-shaped object.

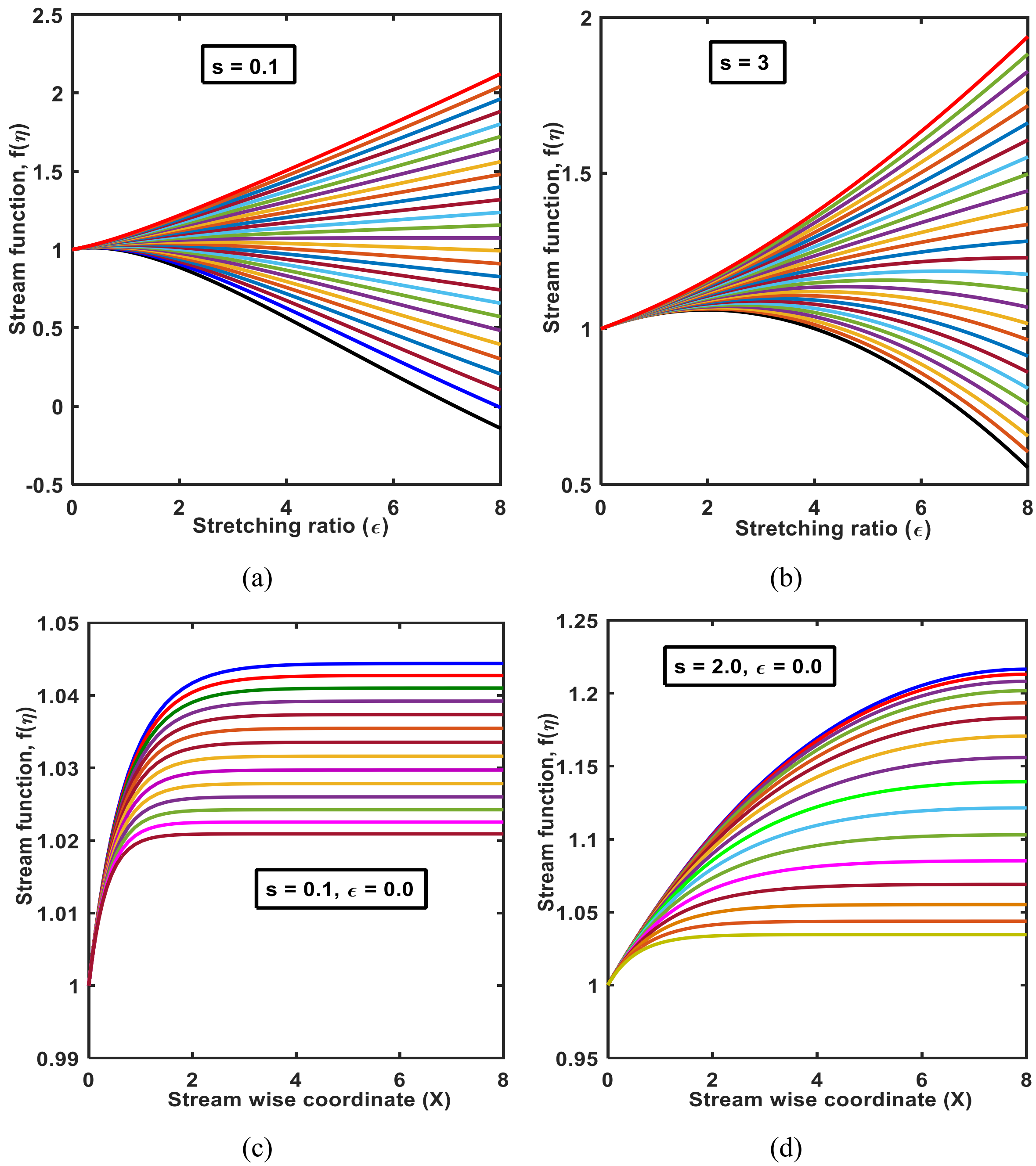

Figure 6. 19 **(a)** Stream lines for stretching ratio parameter (ϵ) when $s = 0.1$ (b) Stream lines for stretching ratio parameter (ϵ) when $s = 3.0$ (c) Stream lines for stream wise coordinate (X) when $s = 0.1$, $\epsilon = 0.0$ (d) Stream lines for stream wise coordinate (X) when $s = 2.0$, $\epsilon = 0.0$

There is also a less-intensification in the isotherms for the thinner bullet-shaped object with its high yield stress. The gap within the streamlines enhances as stream-wise coordinate enhances.

Figure 6.20 (a) – (d) also represents the streamline plotting for both the thinner and thicker bullet-shaped objects. The gap within the streamlines reduces as surfaces thickness parameter, magnetic parameter, and Darcy number enhances. From Figures (a) - (d) it is revealed that the flow pattern growth descends as the magnetic parameter and surface thickness parameter effect ascends whereas the reverse trend happens for the Darcy number. It is also noticed that the isotherms look reduced in thinner bullet-shaped objects and the stream plots are less shaded than the thicker bullet-shaped object. There is also a less-intensification in the isotherms for the thinner bullet-shaped object with its high yield stress.

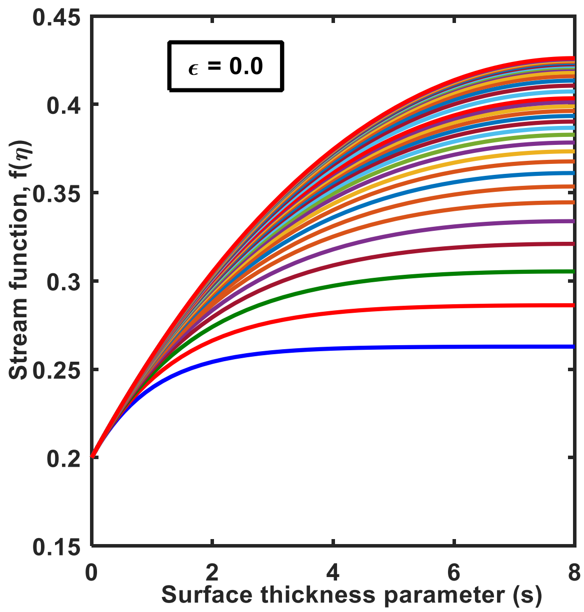

(a)

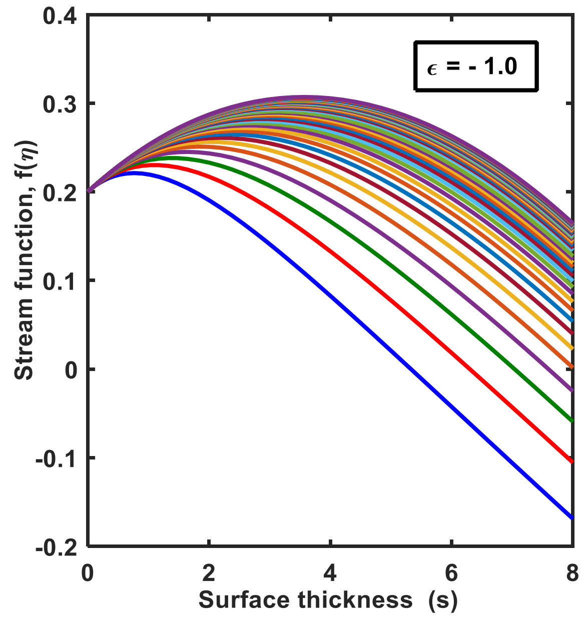

(b)

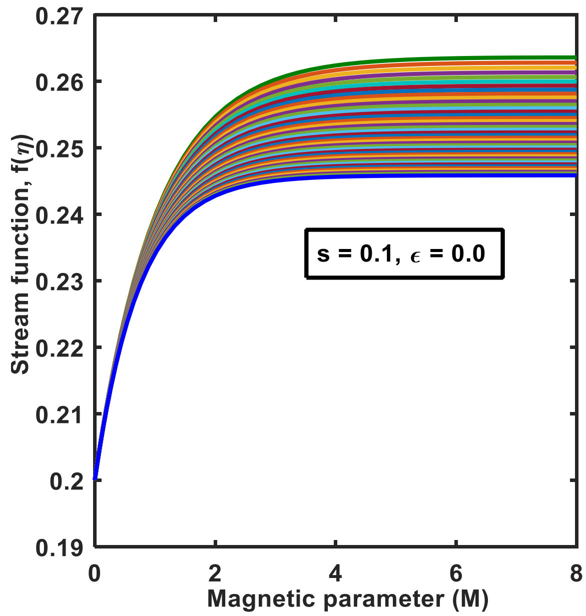

(c)

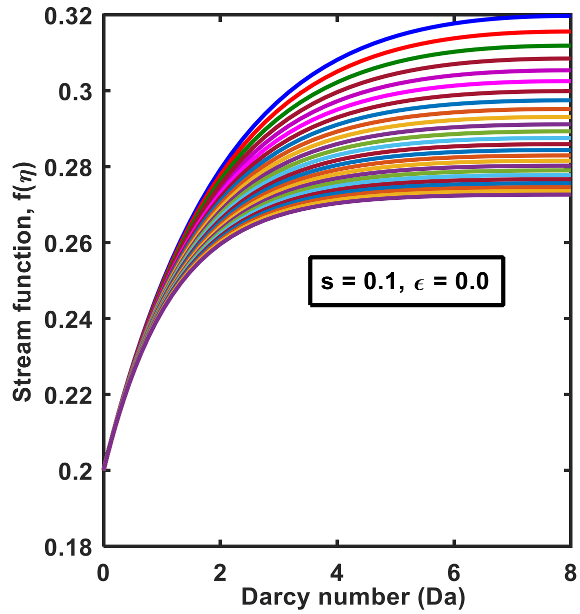

(d)

Figure 6. 20 (a) Stream lines for surface thickness parameter (s) when $\epsilon = 0.0$ (b) Stream lines for surface thickness parameter (s) when $\epsilon = -1.0$ (c) Stream lines for magnetic parameter (M) when $\epsilon = 0.0$, s = 0.1, and (d) Stream lines for Darcy number (Da) when $\epsilon = 0.0$, s = 0.1.

Table 6.2 displays the variation in Nusselt number for different values of the magnetic parameter (M), unsteady parameter (A), heat generation parameter (Q^*), surface thickness parameter (s), mixed convection parameter (λ), drag inertia coefficient (γ), Eckert number (Ec), location parameter (X), suction parameter (f_w), and Prandtl number (Pr) for various movement of the bullet-shaped object. From this table, it is possible to observe that the heat transfer rate increases for the magnetic parameter (M), unsteady parameter (A), location parameter (X), suction parameter (f_w), and Prandtl number (Pr) but decreases for heat generation parameter (Q^*), surface thickness parameter (s), and Eckert number (Ec) in the case of $\epsilon = 0.0$, and $\epsilon = 0.2$. On the other hand, mixed convection parameter (λ), Darcy number (Da), and drag inertia coefficient (γ) do not affect the rate of heat transfer. Therefore, heat transfer rate is high in $\epsilon = 0.2$ cases, when compared with $\epsilon = 0.0$ case. At this point, it is highlighted that for reducing the heat transfer rate we have to use static ($\epsilon = 0.0$) bullet-shaped object.

Table 6. 2 Values of Nusselt number which is equivalent to temperature gradient for different values of *M, A, Q*, ϵ, λ, γ, Ec, X,* f_w, *Da,* and Pr

M	A	Q^*	s	λ	γ	Ec	X	f_w	Pr	Da	$\lVert -\theta'(0) \rVert$ $\epsilon = 0.2$	$\lVert -\theta'(0) \rVert$ $\epsilon = 0.0$
0.5	0.2	0.5	0.2	0.5	0.5	0.2	0.5	1.0	0.71	5.0	**9.2492**	**8.8181**
5.5	0.2	0.5	0.2	0.5	0.5	0.2	0.5	1.0	0.71	5.0	**8.9594**	**8.5771**
10.5	0.2	0.5	0.2	0.5	0.5	0.2	0.5	1.0	0.71	5.0	**8.6957**	**8.3659**
0.5	**0.4**	0.5	0.2	0.5	0.5	0.2	0.5	1.0	0.71	5.0	**9.3315**	**8.9134**
0.5	**0.6**	0.5	0.2	0.5	0.5	0.2	0.5	1.0	0.71	5.0	**9.4155**	**9.0102**
0.5	**0.8**	0.5	0.2	0.5	0.5	0.2	0.5	1.0	0.71	5.0	**9.5012**	**9.1086**
0.5	0.2	**0.5**	0.2	0.5	0.5	0.2	0.5	1.0	0.71	5.0	**9.2492**	**8.8181**
0.5	0.2	**1.5**	0.2	0.5	0.5	0.2	0.5	1.0	0.71	5.0	**9.1221**	**8.6873**
0.5	0.2	**2.5**	0.2	0.5	0.5	0.2	0.5	1.0	0.71	5.0	**8.9924**	**8.5536**
0.5	0.2	0.5	**0.2**	0.5	0.5	0.2	0.5	1.0	0.71	5.0	**9.2492**	**8.8181**
0.5	0.2	0.5	**0.3**	0.5	0.5	0.2	0.5	1.0	0.71	5.0	**6.4382**	**6.1327**
0.5	0.2	0.5	**0.4**	0.5	0.5	0.2	0.5	1.0	0.71	5.0	**5.1291**	**4.8903**
0.5	0.2	0.5	0.2	**0.5**	0.5	0.2	0.5	1.0	0.71	5.0	**9.2492**	**8.8181**
0.5	0.2	0.5	0.2	**1.5**	0.5	0.2	0.5	1.0	0.71	5.0	**9.2492**	**8.8181**
0.5	0.2	0.5	0.2	**2.5**	0.5	0.2	0.5	1.0	0.71	5.0	**9.2492**	**8.8181**
0.5	0.2	0.5	0.2	0.5	**0.5**	0.2	0.5	1.0	0.71	5.0	**9.2492**	**8.8181**
0.5	0.2	0.5	0.2	0.5	**1.5**	0.2	0.5	1.0	0.71	5.0	**9.2492**	**8.8181**
0.5	0.2	0.5	0.2	0.5	**2.5**	0.2	0.5	1.0	0.71	5.0	**9.2492**	**8.8181**
0.5	0.2	0.5	0.2	0.5	0.5	**0.2**	0.5	1.0	0.71	5.0	**9.2492**	**8.8181**
0.5	0.2	0.5	0.2	0.5	0.5	**0.4**	0.5	1.0	0.71	5.0	**8.4852**	**7.6875**
0.5	0.2	0.5	0.2	0.5	0.5	**0.6**	0.5	1.0	0.71	5.0	**7.7237**	**6.5578**
0.5	0.2	0.5	0.2	0.5	0.5	0.2	**0.5**	1.0	0.71	5.0	**9.2492**	**8.8181**
0.5	0.2	0.5	0.2	0.5	0.5	0.2	**1.0**	1.0	0.71	5.0	**10.5666**	**10.0822**

0.5	0.2	0.5	0.2	0.5	0.5	0.2	**1.5**	1.0	0.71	5.0	**12.2154**	**11.6588**
0.5	0.2	0.5	0.2	0.5	0.5	0.2	0.5	**1.0**	0.71	5.0	**9.2492**	**8.8181**
0.5	0.2	0.5	0.2	0.5	0.5	0.2	0.5	**1.2**	0.71	5.0	**10.0655**	**9.6031**
0.5	0.2	0.5	0.2	0.5	0.5	0.2	0.5	**1.4**	0.71	5.0	**10.8885**	**10.3441**
0.5	0.2	0.5	0.2	0.5	0.5	0.2	0.5	1.0	**0.71**	5.0	**9.2492**	**8.8181**
0.5	0.2	0.5	0.2	0.5	0.5	0.2	0.5	1.0	**1.0**	5.0	**10.1785**	**9.2185**
0.5	0.2	0.5	0.2	0.5	0.5	0.2	0.5	1.0	**7.0**	5.0	**29.4108**	**17.8296**
0.5	0.2	0.5	0.2	0.5	0.5	0.2	0.5	1.0	0.71	**5.0**	**9.2492**	**8.8181**
0.5	0.2	0.5	0.2	0.5	0.5	0.2	0.5	1.0	0.71	**7.0**	**9.2492**	**8.8181**
0.5	0.2	0.5	0.2	0.5	0.5	0.2	0.5	1.0	0.71	**10.0**	**9.2492**	**8.8181**

6.4 Correlation and Regression Analysis for Skin Friction Coefficient

From Table 6.3 it is observed that the unsteady parameter (A) and drag inertia coefficient (γ), are positively correlated with the skin friction but magnetic parameter (M), Darcy number (Da), location parameter (X), mixed convection parameter (λ), surface thickness parameter (s), and suction parameter (f_w) are positively correlated. Therefore, a positive correlation indicates that higher values for one variable tend to be related to higher values for the other variable but a negative correlation indicates that higher values for one variable tend to be related to lower values for the other variable. Hence, the skin friction is a decreasing function of the magnetic parameter (M), Darcy number (Da), location parameter (X), mixed convection parameter (λ), surface thickness parameter (s), and suction parameter (f_w) but an increasing function of the unsteady parameter (A), and drag inertia coefficient (γ).

On the other hand, it is seen that the statistically significant parameters are highlighted in the tables because the numerical values of these parameters are greater equal to 0.25. Therefore, at least a 95% chance for the true relationship between these controlling parameters and velocity gradient.

Table 6. 3 Correlation coefficient between the velocity gradient and controlling parameters by taking 3rd order coefficient in the case of $\varepsilon > 1$

	M	A	Da	s	λ	γ	X	f_w
M	1.00							
A	-0.03	1.00						
Da	-0.07	-0.09	1.00					
s	-0.08	-0.10	-0.09	1.00				
λ	-0.07	-0.09	-0.08	-0.09	1.00			
γ	-0.07	-0.09	-0.08	-0.09	-0.08	1.00		
Ec	-0.07	-0.09	-0.08	-0.09	-0.08	-0.08		
X	-0.07	-0.09	-0.08	-0.09	-0.08	-0.08	1.00	
f_w	-0.07	-0.09	-0.08	-0.09	-0.08	-0.08	-0.08	1.00
$f''(\eta)$	-0.28	0.43	-0.32	-0.25	-0.15	0.35	-0.25	-0.26

Table 6.4 depicts that the unsteady parameter (A), surface thickness parameter (s), and mixed convection parameter (λ), is negatively correlated with the skin friction but magnetic parameter (M), Darcy number (Da), location parameter (X), drag inertia coefficient (γ), and suction parameter (f_w) are positively correlated. Therefore, the skin friction is an increasing function of the magnetic parameter (M), Darcy number (Da), location parameter (X), drag inertia coefficient (γ), and suction parameter (f_w) but a decreasing function of the unsteady parameter (A), surface thickness parameter (s), and mixed convection parameter (λ)

Table 6. 4 Correlation coefficient between the velocity gradient and controlling parameters by taking 2nd order coefficient in the case of $\varepsilon < 1$

	M	A	s	λ	γ	X	fw	Da
M	1.00							
A	-0.03	1.00						
s	-0.06	-0.07	1.00					
λ	-0.07	-0.09	-0.07	1.00				
γ	-0.07	-0.09	-0.07	-0.08	1.00			
Ec	-0.07	-0.09	-0.07	-0.08	-0.08			
X	-0.07	-0.09	-0.07	-0.08	-0.08	1.00		
fw	-0.07	-0.09	-0.07	-0.08	-0.08	-0.08	1.00	
Da	0.03	0.04	0.03	0.04	0.04	0.04	0.04	1.00
Pr	-0.04	-0.05	-0.04	-0.05	-0.05	-0.05	-0.05	-0.45
$f''(\eta)$	0.27	-0.19	-0.31	-0.17	0.19	0.27	0.91	0.19

In Table 6.5, the parameters heat generation and Eckert number are not statistically significant because the P – VALUE is not less than 0.05 which are highlighted in the table. So from Table 6.5, the significant variables are magnetic parameter, unsteady parameter, location parameter, mixed convection parameter, stretching ratio parameter, surface thickness parameter, Drag inertia coefficient, suction parameter, and Darcy number.

Table 6. 5 Regression analysis between the velocity gradient and controlling parameters by taking 1st order coefficient

Regression Statistics						
Multiple R	1.00					
R Square	0.99					
Adjusted R Square	0.96					
Standard Error	0.28					
Observations	42.00					
	df	SS	MS	F	Significance F	
Regression	12.00	344.48	28.71	393.11	0.00	
Residual	30.00	2.39	0.08			
Total	42.00	346.87				
	Coefficients	Standard Error	t Stat	P-value	Lower 95%	Upper 95%
Intercept	-10.77	0.34	-31.85	0.00	-11.47	-10.08
M	-0.18	0.02	-10.81	0.00	-0.21	-0.14
A	-0.16	0.09	-2.02	0.05	-0.35	0.00
Q^*	0.03	0.03	1.29	0.21	-0.02	0.09
ϵ	6.85	0.41	16.64	0.00	6.01	7.70
λ	0.11	0.06	1.95	0.06	-0.01	0.23
γ	0.36	0.06	6.27	0.00	0.24	0.48
Ec	-0.04	0.09	-0.47	0.65	-0.23	0.14
X	-1.58	0.08	-19.15	0.00	-1.75	-1.41
fw	-4.60	0.09	-51.26	0.00	-4.79	-4.42
Da	1.18	0.41	2.86	0.01	0.34	2.02
s	13.65	0.82	16.57	0.00	11.97	15.34

From this table, the regression model can be written as

$$f''(\eta) = -10.8 - 0.2M - 1.6X + 0.03Q^* - 0.04Ec + 0.1\lambda - 0.2A + 6.9\varepsilon + 0.4\gamma - 4.6f_w + 1.2Da + 13.7s$$

From this regression model, it is observed that if we increase the one unit value of the controlling parameter M, then the average decrease of the skin friction by -10.0. In the same way, we can predict the other values of the skin friction for the remaining parameters. It is also mentioned that the negative coefficient of the parameters means a decrease of the velocity gradient and the positive coefficient means an increase of the velocity gradient.

6.5 Correlation and Regression Analysis for Nusselt number

From Table 6.6 it is observed that the Nusselt number is negatively correlated with magnetic parameter (M), heat generation parameter(Q^*), Eckert number (Ec), surface thickness parameter (s) and drag inertia coefficient (γ) whereas positively correlated with unsteady parameter (A), Prandtl number (Pr), location parameter (X), and suction parameter (f_w). Therefore, the Nusselt number is an increasing function of the unsteady parameter (A), Prandtl number (Pr), location parameter (X), and suction parameter (f_w), and decreasing function of magnetic parameter (M), heat generation parameter(Q^*), Eckert number (Ec), surface thickness parameter (s) and drag inertia coefficient (γ).

Table 6. 6 Correlation coefficient between the temperature gradient and controlling parameters by taking 3rd order coefficient

	M	A	Q^*	Pr	s	γ	Ec	X	f_w
M	1.00								
A	-0.06	1.00							
Q^*	-0.06	-0.06	1.00						
Pr	-0.05	-0.05	-0.05	1.00					
s	0.00	0.00	0.00	0.00	1.00				
γ	-0.07	-0.07	-0.07	-0.06	0.00	1.00			
Ec	-0.07	-0.07	-0.07	-0.06	0.00	-0.08	1.00		
X	-0.07	-0.07	-0.07	-0.07	-0.07	-0.07	-0.06	1.00	
f_w	-0.06	-0.06	-0.06	-0.05	0.00	-0.07	-0.07	-0.04	1.00
$\theta'(\eta)$	-0.11	0.13	-0.29	0.67	-0.16	-0.13	-0.43	0.23	0.36

Table 6.7 represents the regression analysis for the controlling parameters and temperature gradient. It is noticed that the stretching ratio parameter, mixed convection parameter, and Darcy number does not statistically significant because the P-values is greater than 0.05 whereas the significant variables are magnetic parameter, unsteady parameter, heat generation parameter, location parameter, surface thickness parameter, Prandtl number, Drag inertia coefficient, suction parameter, and Eckert number.

From Table 6.7, the regression model is
$\theta'(\eta) = 8.68 - 0.05M + 0.67\,\mathrm{Pr} - 0.11Q^* - 1.21Ec + 0.03\lambda + 0.57A + 0.15\varepsilon - 8.53s - 0.14\gamma + 2.13f_w - 0.02Da$
From this model, it is observed that if we change the one-unit value of the parameter M then we will get the average decrease of the temperature gradient. It is also mentioned that the negative coefficient of the parameters means a decrease of the temperature gradient and the positive coefficient means the increase of the temperature gradient.

Table 6. 7 Regression analysis between the temperature gradient and controlling parameters by taking 1st order coefficient

Regression Statistics						
Multiple R	0.94					
R Square	0.89					
Adjusted R Square	0.84					
Standard Error	0.45					
Observations	43.00					
	df	SS	MS	F	Significance F	
Regression	11.00	49.27	4.48	21.80	0.00	
Residual	31.00	6.37	0.21			
Total	42.00	55.64				
	Coefficients	Standard Error	t Stat	P-value	Lower 95%	Upper 95%
Intercept	8.68	1.64	5.29	0.00	5.33	12.03
M	-0.05	0.03	-1.81	0.05	-0.10	0.01
A	0.57	0.31	1.85	0.04	-0.06	1.20
Q^*	-0.11	0.03	-4.37	0.00	-0.17	-0.06
ϵ	0.15	0.23	0.65	0.52	-0.32	0.62
λ	0.03	0.13	0.22	0.83	-0.24	0.29
Pr	0.67	0.07	10.1	0.00	0.54	0.81
s	-8.53	3.21	-2.66	0.01	-15.07	-1.99
γ	-0.14	0.07	-2.01	0.05	-0.28	0.00
Ec	-1.21	0.19	-6.42	0.00	-1.59	-0.82
Da	-0.02	0.01	-1.40	0.17	-0.04	0.01
f_w	2.13	0.40	5.27	0.00	1.31	2.96

For the affirmation of the present numerical method, it has been compared to MATLAB routine bvp4c which is a shooting iterative scheme. This has been depicted in Table 6.8. From Table 6.8, it is observed that the present results completely agree with the results obtained by bvp4c. It is noticed that convergence of SQLM occurs as early as the fifth iteration and the method is very faster which saving CPU time. This provides confidence to the proposed method. It is also observed in Table 6.8 that the friction factor and heat transfer rate are greatly affected by the surface thickness parameter (s).

Table 6. 8 Comparison of the SQLM results of velocity gradient and temperature gradient with those obtained by bvp4c for different values of the surface thickness parameter (s) by taking $M = X = \lambda = \gamma = Ec = 0.5$, $\Pr = 1.0$, $A = f_w = 0.1$, $\mathrm{Da} = 5.0$, $\epsilon = Q^* = 1.5$

Parameter	$f''(0)$			$\lVert -\theta'(0) \rVert$		
s	SQLM	bvp4c	% Of error	SQLM	bvp4c	% Of error
0.10	5.908170	5.908149	0.0000035	5.420916	5.420909	0.0000013
0.15	4.398754	4.398695	0.0000134	3.790928	3.790942	-0.0000035
0.20	3.597668	3.597645	0.0000063	2.971469	2.971479	-0.0000034
0.25	3.091667	3.091659	0.0000026	2.476453	2.476443	0.0000042
0.30	2.738730	2.738695	0.0000125	2.143961	2.143958	0.0000014

CHAPTER SEVEN

CONCLUSION AND RECOMMENDATIONS

Conclusion and recommendations have been incorporated in this chapter. Numerical computations have been carried out for encountered linear and non-linear ordinary and partial differential equations in various flow problems. The governing equations have been solved under particular initial and boundary conditions with the help of SQLM and the standard software package MATLAB.

7.1 Conclusion

The axisymmetric MHD boundary layer flow and heat transfer have been analyzed in this dissertation while the bullet-shaped object moves with power-law velocity in a Newtonian fluid. In sequence, the fluid flow and heat transfer have been investigated in two types of flow geometries such as the thicker surface $(s \geq 2)$ and the thinner surface $(0 < s < 2)$ of the bullet-shaped object. The influence of mentioned controlling parameters on velocity profile, temperature profile, skin friction coefficient, and Nusselt number has also been studied. The transformed ordinary differential equations have been solved using SQLM. This method was found to be very accurate with tolerance levels of between 10^{-12} and 10^{-13}. The numerical computations have been done through the collocation method by MATLAB package. The accuracy and convergence of the SQLM have been determined with the error infinity norms and the residual error infinity norms, respectively.

The present analysis enables us to draw the following conclusions:

I. The SQLM along with the Chebyshev collocation method provides a more accurate and quicker convergence scheme.

II. Velocity profile squeezes for the limit $\varepsilon > 1$ and in the limit, $\varepsilon < 1$ the velocity profile expands with increasing the shape and size (surface thickness parameter, s) of the bullet-shaped object but the boundary layer thickness expands in both cases.

III. The skin friction coefficient is higher in the limit $\varepsilon > 1$ compared to the case $\varepsilon < 1$. Therefore, for reducing the friction between the fluid particles and the surface of the bullet-shaped objects we have to apply $\varepsilon < 1$ case.

IV. The velocity profile and momentum boundary layer thickness expand due to the effects of the magnetic parameter (M), mixed convection parameter (λ), location parameter (X), Darcy number (Da), suction parameter (f_w), and stretching ratio parameter (ϵ) whereas surface thickness parameter (s), unsteady parameter (A), drag inertia coefficient (γ), and Eckert number (Ec) have a reverse effect on it in the case of $\varepsilon > 1$ for both of the thicker $(s \geq 2)$ and the thinner $(0 < s < 2)$ surfaces of the bullet-shaped object. On the other hand, in the case of $\varepsilon < 1$ the velocity profile squeezes but boundary layer thickness enhances due to the effects of the magnetic parameter (M), Darcy number (Da), suction parameter (f_w), and location parameter (X) whereas surface thickness parameter (s) and unsteady parameter (A) have a reverse effect on it.

V. In the case of the thinner bullet-shaped object, $(0 < s < 2)$ the fluid velocity profile converges asymptotically to the free stream velocity at infinity whereas for a thicker bullet-shaped object $(s \geq 2)$ boundary conditions do not satisfy.

VI. Within the boundary layer region is to find lower due to the effects of Prandtl number (Pr), stretching ratio parameter, location parameter, unsteady parameter, and suction parameter (f_w) whereas surface thickness parameter, magnetic parameter, heat generation parameter (Q^*), Darcy number, drag inertia coefficient, and Eckert number (Ec) have a reverse effect on the fluid temperature throughout the boundary layer region. In the case of a thicker bullet-shaped object, $(s \geq 2)$ the temperature profile does not approach the ambient condition asymptotically but intersects the axis with a steep angle and the thermal boundary layer structure has no definite shape. In the case of a thinner bullet-shaped object, $(0 < s < 2)$ the temperature profile converges the ambient condition asymptotically and the boundary layer structure has a definite shape.

VII. Heat transfer rate is high in the case of stretching bullet-shaped object (ϵ = 0.2 cases) compare to the static bullet-shaped object (ϵ = 0.0 case). At this point, it is highlighted that for reducing the heat transfer rate we have to consider the static bullet-shaped object.

VIII. A thinner bullet-shaped object acts as a good cooling conductor compared to a thicker bullet-shaped object for both the cases of fixed and moving $(\varepsilon = 0 \text{ or} > 0)$ bullet-shaped objects.

IX. The skin friction coefficient at the bullet-shaped object decreases with increasing the magnetic parameter, unsteady parameter, location parameter, suction parameter, Darcy number, and drag inertia coefficient in the case of $\varepsilon > 1$.

X. The wall friction can be reduced much when a thinner bullet-shaped object $(0 < s < 2)$ is used rather than the thicker bullet-shaped object $(s \geq 2)$ in the case of stretching bullet-shaped object.

XI. The skin friction is a decreasing function of the magnetic parameter, unsteady parameter, location parameter, injection parameter, Darcy number, and drag inertia coefficient when $\varepsilon > 1$ but an increasing function of stretching ratio parameter, surface thickness parameter, and mixed convection parameter.

XII. A thin momentum boundary layer thickness has been found in a thinner bullet-shaped object $(0 < s < 2)$ than the thicker bullet-shaped object $(s \geq 2)$.

XIII. The thinner bullet-shaped object $(0 < s < 2)$ represents a thinner thermal boundary layer because the heat transfer rate is higher than the thicker bullet-shaped object $(s \geq 2)$.

XIV. At the bullet-shaped object the heat transfer rate is a decreasing function of the magnetic parameter, Eckert number, Darcy number, drag inertia coefficient, heat generation parameter, and surface thickness parameter while heat transfer rate is an increasing function of Prandtl number (*Pr*), suction parameter, location parameter, mixed convection parameter, stretching ratio parameter, and unsteady parameter.

XV. The skin friction coefficient is positively correlated with the unsteady parameter (A) and drag inertia coefficient (γ) but negatively correlated with the magnetic parameter (M), Darcy number (Da), location parameter (X), mixed convection parameter (λ), surface thickness parameter (s), and suction parameter (f_w). On the other hand, no correlation exists with the heat generation parameter, Prandtl number, and Eckert number.

XVI. At the bullet-shaped object heat transfer rate is negatively correlated with the magnetic parameter, Eckert number, Darcy number, drag inertia coefficient, heat generation parameter, and surface thickness parameter but it are positively correlated with the Prandtl number, injection parameter, location parameter, mixed convection parameter, stretching ratio parameter, and unsteady parameter.

XVII. The skin friction decreases with the increasing effects of surface thickness parameter, in the case of the steady flow but enhances in the case of the unsteady flow. The rest of the controlling parameters have a similar effect on fluid velocity and skin friction for both the steady and unsteady flow.

7.2 Recommendations

The present work has been carried out the axisymmetric boundary layer flow and heat transfer over a power-law stretching bullet-shaped object by using the SQLM. Since, the result indicates that the velocity and temperature distribution converge asymptotically to the free stream velocity at infinity in the case of the thinner bullet-shaped object $(0 < s < 2)$ whereas in the case of a thicker bullet-shaped object $(s \geq 2)$ it does not satisfy the far-field boundary conditions, so it is suggested to study this problem in the laboratory experiment for the application in the real-world problem. The present work can extend for further research:

- to determine the appropriate geometrical parameters of the bullet-shaped object such as width, thickness, angle of attack, and orientation.

- to determine the effects of various parameters such as variable fluid properties, thermal conductivity, and the number & the dimensions of pores on thermal heat and fluid flow.
- can be oriented in three-dimensional modeling and simulation studies of the bullet-shaped object by considering non-Newtonian fluids.

REFERENCES

[1] Schlichting, H., and Gersten, K., "Boundary layer theory", 8th ed. Berlin: Springer-Verlag, 2000.

[2] Falkner, V. M., and Skan, S. W., " Some Approximate Solutions of the Boundary Layer Equations", *Philos. Mag.* vol.12, pp.865 – 896, 1931.

[3] Prandtl, L., "About fluid movements with very little friction", *In 1904 negotiations of the third International Congress of Mathematicians*, Heidelberg, Germany, Aug. 1904, pp. 484–491.

[4] Shateyi, S. and Muzara, H., "On Numerical Analysis of Carreau–Yasuda Nanofluid Flow over a Non-Linearly Stretching Sheet under Viscous Dissipation and Chemical Reaction Effects", *Computation* 2020, vol.8, pp. 1 -19, 2020.

[5] Bellman, R., Kalaba, R., "Quasi-linearization and nonlinear boundary value Problems", American Elsevier Publishing Company, New York, 1965.Abbasbandy, S., and Hayat, T., "Solution of the MHD Falkner-Skan flow by homotopy analysis method", *Commun. Nonlinear. Sci. Numer. Simul.*, vol. 14, pp. 3591–3598, 2009. 7

[6] Bellman, R., Jacquez J., Kalaba, R., and Schwimmer, S., "Quasi-linearization and the estimation of chemical rate constants from raw kinetic data", *Math. Biosci.,* vol.1, pp.71-76, 1967.

[7] Abbasbandy, S., and Hayat, T., "Solution of the MHD Falkner-Skan flow by homotopy analysis method", *Commun. Nonlinear. Sci. Numer. Simul.*, vol. 14, pp. 3591–3598, 2009.

[8] Abo-Eldahab, E. M., and Salem, A. M., "Hall effects on MHD free convection flow of a non-Newtonian power-law fluid at a stretching surface", *Int. Commun. Heat Mass Transf.*, vol. 31, pp. 343-354, 2004.

[9] Aftab, A., Javed, I. S., and Muhammad, S., "Dual solutions in a boundary layer flow of a power-law fluid over a moving permeable flat plate with thermal

radiation, viscous dissipation and heat generation/absorption”, *Fluids,* vol. 3, pp. 1-6, 2018.

[10] Ahmad, B., Nieto J. J., and Shahzad N., “Generalized quasi-linearization method for mixed boundary value problems”, *Appl. Math. Comput.*, vol.133, pp. 423-429, 2002.

[11] Ahmad, B., Nieto, J. J., and Shahzad, N., “The Bellman quasi-linearization method for Neumann problems”, *J. Math. Anal. Appl.*, vol. 257, pp. 356-363, 2001.

[12] Ajala, O. A., Aselebe, L. O., Abimbade, S. F., and Ogunsola, A. W., “Effect of magnetic fields on the boundary layer flow of heat transfer with variable viscosity in the presence of thermal radiation”, *Int. J. Sci. Res. Pub.,* vol. 9, no. 5, pp. 13-19, 2019.

[13] Ajaykumar, M., and Srinivasa, A. H., “Variable viscosity effects on unsteady MHD laminar boundary layer flow and heat transfer over a stretching sheet”, *AIP. Conf. Proc.,* vol. 2277, 2020.

[14] Alam, M. S., Asiya, K. M., Rahman, M. M., and Vajravelu, K., “Effects of variable fluid properties and thermophoresis on unsteady forced convective boundary layer flow along with a permeable stretching/shrinking wedge with variable Prandtl and Schmidt numbers”, *Int. J. Mech. Sci.,* vol. 105, pp. 191–205, 2016.

[15] Alarifi, I. M., Ahmed, G. A., and Osman, M., Liaquat, A. L., Ayed, M. B., Belmabrouk, H., and Tlili, I., “MHD flow and heat transfer over a vertical stretching sheet with heat sink or source effect”, *Symmetry 2019,* vol. 297, pp. 1-14, 2019.

[16] Asaithambi, A., “A finite-difference method for the solution of the Falkner-Skan equation”, *Appl. Math. Comput,* vol. 92, pp.135-141, 1998.

[17] Ashwini, G., and Eswara, A. T., “MHD Falkner-Skan Boundary Layer Flow with Internal Heat Generation or Absorption”, *Int. J. Math. Comput. Phy. Electr. Comput. Eng.,* vol. 6, pp. 556-559, 2012.

[18] Ashwini, G., and Eswara, A. T., “Unsteady MHD decelerating flow over a wedge with heat generation/absorption”, *Int. J. Math. Comput. Sci.,* vol. 1, pp. 303-309, 2015.

[19] Awaludin, I. S., Ishak, A., and Pop, I., “On the Stability of MHD Boundary Layer Flow over a Stretching/ Shrinking Wedge”, *Sci. Rep.,* vol.8, 2018.

[20] Daba, M., Devaraj, P., Subhashini, S. V., “Mixed convection boundary layer flow over a vertical stretching sheet with convective boundary condition and effect of partial slip”, *Front. Heat Mass Transf.,* vol. 6, pp. 1-6, 2015.

[21] Fatheah, A., and Hendi, H., “Analytic Solution for MHD Falkner-Skan Flow over a Porous Surface”, *J. Appl. Math*., vol. 2012, 9 pages, 2012.

[22] Fenuga, O. J., Hassan, A. R., Olanrewaju, P. O., “Mixed convection in MHD flow and heat transfer rate near a stagnation-point on a non-linear vertical stretching sheet”, *Int. J. Appl. Mech. Eng.,* vol.25, pp.37-51, 2020.

[23] Ganapathirao, M., Ravindran, R., and Momoniat, E., “Effects of chemical reaction, heat and mass transfer on an unsteady mixed convection boundary layer flow over a wedge with heat generation/absorption in the presence of suction or injection”, *Heat Mass Transf*., vol.51, pp. 289–300, 2015.

[24] Hartree D. R., “On an equation occurring in Falkner and Skan's approximate treatment of the equations of boundary layer”, Part II, Proc. Cambridge Philos, 1937.

[25] Hayat T., Hussain, M., Nadeem, S., and Mesloub, S., “Falkner-Skan wedge flow of a power-law fluid with mixed convection and porous medium”, *Comput. Fluids*, vol. 49, pp. 22–28, 2011.

[26] Hayat, T., Khan, I., Tamoor, M., Waqas, M., and Alsaedi, A., “Numerical simulation of heat transfer in MHD stagnation point flow of cross fluid model towards a stretched surface”, *Results Phys.,* vol.7, pp.1824–1827, 2017.

[27] Herwig, P. D., and Wickern, D. I., “The effect of variable properties on laminar boundary layer flow”, Heat *Mass Transf.,* vol. 20, pp. 47-57, 1986.

[28] Irfan, M. M., Farooq, M. A., Mushtaq, A., and Shamsi, Z. H., “Unsteady MHD Bio-nanofluid Flow in a Porous Medium with Thermal Radiation near a Stretching/Shrinking Sheet”, *Math. Probl. Eng.,* vol. 2020, pp. 14 pages, 2020.

[29] Ismoen, M., Karim, M. F., Mohammad, R., and Kandasamy, R., “Similarity and non-similarity solutions on flow and heat transfer over a wedge with power-law stream condition”, *Int. J. Innov. Mech. Eng. Adv. Mater.*, vol. 1, pp. 5-12, 2016.

[30] Jabeen , K., Mushtaq, M., and R. Akram, M., “Analysis of the MHD Boundary Layer Flow over a Nonlinear Stretching Sheet in a Porous Medium Using Semi-analytical Approaches”, *Math. Probl. Eng.,* vol. 2020, 9 pages, 2020.

[31] Jabeen, K., Mushtaq, M., and Akram, R. M., “A comparative study of MHD flow analysis in a porous medium by using differential transformation method and variational iteration method,” *J. contemp. appl. math.,* vol. 9, pp. 1–15, 2019.

[32] Jenifer, A. S., Saikrishnan, P., Lewis, R. W., “Unsteady MHD Mixed Convection Flow of Water over a Sphere with Mass Transfer,” *J. Appl. Comput. Mech.,* vol. 7, pp. 935-943, 2021.

[33] Kandasamy, R., Periasamy, S. R., and Prabhu, K. K., “Effects of chemical reaction, heat and mass transfer along with a wedge with heat source and concentration in the presence of suction or injection”, *Int. J. Heat Mass Transf.,* vol.48, pp. 1388–1394, 2005.

[34] Keshtkar, M., “The Falkner-Skan Flow over a Wedge with Variable Parameters”, *Int. J. Appl. Sci. Agric.*, vol. 9, pp.453-463, 2014.

[35] Krishna, V. M., Ahamad A. N., and Chamkha, A. J., “Hall and ion slip impacts on unsteady MHD convective rotating flow of heat generating/absorbing second-grade fluid”, *Alex. Eng. J.,* vol.60, pp. 845-858, 2021.

[36] Krishna, V. M., Ahamad, A. N., and Aljohani, F. A., "Thermal radiation, chemical reaction, Hall and ion slip effects on MHD oscillatory rotating flow of micro-polar liquid", *Alex. Eng. J.,* vol. 60*, ,*pp. 3467-3484, 2021.

[37] Krishna, V. M., Ahamad, A. N., and Chamkha, A. J., "Hall and ion slip effects on unsteady MHD free convective rotating flow through a saturated porous medium over an exponentially accelerated plate", *Alex. Eng. J.*, vol.59, pp. 565-577, 2020.

[38] Krishna, V.M., Reddy S. G., and Chamkha, A. J., "Heat and mass transfer on MHD free convective flow over an infinite non-conducting vertical flat porous plate", *Int. J. Fluid Mech. Res.,* vol. 46, pp.1-25. 2019.

[39] Kumar, P., and Krishnan, K., "Analysis of axisymmetric boundary layers", *J. Fluid Mech.*", vol. 849, pp. 927-941, 2018.

[40] Lakshmikantham, V., "An extension of the method of quasi-linearization", *J. Optim. Theory Appl.,* vol 82, pp 315-321, 1994.

[41] Lin, L., Zheng, L., Chen, Y., and Liu, F., "Fractional boundary layer flow and heat transfer over a stretching sheet with variable thickness", *J. Heat Transf.,* vol. 140, 9 pages, 2018.

[42] Mandelzweig, V. B., and Tabakin, F., "Quasi-linearization approach to nonlinear problems in physics with application to nonlinear ODEs", *Comput. Phys. Commun.,* vol. 141, pp 268-281, 2001.

[43] Marneni, N., and Ashraf, M., "Mixed convection flow over a permeable stretching wedge in the presence of heat generation/absorption, viscous dissipation, radiation, and ohmic heating", *Chem. Eng. Trans.,* vol. 45, pp. 955-960, 2015.

[44] Megahed, A. M., Reddy, G. M. and Abbas, W., "Modeling of MHD fluid flow over an unsteady stretching sheet with thermal radiation, variable fluid properties, and heat flux", *Math. Comput. Simul.,* vol. 2021, pp.18 pages, 2021.

[45] Menni, Y., Azzi, Chamkha, A. J., Azzi, A., and Zidani, C., "Numerical Analysis of Fluid Flow and Heat Transfer Characteristics of a New Kind of Vortex

Generators by Comparison with Those of Traditional Vortex Generators", *Int. J. Fluid Mech.*, vol. 47, pp. 23-42, 2020.

[46] Mustaqim, M. J., Fadzilah, M, A., Arifin, M. A., and Bachok, N., "A stability analysis of the stagnation-point flow of heat and mass transfer over a shrinking sheet with radiation and slip effects", *Int. J. Adv. Sci. Eng. Technol.,* vol.6, pp.34 – 38, 2018.

[47] Muthukumaran, C., and Bathrinathan, K., "Mathematical modeling of mixed convection boundary layer flow over a stretching sheet with viscous dissipation in presence of suction and injection", *Symmetry*, vol. 12, 15 pages. 2020.

[48] Muzara, H., Shateyi, S., and Marewo, G. T., "A numerical analysis of laminar boundary layer flow of a Jeffrey fluid past a vertical porous plate in the presence of thermal radiation and chemical reaction", *JP J. Heat Mass Transf.,* vol.17, pp. 309-340, 2019.

[49] Muzara, H., Shateyi, S., and Marewo, G. T., "On the bivariate spectral quasi-linearization method for solving the two-dimensional Bratu problem", *Open Phys.,* vol. 16, pp. 554-562, 2018.

[50] Muzara, H., Shateyi, S., and Marewo, G. T., "Spectral Quasi-Linearization Method For Solving The Bratu Problem", *Adv. Appl. Fluid Mech.,* vol. 21, pp. 449-463, 2018.

[51] Nageeb, A. H., Precious, S., and Sandile, S. M., "On unsteady MHD mixed convection in a nanofluid due to a stretching/shrinking surface with suction/injection using the spectral relaxation method", *Bound. Value Probl.,* vol. 2015, pp. 1-17, 2015.

[52] Nageeb, A., Haroun, H., Mondal, S., and Sibanda, P., "Effects of thermal radiation of mixed convection in an MHD nanofluid flow over a stretching sheet using a spectral relaxation method", *Int. J. Math. Comput. Phy. Electr. Comput. Eng.,* vol. 11, pp. 52-61, 2017.

[53] Najwa, N., Bachok, N., and Arifin, M. N., "Stability of Dual Solutions in Boundary Layer Flow and Heat Transfer over an Exponentially Shrinking Cylinder", *Indian J. Sci. Technol.*, vol. 9, 2016.

[54] Nandy, S. K., Mandal, R. K., "MHD stagnation-point flow and heat transfer of nanofluid over a shrinking surface", *J. Nanosci. Nanotechnol.,* vol. 1, pp. 183-192, 2015.

[55] Naramgari, S., and Sulochana, C., "MHD flow over a permeable stretching /shrinking sheet of a nanofluid with suction /injection", *Alex. Eng. J.*, vol. 55, pp. 819–827, 2016.

[56] Nasrin, R., and Alim, M. A., "Semi-empirical relation for forced convective analysis through a solar collector", *Sol. Energy,* vol. 105, pp. 455-467, 2014.

[57] Nield, D. A., and Bejan, A., "Convection in Porous Media", 3rd Edition. Springer-Verlag, New York, 2006.

[58] Nieto, J., "Generalized quasi-linearization method for a second-order ordinary differential equation with Dirichlet boundary conditions", *Proc. Amer. Math. Soc.,* vol. 125, pp. 2599-2604, 1997.

[59] Norihan, A. B., Wan, M. K., Adly, W. Z., Rohana, A. H., Biliana, B., and Ishak, A., "Boundary layer flow over a stretching sheet with a convective boundary condition and slip effect", *World Appl. Sci. J.,* vol. 17, pp. 49-53, 2012.

[60] Rajagopal, K. R., Gupta, A. S., and Na, T., Y., "A note on the Falkner–Skan flows of a non-Newtonian fluid", *Int. J. Non Linear Mech.,* vol. 18, pp. 313–320, 1983

[61] Raju, C. S. K., Sandeep, N., Sulochana, C., Sugunamma, V., and Jayachandra, B. M., "Radiation, inclined magnetic field and cross-diffusion effects on flow over a stretching surface", *J.* Nigerian *Math. Soc.,* vol. 34, pp.169–180,2015.

[62] Ramesh, B. K., Shreenivas, R. K., Achala, L. N., and Bujurke, N. M., "Similarity solutions of the MHD boundary layer flow past a constant wedge within porous media," *Math. Probl. Eng.,* vol. 2017, 11 pages, 2017.

[63] Reddy, M. V., Lakshminarayana, P., Vajravelu, K., “A comparative study of MHD non-Newtonian fluid flows with the effects of chemical reaction and radiation over a stretching sheet”, *Comput. Therm. Sci., An Int. J.,* vol. 13, pp. 17-29, 2021.

[64] Reddy, N. B., Poornima, T., and Sreenivasulu, P., “Influence of variable thermal conductivity on MHD boundary layer slip flow of ethylene-glycol based Cu nanofluids over a stretching sheet with convective boundary condition”, *Int. J. Eng. Math.,* vol. 2014, 10 pages, 2014.

[65] Rehman, A., Salleh, Z., and Gul, T., “Heat transfer of thin-film flow over an unsteady stretching sheet with dynamic viscosity”, *J. Adv. Res. Fluid Mech. Therm. Sci.* vol. 81, pp. 67-81, 2021.

[66] Rudra, K. D., and Sharma, S., “Effects of variable viscosity on mixed convection heat and mass transfer past a wedge with variable temperature”, *Int. J. Math. Archive,* vol. 5, pp. 150-157, 2014.

[67] Rudra, K. D., and Sharma, S., Magnetohydrodynamic mixed convection flow past a wedge under variable temperature and chemical reaction”, *Am. J. Comput. Appl. Math.*, vol. 3, pp. 74-80, 2013.

[68] Sakiadis, B. C., “Boundary-layer behavior on continuous solid surfaces: I. Boundary-layer equations for two dimensional and axisymmetric flow”, AICHE J., vol. 7, pp. 26–28, 1961.

[69] Salleh, S. N. A., Bachok, N., Arifin, M. N., and Ali, M. F., and Pop, I., “Magnetohydrodynamic Flow Past a Moving Vertical Thin Needle in a Nanofluid with Stability Analysis”, *Energies* 2018, vol.11, 2018.

[70] Samuel Raj, J. W., and Devi, S. P. A., “Numerical analysis of nonlinear radiation, viscous and Ohmic dissipation effects on steady Magnetohydrodynamic forced convection flow over a shrinking surface with internal heat generation/absorption”, *Int. j. sci. res. math. stat. sci.,* vol. 7, pp. 09-16, 2020.

[71] Seddeek, M. A., Afify, A. A., and Al- Hanaya, A. M., “Similarity solutions for a steady MHD Falkner-Skan flow and heat transfer over a wedge considering the

effects of variable viscosity and thermal conductivity", *Appl. Appl. Math.,* vol. 4, pp. 301 – 313, 2009.

[72] Shaw, S., Kameswaran, P. K., and Sibanda, P., "Effects of slip-on nonlinear convection in nanofluid flow on stretching surfaces", *Bound. Value Probl.,* vol. 2016, pp.1-11, 2016.

[73] Soid, S. K., Ishak, A., and Pop, I., "Unsteady MHD flow and heat transfer over a shrinking sheet with ohmic heating", *Chin. J. Phys.,* vol. 55, pp.1626–1636, 2017.

[74] Srinivas, M., and Kishan, N., "Unsteady MHD flow and heat transfer of nanofluid over a permeable shrinking sheet with thermal radiation and chemical reaction", *Am. J. Eng. Res.,* vol. 4, pp. 68-79, 2015.

[75] Sulochana, C., Sandeep, N., Sugunamma, V., and Kumar, B. R., Aligned magnetic field and cross-diffusion effects of a nanofluid over an exponentially stretching surface in a porous medium", *Appl. Nanosci.,* vol. 6, pp. 737–746, 2015.

[76] Ullah, I., Shafie, S., and Khan, I., "Heat generation and absorption in MHD flow of Casson fluid past a stretching wedge with viscous dissipation and Newtonian heating", *J. Technol*., vol.80, pp.77–85, 2018.

[77] Yohannes, K. Y., and Shankar, B., "Heat and mass transfer in MHD flow of nanofluids through a porous media due to a stretching sheet with viscous dissipation and chemical reaction effects", *Caribb. J. Sci. Technol.,* vol.1, pp. 1-17, 2013.

[78] Nandy, S. K., Sidui, S., Mahapatra, T. R., "Unsteady MHD boundary-layer flow and heat transfer of nanofluid over a permeable shrinking sheet in the presence of thermal radiation", *Alex. Eng. J.*, vol. 53, pp. 929–937, 2014.

[79] Shateyi, S. and Muzara, H., "On the Numerical Analysis of Unsteady MHD Boundary Layer Flow of Williamson Fluid Over a Stretching Sheet and Heat and Mass Transfers", *Computation* 2020, vol. 8, 2020.

[80] Afridi, I. M., and Qasim, M., "Entropy generation and heat transfer in boundary layer flow over a thin needle moving in a parallel stream in the presence of nonlinear Rosseland radiation", *Int. J. Therm. Sci.,* vol. 123, pp. 117-128, 2018.

[81] Shateyi, S., Mabood, F., and Marewo, G. T., "On a New Numerical Approach on Micropolar Fluid, Heat and Mass Transfer Over an Unsteady Stretching Sheet Through Porous Media in the Presence of a Heat Source/ Sink and Chemical Reaction", chap. 12, pp. 289-312, INTECH, 2016.

[82] Shateyi, S. and Muzara, H., "Unsteady MHD Blasius and Sakiadis Flows with Variable Thermal Conductivity in the Presence of Thermal Radiation and Viscous Dissipation", *Front. Heat Mass Transf.,* vol.14, pp. 1- 11, 2020.

[83] Motsa, S. S., Dlamini, P. G., and Khumalo, M., "Spectral Relaxation Method and Spectral Quasi-linearization Method for Solving Unsteady Boundary Layer Flow Problems", *Adv. Math. Phys.,* vol. 2014, pp.1–12, 2014.

[84] Kadijah, M. A., "Numerical studies for MHD flow and gradient heat transport past a stretching sheet with radiation and heat production via DTM", *Appl. Appl. Math.,* vol 13, pp. 915-924, 2016.